Advancing the robustness of polarization and time bin quantum key distribution for free-space channels

by

Ramy Tannous

A thesis
presented to the University of Waterloo
in fulfillment of the
thesis requirement for the degree of
Doctor of Philosophy
in
Physics (Quantum Information)

Waterloo, Ontario, Canada, 2023

Examining Committee Membership

The following served on the Examining Committee for this thesis. The decision of the Examining Committee is by majority vote.

External Examiner:	Nicholas Peters Quantum Information Science Section , Oak Ridge National Laboratory
Supervisor:	Thomas Jennewein Associate Professor, Dept. of Physics & Astronomy, University of Waterloo
Internal Member:	Norbert Lütkenhaus Professor, Dept. of Physics & Astronomy, University of Waterloo
Internal-External Member:	Michael Reimer Associate Professor, Dept. of Electrical and Computer Engineering, University of Waterloo
Other Member:	Kostadinka Bizheva Professor, Dept. of Physics & Astronomy, University of Waterloo

Author's Declaration

This thesis consists of material all of which I authored or co-authored: see Statement of Contributions included in the thesis. This is a true copy of the thesis, including any required final revisions, as accepted by my examiners.

I understand that my thesis may be made electronically available to the public.

STATEMENT OF CONTRIBUTIONS

This thesis contains work done in collaboration with others but to which I made the major contribution. The contributions are listed below.

Chapter 1:
Ramy Tannous wrote the introductory chapter.

Chapter 2:
Thomas Jennewein conceived the idea of an inline polarization modulation system with input from Jean-Philippe Bourgoin, Brendon Higgins, and Ramy Tannous.
Daniel Kun and Ramy Tannous built a prototype and tested it.
Wilson Wu, Paul Godin, and Ramy Tannous improved the prototype and tested it. Ramy Tannous performed the analysis of the results.
Ramy Tannous wrote the chapter text.

Ramy Tannous and Thomas Jennewein conceived the concept of the moving RFI experiments.
Sebastian Slaman prepared the transmitter telescope setup.
Chithrabhanu Perumangatt and Ramy Tannous conducted the initial source characterizations.
Ramy Tannous put together the experimental setup with the guidance of Brendon Higgins. The experiments were conducted by Ramy Tannous with the assistance of Stéphane Vinet, Wilson Wu, Kimia Mohammadi, and Brendon Higgins.
Brendon Higgins wrote the coarse tracking and pointing software.
Ramy Tannous wrote the analysis software and utilized it to obtain the results.
Ramy Tannous wrote the chapter text.

Chapter 3:
Ramy Tannous and Thomas Jennewein conceived the concept of a full passive time bin scheme.
Jeongwan Jin built the field widened interferometer while Ramy Tannous put together the remainder of the experimental setup. Ramy Tannous performed the experiments with the assistance of Stéphane Vinet, Wilson Wu, and Dogan Sinar.
Ramy Tannous wrote the analysis software code and used it to analyze the results.
Ramy Tannous wrote the chapter text.

Chapter 4:
Ramy Tannous and Thomas Jennewein conceived the concept of an reflection based field widened interferometer.
Design validation with optical design software was conducted by Ramy Tannous. The numerical simulations were also performed by Ramy Tannous.
Prototyping and hardware testing was done by Ramy Tannous with the assistance of Tabitha Arulpragasam and Dogan Sinar.
Ramy Tannous performed the data analysis.
Ramy Tannous wrote the chapter text.

Chapter 5:
Thomas Jennewein and Ramy Tannous conceived the idea of a monolithic chassis for an interferometer.
Ramy Tannous conceived and performed the analytical calculations of the thermal expansion of functionally graded materials.
Ramy Tannous and Dogan Sinar designed and tested flexure devices.
The design of the monolithic chassis was conducted by Ramy Tannous with a lot of guidance from Mark Kirby and support of Dogan Sinar.
Ramy Tannous, Dogan Sinar and Tabitha Arulpragasam tested the optical and mechanical performance of the final structure.
Sagar Patel, Vlad Parserin, Mark Kirby, Issa Rishmawi, and Prof. Mihaela Vlassae conducted the material selection, adjusted the parameters of the manufacturing, and coordinated the construction of the enclosure.
Ramy Tannous wrote the chapter text.

Chapter 6:
Ramy Tannous wrote the concluding chapter.

ABSTRACT

Quantum networks are an emerging technology that aims to harness the power of quantum mechanics to revolutionize communication and computation. Many countries are establishing national quantum networks to modernizing their communication and computational infrastructure. Satellites are necessary to extend the distances between communication nodes to a global scale. Creating a global quantum network requires many such nodes to be built, increasing the overhead of a network. Thus, to increase adoption, reducing the overhead and increasing the robustness of the systems employed by these nodes are necessary.

In this thesis, we begin by developing an upgraded polarization modulation system for the weak coherent pulse source that will be used to connect with the Quantum Science and Encryption Satellite (QEYSSat). This new system is an inline optical fiber solution that completely avoids the stability and alignment issues that were present in previous versions. The inline scheme reduces the need for realignment and maintenance. The performance of the prototype system is analyzed and investigated. Another aspect of the QEYSSat mission is investigated. Particularly the feasibility of the 6-state 4-state reference frame independent (RFI) protocol for a moving free-space channel. By using RFI protocols, the random polarization rotations that occur in optical fibers can be compensated for, particularly in the optical fiber that connects the source to the QEYSSat ground station telescope. Thus eliminating the need for active polarization compensation systems. The robustness of the protocol to overcome polarization misalignment is investigated in the context of a QEYSSat pass.

Second, a fully passive time bin quantum key distribution scheme is developed and investigated. This scheme removes the need for active phase alignment of the interferometers between the two communication parties. Proof-of-concept experiments are conducted over several challenging channels, particularly highly multi mode optical fibers. This scheme is then used to investigate the feasibility of using near-infrared time bin encoded photons in a standard telecommunication optical fiber. Near-infrared is particularly interesting as many single quantum sources produce photons within this regime. The passive scheme is also tested in a moving free-space time bin demonstration. The results of these demonstrations are discussed, including the challenges that were encountered.

Third, a novel optical design for a field widened interferometer is investigated. The new optical design employs a fully reflective imaging system that is similar to an Offner relay. The new optical design allows for long relative path delays while maintaining a relatively compact physical footprint. The performance of the interferometer is tested for both single mode and multi mode signals. In addition, the achromatic performance of the design is tested. The device is also tested in a quantum sensing scenario, demonstrating its practicality beyond quantum communications.

Finally, a prototype of a monolithic chassis for the Offner relay interferometer is built using additive manufacturing with the objective of increasing the robustness of the interferometer. As part of the monolithic chassis, flexure devices are studied to be used instead of standard optomechanical components to provide the necessary degrees of freedom for optical alignment purposes. In addition, the thermal stability of the chassis is studied using finite element analysis with standard materials and an analytical analysis with functionally graded materials.

Through various studies, experiments, and component design, this thesis has advanced the practicality of both polarization and time bin encoding for free-space channels. Particularly increasing the potential for satellite deployable time bin interferometers. This work contributes to the long line of progress leading towards realizing a global quantum network.

ACKNOWLEDGMENTS

There are so many people to thank for the many experiences and growth that I have gained throughout my journey in graduate school and particularly in the field of quantum information. A large part of my experience was shaped by the people I interacted with along the way. To start, I would like to express my deepest gratitude to my supervisor Thomas Jennewein. Thank you for giving me so many opportunities to be curious and to grow as a scientist and researcher. I truly enjoyed all of our science conversations, brainstorming sessions, and journal club discussions. Your guidance and network has opened up so many opportunities for my that I am ever grateful for. I am looking forward to continuing to work together in the future.

I would also like to thank my Advisory Committee members: Norbert Lütkenhaus, Raymond Laflamme, and Michael Reimer for their discussions, guidance and feedback over the years. I would also like to thank Kostadinka Bizheva for joining my defense committee on short notice. I thank Nicholas Peters for being the external examiner of my defense.

I would like to thank the members past and present of the Quantum Photonics Laboratory. There are too many of you to mention but thank you for the helpful discussions, advice, hard work, crazy late nights, stargazing with the lab's many telescopes, and just general fun. The people you work with have a great influence on your experience, thank you for making it a good one. I look forward to seeing what the future has waiting for all of you. I would especially like to the thank the "Fun Office" of past and present (you know who you are), thank you all for making coming into work worth it. I appreciate all the amazing discussions, silly shenanigans, rude squash shots, and fun that was had. My experience wouldn't have been the same without all of you.

Thank you to all my friends that I met during my graduate school career. Especially those that have been there throughout the majority of my graduate studies. Many of you are all over the world now, but the experiences we shared together are truly memorable. Thank you for the many adventures, beach volleyball spikes, ultimate layouts, tennis/squash digs, sports ball viewings, inside jokes, laughs, and late nights. So much fun was had and shared throughout the years, and I look forward to many more. A special thanks to Rhyse Maryniuk for putting up with me for so many years and for feeding many carrots. I would also like to thank Matthew Brown for

being my idea soundboard with many helpful late night discussions. Thank you to my friends in Saskatchewan, thank you for being curious about what I do, supporting me from afar, and staying in touch despite the distance. To Shandelle Stroeder, thank you for supporting my crazy endeavors from afar, joining me on some fun adventures, and for supporting me even through the toughest of times.

I would also like to thank the IQC and physics staff, students and faculty, who have no idea how many times they have been super helpful and a joy to be around. Particularly the IQC staff, thank you for being helpful and going out of your way to help me on several occasions. I would like to thank Mark Kirby for the extremely beneficial advice on mechanical design, "how to design for additive", and on becoming a "Fusion Jedi". Brian Moffat for entrusting me with a lot of responsibility, maybe too much sometimes.

Thank you to all the funding agencies that helped me focus on my research throughout this degree: NSERC Canadian Graduate Scholarship, and the University of Waterloo for my personal funding. To CSA, NSERC, Ontario Ministry of Research and Innovation, CIFAR, Industry Canada, CFI, TQT, and DRDC for the research funding. Without these funds, none of this work would have been possible. I would also like to thank the Python Software Foundation and the public contributing community for many of the tools and tricks used in this thesis.

I would like particularly thank my family, my parents Victoria and George, and my brothers Fouad and Waseem for supporting me and encouraging me from afar. I could not have achieved this without your unconditional support.

There are so many people who have helped me along the way in many different ways. I am truly lucky and could not have achieved this degree without so many wonderful people.

DEDICATION

I dedicate this work to all those in need of perseverance while pursuing their passion.

Table of Contents

List of Figures

List of Tables

List of Abbreviations

AM Additive manufacturing 134, 135, 142–144, 148, 161, 162, 166, 169, 170, 172, 176, 192

APT Aquisition tracking and pointing 37–39, 43, 92, 93

AWG Arbitrary waveform generator 23, 25

CM Curved mirror xxi, 107, 109, 111–113, 121, 149, 151, 162, 164, 170

CSA Canadian Space Agency 1, 2, 12, 31

CTE Coefficient of thermal expansion 136, 138, 140, 148–150

CW Continuous wave 27, 31

EPS Entangled photon source 22, 44, 65–67, 69, 75, 78, 84, 101

FFT Fast Fourier transform 189

FM Flat mirror xxi, 107, 109, 111, 112, 121, 140

FWHM Full width at half maximum 14

GRIN Graded index 82, 92, 102

HWP Half-wave plate 30

IPMS Inline polarization modulation system xvi, 24–31, 40, 60, 197

LBD Lateral beam displacer 108, 121

LEO Low Earth Orbit 12, 21, 93

LP Linear polarizer 24, 26, 27

LPBF Laser powder bed fusion 143, 149, 162, 170, 172, 177

MMF Multi mode fiber 65, 67, 72, 75–78

MSAM Multi-scale additive manufacturing lab 133, 145, 146, 148, 149, 177

MZI Mach-Zehnder interferometer 22–24, 29, 30

NIR Near-infrared 79, 85, 89, 102, 198, 199

OD Optical density filter 40

ORI Offner relay interferometer xviii, xix, xxi, xxii, 105, 108–115, 117–124, 126, 128–133, 135, 139, 149–151, 162, 170, 188, 189, 191, 192

P Polarizer 28

PBS Polarization beam splitter 23, 42

PD Photodiode 26, 28

PM Phase modulator 23–26, 30

PMF Polarization maintaining fiber xvii, 24, 25, 27, 29, 31, 40–44, 60, 67, 69, 72, 74–76, 82, 84, 91, 197

PORI Printed Offner relay interferometer xx, xxii, 133, 170, 178–182, 184–188, 191, 192

POVM Positive operator-valued measure 45

PRBM Pseudo-rigid body model 18, 19

PRM Prism mirror 108, 109, 121

PTC Polarization to time bin converter xvii, 66–68, 75, 82, 84, 91, 93, 98, 101, 102

QBER Quantum bit error rate 26, 28, 29, 31, 33, 48, 52, 54–57, 60, 73–78, 80, 84, 86, 87, 89, 96, 98, 194, 197

QEYSSat Quantum Encryption and Science satellite 1, 2, 12, 13, 21–24, 29, 31, 33, 41, 42, 57, 59, 60, 194, 195, 197

QKD Quantum key distribution 3, 5, 12, 13, 22, 33, 34, 59, 62, 78, 80, 91, 104, 195

QPL Quantum Photonics Laboratory 1, 2, 12, 22, 31, 37, 197

RFI Reference frame independent 13, 14, 22, 33, 34, 41, 56, 60, 63, 64, 73, 76, 91, 195

RFI-QKD Reference frame independent quantum key distribution xvii, 59, 62, 63, 65–67, 71, 78, 84, 102, 104, 197

SiAPD Silicon avalanche photodiode 12

SMF Single mode fiber 67

SPAD Sinlge photon avalanche photodiode 2

SPD Single photon detectors 65

TA Time bin analyzer xvii, xviii, 67–72, 74–76, 78, 84, 91–93, 95, 98, 101, 102

WCPS Weak coherent pulse source xvi, 22, 27, 29–32, 194, 197

Chapter 1

Introduction

1.1 My time in the Quantum Photonics Lab

I joined the Quantum Photonics Laboratory (QPL) in September 2016 and completed a MSc. in August of 2018, under the supervision of Prof. Thomas Jennewein. This experience and the announcement of the Canadian Space Agency (CSA) funded Quantum Encryption and Science (QEYSSat) mission led me to pursue a Ph.D., starting in September 2018, in the development of quantum networks. Over the next five years, I have been given ample opportunities to pursue exciting research and be a part of a space mission from its announcement date, something truly unique for a graduate student. An experience that I shared with many of my graduate colleagues is that from March to September 2020, the Covid-19 outbreak suspended all in-person laboratory activities for QPL. All projects, save some theoretical studies, were put on hold during this time.

Nonetheless, throughout my time in the QPL I was involved in several projects, many of which did not make it into this thesis. I am happy to say I have collaborated with many great colleagues. From September 2018 to December 2019 I supported the development of a new fiber-based photon source led by visiting scholar Mengyu Xie and continued by Youn Seok Lee to be integrated into a new interferometer configuration. From September 2018 to June 2019, I conducted theoretical examination of the 6-state 4-state protocol in preparation for the delivery of an entangled photon source from the SpooQy lab of Prof. Alexander Ling. In May 2019, Chithrabhanu Perumangatt brought the SpooQy source from Singapore and together we conducted the initial testing. From June 2019 to March 2020, (resumed in September 2020 to May 2021), preparations for the moving tests were conducted with the help of Brendon Higgins. The moving tests themselves were conducted from July 2021 to December 2022 with the help of Stépahne Vinet, Wilson Wu, and Kimia Mohammadi. These are, as far as I know, the first

moving quantum key distribution demonstrations without any active polarization compensation systems.

From January 2019 until present, I have had the pleasure of working with and advising Simon Carrier from l'Université de Sherbrooke on an integrated single photon avalanche diode (SPAD) array that is dedicated to sifting data for time bin encoded photons. In October 2021, we conducted laboratory tests of the SPAD array at the University of Waterloo. From October 2019 to March 2020, visiting student Daniel Kun and I worked on advancing the weak coherent pulse source, particularly working on a new prototype polarization modulation system. Since then, I have worked with Wilson Wu and Paul Godin on progressing this prototype towards a deliverable system for the CSA.

From September 2019 to December 2020, I investigated the design of a novel field widened interferometer, an idea that was conceived by Prof. Thomas Jennewein and I in September 2019. This design continues to be refined today. From January 2021 to June 2022, a prototype of this design was made and tested with the help of Dogan Sinar and Tabitha Arulpragasam. From October 2020 to March 2021, I had the pleasure of working with Sagar Patel, Vlad Parserin, Mark Kirby, Issa Rishmawi, and Prof. Mihaela Vlassae of the Multi-Scale Additive Manufacturing Lab (MSAM). With their assistance, I was able to produce an interferometer chassis using additive manufacturing. This is a particularly great achievement since as a physicist I had little to know mechanical design background. With this device, Dogan Sinar and Tabitha Arulpragasam assisted in testing the device (March 2021 to June 2022).

In October 2021, Prof. Thomas Jennewein and I conceived the idea of a fully passive time bin scheme. From this concept, from October 2021 to December 2022, many experiments were conducted using this scheme over various quantum channels. This work was done with the help of Wilson Wu, Stéphane Vinet and Dogan Sinar. Since January 2022, I have supported the work of Stéphane Vinet on a bright entangled photon source.

In parallel with all these aforementioned projects, throughout my Ph.D., I have been one of the technical leads on developing QPL's quantum ground station for QEYSSat. This involved working with Youn Seok Lee, Paul Oh, Paul Godin, Wilson Wu, Kimia Mohammadi, Brendon Higgins, Matt Piatt, and Brian Moffat on various projects, such as the implementation of a polarization compensation system, the development of a polarization analysis pick-off, upgrading the overall weak coherent pulse, and the procurement of ground station equipment. All my experimental activities for this thesis ceased in December 2022. However, several projects continued during the writing process, particularly those that support the QEYSSat mission.

I will now use "we" rather than "I" to follow scientific writing conventions. Each chapter is prefaced with a statement of contribution to give credit to those that have helped me along the way.

1.2 Quantum key distribution

Quantum key distribution (QKD) is an application of quantum technology that provides means of generating and sharing information-theoretically secure secret keys between two remote parties (Alice and Bob) with security based on quantum mechanical principles. First introduced in 1984 with the advent of the BB84 protocol [1], QKD has become one of the most mature use cases of quantum information, with many different forms of QKD protocols appearing [2, 3, 4, 5]. The security in the majority, if not all, QKD protocols relies on the completeness of quantum mechanics [6, 7]. This general statement implies that any adversary to the key exchange is at least limited by the laws of quantum mechanics (i.e. cannot be unphysical) and by consequence, the no-cloning theorem applies[1].

The no-cloning theorem is a fundamental result in quantum mechanics that states that it is impossible to create an exact copy of an unknown quantum state [8]. It is essential for the security of QKD because it ensures that an eavesdropper (Eve) cannot measure or copy the shared quantum states without being detected.

While QKD is considered to be highly secure, there are still some practical limitations and potential vulnerabilities that need to be addressed. The vulnerabilities are mostly due to the physical implementation of the system; theses include side channel attacks, and the "blinding attack" [9]. Several studies attempt to address or mitigate the issues of practical implementations of QKD. The most notable is the decoy state protocol overcoming the photon number splitting attack [10]. Nonetheless, these vulnerabilities do not influence the security of the key once it is successfully generated using QKD. Thus, unlike many other key generation methods, the keys generated via QKD are future-proof.

Typically a standard quantum communication channel will perform the following steps:

1. **Initial authentication:** During any QKD exchange, Alice and Bob share an authenticated channel on which Eve cannot impersonate Alice or Bob. The establishment of the authenticated channel is assumed to be done prior to any key exchange and can remain valid for as long as the quantum channel between Alice and Bob remains unimpeded.

2. **Determine predefined parameters:** First, it is important that all parties involved in the QKD channel agree on the specific protocol to use, which will differ based on the hardware and implementation. Furthermore, many protocols require pre-established parameters that are constant between Alice and Bob. For example, in a phase-based encoding (such as in twin field QKD), the parties involved need to determine which sets of phases to use,

[1] In fact in relevant security proofs [7], the eavesdropper is only limited by the laws of quantum mechanics.

as there is an infinite number. In BB84, this would be the agreement on the two sets of mutually unbiased bases that are used to encode the quantum information.

3. **Photon exchange:** The photon carrying the quantum information are exchanged between all parties involved and creates remote correlations. The exact details of how this is performed can vary widely based on the exact protocol implemented. Further details can be found in the literature [5]. At the end of this step, the measurement results are known as the raw key.

4. **Basis reconciliation:** Many protocols require the parties involved to share information about what measurement basis was used to either encode or measure the information of the qubits. This is used to determine whether to keep or discard the results of a photon exchange based on whether or not the parties involved believe that their measurement[2] results should be correlated. At the end of this step, the measurement results are known as the sifted key.

5. **Parameter estimation:** With the sifted key, the key exchange parties must now determine whether or not to proceed further. Error rates are determined by using a subset of the sifted key. Given the protocol, below a certain error rate threshold, the protocol may proceed. While above this threshold, it is assumed[3] that an eavesdropper is strongly correlated to the sifted key, and thus it must be discarded. The subset of the sifted key used is discarded and not used in the final secret key.

6. **Error correction:** Provided the shifted key passes the parameter estimation step, error correction must be done to ensure that the key exchange parties share the same sifted key. There are many error correction protocols, some of the most common are Low Density Parity Check [11, 12, 13, 14] and CASCADE algorithms [15, 16].

7. **Privacy amplification:** This final step is to attempt to completely remove the eavesdropper correlation to the key. There are many ways to achieve this, however a common method is to use universal hash functions [17, 18]. Once this process is complete, the key exchange parties should now each possesses a copy of the exact same secret key that should be completely uncorrelated to any information an eavesdropper may have obtained.

With the secret key, Alice and Bob can perform their choice of encryption or authentication protocols that require a symmetric key [19, 20]. In this thesis, the error correction and privacy

[2] In a prepare & measure scheme, this would be whether or not the encoding basis matches the measurement basis. Therefore, it is whether or not the encoded qubit is correlated to the measured qubit.

[3] I say assumed here because in some cases it may be that the hardware has malfunctioned, however in the spirit of security all errors are due to an eavesdropper.

amplification steps are not performed, but their performance and bit consumption are estimated and accounted for during the various analyses.

Although encryption key sharing is the primary application of QKD hardware, the same devices can be used to establish a quantum network. In the community, there are countless research projects that are advancing the feasibility of quantum networks, from tackling the connectivity problem [21, 22], to breaking distance records [23, 24, 25], and developing space missions [5, 26]. In fact, many countries that have already begun to establish quantum key distribution networks [27, 28, 29], with more to come [30, 31, 32]. Thus, there is a growing need for practical and robust quantum network hardware capable of interfacing between satellite and terrestrial nodes.

1.3 Encoding quantum information on photons

In order to perform quantum key distribution, quantum information must be encoded on the flying qubits, i.e. photons. Although there are many different degrees of freedom to encode the information, (e.g. frequency [33], path [34], orbital angular momentum [35]), here we will describe the two types of encoding used throughout this work; polarization encoding, and time bin encoding.

1.3.1 Polarization encoding

The polarization of a photon can be well defined via the direction of oscillation of the electric field. Although, polarization itself is not inherently quantum, but rather the polarization of a single photon, combined with the superposition principle of electromagnetic waves, can create a quantum system. The polarization of a photon can represented by a spin-$\frac{1}{2}$ system. By using two orthogonal polarizations, e.g. horizontally (H) and vertically (V) polarized light, one has the eigenstates of one of the Pauli spin operators. This forms a basis of two orthogonal states that can represent the 0 and 1 state and are written as

$$|H\rangle = |0\rangle = \begin{pmatrix} 1 \\ 0 \end{pmatrix}, \tag{1.1}$$

$$|V\rangle = |1\rangle = \begin{pmatrix} 0 \\ 1 \end{pmatrix}. \tag{1.2}$$

Table 1.1: Examples of three mutually unbiased bases in polarization encoding.

Polarization	Ket	Matrix
$\|H\rangle$	$\|0\rangle$	$\begin{pmatrix}1\\0\end{pmatrix}$
$\|V\rangle$	$\|1\rangle$	$\begin{pmatrix}0\\1\end{pmatrix}$
$\|D\rangle$	$\frac{\|0\rangle+\|1\rangle}{2}$	$\begin{pmatrix}1\\1\end{pmatrix}$
$\|A\rangle$	$\frac{\|0\rangle-\|1\rangle}{2}$	$\begin{pmatrix}1\\-1\end{pmatrix}$
$\|R\rangle$	$\frac{\|0\rangle+i\|1\rangle}{2}$	$\begin{pmatrix}1\\i\end{pmatrix}$
$\|L\rangle$	$\frac{\|0\rangle-i\|1\rangle}{2}$	$\begin{pmatrix}1\\-i\end{pmatrix}$

The two Pauli spin operators have eigenstates that are superpositions of the eigenstates in the $|H\rangle$ and $|V\rangle$ basis. These polarization states are shown in Table. 1.1. Now, if any of these states is measured in the same basis that it was produced from, the measurement results will yield the original state with certainty. However, a state that is measured in either of the two mutually unbiased bases will result in a random outcome that is uniformly distributed over all the outcomes of the measurement[4]. This phenomenon occurs in all other encoding types and is not exclusive to polarization.

1.3.2 Time bin encoding

Time bin encoding is typically the encoding of choice used in fiber optic quantum channels [36, 37]. In a two party quantum communication exchange that uses time bin encoding, the sender and receiver both have identical interferometers that will encode and measure the time bin qubits (Figure. 1.1). After passing through the measurement interferometer, a histogram of the accumulated photon counts will have three distinct time bin peaks. The two outside time

[4] In this case it is 50%

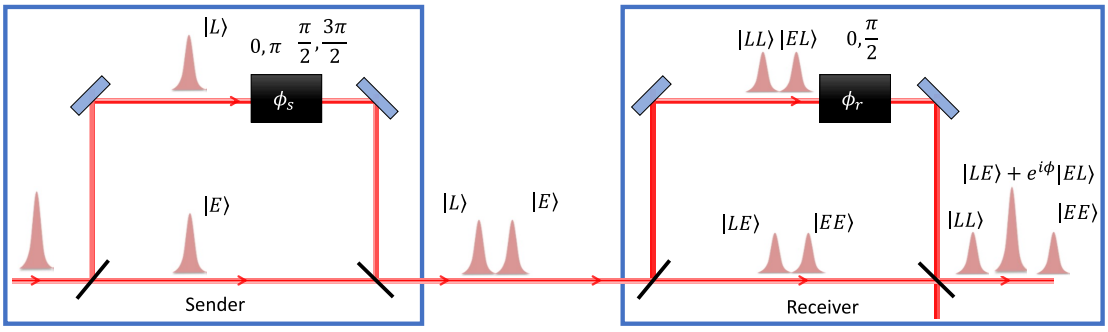

Figure 1.1: Schematic of a prepare & measure time bin quantum communication channel. Both optical outputs of the receiver interferometer are typically used, however only one is shown.

bins (known as the satellite time bins) typically form the computational basis. No interference effects are observed in these time bins thus no phase information is measured in this basis. The middle time bin can form an infinite number of superposition bases on which interference effects can be measured and thus phase information can be encoded. Although an infinite number of superposition bases can be made, for practical purposes this is typically limited to one or two, such as in BB84 [1].

The phase encoding in time bin is typically created by the relative phase difference between the two paths of the sender interferometer[5]. In order to properly measure the phase, the measurement interferometer must have a relative phase difference between its two paths be an integer multiple of the sender's relative phase (Figure. 1.1). For example, if a π phase difference is encoded, then the measurement interferometer must have a relative phase difference of $n\pi$ where $n = 0, 1, 2, \ldots$. Ideally, $n \leq 2$ (i.e. small) as the phase difference is typically associated with a time delay and thus for large n the coherence length of the light becomes a factor.

For the success of the link it is very important that the phase encoding information have a well defined reference that is shared between the sender and receiver. The sender's and receivers phase difference of their respective interferometers must have the same 0 phase reference (modulo π) as the measurement interferometer[6]. Many different environmental effects can cause the 0 phase reference to be different, particularly temperature and mechanical fluctuations are discussed in Chap. 5. There are several ways to combat the changes in the reference phase, the most common is to use a bright reference laser whose phase is monitored and an active feedback

[5] In many cases this is achieved by a electro-optic phase modulator placed in one of the interferometer paths

[6] Effectively this means that the phase of Alice and Bob's respective interferometers just needs to sum to zero modulo π. For example, if Alice encodes $\frac{\pi}{2}$ then in order to properly resolve the phase, Bob must have a phase difference of $\frac{n\pi}{2}$ where $n = 1, 3, 5, \ldots$.

loop adjusts one or both of the interferometers to compensate for the phase drifts. However, there are several drawbacks to this approach, particularly that additional overhead is required for its implementation. Furthermore, in the case of free-space links the bright reference laser could experience intensity fluctuations due to atmospheric turbulence (scintillation, Sec. 1.4.1.3) and make it difficult to monitor the reference phase.

1.4 Quantum Channels

Connecting two communication parties over long distances is an integral part of a global quantum network. This is implemented using two types of channels, optical fibers and free-space[7]. Optical fiber channels are quite robust as they can provide connections between two parties without a direct line of sight. Another benefit of using optical fiber links is that large-scale telecommunication fiber networks are already in place due to the telecommunications industry. Quantum signals can be directly inserted into the active telecommunication fibers which will significantly reduce the need to install new infrastructure, and thus reducing the adoption costs. However, birefringence in the optical fibers causes many issues for polarization encoded schemes and thus fiber optical links generally favor phase and time bin encoding. Another challenge is the absorption losses exhibited by optical fibers. For classical telecommunication protocols losses are typically not an issue as repeaters and amplifiers may be used. Unfortunately, despite the recent progress in quantum memories and repeaters [40], there is currently no off-the-shelf implementation of quantum repeaters. Thus, due to the losses, optical fiber links are typically limited to distances of a few hundred kilometers [41, 42].

For long distances, free-space links are used to overcome the absorption losses, as the scaling of loss with distance in a free-space channel is quadratic [43], versus the exponential losses in optical fiber [44]. However, free-space links must overcome the challenges of atmospheric turbulence and the need for a clear direct line of sight. The effects of atmospheric turbulence are worse for terrestrial point-to-point links as a thick atmosphere is present throughout the link. Furthermore, terrestrial links have to consider the curvature of the Earth for the direct line of sight link. Thus, despite the reduced absorption losses, terrestrial free-space links are still limited to a few hundred kilometers [45].

Satellites offer a means to increase the transmission distance between two communication parties. The satellite can connect two parties by being a trusted or untrusted node. The latter typically requires the satellite to link two ground stations simultaneously, however advances in

[7] Several other channels exist such as submarine [38, 39], however, here we discuss the most common channels used.

quantum memory technology can allow for non-line of sight links. In contrast, trusted nodes can be used to connect two ground stations at different times [46, 47]. In contrast to terrestrial links, satellite free-space channels suffer from only a few kilometers of atmospheric turbulence and absorption since only a small portion of the link is within the turbulent atmosphere[8].

There are two types of directions for a ground to space quantum link: downlinks where the photons are generated on the satellite and sent to receivers on the ground, and uplinks where the photons are generated at a ground station and sent to a satellite receiver. Using an uplink has some advantages over the downlink configuration. For instance, receiver satellites have a relatively simple design due to the less demanding classical processing and storage requirements. Furthermore, uplinks have the flexibility of utilizing different novel quantum sources with the same receiver apparatus, such as quantum dot sources [48]. However, under similar conditions, an uplink configuration has a lower link performance than a downlink due to the atmospheric turbulence effects (Sec. 1.4.1.3) [49]. This is due to the beam propagation being affected at the start of its optical path as opposed to the end.

1.4.1 Distortion mechanisms in free-space channels

A free-space link experiences losses and distortions due to the effects of the atmosphere. These losses and distortions can come from a number of contributing factors including, beam diffraction, atmospheric absorption, scattering, beam wander due to turbulence and equipment error, and finally total system throughput [43]. Obviously, many of these factors can be minimized by proper design choices, particularly the latter.

Beam diffraction, atmospheric absorption and scattering are important factors to consider when designing a free-space optical link. However, theses are not a major focus of this thesis and the works contained and are therefore very briefly described below. Nonetheless, the reader is encouraged to review the relevant literature on this topic [49, 43, 50]. The effects mechanisms that significantly contribute to wavefront distortions, such as beam wander due to turbulence and equipment error, are described in detail as they are a major inhibitor to the widespread adoption of time bin encoding over free-space (see Sec. 1.6).

1.4.1.1 Diffraction

A collimated Gaussian beam in free-space will have some minimum beam radius or waist that will naturally expand as the light propagates. This expansion is called diffraction. Even in the

[8] At a certain altitude the atmospheric density is reduced such that turbulence is no longer an issue.

vacuum of space, a Gaussian beam will eventually diverge due to diffraction. Diffraction is a fundamental property of waves, including light, and it causes a beam of light to spread out as it propagates through space. In terms of an optical (or quantum) communications link, even with the absence of other loss mechanisms, there would still be an induced loss due to the finite size of the receiver [9]. Thus, optimization of the transmitter and receiver apertures can be done to minimize this effect [49].

1.4.1.2 Absorption and scattering

The composition of the material that the light is propagating through can cause absorption and scattering. In free-space channels, the chemical composition of the atmosphere plays a role in both absorption and scattering. For absorption, it is the specific chemicals (i.e. N_2, CO_2, H_2O) that determine the specific absorption bands of the atmosphere. This can cause losses in transmission at specific wavelengths, and thus the source wavelength must be selected appropriately.

Although there are many types of scattering that can occur in the atmosphere, there are three types of scattering that are relevant for low power free-space quantum links; Rayleigh, Mie, and nonselective scattering [51, 52]. The type of scattering is influenced by the the size of the particle that the the light interacts with. Raleigh scattering is caused by elastic scattering of light by particles much smaller than the wavelength of the light. The amount of Rayleigh scattering is inversely proportional to the fourth power of the wavelength. Mie scattering is caused by larger particles in the air, such as aerosol particles or pollen, that are on the order of the wavelength of light. Nonselective scattering occurs when the particles are much larger than the wavelength of light, e.g. water droplets. This type of scattering has the smallest wavelength dependent and the reason that clouds appear white. Overall, for the success of a free-space quantum channel, source wavelength selection is a very important criteria in reducing the losses due to scattering.

1.4.1.3 Atmospheric turbulence

Atmospheric turbulence is generally caused by the irregular movement of air masses in the atmosphere. These irregularities can be caused by various meteorological factors, but can mostly be attributed to thermal effects. Regardless, theses irregularities create small pockets of air with different densities. This causes localized differences in the index of refraction of the air and can lead to scintillation, beam wander, beam spreading, and coma (among other higher order effects). The magnitude of the atmospheric turbulence depends on the location and distance of

[9] This is provided that the receiver telescope is sufficiently far that the spot size of the signal is larger than its aperture.

atmosphere that the light is propagating through. The more atmosphere one must pass, the higher amount of atmospheric turbulence will be experienced.

Atmospheric turbulence can be quantified using the refractive index structure constant (C_n^2) which is essentially a metric of the strength of the atmospheric turbulence. There are several models that attempt to predict the C_n^2 for different scenarios and atmospheric conditions [53, 51, 54]. However, due to the complexity of modeling such systems, none of the models perfectly match the measured data obtained through the various measurement campaigns [55, 56]. Nonetheless, from a qualitative perspective, the higher the C_n^2 the stronger the atmospheric turbulence effects.

Scintillation is the rapid fluctuation of the intensity of the light beam. When the beam is larger than the regions of different indices of refraction, scintillation can be seen as a shimmering effect. Scintillation has little to no effect on the performance for polarization encoding based free-space links as it is the average long-term intensity[10] that contributes to the key generation. However, for time bin encoded free-space channels, scintillation can be detrimental as it causes wavefront distortions which negatively affects the performance of the system.

Beam wander is typically seen when the beam is smaller than the different air pockets. The beam is deflected and causes pointing errors in short time scales. In terms of losses, beam wander causes the optical signal to miss the receiver temporarily or strain the pointing system used. This must be accounted for in both polarization and time bin encoding quantum channels. However, beam wander also causes slight changes in the angle of incidence of the beam on the receiver telescope which has the most significant impact on time bin encoding schemes.

Beam spreading and coma are similar effects as they are caused by higher order phase errors that are introduced into the beam. Beam spreading is an increase in the diffraction of the optical signal and over a long distance, results in a larger than anticipated broadening of beam. This can reduce the amount of power received at the receiver and make it more difficult to maintain a stable link. Coma is a wavefront distortion that causes the beam of the transmitted signal to become elongated in one direction[11], similar to the effect of astigmatism in human eyes. As with the other wavefront distortions, coma has a negative effect on the performance of time bin free-space channels.

All of these atmospheric turbulence effects are typically addressed by adaptive optics, which increases the overhead of the system used [57, 58, 59, 60, 61]. This is particularly necessary for time bin encoding as the affects of atmospheric turbulence are much more pronounced. Sec. 1.6 discusses in detail the effects of wavefront distortions and angle of incidence on the performance of a time bin system.

[10] More accurately the average long-term collection of photons.

[11] In the plane perpendicular to the optical axis

1.4.1.4 Equipment pointing error

Although there are many solutions and feedback systems that can be used to properly align the sender and receiver telescopes in a free-space optical link, the accuracy of these systems can be a contributor to losses in the form of a long-term beam wander. More specifically, the pointing errors of the system can be averaged over time and be expressed as beam broadening [62, 63]. Larger receiver telescope apertures can help to relax the pointing requirements of the system, but for satellites, telescope apertures are typically restricted. Pointing errors do not only contribute to losses, but also contribute to variations in angles of incidence. As discussed further in Sec. 1.6, these angles of incidence can have a detrimental effect on the performance of the quantum channel particularly for time bin encoding.

1.4.2 Quantum Encryption and Science Satellite

Recently there have been many implementations of optical quantum devices being deployed as payloads on satellites [26, 47]. Of particular note is the soon to be launched Quantum Encryption and Science Satellite (QEYSSat) that is funded by the Canadian Space Agency (CSA) [64, 65]. The QEYSSat science team is led by Prof. Thomas Jennewein. The Quantum Photonics Laboratory (QPL) is commissioned with supporting the project through technical expertise of quantum sources and ground station hardware. The development and conceptual design of one such source is discussed in Sec. 2.1. Honeywell Aerospace is contracted to manufacture the satellite and some of the ground station supporting hardware [66]. QEYSSat will be launched in a low Earth orbit (LEO) similar to other quantum network satellites [26].

QEYSSat is a trusted node receiver that has the ability to measure four linear polarizations in two mutually unbiased bases. Thus, the primary links that QEYSSat will perform are uplink scenarios. Although, QEYSSat will also have a downlink source [67, 68], this is not discussed in this thesis. The uplink polarization state measurement is done using a free-space passive[12] 4-state analyzer. The four polarizations are measured using four single photon detectors particularly silicon avalanche photo diodes (SiAPD). The wavelength of the optical uplink for QEYSSat is selected to be from 780 nm to 795 nm due to several factors including the wavelength range of available single photons sources, the windows of low atmospheric absorption, and detector efficiency [49].

The primary objective of QEYSSat is to demonstrate long distance QKD and entanglement distribution. The protocols that will be tested are BB84 [1] and BBM92 [69]. However, other

[12] Passive here refers to the means by which the receiver selects its measurement basis. Passive systems typically use a beam splitter (in this case a 50:50 splitter)

protocols, such as the 6-state 4-state protocol [70], may be tested during the extended science mission. The feasibility of using the 6-state 4-state protocol is discussed in Sec. 2.2.

1.5 6-state-4-state protocol

Reference frame independent (RFI) protocols allow for the two parties in a point-to-point quantum communication link to remove the constraint of a shared frame of reference. For example, in polarization encoding, this can be a shared geometric reference, i.e. what is considered horizontal or vertical. Such protocols have been proposed for a six-state entangled case [71]. However, for situations where resources are limited due to the strict power, and space limits, such as payloads for airplanes [72] and satellites [66], reducing the number of states used in the RFI protocol can be desired.

The 6-state 4-state protocol [70], which is used in several experiments in this thesis, is beneficial because one of the parties only requires a 4-state measurement. This is an important detail since many free-space receivers, such as QEYSSat, limit the number of detectors in order to limit resource requirements. Therefore the 6-state 4-state protocol is briefly described for the reader below. Although, the description below is for an entanglement based system, much like most QKD protocols, it can be easily modified for a prepare & measure scheme.

Alice and Bob share a state ρ_{AB} on which Alice makes a 6-state measurement, measuring in the computational (Z) basis and the superposition (X, Y) bases. Bob makes a 4-state measurement, measuring in the computational (Z) basis and a superposition (X) basis. The computational basis is fixed while the superposition bases are free to drift or rotate. Alice and Bob use the correlations in the computational basis ($\langle Z_A \otimes Z_B \rangle$) for the key generation. The correlations in the superposition bases ($\langle X_A \otimes X_B \rangle$, $\langle Y_A \otimes X_B \rangle$) are used to form a correlation parameter or C-parameter

$$C = \sqrt{\langle X_A \otimes X_B \rangle^2 + \langle Y_A \otimes X_B \rangle^2}, \tag{1.3}$$

where $C \leq 1$, with the equality indicating a maximally entangled state. Thus the objective of the two parties is to confirm that C is as close as possible to unity, and $C < 1$ is attributed to the presence of an eavesdropper. An error rate for the computational and superposition bases can be defined as,

$$QBER_{ZZ} = \frac{1 - \langle Z_A \otimes Z_B \rangle}{2}, \quad QBER_C = \frac{1 - \langle C \rangle}{2}, \tag{1.4}$$

where C is given by eq. 1.3. Generally, C is the amplitude of the maximum achievable visibility in the superposition bases. If there was no rotation/drift in the superposition correlations this would mean that the correlation values would be at fixed values and the maximum would be realized in one of the bases, for example $\langle X_A \otimes X_B \rangle = 1$ and $\langle Y_A \otimes X_B \rangle = 0$. However, in most use cases for an RFI protocol, $\langle X_A \otimes X_B \rangle$ and $\langle Y_A \otimes X_B \rangle$ will vary in value depending on the reference frame rotations/phase drifts in the channel and thus will not be at the maximum correlation value. Despite the rotations/phase drifts, the C-parameter will remain constant, provided that the rotations/phase drifts do not change too rapidly and sufficient counts are collected due to the statistical nature of C. Analysis on the robustness and statistical nature of C will be presented in detail in Sec. 2.2.3.

1.6 Time bin over free-space channels

Although time bin encoding is primarily used in fiber optic quantum channels, there are several reasons to use it over free-space channels. First, the group velocity dispersion over free-space channels is negligible ($-0.00597\,\mathrm{ps\,nm^{-1}\,km^{-1}}$ at 1550 nm in standard air at 15 °C) compared to optical fiber channels ($21.912\,\mathrm{ps\,nm^{-1}\,km^{-1}}$ at 1550 nm in fused silica). Thus the pulse width of the time bins over a free-space channel will not significantly change (3.5 ps over a 200 km link with a full width at half maximum (FWHM) of 3 nm for a 1550 nm signal [73]). Even when including the contributions of atmospheric turbulence on the perceived pulse width, the pulse width jitter is still relatively small, e.g. 4.5 ps for the 1550(3) nm signal traveling in 200 km of atmosphere [74]. Note for a 785 nm signal with a 3 nm FWHM ($-0.0631\,\mathrm{ps\,nm^{-1}\,km^{-1}}$ dispersion in free-space and $-114.28\,\mathrm{ps\,nm^{-1}\,km^{-1}}$ in optical fibers), the combination of dispersion and jitter through the atmosphere increases to 38 ps over the 200 km link. However, this is assuming that the light travels entirely through the atmosphere for 200 km, whereas in reality the effects would be reduced for a satellite link as the atmosphere becomes less dense. Second, while polarization encoding continues to be the standard for free-space channels, such systems can suffer from polarization rotations due to the stress of the optical elements of the transmitter or receiver system [75], and cannot be used over a depolarizing channel [76]. This causes additional system overhead and can be difficult to maintain without active compensation systems. Time bin encoding does not suffer from changes in the birefringence of the optical elements and it is not affected by depolarizing channels nor polarizing elements. The latter is particularly promising as it allows for the use of atomic line band pass filters [77] that are intrinsically polarizing since they use the Faraday effect to filter the incoming light to a very narrow frequency[13]. This is of particular interest for high noise environments such as daylight free-space channels [78, 79, 80, 81].

[13] However, the signal bandwidth and pulse width would become an issue.

Furthermore, creating highly polarized and well defined polarizations can be difficult, especially across a large telescope aperture. Finally, using time bin encoding in free-space channels simplifies interface with the optical fiber channels. Rather than constantly converting between time bin and polarization encoding, one could simply use time bin encoding for both channel types.

Despite the advantages, there are several challenges to using time bin encoding over a free-space channel. As aforementioned, the phase reference of the sender and receiver interferometer must be well defined and stable. Many moving platforms have a limited electronics and space budget, so adding additional hardware to stabilize the phase is typically not desired. In addition to this issue, a major problem for using time bin over free-space is the effects of atmospheric turbulence on the quality of the observed interference. Wavefront distortions and beam wander reduce the interference visibility by effectively turning the incoming signal into a multi mode signal. As explained further below (Sec. 1.6.1), the unbalanced interferometers used in time bin encoding are typically not suitable for multi mode signals, and thus for free-space quantum channels. The problem is worse for moving channels as the angle of incidence of the incoming beam is much more variable due to the difficulties involved in pointing and tracking systems. Thus in order to use time bin encoding over free-space channels, one must overcome the issues of atmospheric turbulence, or more simply create an unbalanced interferometer that can be used with multi mode signals.

1.6.1 Field-widened interferometers

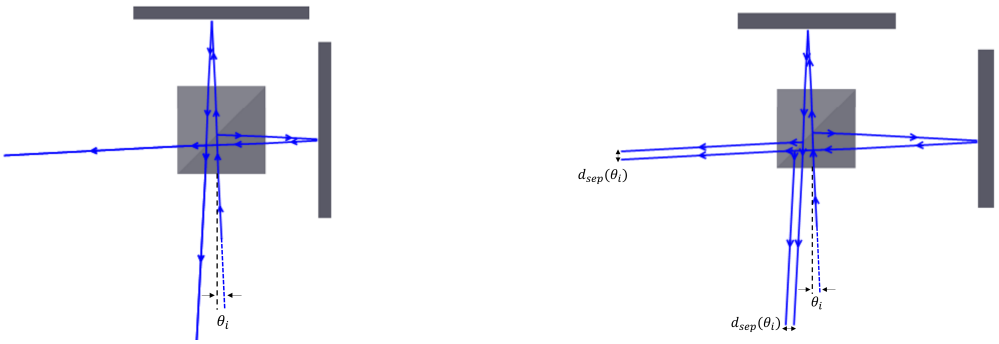

(a) Balanced Michelson (b) Unbalanced Michelson

Figure 1.2: (a) A balanced interferometer has no dependence of the overlap of the two paths based on the angle of incidence. (b) In an unbalanced interferometer, the paths become separated as the angle of incidence of the input beam is increased.

In order to have a high interference at the output of an interferometer, the light from the

two optical paths of the interferometer must occupy the same spatial mode, i.e. have the same $\vec{k}$. When dealing with multi mode signals, several spatial modes and $\vec{k}$ will be incident on the interferometer. To first order this can be approximated as rays with different angles of incidence. In a balanced interferometer, there is no issue and all signals will propagate and fully overlap when recombined at the output to interfere. This is because the angle of the rays emerging from the two paths is the same (Figure .1.2a). However, in the unbalanced case (Figure. 1.2b), the rays with different angle of incidence will propagate along the unbalanced arms and displace a distance $d_{\text{sep}}(\theta_i)$ at the output that is dependent on the angle of incidence θ_i at which the ray entered the interferometer. The larger θ_i, the larger the displaced distance $d_{\text{sep}}(\theta_i)$ and the lower the interference quality. This issue is not only relevant for free-space channels, but also for situations that use multi mode signals, i.e. time bin over highly multi mode fibers (Chap.3). In a similar manner to the angles of incidence, the various $\vec{k}$ of the multi mode signal will not properly overlap at the recombination of the two interferometric arms and hence the system will suffer from a reduced interference quality.

This issue is commonly overcome by using a spatial filter to remove all the light except for a single $\vec{k}$ [82, 83]. This typically comes at the price of a large amount of loss and a low photon throughput, something that is very undesirable for quantum networks. One can use adaptive optics to overcome the losses and reshape the wavefront and modal shape of the incident beam such that a large amount of the incident signal occupies a single mode [57].

However, to avoid using another active feedback system, one must use a special time bin interferometer that can maintain a high interference visibility with multi mode signals [84]. These interferometers, called field widened interferometers, were first developed for astronomy [85], were tested for quantum applications in Ref. [84], and have been used in quantum communication applications [86, 87].

As shown in Figure. 1.2b, the unbalanced interferometer experiences a reduced visibility due to the different angles of incidence, or spatial modes. However, for a field widened interferometer, the two paths of the interferometer are corrected such that the input optical signal is imaged to the output beam splitter such that $d_{\text{sep}}(\theta_i) = 0$ for any θ_i that is incident on the interferometer[14] as shown in [84]. Effectively, the system corrects the geometric (or angular) difference between the two paths while maintaining the time delay difference.

Previous works have demonstrated various different correcting optics techniques, such as using a piece of optically dense material in a balanced interferometer to create the illusion of an unbalanced interferometer [87, 84, 88], or by using a 4-f lens imaging system to correct the difference in output of each path [76]. Examples of each are shown in Figure. 1.3a and Figure. 1.3b.

[14] Any θ_i that is reasonable within the input NA of the interferometer.

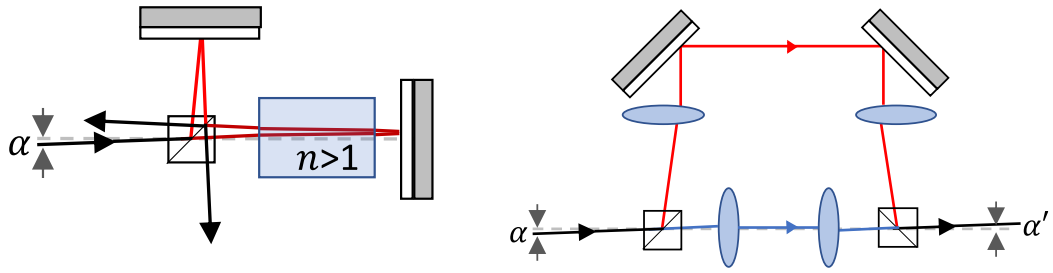

(a) (b)

Figure 1.3: Concepts of field widened interferometers using optically dense material (a) and a 4-f lens imaging system (b).

These field widened interferometers were used in the first demonstration of time bin encoded quantum signals being sent over a free-space quantum channel [76]. This demonstration showed the feasibility of the optical design concept that allowed the time bin interferometers to be used in such a setting. Although, the experiment was a success there are still a few challenges that remain. An active phase stabilization system was still employed to maintain the phase reference between the two interferometers. This is addressed in Chap. 3 by employing the 6-state 4-state protocol for time bin encoding. In addition, the field widened interferometer used was not stable due to their large size and were particularly vulnerable to thermal and vibrational noise. Work towards developing better interferometers is presented in Chap. 4 and a robust enclosure in Chap. 5.

1.7 Theory of flexures and compliant materials

Mechanical flexure devices, also known as compliant mechanisms, are widely used in various engineering and scientific applications, including optical and mechanical systems, sensing devices, and atomic force microscopy [89]. These devices consist of thin, flexible components that can bend or deform under mechanical stress, providing precise and repeatable motion or displacement. In Chap. 5 describes flexure devices are built and tested as replacements for optomechanical devices, since flexure devices have several advantages over traditional mechanical devices [89, 90, 91, 92]:

1. **High precision:** Flexure devices can provide highly precise motion and positioning with minimal friction and hysteresis. This makes them ideal for applications that require accurate and repeatable motion, such as in microscopy or precision machining.

2. **Lubrication-free:** Flexure devices do not require lubrication, which can reduce maintenance requirements and eliminate the risk of contamination in cleanroom environments. This can be an important advantage in applications where lubrication is difficult or impossible to apply, such as in vacuum or space environments.

3. **Increased lifespan:** Flexure devices have no sliding or rolling parts, which means they are less prone to wear and tear. This can improve their reliability and lifespan compared to traditional mechanical devices.

4. **Lightweight and compact:** Due to the reduced number of components flexure devices are typically more lightweight and compact compared to traditional devices. This makes them ideal for applications where space is limited or weight is a critical factor, such as in satellites and other aerospace applications.

5. **Multidirectional motion:** Flexure devices can provide multidirectional motion and deformation, which makes them versatile and particularly applicable for optical alignment where many degrees of freedom are typically required. See the TSK-45 tip-tilt and optical axis translation in Chap. 5.

6. **No backlash:** Flexure devices do not have "backlash", which means they can provide bidirectional motion without play. Traditional spring mechanisms suffer from backlash which can create alignment difficulties in highly sensitive optical apparatus.

The physical mechanism of flexure devices can be understood in terms of the principles of elasticity and deformation. Elasticity is the property of a material to deform under stress and return to its original shape when the stress is removed. When a force is applied to a flexure device, the elastic material deforms, resulting in a change in shape or position which is restored once the force is removed. The deformation of the device or material can be controlled and harnessed to achieve very precise movements or displacements. The design and operation of mechanical flexure devices relies on several key parameters, including the material properties of the flexure, the geometry of the device, and the applied forces. The material properties of the flexure, such as Young's modulus, determine the amount of deformation that can be achieved for a given force [93]. The geometry of the device, including the shape and size of the flexure, also plays a critical role in determining the device's performance characteristics, particularly its range of motion and sensitivity, as is seen in the testing done in Chap. 5. Finally, the applied forces must be carefully controlled to avoid exceeding the elastic limits of the device as this will plastically deform the material and thus damage the device.

Although, most engineers use a finite element analysis approach, an analytical method called the pseudo-rigid body model (PRBM) can be used for designing and analyzing flexure-based

devices [89]. The PRBM is based on the assumption that the flexure behaves like a rigid body, but with a set of equivalent compliance parameters that represent the deformation of the flexure, i.e. pivot points in the form of torsional springs. These parameters can be determined by analyzing the flexure's geometry and material properties. A compliance matrix is created from these parameters and can help the designer to predict the behavior of the flexure-based device under various loading conditions. The flexure is typically modeled as a set of parallel beams or links that are connected in series or parallel to achieve the desired motion. The compliance matrix of the flexure is calculated by considering the individual contributions of each link or beam to the overall compliance of the mechanism.

One of the advantages of the PRBM is that it allows the designer to optimize the design of the flexure-based device for specific performance criteria, such as range of motion, stiffness, or sensitivity. By adjusting the geometry and material properties of the flexure, the designer can control its compliance matrix and achieve the desired performance characteristics. For a good resource and many examples on the dynamics of flexures, the reader is encouraged to look at Ref. [89], particularly A1 of chapter 5. Other references about the design of flexures and compliant materials are Refs. [90, 92].

Although we do not use the PRBM in Chap. 5, there are some considerations that can be made based on the results of such analysis that should be considered in the design process. Considering that the results of PRBM analysis for the stiffness (k_{stiff}) of what is known as the equivalent torsional spring for a fixed-free beam[15] (see chapter 5 of Ref.[89]) is given by

$$k_{\text{stiff}} = 2.25\frac{EI}{L}, \tag{1.5}$$

where E is the Young's modulus of the material, I is the second moment of area of the cross section, and L is the length of the flexure segment that is bending. The torsional spring in Figure. 1.4b is placed at the point of highest strain, i.e. where the elastic behavior is experienced. Nonetheless, it should come to no surprise that the stiffness of the equivalent torsional spring is dependent on the material selection (E) and the geometry of the device (I, L) (see Figure. 1.4a). The displacement of the beam in the horizontal and vertical plane (a and b respectively) are given by,

$$a = (1-\gamma)L + \gamma L\cos\Theta \tag{1.6}$$

$$b = \gamma L\sin\Theta, \tag{1.7}$$

where γ is the characteristic radius factor, which is the ratio between the length of the beam and the length of the pseudo-rigid link. In Figure. 1.4b, for this particular example $\gamma = 0.85$, but

[15] The more accurate description for the flexures used in Chap. 5 is the fixed-guided beam. However, the fixed-free beam is sufficient for the purposes of this introduction, while the more detailed analysis can be left to the engineers.

generally γ is determined based on the geometry of the device and the direction of the applied force. Nonetheless, Eq. 1.7 provides a means to predict the displacement of the flexure device using its dimensions.

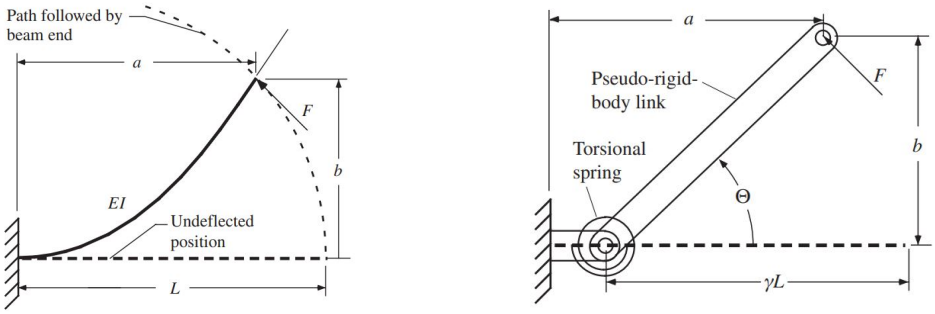

(a) (b)

Figure 1.4: The fixed-free beam (a) and its corresponding pseudo-rigid body model (b). Both figures are taken directly from chapter 5 of Ref. [89].

Once a material is selected, the main features of Eq. 1.5 that are to be considered in the design of a flexure is the cross section, or thickness of the compliant beam, and its length. The desired range of motion is achieved by fine tuning these parameters and using finite element analysis to determine if the resulting device behaves as expected. Overall, by controlling the material properties, geometry, and applied forces, flexure devices can be designed to provide precise and repeatable motion or displacement for a wide range of engineering and scientific applications.

Chapter 2

Enhancements for the QEYSSat ground to space link

An important milestone prior to start of the QEYSSat mission was the demonstration of a ground to airplane quantum communications channel [72]. However, despite the good performance, there were still some areas that needed improvement. This chapter focuses on two crucial enhancements that can further advance the performance of the quantum sources for QEYSSat. The first issue addressed is the stability of the weak coherent pulse source used in Ref. [72]. The previous design was vulnerable to air currents, leading to undesired errors, and required constant realignment to function properly. In Sec. 2.1, a new design is proposed, which is more robust and reduces the need for constant realignment. Making the new design practically plug-and-play, which is suitable for delivery to the various QEYSSat stakeholders. The second issue addressed is the need for an active polarization stabilization system at the output of the transmitter telescope. In Ref. [72], three rotating wave plates were used which can introduce undesired beam wander to the quantum signal and result in increased losses (Sec. 1.4.1.3). Sec. 2.2 proposes and studies using reference frame independent protocols, which eliminates the need for active polarization stabilization. Specifically, the feasibility of the 6-state and 4-state protocols is explored in the context of a LEO satellite link. The success of these tests removes the need for active polarization compensation, which reduces the additional hardware required in the transmitter system.

Statement of contribution

- **Inline polarization modulation system for the QEYSSat mission** Prof. Thomas Jennewein conceived the idea of using an inline polarization modulation system with some

input from Jean-Philippe Bourgoin, Brendon Higgins, and myself. Danial Kun and I performed the initial experiments and data collection. Paul Godin, Wilson Wu, and I performed the integration with the WCPS laser setup and testing. I conducted the analysis of the results shown.

- **Indoor moving 6-state 4-state demonstration** Prof. Thomas Jennewein and I conceived the idea of the moving RFI QKD experiments. Sebastian Slaman made the transmitter telescope assembly. I prepared the experimental setup and conducted the pointing systems tests with the guidance of Brendon Higgins. Chithrabhanu Perumangatt and I conducted the initial source characterizations. Stéphane Vinet, Wilson Wu, Kimia Mohammadi, and I conducted the experiments and data acquisition. Brendon Higgins assisted with troubleshooting the tracking and detection systems. I conducted the data analysis of the results presented.

2.1 Robust weak coherent pulse source for QEYSSat

The Quantum Encryption and Science Satellite (QEYSSat) is an integral part in Canada's development of quantum networks [66]. The QEYSSat mission is a technology demonstration that has a mission objective of performing a proof-of-principle uplink quantum communication experiment (see Sec. 1.4.2). Honeywell Aerospace is contracted to design and build the receiver satellite while the QPL group at the University of Waterloo is tasked with the quantum source design and University of Waterloo ground station development. There are two quantum sources that QPL is developing, a weak coherent pulse source (WCPS) and an entangle photon source (EPS). Discussion of the EPS is beyond the scope of this work, however it is based on a clever interferometer design [94]. In this section, some conceptual details of the new weak coherent pulse source design are provided, along with the testing of some supporting hardware components.

Following the work done for the airborne experiments of Ref. [72], there were several challenges that were identified for the baseline WCPS design that was used in those experiments. The first is that the source was quite unstable to temperature fluctuations and vibration noise. This is due to the Mach-Zehnder interferometer (MZI) that was used to create the polarization states, as seen in Figure. 2.1. Free-space delay lines are used to compensate for deviations in the path length of the two MZI arms. This allows for manual fine adjustments to obtain high-visibility of interference, and thus, high-quality output polarization states. However, these delay lines can cause intensity fluctuations which lead to polarization rotations. Such instabilities have been observed during outdoor operation of the WCPS during the experiments of Ref. [72, 76]. Furthermore, the free-space bridges needed to be realigned and calibrated regularly. Such a system

is not ideal for a practical quantum communication link, especially in the context of the QEYSSat mission where the sources will be at the Canadian Space Agency headquarters in St-Hubert. It is not ideal to require a technician to constantly readjust the system in order to achieve optimal performance. To overcome this issue, an inline polarization modulation setup is proposed and tested for improved stability and ease of alignment. By removing the free-space bridges of the old design and keeping everything in optical fibers, the new design promises to be a plug-and-play solution that requires little to no maintenance. Sec. 2.1.1 describes the new setup in detail and Sec. 2.1.2.2 presents some of the prototyping results.

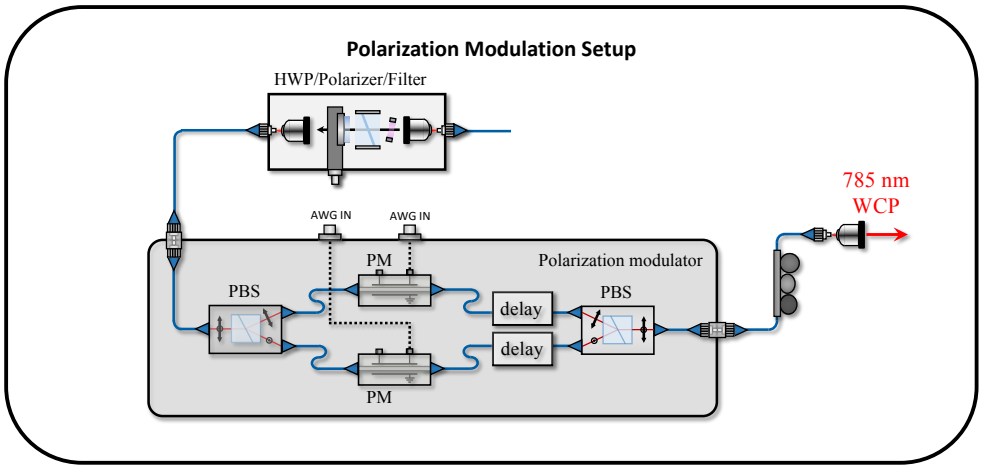

Figure 2.1: The baseline polarization modulation setup employs a Mach–Zehnder interferometer (MZI) to set the polarization state of the outgoing photons. The MZI consists of two polarizing beam splitters (PBS), two phase modulators (PM) and two free-space delay lines. Its output depends on the setting of the phase modulators (PMs), which are controlled by voltages applied by the arbitrary waveform generator (AWG). Some figure elements were created by Dr. Youn Seok Lee.

2.1.1 Inline Polarization Modulation Setup

The inline polarization modulation setup (IPMS) is an inline configuration based on two phase modulators (PMs), optics to manipulate polarization, and polarization maintaining fibers (PMF). The idea is to remove the free-space air bridges and to use the same concepts of the MZI setup, but put everything inline along the same optical fiber. This can be achieved due to the fact that PMF can separate two polarization modes with a high extinction ratio. Effectively, each polarization mode in the PMF acts as one "arm" of the MZI setup. However, the two arms are protected from the air currents that can cause rapid phase changes, and with the air gap delay lines completely removed, there is virtually no coupling losses to contend with.

The inline polarization modulation setup is based on designs found in Refs. [95, 96, 97] and a schematic of the setup can be seen in Fig. 2.2. The IPMS uses an input linear polarizer (LP) and half-wave plate to evenly couple a pulse into its horizontal (H) and vertical (V) components along each of the principal axes of the polarization maintaining fiber (slow and fast axis). Then the relative phase between the components of the pulses traveling in each axis is properly tuned to create any one of the four mutually unbiased polarization states at the output: diagonal (D), anti-diagonal (A), right-circular (R), and left-circular (L) states. The four polarization states are converted to the four linearly polarized states (H, V, D, A) after passing through a quarter-wave plate. When implemented for the QEYSSat mission, this quarter-wave plate will be located in the optical path prior to or at the transmitter telescope.

A major technical challenge of the IPMS is the compensation for the temporal walk-off that is caused primarily by the PMFs. This compensation is critical for the functionality of the IPMS. Any birefringent element, i.e. PMF and phase modulators, cause temporal walk-off between light propagating along the two different principal axes. This is caused by the difference in group velocities that are present in any birefringent material. The walk-off can be compensated by rotating the polarization by 90° at some point in the IPMS where the walk-off induced in the first length of the IPMS can be fully compensated by the second length. An ideal location for the rotation is after the first phase modulator and prior to the second. Since it is required that the pulse traveling through the slow axis of PM1 will then pass through the fast axis of PM2. The walk-off is compensated by adding additional lengths of PMF as needed in each leg of the IPMS. Though there are several ways to achieve the compensation, using PMF is the most robust, cost effective, and requires the least overhead. Additional information on how the walk-off affects the source performance can be found in the Master's thesis of Wilson Wu (in preparation).

In Figure. 2.2, a free-space bridge with a half-wave plate is used to rotate the polarization by 90°. This is only used for prototype testing and the final implementation of the IPMS will use a completely fiber based solution by rotating the alignment key of the PMF by 90°. A completely fiber based solution avoids coupling losses across the free-space bridge and avoids the concern

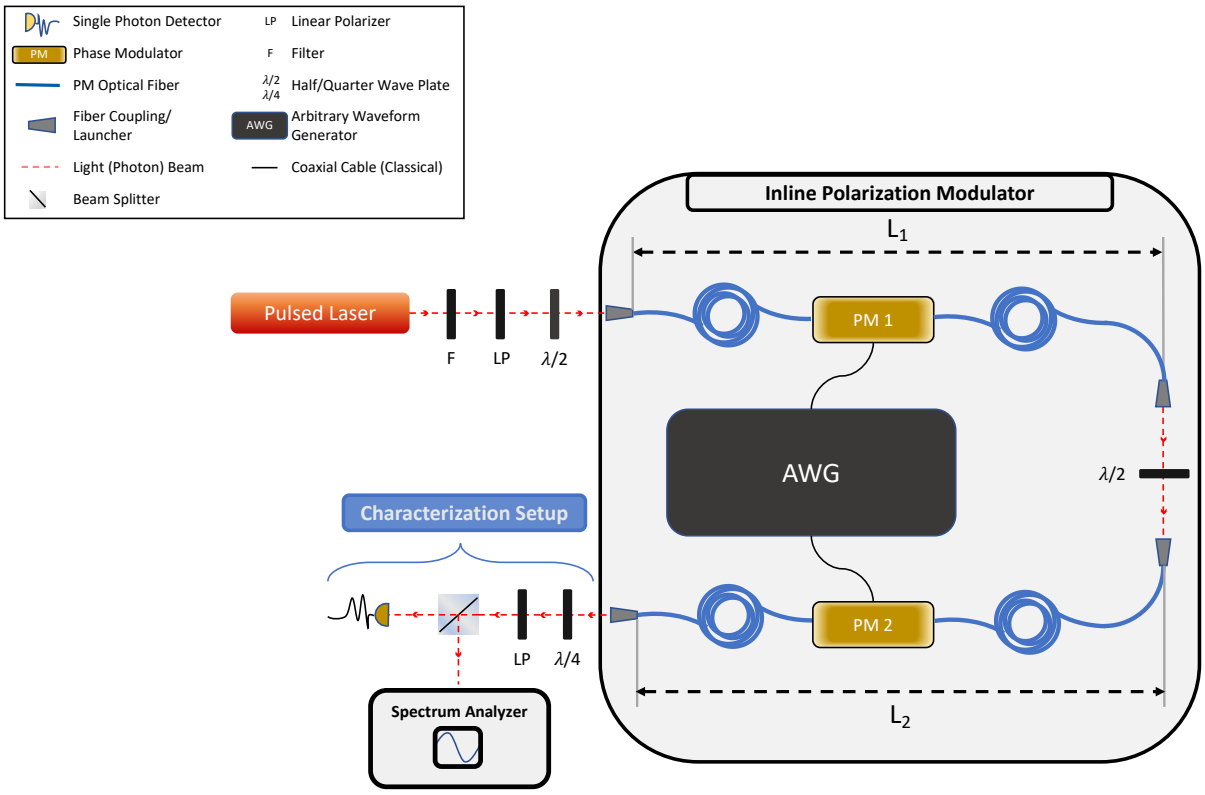

Figure 2.2: The polarization modulation setup is preceded by a filter-polarizer-HWP setup, filtering out unwanted wavelengths from frequency-doubling from the non-linear medium and subsequently setting a diagonal polarization for polarization modulation. The inline polarization modulation setup consists of two phase modulators (PMs), polarization rotating optics and PMFs. Its output depends on the setting of the phase modulators, which are controlled by voltages applied by the arbitrary waveform generator (AWG).

of long-term stability of the coupling. However, alignment of the PMF key is critical as rotation errors can have a negative effect on the polarization output and thus increases the intrinsic error rate of the system. Therefore, manufacturing tolerances must be tight to ensure a low intrinsic error rate. Furthermore, the physical footprint of the IPMS is substantially reduced by the use of all fiber based components.

The two phase modulators in Figure. 2.2 are necessary due to the difficulty to find function generators that can operate at fast duty cycles ($>$ 300MHz) and output sufficiently high voltages without an amplifier. Amplifiers typically distort signals and are thus not ideal for this appli-

cation, where the polarization states must be set very accurately, i.e. $< 1\%$ intrinsic error rate. If it was possible to provide sufficient voltage at such high repetition rates, then a single phase modulator could be used. However, here one phase modulator can only provide up to a π phase shift, thus with two a full 2π may be achieved.

2.1.2 Polarization Visibility

2.1.2.1 Measurement Setup and Procedure

To quantify the IPMS' capability to properly modulate polarization states with low errors, polarization visibility measurements were made. The visibility allows the user to quantify the quality of the output polarization and is found by measuring the polarization with a linear polarizer and a photodiode. The current of the PD response is measured using an oscilloscope and read as a voltage, see Fig 2.3. The output polarization is modulated until the PD response is maximized and then minimized. By recording the maximum and minimum values of the PD current, we can calculate the visibility of the setup via

$$\text{Vis} = \frac{I_{\text{max}} - I_{\text{min}}}{I_{\text{max}} + I_{\text{min}}}, \tag{2.1}$$

where I_{min} and I_{max} are the minimum and maximum intensity values as observed by the oscilloscope. The ideal visibility result is $\text{Vis} = 1$, indicating the modulation setup can perfectly set polarization states, without any issues. In reality, imperfections and background noise lead to deviations from the ideal and a quantum bit error rate (QBER) can be calculated by $(1 - \text{Vis})/2$. To facilitate the measurements, the phase modulators are driven (one at a time) such that a π phase shift is applied so the intensity reaches both I_{max} and I_{min} at least once per period.

The apparatus that used to obtain measurement results from the IPMS is shown in Fig. 2.2 under "Characterization Setup" and the physical setup is presented in Fig. 2.3. The measurement consists of applying a ramp voltage, seen in Fig. 2.4a, to one of the two PMs in Fig. 2.5a such that the polarization state is rotated over a phase $\phi > \pi$. The output of the PMs is rotating from H to D, to V, to A (depending on the phase applied). This output polarization is then measured by a linear polarizer set at a fixed angle, e.g. to allow all H polarized light to pass through but block all V polarized light. The light is then incident on a photodiode that measures the intensity of the light that passed through the polarizer and the current response is measured with an oscilloscope as a voltage across the terminating resistor. The photodiode output should resemble a sinusoidal curve as seen in Fig. 2.4b, and when the voltage in Fig. 2.4b reaches a maximum, the output polarization of the IPMS is as close to the LP setting as it can possibly produce (in this example H

polarized). Conversely, when the voltage reaches a minimum, that means the output polarization of the IPMS is as close to being anti-aligned to the LP setting as it can produce (in this example V polarized). We quantify the quality of the output in terms of polarization visibility. A ramp voltage is used to achieve a sinusoidal response from the applied phase. A linear phase change will result in a sinusoidal change in the intensity at the measurement polarizer.

2.1.2.2 Results and Analysis

The visibility was measured using two laser sources, a continuous wave (CW) external cavity diode laser (Toptica DLPro) and a 0.2 ps mode-locked pulsed laser (Mira 900). A fast photodiode (LeCroy OE425) is used in both cases and has a bandwidth much larger than the repetition rate of the pulsed laser (4.5 GHz compared to 80 MHz), thus there is no saturation of the measurement device. The CW laser is used to get an upper bound on the visibility of the IPMS, as the temporal walk-off caused by the PMF would be minimal for a CW laser. These results are shown in Fig. 2.6a with the IPMS consistently provided visibilities above 99.0%. This indicates that for longer pulse widths, i.e., greater than 100 ps, the visibility should be of similar quality. Conversely, the pulsed light source consistently produced visibility of 85.0%, shown in Figure. 2.6b. The low visibility of the pulsed source is primarily due to the temporal walk-off of the narrow pulse width of the pulsed laser source used for prototyping experiments. Compensation for the temporal walk off is critical to increasing the visibility and was done using additional lengths of PMF available in the laboratory, the shortest of which is approximately 20 cm long. For future iterations of the IPMS (Sec. 2.1.2.3), the lengths of PMF used for compensation will be made in-house which will compensate the exact temporal walk-off. We note that the narrow pulse width of the laser source used to characterize the system, approximately 0.2 ps, is four orders of magnitude smaller than that of the the WCPS laser source used in Ref. [72] and that of the current WCPS laser setup, which is around 100 ps, and significantly impacts the measured visibility in the lab compared to that of the WCPS laser setup.

2.1.2.3 Integration with WCPS laser setup

The IPMS was integrated with the weak coherent pulse source laser setup and arbitrary waveform generator. The weak coherent pulse source laser setup produces pulses that have a 100 ps pulse width. The IPMS that was tested has significant improvements compared to the previous prototype tested in Sec. 2.1.2.2. Custom compensating PMF lengths were used to improve the visibility of the system and the free-space bridge for polarization rotation was replaced with a properly keyed PMF. The visibility of the improved IPMS with the WCPS laser setup is 97%

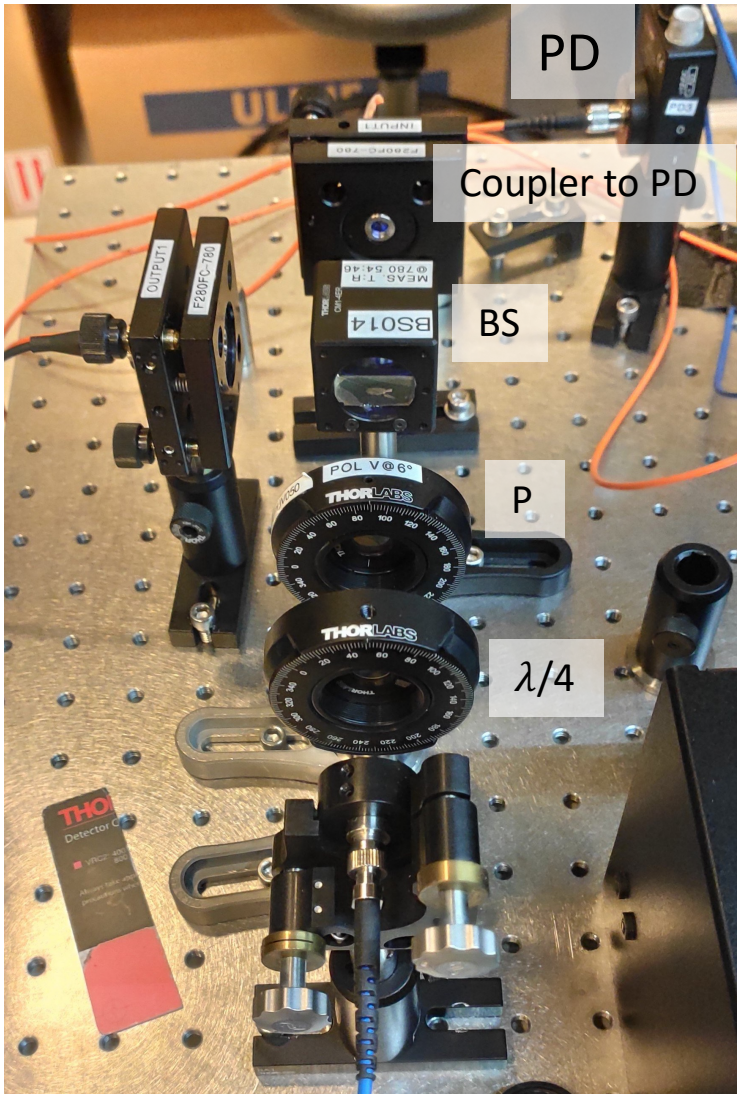

Figure 2.3: Visibility measurement setup used to characterize the output polarization quality of the IPMS. The quarter-wave plate ($\lambda/4$) allows to measure all superposition states (R,D,L,A) created by the IPMS as the basis states (H,D,L,A). The polarizer (P) is set to an angle corresponding to one of the four states. The transmitted light is then coupled into a photodiode (PD) for detection using an oscilloscope. Visibility is defined in Eq. 2.1.

which gives an intrinsic QBER of 1.5%. Figure. 2.7b shows the four polarization states as measured at the output of the IPMS with a single photon detector. Although this is a significant

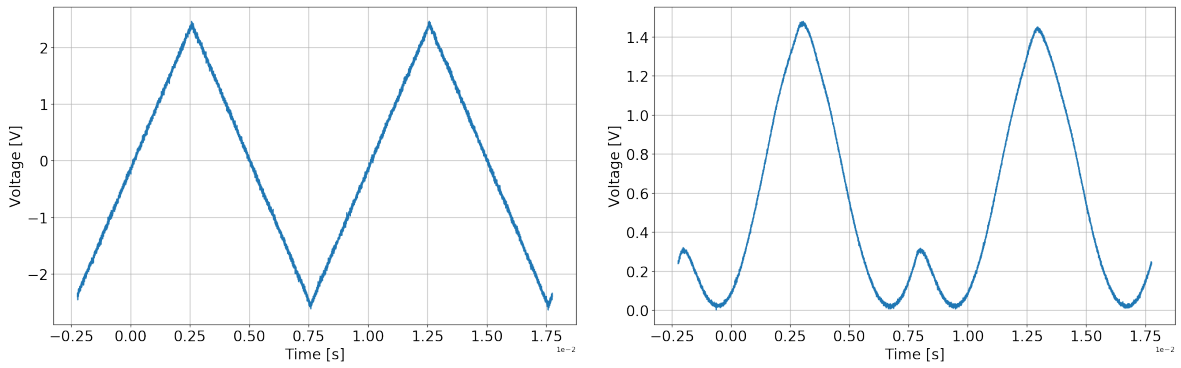

(a) (b)

Figure 2.4: Modulation input voltage and response curve. The input used was a linear ramp voltage while the response from the photodiode has a sinusoidal shape. (a) Function generator output of ramp voltage with $V_{pp} = 5\,V$. (b) Photodiode response as measured on an oscilloscope. The sinusoidal curve is a typical response when driving a phase modulator with a ramp voltage.

improvement compared to the 85% previously reported with the 0.2 ps source, it is still currently not sufficient since the requirement for QEYSSat is an intrinsic source QBER of $< 1\%$. Nonetheless, at the time of writing, progress is being made to improve the walk-off mismatch and the rotation errors caused by each connection of PMF.

2.1.3 Phase Stability

A qualitative study of the phase and vibrational stability of the IPMS has been done. The previously implemented MZI setup [72] is very sensitive to temperature fluctuations and mechanical vibrations. This is primarily due to the air gaps (delay lines) used in the MZI, coupled with the inherent interferometer characteristics of the setup. These delay lines can cause intensity fluctuations which lead to polarization rotations and an increase in the intrinsic error rate of the system. Such instabilities have been observed during operation of the WCPS in field tests and is the motivation for the study of the IPMS.

In comparison, the IPMS setup is relatively stable over time. Observed phase drifts were small over the course of a 30 minute period in the laboratory setting, as seen in Figs. 2.8a and 2.8b. Theses preliminary results of the phase stability indicate phase drifts on the order of 0.0037 rad/s. These small drifts are primarily due to instability in the function generator driving the phase modulators. Nonetheless, this slow drift can be easily compensated by applying a

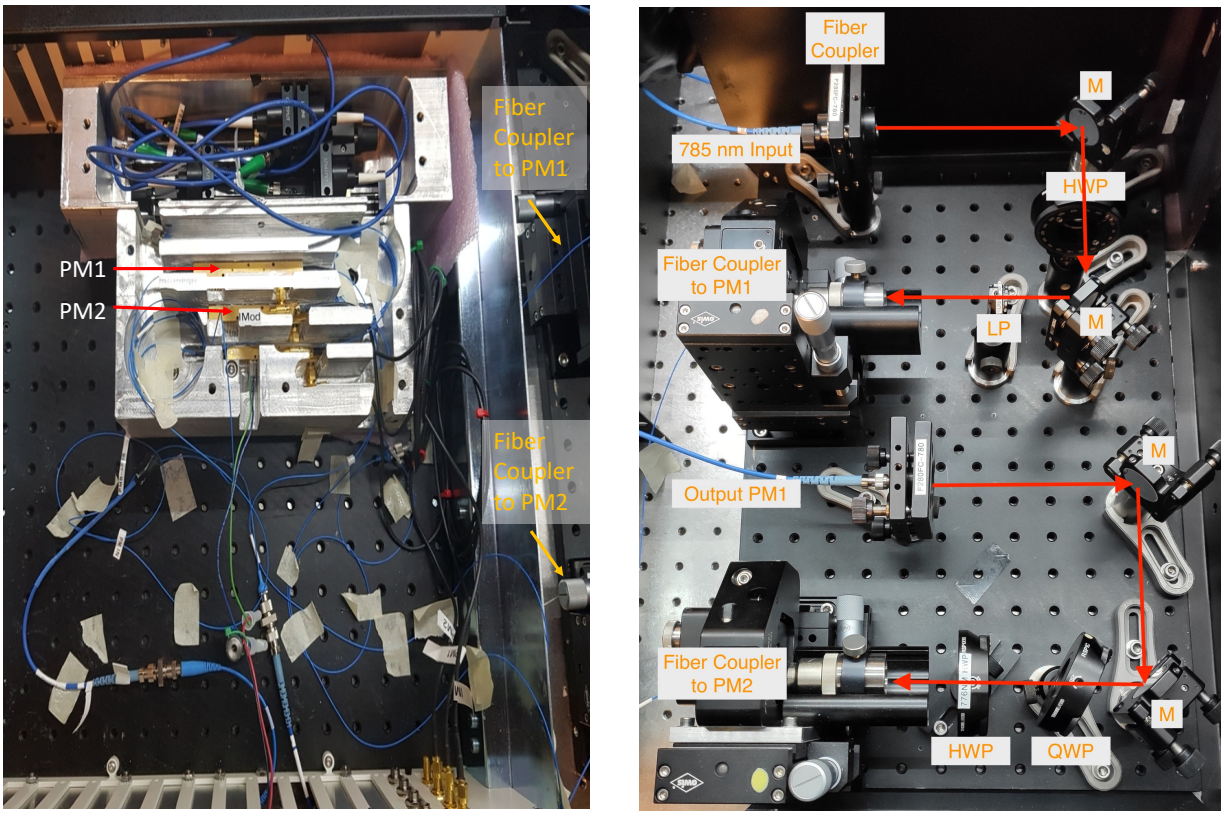

(a) (b)

Figure 2.5: Experimental setup for the prototype WCPS inline polarization modulation setup (IPMS). The optics were placed on a breadboard next to the modulation box for prototyping. (a) Polarization modulation setup box containing the phase modulators. A field implementation of the setup would see all the optics from Fig.2.5b placed in such a box. For this prototype, the phase modulators have been placed in an insulating metal enclosure. (b) free-space fiber bridge between each phase modulator. The HWP preceding the PM2 fiber coupler rotates the polarization by 90° relative to the previous optical fiber (output PM1).

bias voltage to one of the PMs or by using a polarization a feedback system to compensate for this.

Furthermore, qualitative stability tests were conducted by attempting to cause phase drifts by blowing air on the setup, and by physically vibrating and shaking the setup. Qualitatively, there was little to no impact on the phase stability of the system indicating that the inline setup is quite stable compared to the previous MZI setup. This comes as no surprise since the inline

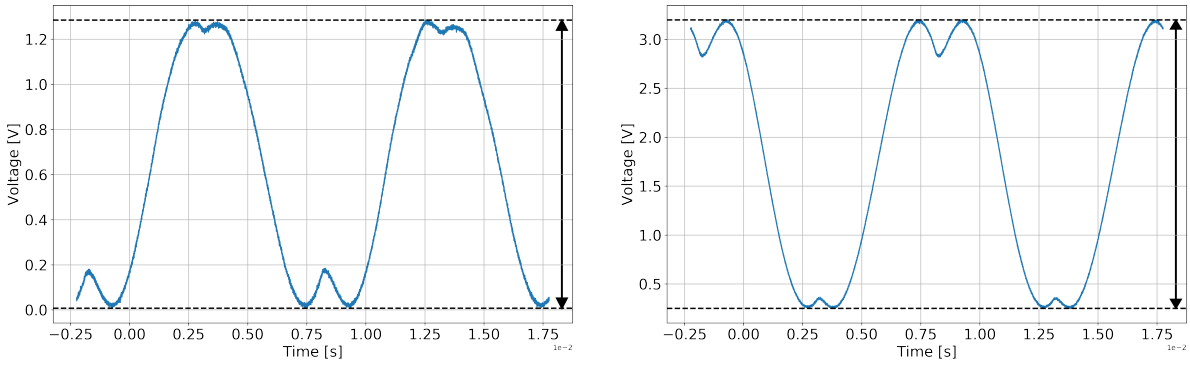

(a) (b)

Figure 2.6: (a) Photodiode response of CW laser light modulated by the inline polarization modulation setup, the minimum and maximum responses are shown with the dashed lines. These are used to determine the visibility of 99.2%. (b) Photodiode response of mode-locked laser light modulated by the inline polarization modulation setup, the minimum and maximum responses are shown with the dashed lines. These are used to determine the visibility of 85.6%.

setup is fully enclosed in the optical fibers and is thus only as environmentally sensitive as the phase modulators and the PMFs. It is also important to note that the setup was not shielded from the outside (i.e. in some enclosure) which would be the case in the final implementation for QEYSSat. Therefore, it is expected that the stability would improve substantially.

2.1.4 Conclusions and Future Steps

The concept IPMS is a promising improvement for the QEYSSat weak coherent pulse source. The stability and physical footprint of the system are improved by using a fully optical fiber based system. The lack of free-space bridges reduces the need for realignment and adjustment, thus the IPMS is a plug-and-play system that requires little to no maintenance. The next steps are to improve the intrinsic QBER by reducing the walk-off mismatch and the rotation errors of each PMF connection. The final steps are to fully implement the IPMS with the final WCPS subsystems, including the arbitrary waveform generator. Final source validations are to be conducted, including a full systems test with a moving free-space receiver. The final WCPS will be used by both the QEYSSat ground station at the CSA headquarters in St-Hubert, Quebec and at the QPL ground station in Waterloo, Ontario.

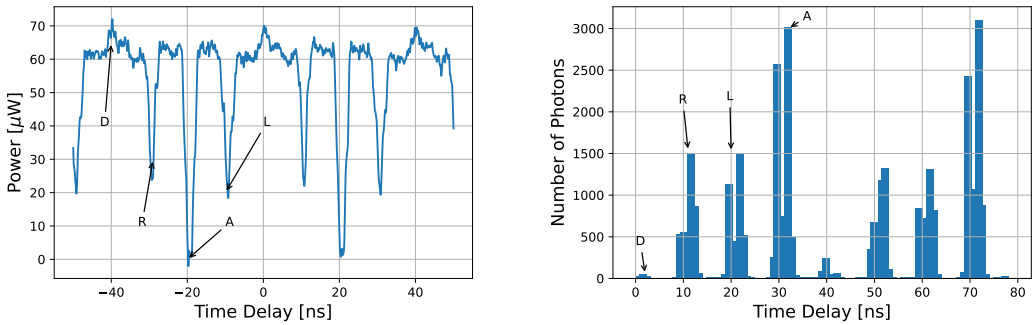

(a)

(b)

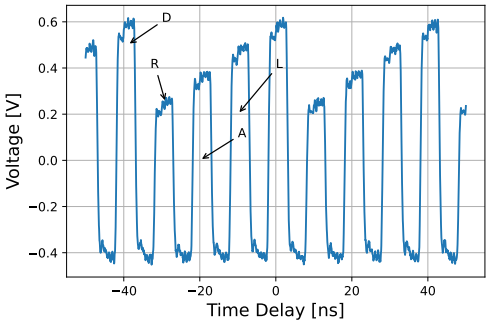

(c)

Figure 2.7: (a) Intensity as measured by a fast photodiode with four polarization states indicated. A continuous wave laser was used to obtained these results. (a) Single photon counts measured using the single photon detectors. The four polarization states are indicated. The WCPS laser setup is the source of the photons. (b) Voltages used to drive the phase modulators. Each voltage corresponds to a unique polarization.

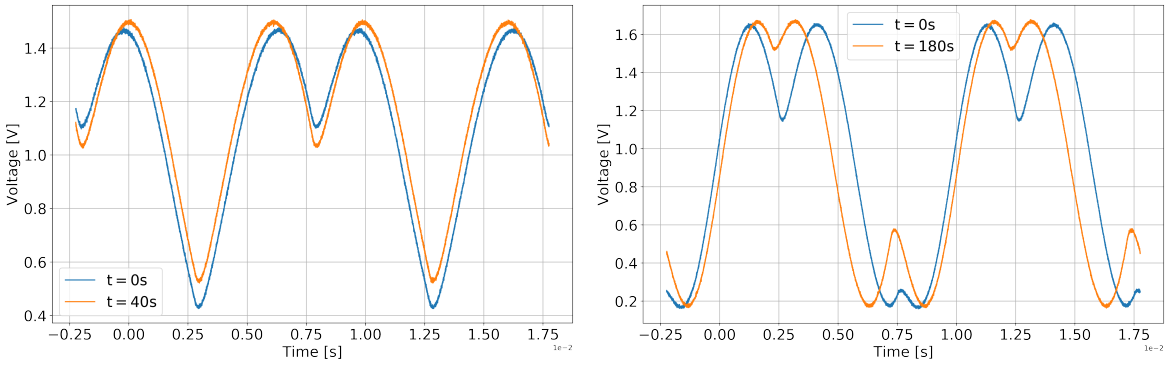

(a) (b)

Figure 2.8: (a) Waveform snapshots taken at times 40 s apart, demonstrating the stability of the setup. (b) Waveform snapshots taken at times 180 s apart, demonstrating the stability of the setup.

2.2 Indoor Moving 6-state 4-state Demonstration

Expanding quantum networks to a global scale requires moving receivers such as satellites. Though quantum repeaters are a promising approach, their implementation requires a lot of research and development [40]. Quantum satellites are quite developed and are becoming a commercially viable option. Implementing and testing protocols to these platforms is quite important for the implementation of a quantum internet. However, launching satellites, though has very recently reduced in cost [98], still requires a lot of time and effort for development. In order to test various protocols and schemes in a controlled and cost effective environment, a lab-based moving platform quantum channel is established for the Quantum Photonics Laboratory. This test bench allows for protocol and quantum source testing without the need for high-cost moving platform experiments.

The main focus of these experiments in this section is to test the robustness of the 6-state 4-state reference frame independent (RFI) QKD protocol [70] under conditions similar to a QEYSSat pass. During a satellite pass or when tracking a moving platform, the transmitter telescope will move (i.e. following the moving receiver). During this movement, the optical fiber that is used to transfer the quantum signal from the single photon source to the transmitter telescope will potentially be stressed and strained. Such stresses on the fibers will cause polarization rotations that need to be corrected in order to maintain a good quality quantum channel. Without said corrections, the polarizations leaving the transmitter telescope may not be the same polarization produced by the quantum source, and thus could unnecessarily increase the QBER

of the link.

Many current quantum communication implementations use active polarization compensation systems that typically require a small "pick-off" or additional overhead to characterize the polarization misalignment that can occur during a QKD link [72]. However, the use of a "pick-off" is not ideal as photon losses are usually a dominant factor in the signal to noise ratio of most quantum channels. Thus, reducing the amount of signal just to ensure proper operation of the channel is not ideal, especially in the photon starved regime (high link loss). Additionally for free-space channels, some active compensation techniques, such as rotating wave plates, can cause beam pointing errors that unnecessarily increase the losses of the channel. Furthermore, any additional overhead can increase costs of deployment and thus hinder the adoption of quantum communication systems. Solutions that do not require any active polarization compensation systems, such as RFI protocols, are therefore desirable. Hence, the need to test the 6-state 4-state protocol with a moving quantum channel.

2.2.1 Moving Link Subsystems

Overall, the moving platform consists of three subsystems, the transmitter, the receiver, and the quantum source (Figure. 2.9). The transmitter subsystem is a stationary sender or Alice, which has the primary purpose of emulating a quantum ground station. Typically, this will consist of a transmitter telescope which is equipped with the tracking and pointing systems and all their supporting hardware. The transmitter subsystem connects to the quantum subsystem via an optical channel (typically optical fiber). The quantum source subsystem is the photon generating system that typically consists of the photon source and all of its support hardware. For the purposes of the information in this thesis, the quantum source subsystem will be connected to the transmitter subsystem via an optical channel that is connected to the telescope via the transmitter fine tracking system. This separation allows for multiple different sources to be easily interchanged and tested with the same transmitter and receiver subsystems provided the source bandwidth is compatible with both systems. The transmitter telescope is a commercially purchased Zerochromat telescope that has an 8 inch aperture (Figure. 2.9a). The total transmission for 785 nm light through the Zerochromat is measured to be $61.76 \pm 1.44\%$.

The receiver subsystem consists of a receiver telescope equipped with the tracking and pointing systems, and the photon detection systems. This subsystem is practically identical to the receiver system used in a ground to aircraft experiment [72]. In order to create a moving platform, the receiver subsystem is placed on a rail and dolly system (Figure. 2.10), where the receiver can be moved along the rail by a user over a distance of up to 6.5 m. Although it is not implemented for this work, the rail system can be attached to a electric motor to pull the receiver at a

constant velocity. In this work, the user can pull or push the dolly to approximately the desired speed. This however is not ideal as the system will move with a non-constant velocity and not be perfectly representative of a satellite moving platform. Nonetheless, it is sufficient for the proof-of-principle tests. The receiver telescope is a commercially Sky-Watcher (BK 1206AZ3) refractive telescope (Figure. 2.9c).

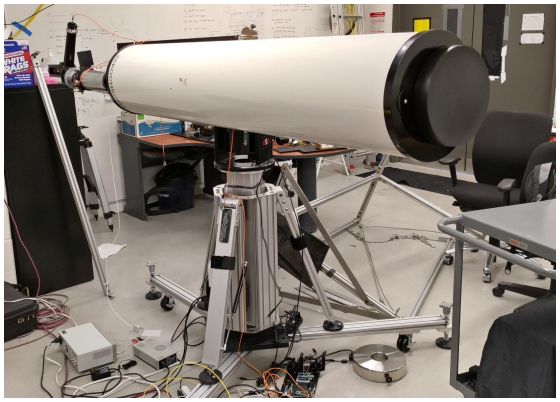

(a)

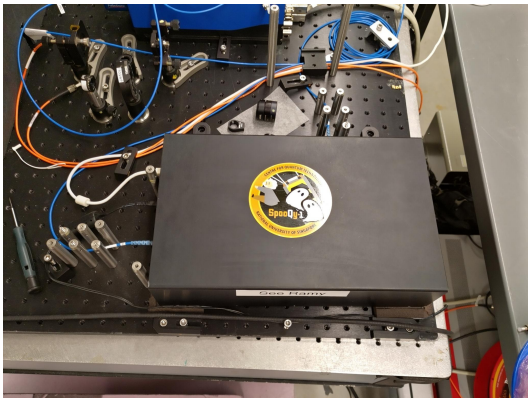

(b)

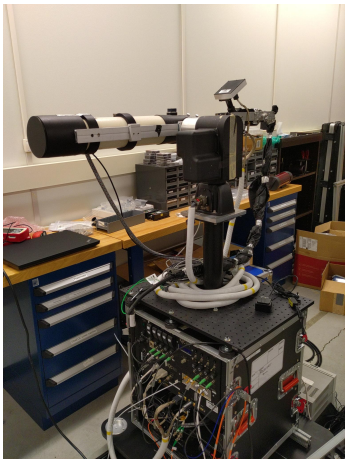

(c)

Figure 2.9: The quantum subsystems of the moving free-space channel. (a) Transmitter subsystem with the large Zerochromat telescope. (b) The quantum source subsystem for the work in this thesis is an entangled photon source provided by the Spooky group from the National University of Singapore. (c) Receiver subsystem with the Sky-Watcher telescope.

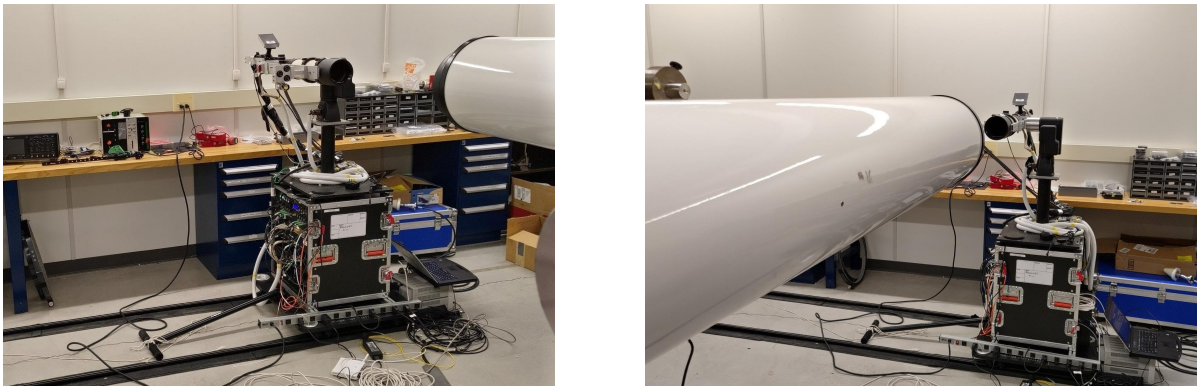

(a) (b)

Figure 2.10: (a) and (b) the receiver system on the rail and dolly that emulates a moving receiver.

2.2.1.1 Tracking and Detector Subsystems

The tracking system for both the transmitter and receiver subsystem includes a coarse pointing system and fine pointing system. The coarse pointing system includes two cameras that provide feedback to the motor mounts of both the transmitter and receiver telescopes. The feedback is created by tracking the movement of a beacon laser spot. An 850 nm beacon laser is placed on both the receiver and transmitter telescope. Although this system is better suited for longer distances (i.e. greater than 100 m), it was still possible to use over the short free-space links. Figure. 2.11 shows the hardware for the coarse pointing system. The three black circles enclosed by the metal rectangle are collimater for the beacon lasers. Typically the three lasers can be used as their divergence is sufficiently large such that the three spots overlap. However, due to the short distance of the link, the spots remain separate and only one beacon spot may be tracked. Therefore, only a single beacon laser is used and is indicated by the red arrow in Figure. 2.11. The beacon camera is mounted on the metal rectangle and is indicated by the red circle in Figure. 2.11. In order to isolate and capture the beacon signal, the camera has a focusing lens, an iris, and a 850 nm filter. The beacon spot centroid is monitored by the pointing software (made by Dr. Brendon L. Higgins) and provides feedback to the motors of the respective telescope mounts. Simply, the software attempts to keep the beacon centroid at a user defined and calibrated location on the camera sensor. The location of the beacon camera in Figure. 2.11a and Figure. 2.11b is reversed in order to be aligned with the beacon laser on the other telescope. This is required geometrically as otherwise the coarse pointing system would not be able to properly align the system.

The fine pointing system consists of a beacon laser on the transmitter that is collinear to the

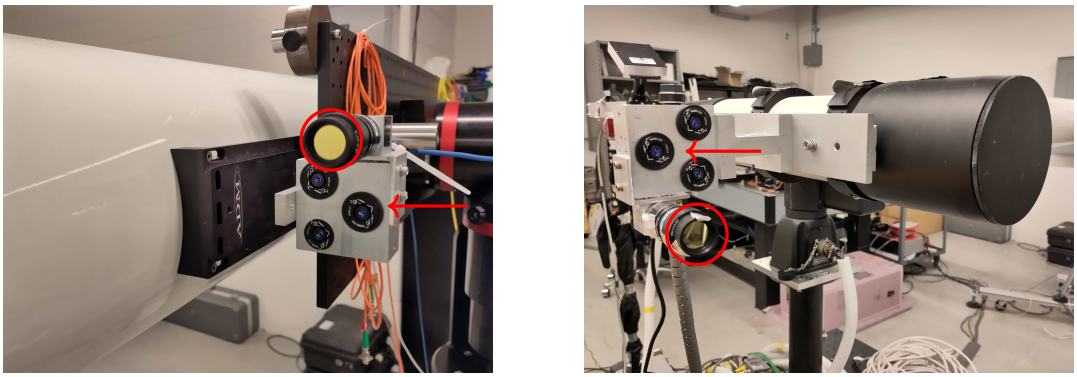

(a) (b)

Figure 2.11: The coarse pointing system of the transmitter (a) and receiver (b) telescopes. The red arrow indicates the collimater beacon laser used for the moving tests. The red circle is indicating the aperture of the beacon camera.

quantum signal which gets received by the detection and compensation unit on the receiver which compensates for the deviations of this beacon. For both the transmitter and receiver, the system that comprises the hardware used for the fine pointing is known as the acquisition, pointing and tracking (APT) unit. The transmitter APT shown in Figure. 2.12a is designed and built by the Institut National d'Optique (INO), the system was optimized for a beacon wavelength of 850 nm and a quantum signal wavelength of 785 nm. This APT is used to make the fine pointing beacon collinear with the quantum signal by the use of a dichroic mirror and some beam shaping optics (i.e. lenses). A user can make adjustments to the beacon and quantum signal alignment with the fine steering mirror in the transmitter APT unit.

The receiver APT shown in Figure. 2.12b and Figure. 2.12c was designed and built by Neptec Design Group, now MDA, in collaboration with QPL members. Its performance and design are described in great detail in Ref. [63]. The receiver APT is designed and optimized for a quantum signal at 785 nm and a beacon at 850 nm. The receiver APT also has a dichroic mirror that splits the beacon from the quantum signal. Once split from the beacon, the quantum signal then passes through a 3 nm filter centered at 785 nm that filters out any unwanted light. In addition, a pinhole is used to further filter any unwanted stray light that is collected by the telescope. Ideally only light that is collinear with the beacon shall pass the pinhole. A quad cell sensor is used to monitor the beacon movement and provides feedback to the control system. The movement of the beacon on the quad cell is translated to a steering mirror that is used to move the quantum signal such that the fiber coupled power is maintained or increased. The accuracy of this system is measured in Ref. [63] as 50 µrad. The beacon laser of the fine pointing system is distinguished from other

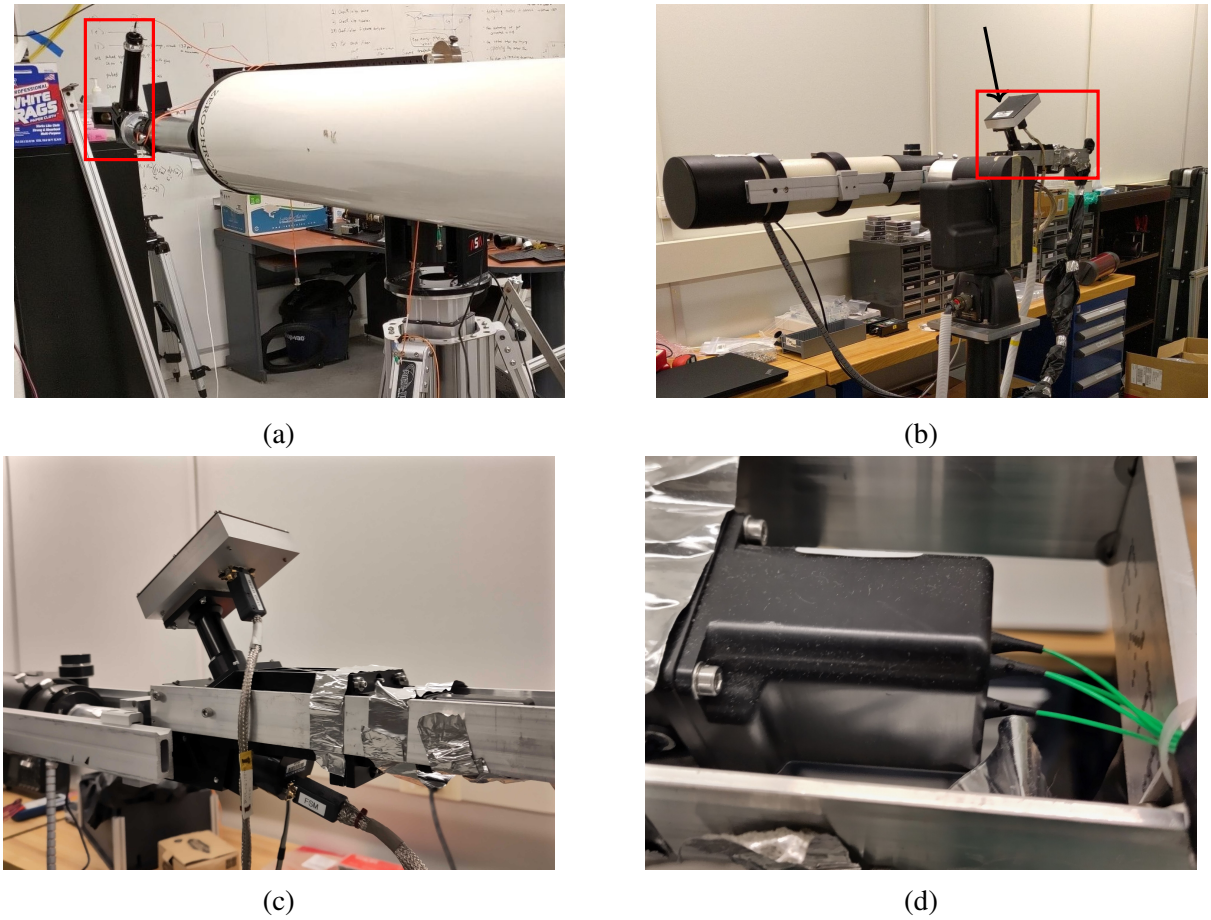

(a) (b) (c) (d)

Figure 2.12: Hardware of the fine pointing system of the moving quantum channel. (a) The fine pointing system APT at the transmitter that is used to combine the beacon laser with the quantum signal. (b) Fine pointing system APT at the receiver telescope. The quad cell module is indicated with the black arrow. In both images the APT is indicated by the red rectangle. (c) Close up view of the receiver APT. (d) Four state polarization analyzer at the back of the receiver APT with the four output multi mode optical fibers, one for each polarization (horizontal, vertical, diagonal, anti-diagonal).

light sources by having a 5 kHz intensity modulation of the beacon laser. The fine pointing software (made by Neptec Design Group), only tracks signals that have this 5 kHz modulation. The feedback of the fine pointing system relies on a calibration between the fine pointing beacon and the quantum signal. A user must calibrate the system by maximizing the throughput of the quantum signal across the entire free-space channel by adjusting an offset parameter in the software between the fine pointing beacon and the quantum signal. Effectively, the user is telling the feedback system which beacon position corresponds to the highest throughput and coupling of the quantum signal in the receiver APT. To simplify the calibration of the offset a bright laser source and a powermeter are used in place of the quantum signal and detector unit. Once the quantum signal is through the spatial and spectral filters, a 4-state polarization analyzer is used to measure the polarization of the quantum signal (Figure. 2.12d). This is a passive 4-state analyzer with multi-mode fiber coupled outputs, one for each polarization. These output fibers are then connected to single photon detectors that are part of the moving receiver subsystem, or power meters when troubleshooting. The overall throughput of the system, starting from the transmitter telescope across the free-space channel and coupled into the multi mode fibers at the output of the receiver telescope, ranged from 25 % to 35 % depending on how well the fine pointing system offset is aligned and the ability of the coarse pointing system to keep the signal within the 0.5° acceptance angle of the APT [63].

2.2.2 Experimental Details

As earlier mentioned, the protocol to be tested is the entanglement based 6-state 4-state protocol. Alice and Bob perform the 6-4 protocol using an entangled photon source. Alice performs a 6-state measurement while Bob performs a 4-state measurement. Bob's equipment is mounted on a dolly and rail system such that it can be moved to emulate a satellite pass. Both the transmitter (Alice) and receiver (Bob) have pointing systems that enable the maintenance of a quantum channel despite the moving receiver and no polarization compensation is applied.

The entangled photon source (EPS) used is provided from the SpooQy group at Centre for Quantum Technologies at the National University of Singapore [99]. This EPS has an intrinsic brightness of 0.56 Mpairs/s/mW. The heralding efficiency of the source, as measured after coupling into the output fibers is between 15 % to 20 % for the experimental results presented below. The entangled photon pairs are produced via a periodically-polled potassium titanyl phosphate crystal that is placed in a Mach Zehnder type interferometer and pumped by a continuous wave 405 nm laser. Details of the source can be found in Ref.[99]. The signal photons are produced at around 785 nm with a bandwidth of 5.02(1) nm full width at half maximum (FWHM), while the idler photons are at 842 nm with a bandwidth of also 5.35(1) nm FWHM. The spectra of the signal and idler are shown in Figure. 2.13. Note that the spectra of the signal and idler photons can

be tuned by adjusting the crystal temperature and the pump laser temperature. Throughout all the experiments that utilized the SpooQy EPS, there were some issues of pump stability. The laser diode would occasionally change output frequency modes. This means the pump laser spectrum changes suddenly which then changes the spectra of both the signal and idler photons. This was observed by both monitoring the correlation quality and the change in the photon transmission through the 3 nm 785 nm spectral filter. The laser temperature and current needed to be adjusted in order to find a stable operating regime, and the set temperature and current are not consistent between system restarts.

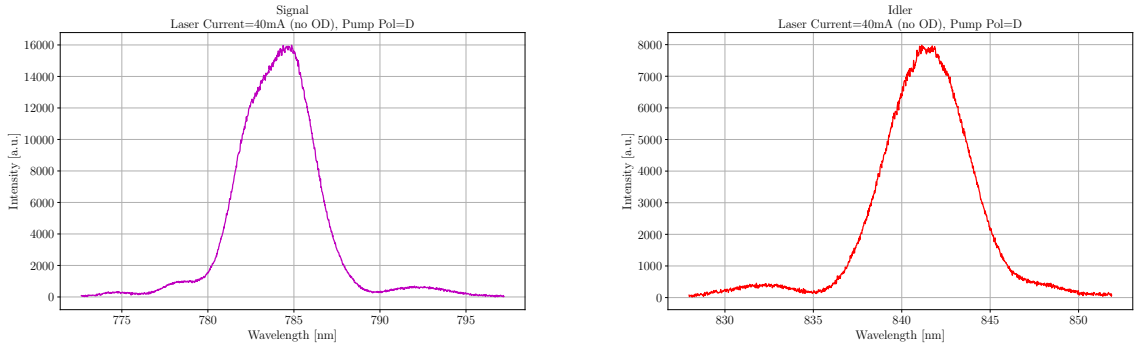

(a) (b)

Figure 2.13: Spectra of the signal (a) and idler (b) photons produced by the SpooQy source. A pump current of 40 mA (900 µW) is used while pumping both paths of the interferometer. No optical density filter (OD) is used to attenuate the pump power. An OD is typically used to reduced the brightness of the source.

As was done in Ref.[70], the entangled photon pairs are coupled to polarization maintaining fibers (PMF). With the horizontal and vertical polarizations aligned to the axes of the PMF, while the superposition polarizations are subject to the birefringence of the fiber. Unlike in Ref. [70], an attempt is made to compensate the walk off induced by the PMFs by introducing a second length of PMF where the key alignment is rotated by 90°, as is done with the IPMS in Sec. 2.1. For example, if a horizontally polarized photon pair is created and coupled to the slow axis of the collection PMF, the second length of PMF will have the horizontal polarized photon travel through the fast axis. This technique attempts to mitigate the degradation in visibility in the superposition bases [100], however there are many challenges with this technique, some of which are discussed in Sec. 2.2.2.2. A detailed discussion of the technique and challenges can be found in the Master's thesis of Wilson Wu (currently in preparation). Just as in Ref. [70], the key map is produced from the detection events in the horizontal-vertical basis (i.e. the computational basis), while the correlations in the superposition are used to calculate the C-parameter (Sec. 1.5). The

main objective of the experiments is to determine whether or not the protocol is robust enough to handle the phase change induced by the stresses of the PMF caused by the moving transmitter, particularly during a QEYSSat pass.

Therefore, in order to properly emulate some of the ground station conditions that would be met during the QEYSSat mission [66], the quantum receiver used in Ref. [72] was placed on a cart and rail system that allows it to move in a linear path. In order to maintain the moving link, a tracking and pointing system was used, similar to that used in Ref. [72]. For our experiment, the 4-state polarization measurement is done by the moving receiver (Figure. 2.12d) while the 6-state measurement is done by a "ground" user as seen in Figure. 2.14. The 6-state analyzer (shown in Figure. 2.15) is the same 6-state analyzer used in Ref. [70] and is capable of measure the horizontal (H), vertical (V), diagonal (D), anti-diagonal (A), left circular (L), and right circular (R) polarizations. A single time-tagging unit is used to record the detections of both Alice and Bob. This is clearly not secure and in a proper implementation one must use two separate time-tagging unit, one each for Alice and Bob. However, a single time-tagging unit is sufficient for demonstration purposes. Furthermore, the experiment is not limited to an entanglement based configuration. In fact, a prepare & measure RFI scheme could be used in place of the entanglement based scheme, however this is not done in this study.

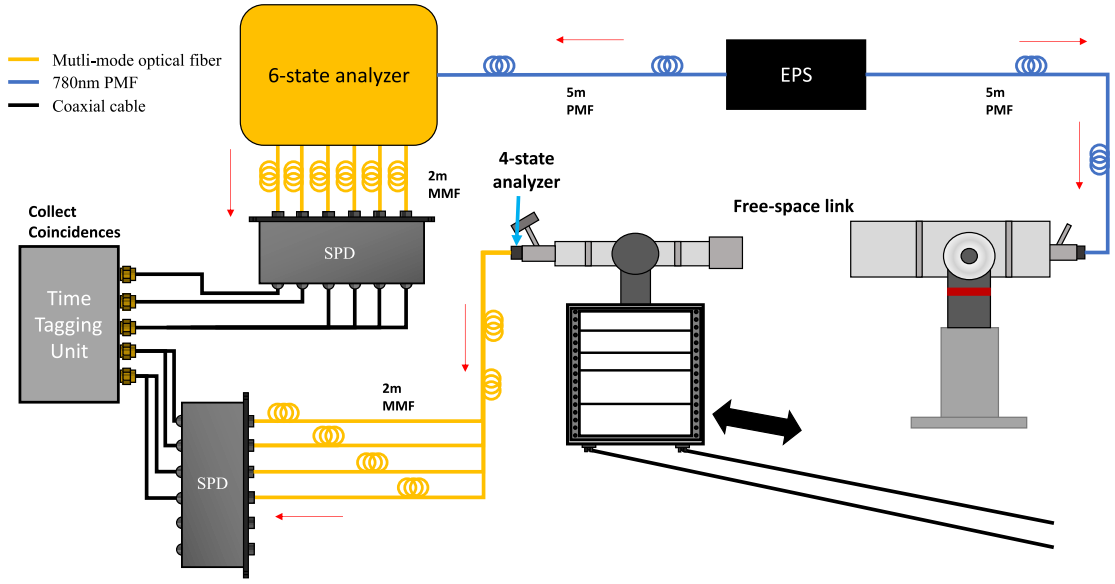

Figure 2.14: Schematic of the indoor moving tests. The system has full tracking and pointing systems that is described in Sec. 2.2.1.1.

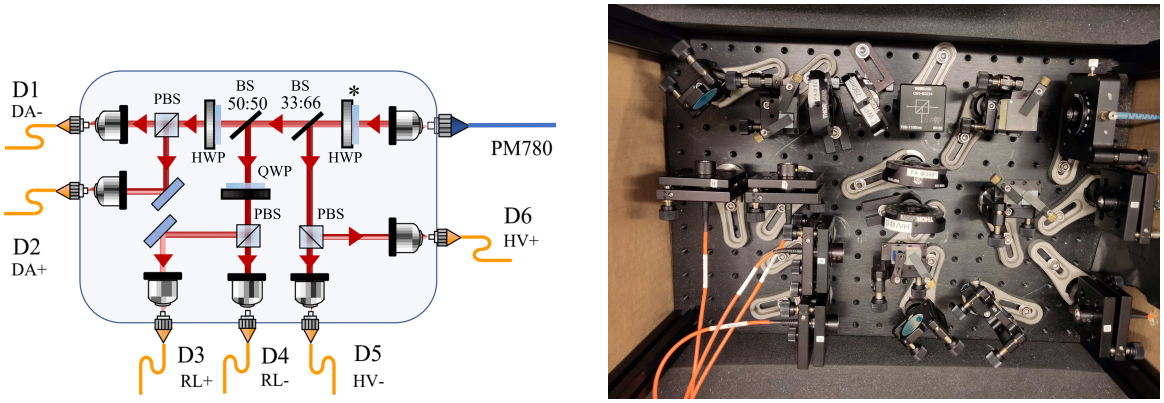

(a) (b)

Figure 2.15: (a) Schematic of the 6-state analyzer, this diagram is slightly modified from Ref.[70]. The half-wave plate marked with * is to align the fast and slow axis of the PMF to the H and V ports of the PBS. HWP: half-wave plate, QWP: quarter-wave plate, PBS: polarizing beam splitter, BS: beam splitter. (b) Photo of the 6-state analyzer. The additional optics are to compensate for birefringence in the optical elements.

2.2.2.1 Emulating a Satellite Pass

The goal was to have the receiver subsystem move such that the angular velocity of the transmitter mount is similar to what the maximum angular velocity would be during a low Earth orbit satellite pass. According to Ref. [101], the altitude for a low Earth orbits can range between 200 km to 2000 km from sea level. These orbits have different velocities based on their altitude and from these orbital velocities one can calculate the angular velocity of a transmitter telescope. There are three assumptions that are made for the following calculations.

1. The orbit is circular and appears as a "straight" pass to the ground station.
2. The orbit speed is constant.
3. The fastest angular speed for the transmitter is at zenith.

For an orbit height of 400 km which is well below the altitude of QEYSSat, the orbital velocity of the satellite would be approximately 7.7 $\mathrm{km\,s^{-1}}$. This corresponds to a transmitter angular velocity upper bound of about 1.1 $^\circ\,\mathrm{s^{-1}}$. Thus, if the 6-state 4-state protocol can handle the phase change caused by a transmitter moving at 1 $^\circ\,\mathrm{s^{-1}}$, it should be sufficient for a QEYSSat pass.

Note that the $1.1\,^{\circ}\,\mathrm{s}^{-1}$ is not the phase change that occurs to the shared entangled state between Alice and Bob and does not directly contribute to the smearing of the C-parameter. The reasons for this are that the optical fiber that is used to transmit the signal photons to the satellite, or other moving receiver, needs to experience some external stress in order to induce a phase change in the entangled state. Quantifying the extent of this stress is beyond the scope of this study. However, the force required to induce the necessary stress would be on the order of $\mathrm{kg\,mm}^{-1}$. Simple strategies can be used to mitigate the effects that the moving transmitter telescope has on inducing stress in the optical fiber. These include but are not limited to: Securing the optical fiber to the telescope such that it does not hang down the back of the telescope, as seen in Figure. 2.16a, and running the optical fiber from the source up the transmitter telescope mount. The latter is ideal as the mount is the axis of rotation and is stationary while the telescope is moving thus minimizing the movement induced stresses (Figure.2.16b).

(a) (b)

Figure 2.16: (a) Optical fiber is run along the transmitter mount to reduce the stresses on the optical fiber while the telescope is moving. (b) Back of the transmitter APT. The optical fiber is secured to the APT unit to avoid unwanted stresses. In both images, blue optical fiber is attached to the transmitter telescope hardware. The red arrows indicate attachment points.

2.2.2.2 Discussion on EPS visibility

Although, the EPS had an intrinsic HV and superposition visibility of $> 98\%$, after coupling into the output PMFs (2m), this was reduced to approximately 98% and 97% respectively. The drop in visibility due to coupling into the PMFs can be attributed to the walk-off induced by the difference in group velocity between the slow and fast axis of the PMF. Furthermore, wave plates

are used to align the polarization to the proper PMF axis, thus any wave plate rotation errors can cause a drop in visibility.

After passing through the crossed PMF (5m), the EPS visibility is measured to be approximately 96% in the HV basis and 95% in the superposition basis. The reduction in visibility in the superposition basis can be attributed to both the reduced visibility in the HV basis and the additional walk-off from the crossed PMF. Although, the crossed PMF is intended to compensate for the walk-off, the length mismatch provides an effective PMF length of 3 m. This is in contrast to the 7 m that would be present if there was no crossed fiber. Ideally, two lengths of 5 m PMF would be used but this was not available for the present tests. The reduced visibility in the HV basis is due to the mismatch in PMF axis alignment between the crossed and uncrossed PMFs. Manufacturing tolerances for the alignment of these axes is up to 2°. We have also measured up to 4°. These significant angular mismatches can cause mode coupling between the two PMF axes and by consequence between the horizontal and vertical correlations. Thus the HV visibility is reduced. More details on the effects of this angular mismatch is found in the Master's thesis of Wilson Wu (in preparation).

2.2.3 Characteristics of C under phase change

As eluded to in Ref. [70] and described in Ref. [102], the C-parameter is a statistical quantity that is dependent on the number of counts collected for its estimation, and how quickly the phase or reference frame is changing during the count collection time interval. For a fixed count rate, the larger the rate of change of the phase, the more smearing occurs in the estimation of C. Thus, it is important to reduce the count collection time interval such that the phase does not change too rapidly during this time period. However, reducing the count collection interval will reduce the number of detections which is detrimental to the key rate. Furthermore, for a fixed phase change, the less counts collected in the estimation of C will increase the variance in the expected value of C. This variance is not discussed in Ref. [102] and hence the model below is an improvement on their analytical approach. Effectively, here we are modeling the dynamics and behaviour of the C-parameter in the presence of a varying phase and a finite number of photon collections. This is an important metric to be aware of when designing an experiment and assessing the phase tolerance of the protocol. However, this approach in investigating the dynamics of the C-parameter is not a complete finite size analysis of the C-parameter, but rather estimates that make some assumptions.

A model is developed to estimate the effects of phase change on the C-parameter. Effectively, the model can calculate the phase resistance, or tolerance of the C-parameter provided some experimental conditions. The model is a Monte Carlo simulation that considers N entangled

photons detected in the time interval t_N. It is assumed that every n states is detected evenly spaced by the interval $\tau = t_N/N$ in the total time interval t_N. The phase change (reference frame rotation) is assumed to be constant over the time interval such that every n entangled photon state has an instantaneous phase of $\phi(n\tau)$. The total of phase variation over the measurement time interval is given by $\phi(t_N)$. For each n entangled state, the detection probabilities of the positive operator-valued measures (POVM) that are involved in estimating the C-parameter are calculated numerically using the Qutip Python package [103, 104]. With these probabilities, a pseudo-random number generator determines the detection results for each n entangled states' single photon events. Each result is then counted and statistics are accumulated for the total N entangled pairs. Once complete, an experimental expectation value approximation is calculated using

$$\langle M \rangle = \frac{M_{++} + M_{--} - M_{+-} - M_{-+}}{\sum M_{ij}}, \tag{2.2}$$

where M is the POVM in question and M_{ij} are the individual detection results. With all the expectation values calculated using Eq. 2.2, a value for the average C-parameter over the time interval t_N is determined. This process is repeated i times for each $\phi(t_N)$ and the average value of the distribution is taken to be the value of $C(t_N)$ with error bounds being the standard deviation of the each distribution.

Figure. 2.17 shows the results of the Monte Carlo simulation for $N = 600$, 3000, 10000, and 50000. Each data point is the average of the distribution of 300 trials with the error bars being the standard deviation of the distribution. The phase is varied from $0 \rightarrow \pi/2$ over the measurement time period, t_N. As seen in Figure. 2.17, the C-parameter value drops as the phase change is increased over the measurement time interval and the smearing effect is observed. Furthermore, Figure 2.18 shows the dependence of the standard deviation from the Monte Carlo simulation of the C-parameter on the number of counts collected over the measurement period. This is also seen by the size of the error bars in Figure. 2.17. As indicated above, lower count rates should increase the observed variance in the C-parameter value that is measured by the system. This is due to the statistical nature of the C-parameter, the lower photon counts one has, the less one is able to fully resolve the expectation values that make the C-parameter. Conversely, more photons counts allow for a better resolution of the expectation values and thus the C-parameter can be better approximated. Hence as the number of counts is increased, the standard deviation tends to zero as seen in Figure. 2.18. This behavior is not captured in the analytical expression provided in Ref. [102].

For systems with low N, i.e. $N < 1000$, it is difficult to quantify the tolerance of the system to changes in phase due to the large standard deviation. However, for large N, the 6-state 4-state protocol can tolerate a change in phase over a 1 s measurement time period of up to 0.519 rad s^{-1}

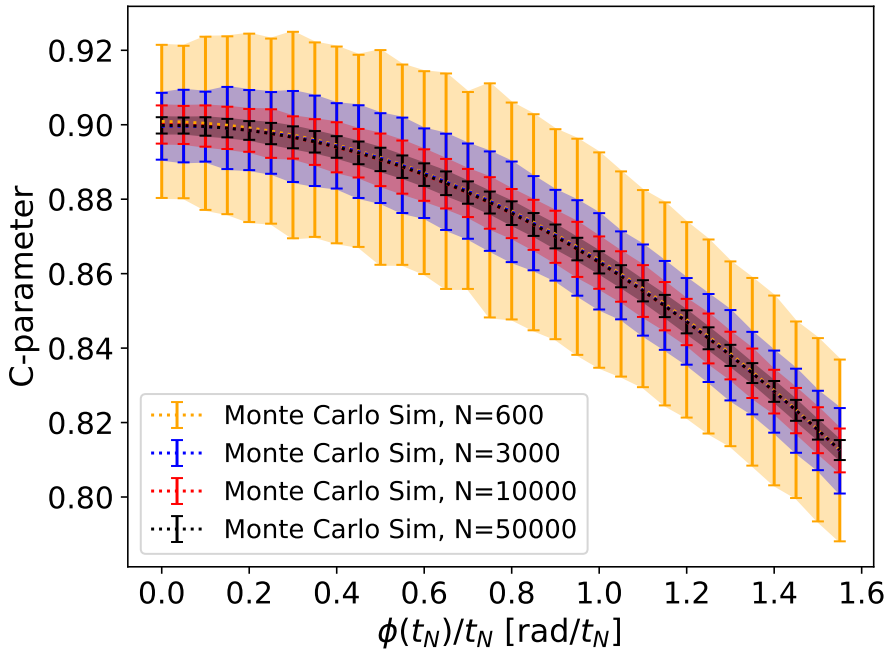

Figure 2.17: Monte Carlo simulations of the C-parameter as the rate of change of the phase is varied from $0 \rightarrow \pi/2$ rad per measurement time interval t_N. Each data point is calculated from the average of 300 trials. The error bars are standard deviation of the distribution of the 300 trials.

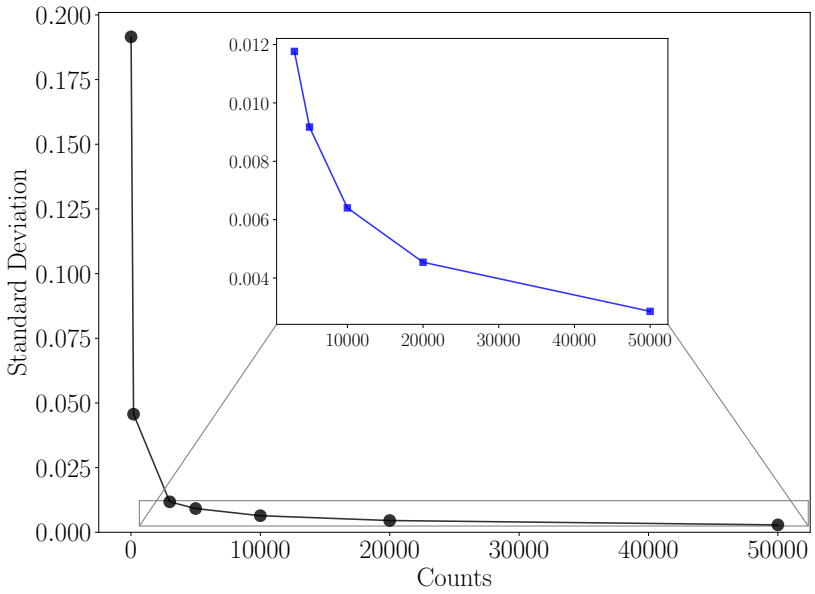

Figure 2.18: The standard deviation of the Monte Carlo distribution of the calculated *C*-parameter for various count rates. The standard deviation of the distribution decreases significantly as more counts are collected over the measurement time period. The inset is for clarity for the standard deviation of the higher count rates.

before a 5% drop in the asymptotic key rate. Thus, for large N, for the protocol to be effective the rate of change of the entangled state's phase must be less than 0.519 rad over the measurement period. For many of the experiments presented in Table. 2.1, N is sufficiently large (≈ 15000).

2.2.4 Results

Several moving tests were done and the results of a selected few are summarized in Table. 2.1. The results of all the passes are found in Appendix. A in Table. A.1. These tests were done over the course of several days. Tests 1-16 are from the same day of experiments while 17-30 combined are from 3 days of trials[1]. For the majority of the experimental passes, the C-parameter had a value of greater than 0.91 with an average QBER of less than 4.8% and 4.2% in the superposition and computational basis respectively (Eq.1.4). The results of the C-parameter and QBER are respectable despite the angular velocity of the transmitter telescope inducing stress in the optical fiber and a total lack of any polarization compensation system.

Note that the last passes have lower coincidence count rates than the tests 1-16, this is a result of an update to the EPS that allowed for fine adjustments to the crystal temperature, which resulted in better spectral control. Prior to this update, the 3 nm 785 bandpass filter would significantly reduce the channel throughput (passes 17-30). However, after this update (pass 1-16), we can see that the coincidence throughput is significantly increased, which generally has a major effect on the finite size key rate and on the key rate analysis of Sec. 2.2.4.2.

[1] In reality there are a lot more data sets that were obtained, however many of them involve troubleshooting or are redundant.

Table 2.1: Results of the moving receiver experiments using for 6-state 4-state protocol with polarization encoding. The error for the mean motor speed is given by the standard deviation of the motor speeds. The other errors are derived from counting statistics. $QBER_C$ and $QBER_{ZZ}$ are found in Eq. 1.4

Laser Current - Pass number	Mean motor speed [deg/s]	Max motor speed [deg/s]	C	$QBER_C$	$QBER_{ZZ}$	Asymp key rate	Coincidence per second	Link length [s]
46mA-1	0.42 ± 0.24	1.19	0.918 ± 0.010	0.041 ± 0.005	0.041 ± 0.004	0.076	17487	59
46mA-2	0.44 ± 0.35	1.29	0.917 ± 0.010	0.041 ± 0.005	0.041 ± 0.005	0.075	16369	26
46mA-6	0.34 ± 0.24	1.10	0.907 ± 0.024	0.047 ± 0.006	0.039 ± 0.006	0.073	15722	31
46mA-7	0.67 ± 0.56	1.96	0.923 ± 0.030	0.038 ± 0.005	0.040 ± 0.008	0.078	15162	25
46mA-8	0.51 ± 0.36	1.31	0.927 ± 0.018	0.036 ± 0.009	0.037 ± 0.006	0.083	14729	44
46mA-9	0.34 ± 0.31	1.42	0.934 ± 0.013	0.033 ± 0.006	0.038 ± 0.004	0.084	15460	47
46mA-14	0.38 ± 0.32	1.93	0.925 ± 0.013	0.037 ± 0.006	0.042 ± 0.005	0.078	10918	27
46mA-15	0.72 ± 0.18	2.10	0.875 ± 0.023	0.062 ± 0.012	0.053 ± 0.009	0.050	7523	25
39mA-17	0.08 ± 0.05	0.1	0.939 ± 0.022	0.030 ± 0.011	0.025 ± 0.006	0.099	3083	439
39mA-18	0.4 ± 0.31	1.42	0.952 ± 0.019	0.024 ± 0.009	0.023 ± 0.005	0.107	2863	146

Continued on next page

Laser Current - Pass number	Mean motor speed [deg/s]	Max motor speed [deg/s]	C	$QBER_C$	$QBER_{ZZ}$	Asymp key rate	Coincidence per second	Link length [s]
41mA-19	0.21 ± 0.19	1.83	0.938 ± 0.035	0.031 ± 0.018	0.030 ± 0.046	0.094	2654	473
39mA-20	0.42 ± 0.24	1.15	0.938 ± 0.029	0.031 ± 0.015	0.019 ± 0.017	0.106	1599	208
48mA-21	0.27 ± 0.20	1.60	0.870 ± 0.022	0.065 ± 0.011	0.047 ± 0.017	0.053	4030	286

Table 2.2: Results of the static pass using for 6-state 4-state protocol with polarization encoding. These are for comparison to the moving tests, no noticeble differences are evident. Full results for all static tests are found in Table. A.3.

Laser Current - Pass number	C	$QBER_C$	$QBER_{ZZ}$	Asymp key rate	Coincidence per second	Link length [s]
46mA-static-1	0.892 $\pm$0.016	0.054 $\pm$0.008	0.049 $\pm$0.005	0.059	13101	29
46mA-static-2	0.909 $\pm$0.023	0.045 $\pm$ 0.011	0.047 $\pm$ 0.004	0.066	14230	29
41mA-static-3	0.936 $\pm$0.018	0.032 $\pm$0.009	0.033 $\pm$0.006	0.090	3262	220
41mA-static-4	0.934 $\pm$0.018	0.033 $\pm$0.009	0.031 $\pm$0.006	0.092	3269	355

Figure. 2.19 shows the applied motor speed of the transmitter and receiver telescope mounts during the some of the moving tests. Figures. 2.19a and 2.19b correspond to the transmitter and receiver applied motor speed during pass 1. The maximum transmitter speed is $1.18\,^{\circ}\,s^{-1}$ with an average speed over pass of $0.42\,^{\circ}\,s^{-1}$. Figures. 2.19c and 2.19d correspond to the transmitter and receiver applied motor speed during the passes 14-16 with each pass corresponding to the large spike in motor speed to about $2\,^{\circ}\,s^{-1}$. In Figure. 2.19c the maximum applied motor speed in the horizontal plane is $2.1\,^{\circ}/s]$ while the average applied motor speed throughout the passes is $0.62\,^{\circ}\,s^{-1}$ over the entire collection period. For these examples the maximum applied motor speed exceeds the required $1.1\,^{\circ}\,s^{-1}$ for the feasibility study and thus the results are indicative of the robustness of the 6-state 4-state protocol. Table. 2.1 lists the statistics for the other passes with all other passes in Table. A.1.

Note that Figure. 2.19 has regions of positive motor speed and negative motor speed. The change in sign is indicative of the moving receiver reaching the end of the rail, something that a satellite obviously would not do but is possible with other moving platforms. Furthermore, there are many regions of sudden acceleration due to the unevenness of the rail and the realities of having a human push a cart in a smooth manner. Some of the passes have a very high variance in the average applied motor speed due to the inconsistency in the human powered receiver's speed. In addition, some of the passes described in Table. 2.1 are for short link times due to sudden changes in the motion of the receiver[2] causing the transmitter pointing system to lose the receiver beacon. The coarse pointing software does have a spiral search algorithm that will deploy when the beacon is lost, however, the parameters of this algorithm were not optimized for these tests. Figure. 2.20 shows what happens to the various expectation values and the C-parameter when tracking is lost and the photon detection rate drops significantly. As described in Sec. 2.2.3, the variance in the observed instantaneous value of the C-parameter will increase significantly with a decrease in count rate.

Figure. 2.21 and Figure. 2.22 show the results for pass 1 and pass 14 respectively. Pass 1 has an average C-parameter value of 0.918 ± 0.010 with no obvious drop in the C-parameter and corresponding QBER of 0.041 ± 0.005 and 0.041 ± 0.004 in the superposition and computational basis respectively. This gives to an asymptotic key rate of $0.076\,\text{bits/coincidence}$. Despite the transmitter telescope moving at an average speed of $0.42\,^{\circ}\,s^{-1}$ and a maximum speed of $1.19\,^{\circ}\,s^{-1}$, there is no obvious drop in the C-parameter nor key rate. For pass 14 (Figure. 2.22), the average C-parameter is found to be 0.925 ± 0.013 and has a corresponding QBER of 0.037 ± 0.006 and 0.042 ± 0.005 in the superposition and computational basis respectively. These results give an average asymptotic key rate of $0.076\,\text{bits/coincidence}$. Again these results are achieved despite the transmitter telescope moving and having an average speed of $0.38\,^{\circ}\,s^{-1}$ and

[2]These are the realities of using humans to push the receiver cart.

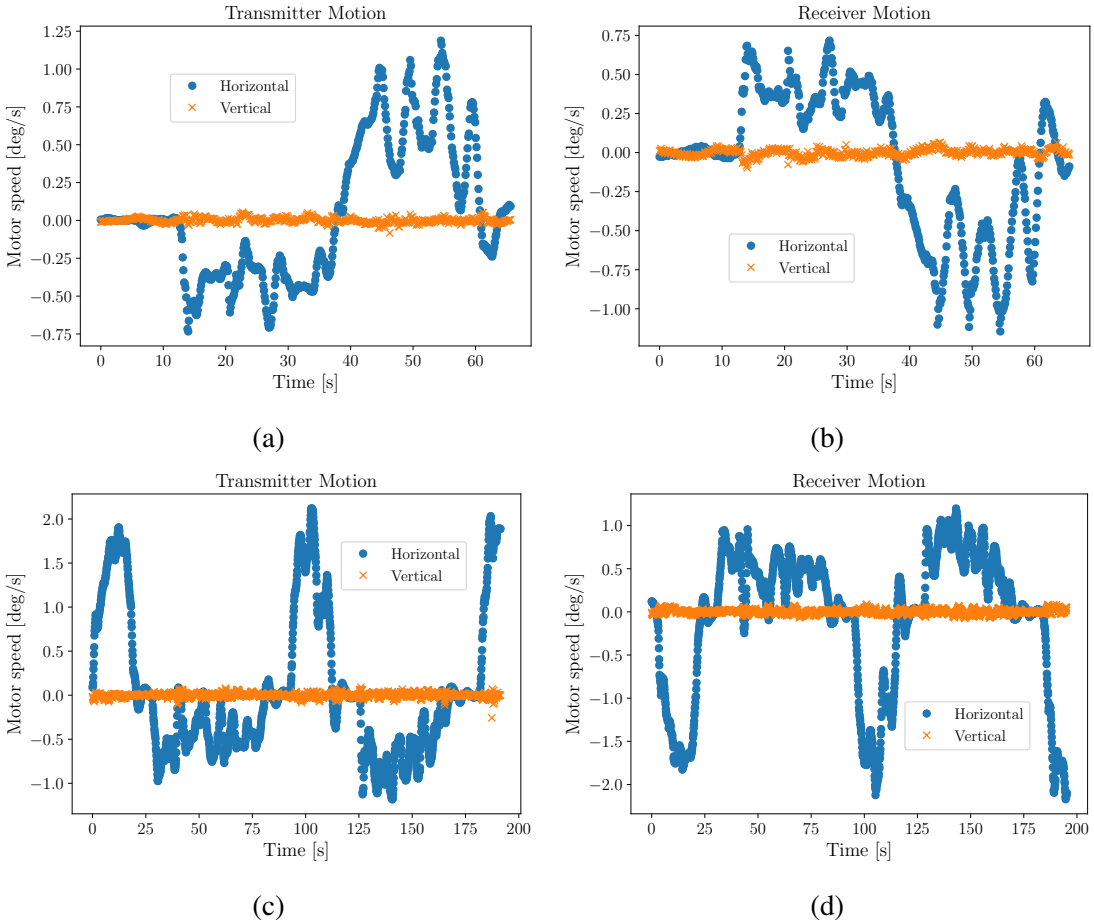

Figure 2.19: Transmitter and receiver applied motor speed for the horizontal and vertical axes. Transmitter (a) and receiver (b) applied motor speed for two full lengths of the rail. Here the maximum transmitter horizontal motor speed is $1.19\,^{\circ}\,\mathrm{s}^{-1}$ while the average applied motor speed throughout both passes is $0.42\,^{\circ}\,\mathrm{s}^{-1}$. The tracking was not lost. Transmitter (c) and receiver (d) applied motor speed for four full lengths of the rail. The maximum transmitter horizontal motor speed is $2.1\,^{\circ}\,\mathrm{s}^{-1}$ while the average applied motor speed throughout the passes is $0.62\,^{\circ}\,\mathrm{s}^{-1}$. At approximately 190 s the tracking system lost the link.

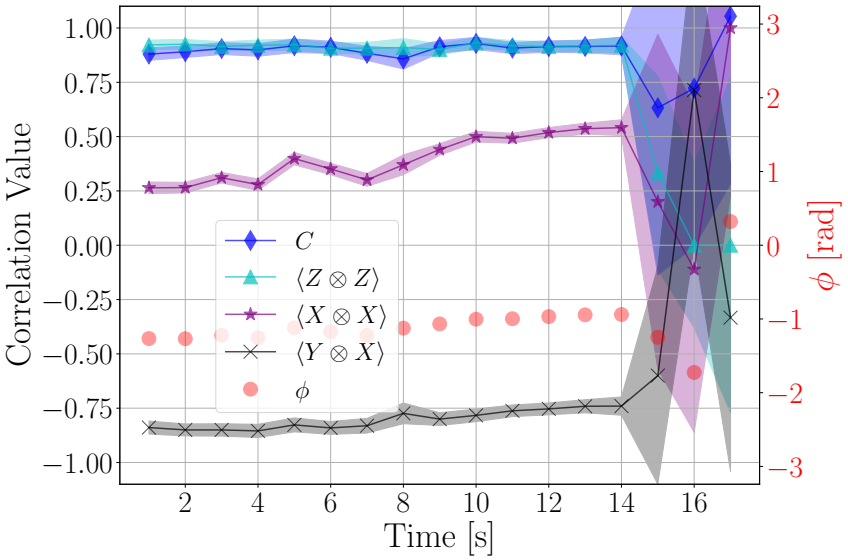

Figure 2.20: Example of tracking being lost during the moving link. Note that all the expectation values including the C-parameter vary wildly in the regions where the tacking is lost and photon count rate is dominated by dark counts. Tracking lost at approximately 15 s.

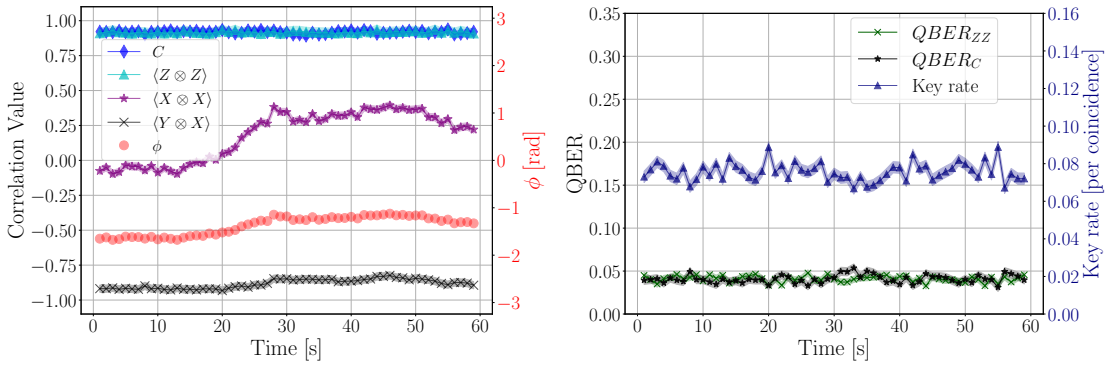

(a) (b)

Figure 2.21: Results of the moving polarization based 6-state 4-state protocol demonstration. (a) Measured correlation values and phase as a function of time over the 60 s pass that included a maximum transmitter speed of $1.19\,^{\circ}\,\mathrm{s}^{-1}$ (Figure. 2.19c). Despite the moving transmitter, the C-parameter remained relatively stable at 0.918 ± 0.010. (b) The corresponding key rate and QBER. All errors are shown as shaded regions and are approximated by Poissonian count errors.

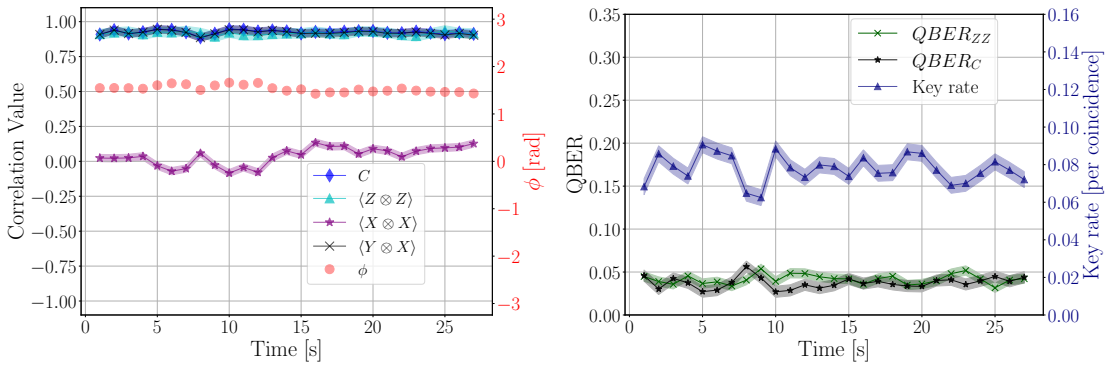

(a) (b)

Figure 2.22: Results of the moving polarization based 6-state 4-state protocol demonstration pass 14. (a) Measured correlation values and phase as a function of time over the relatively fast 25 s pass that included a maximum transmitter speed of $1.93\,^\circ\,\mathrm{s}^{-1}$ (Figure. 2.19a). Despite this high tracking speed, the C-parameter remained relatively stable at 0.925 ± 0.013. (b) The corresponding key rate and QBER. All errors are shown as shaded regions and are approximated by Poissonian count errors.

a maximum speed of $1.93\,^\circ\,\mathrm{s}^{-1}$.

All the results presented in Table. 2.1 are achieved despite the lack of active polarization alignment and compensation. In fact the system is entirely passive, beyond the tracking and pointing system. Furthermore, our results of the moving links are comparable to those of the same system but maintaining a static link (see Table. 2.2). Full static link results are found in Appendix. A in Table. A.3. Nonetheless, the fact that the moving tests are comparable to the static system means that 6-state 4-state protocol can handle the the polarization drifts and changes that occur due to the motion of the transmitter telescope.

2.2.4.1 Link efficiency

One of the challenges for these experiments is the losses experienced over the free-space channel. The transmitter spot size is larger than the receiver aperture such that approximately 50% of the transmitter light is lost. The overall measured throughput of the system including the heralding efficiency of the source and the detector efficiencies is calculated from the coincidence and signal counts using

$$\eta_i = \frac{N_c}{S_i}, \tag{2.3}$$

where η_i and S_i are the efficiency of the channel and single photon counts for party i. N_c is the total coincidence counts. For the moving 6-state 4-state tests, the overall channel efficiency for the signal photons (Bob) is $\eta_B = 1.103 \pm 0.001\%$. The channel efficiency for the idler photons (Alice) is $\eta_A = 7.828 \pm 0.008\%$. These values can vary depending the link and source stability.

2.2.4.2 Key rate analysis

There is currently no known way to fully and completely handle the 6-state 4-state C-parameter in a finite size setting, however, Sheridan et al. [102] have done some analysis for the 6-state 6-state RFI protocol. Thus, for our analysis, we make the assumption that the correlations of the entangled state shared between Alice and Bob are symmetric ($\langle X_A \otimes X_B \rangle^2 = \langle Y_A \otimes Y_B \rangle^2$ and $\langle Y_A \otimes X_B \rangle^2 = \langle X_A \otimes Y_B \rangle^2$) such that we can take the 6-state 4-state C-parameter (C_{64}) and relate it to the 6-state C_{66} as $C_{66} = 2C_{64}^2$. Proper investigation of this assumption is a topic of further study as one cannot assume that this is a given. Furthermore, future work will be done to use modern numerical finite size key analysis techniques [105]. The key rate estimates presented here are derived from Eq. 2.4 and are only to be used as indicative measures as it is are not a complete finite size analysis with a formal security proof. Future work is required to correctly implement a finite size analysis. Nonetheless, estimates are found using equations (2) and (3) from [102], the expression for the secret-key length secure against coherent attack for our system is given by

$$\begin{aligned} r_N = &\frac{n}{N}[1 - I_E(Q', C') - n_Q f h(Q') - \log_2 \frac{2}{\varepsilon_{\text{EC}}} - 2\log_2 \frac{1}{\varepsilon_{\text{PA}}} - 7\sqrt{\frac{\log_2(2/\bar{\varepsilon})}{n}} \\ &- \frac{30}{N}\log_2(N+1)], \end{aligned} \tag{2.4}$$

where N is the total raw key (signals sent by Alice and detected by Bob), n is the number of detections in the key map (computational) basis, C' (Q') is the observed C-parameter (error rate in the key map basis) modified to account for the detection statistics [102], and I_E is the upper bound on the information that Eve can gain. Here, N, n, C', and Q' are determined from the detections of the entire block of data being considered. The expressions for these terms can be found in Ref. [102]. The other key rate parameters are found in table 2.3.

For the experiments shown in Table. 2.1, a such a key rate analysis is done. For these key rate estimates, the total detections in the pass are separated into blocks of data of different sizes ranging from 1 s to the entire link length. For each block, the coincidences are combined to calculate a C-parameter and QBER on a per block basis. Then the secret obtained from each block is combined to form the final key. For some passes, no secret key could be obtained due to

Table 2.3: Parameters of the key rate analysis as done in Ref. [102] for Eq. 2.4. Note that this is not a complete finite size analysis and is only used as an indicative measure.

Parameter	Description	Value
$\bar{\varepsilon}$	Smooth min entropy estimation error	2.5×10^{-9}
$\varepsilon_{\mathrm{EC}}$	Error correction failure probability	2.5×10^{-9}
$\varepsilon_{\mathrm{PA}}$	Privacy amplification failure probability	2.5×10^{-9}
$\varepsilon_{\mathrm{PE}}$	Parameter estimation failure probability	2.5×10^{-9}
n_Q	Fraction of computational basis used to estimate the QBER	0.1
f	Error correction factor	1.2

the short length of the pass, thus the pass is artificially lengthened by appending the same pass to the existing one until secret key is obtained. This is obviously not secure and only done for investigation purposes, i.e. to see if a longer pass with similar parameters would obtain a secret key. Creating longer passes becomes a data storage problem as a few seconds of data can create Gigabytes of raw detection time stamp data. This type of data was used for pass 1-16 and hence the shorter pass times. While for passes 17-30 the coincidences are analyzed on the time-tagging unit during the passes, thus the longer link times. This problem will not be such a significant issue for an implementation with QEYSSat.

Table. 2.4 shows the results of the key rate analysis using Eq. 2.4[3]. For many passes, two entries are provided, one with the block size that produced the largest key estimate and one with the highest number of secret bits per second. In some cases the largest key estimate is produced by many smaller blocks of the same size combined together. The largest estimated key in Table. 2.4 is for pass 19 with a key length estimated to be 169575. However, the pass with the largest estimated number of bits per second is pass 1, which achieved a key rate of 948 bits/s. The differences in performance between passes is based almost entirely on the performance of the entangled photon source between different days. As with the asymptotic case, we compare our results to the static case shown in Table. 2.5. Data for the key rate analysis for all the passes are found in Table. A.2 and Table. A.4. As a reminder to the reader, although we perform a key rate estimates here, there is no known solution to calculate the finite size effects for the 6-state 4-state protocol without the assumptions made to obtain Eq. 2.4.

[3] As a reminder to the reader, these estimates are to be only considered as indicative and a complete security analysis is required.

Table 2.4: Key rate estimates based on Eq. 2.4 for the moving channel passes. The passes are in the same order as Table. 2.1. Two entries for each experiment are shown, one with the largest key and one with the highest number of bits per second (indicated with a ˆ by the experiment number). For some passes, a single block size satisfies both maximum conditions. * indicates that the link is artificially lengthened in order to obtain secret key, this is obviously not secure.

Pass	C_{64}	$QBER_{ZZ}$	Key fraction	Total counts	Total key	bits per second	block size [s]	Link length [s]
1	0.901	0.0409	0.0460	1030078	47357	802	59	59
1ˆ	0.900	0.0414	0.0537	795305	42700	948	45	59
2ˆ	0.900	0.0404	0.0516	723263	37287*	847	44	26
2	0.900	0.0407	0.0450	850572	38258*	735	52	26
6	0.878	0.0385	0.0245	486919	11922	384	31	31
8	0.922	0.0363	0.0483	647039	31260	710	44	44
8ˆ	0.923	0.0358	0.0531	587035	31167	779	40	44
9	0.927	0.0377	0.0527	628608	33122	828	40	47
14	0.924	0.0417	0.0531	1177756	62583*	579	108	27
14ˆ	0.924	0.0414	0.0563	668985	37686*	607	62	27
15	0.859	0.0511	0.00405	375552	1523	30	50	25
17ˆ	0.884	0.0245	0.0929	929637	85468	256	111	439
17	0.885	0.0245	0.0899	1245858	117102	226	129	439
18ˆ	0.942	0.0232	0.139	240417	33511	394	85	146
18	0.907	0.0229	0.0973	407477	39640	271	146	146
19	0.925	0.0270	0.152	1135319	169575	360	235	473
20	0.912	0.0190	0.0791	311141	25708	115	111	208
21	0.830	0.0468	0.0620	1111894	68937	241	286	286

Table 2.5: Key rate estimates based on Eq. 2.4 for the static channel. The passes are in the same order as Table. 2.2. Two entries for each experiment are shown, one with the largest key and one with the highest number of bits per second (indicated with a ˆ by the experiment number). For some passes, a single block size satisfies both maximum conditions. * indicates that the link is artificially lengthened in order to obtain secret key, this is obviously not secure.

Pass	C_{64}	$QBER_{ZZ}$	Key fraction	Total counts	Total key	bits per second	block size [s]	Link length [s]
static-1	0.900	0.0494	0.0425	1518132	64508*	556	116	29
static-1ˆ	0.904	0.0495	0.0491	830750	40818*	647	63	29
static-2	0.907	0.0469	0.0385	824534	31724*	546	58	29
static-3	0.931	0.0329	0.1403	693694	97346	442	220	220
static-3ˆ	0.933	0.0333	0.150	426831	63936	459	139	220
static-4	0.919	0.0305	0.140	1097876	152216	418	182	355

2.2.5 Conclusion and Discussions

The results of the moving platform tests of the 6-state 4-state RFI-QKD protocol are quite promising as the need for active polarization control was completely removed. Furthermore, the phase change that was induced by the optical fiber during the moving tests was sufficient slow, thus meriting the use of RFI-QKD protocols. Typical solutions require having state monitoring systems and induce extra losses to the photon throughput. These results are significant in that they demonstrate the feasibility of using RFI-QKD protocols for moving platforms. The importance of these results should not be underplayed as virtually every moving QKD system that employs polarization has used an active feedback loop to maintain polarization alignment. Overall, these results are of the first free-space moving RFI-QKD experiment and first polarization free-space link that lacks an active polarization compensation system in the channel. These results are quite significant for QEYSSat as there was no appreciable drop in the C-parameter despite the relatively fast transmitter motor speed that were sufficiently higher than the expected maximum angular velocity for a QEYSSat pass. Overall these results reduce the overhead, the intrinsic photon losses, and costs of quantum communication systems.

Future work is to improve the EPS efficiency and entanglement visibility. Particularly, using custom made fiber lengths to maximize the temporal walk-off compensation experience when

passing through the PMFs. Further work can be done to optimize the free-space link, in particular motorizing the receiver such that constant transmitter mount speeds can be obtained. In addition, optimizing the coarse pointing software parameters and hardware in order to minimize the chance of losing the tracking beacon.

2.3 Summary

In this chapter, two studies are done to make improvements to the existing QEYSSat ground station hardware. The first improved the stability and robustness of the weak coherent pulse source, particularly the polarization modulation setup. This was achieved by creating what is called the inline polarization modulation system. The new system eliminates the need for constant realignment and is practically plug-and-play. The current intrinsic QBER of the IPMS is 1.5% which must be improved for QEYSSat. The second study investigated the feasibility of using the 6-state 4-state RFI protocol for QEYSSat. This would eliminate the need for an active polarization alignment system and thus decrease the intrinsic photon losses of the QEYSSat ground station. The results of the moving RFI demonstrations are quite promising as no drop in the quality of the quantum channel is measured despite the lack of active polarization alignment. This could significantly reduce the overhead of free-space channels that employ polarization encoding.

Chapter 3

Reference frame independent time bin quantum key distribution over challenging channels

In this chapter, the 6-state 4-state protocol is adapted for time bin encoding and used in various difficult quantum channels. First, the protocol is used to develop and demonstrate a fully passive time bin quantum key distribution system. This system has no active components, thus is suitable for challenging channels and is tested over a highly multi mode fiber channel. This protocol is then used to perform a proof-of-concept demonstration of sending time bin encoded near-infrared photons through a 3.2 km telecommunications fiber. The higher order modes of this channel are studied in detail with the results indicating that this is a promising avenue for integrating many quantum sources with the current optical infrastructure. Finally, the protocol is used to demonstrate a moving free-space time bin experiment. The results of the free-space tests demonstrate the need for robust and compact field widened interferometers.

Statement of contribution

- **Fully passive RFI time bin QKD** Prof. Thomas Jennewein and I conceived the idea of a fully passive reference frame independent time bin scheme. Jeongwan Jin constructed the field widened interferometer used. I build the remainder of the experimental setup. I conducted the data collection with the assistance of Dogan Sinar, Stéphane Vinet, and Wilson Wu. I wrote the analysis code and produced the results presented.

- **Time bin qubit transfer in the presence of higher order spatial modes** Prof. Thomas Jennewein and I conceived the idea sending near-infrared photons over telecommunication fibers. I performed the experiments with some assistance from Stéphane Vinet and Wilson Wu. I performed the data analysis and produced the results presented.

- **Indoor moving free space time bin demonstration** Prof. Thomas Jennewein and I conceived the idea of the experiments. I prepared the experimental setup and conducted the pointing systems tests with the guidance of Brendon Higgins. Stéphane Vinet, and I conducted the experiments and data acquisition. Brendon Higgins assisted with troubleshooting the tracking and detection systems. I conducted the data analysis of the results presented.

3.1 Fully passive RFI time bin QKD

As described in Chap. 3.3, time bin encoding for quantum key distribution continues to be the choice of encoding for optical-fiber quantum networks. However, significant effort is typically required to align the sender and receiver interferometers' relative phase which creates additional technical overhead to successfully perform QKD in both free-space and optical fiber links [76, 106]. There has been a substantial effort in improving the passive phase stability of the time bin interferometers [88]. However, these passive solutions that rely on the robustness of the interferometer chassis, still require active phase stabilization between the sender and receiver in order to phase lock the two interferometers. The use of reference frame independent quantum key distribution (RFI-QKD) protocols avoids the requirement for active phase locking of the two interferometers and can be applied in both a prepare & measure and an entanglement based schemes [71]. Another solution is to use ultrafast techniques (using time bins on the order of picoseconds) to reduce the size of the time bin interferometers such that it is unlikely the relative phase of the interferometer changes [107]. Such systems are very useful but are difficult to implement in free-space links and can become quite costly when deployed over a large quantum network.

As is demonstrated with polarization in Chap. 2.2, the specific benefit of RFI-QKD protocols is that while the relative phase in the shared state between Alice and Bob is allowed to drift, one can still recover entanglement and perform QKD. This translates to the time bin case by removing the need for actively stabilizing the two interferometers involved in the communication channel. That is, the two interferometers' relative phase is allowed to drift, but the channel purity between the two key exchange parties can still be determined, provided the phase drift is relatively "slow" to allow for the sufficient estimation of the channel parameters (Sec. 2.2.3).

Time bin RFI-QKD demonstrations have been performed over free-space channels and over fiber optical channels using single mode interferometers and active basis choice [82, 108]. However, the use of single mode interferometers can result in significant photon throughput losses particularly over a highly multi mode channel, and thus effect the overall performance of the system. In the work presented below, field widened time bin interferometers are used and significantly reduce the required spatial mode alignment to achieve a high key rate [109]. Furthermore, previous studies used active basis and phase encoding which generally requires additional system overhead due to pulse synchronization and power requirements, both of which can be challenging for moving platforms such as airplanes [72], drones [110], or satellites [111, 66]. Particularly for the latter, where space and power requirements of satellites can be quite limiting. Thus systems that require the least amount of operational overhead are ideal in deploying a quantum network.

In this section, a time bin version of the 6-state 4-state RFI protocol is used [70]. The protocol is described in detail in Sec. 3.1.1. Active basis selection is avoided by using a passive 6-state analyzer for the 6-state measurement, while the 4-state measurement is inherently passive for a time bin measurement (i.e. the two bases are the computational and superposition basis). Furthermore, the use of a field widened interferometer at the receiver allows for testing the protocol over challenging channels, such as highly multi mode fibers. Thus, this work is the demonstration of a fully passive entanglement based 6-state 4-state time bin RFI-QKD that requires no phase stabilization or active basis selection. Due to the simplicity of the scheme, it can be considered a plug-and-play system. This is particularly important for free-space channels because using active phase alignment over a fluctuating channel, such as a turbulent atmosphere, is difficult as a reference laser would suffer from random intensity fluctuations. Hence the pursuit of a fully passive RFI-QKD time bin system.

3.1.1 Time Bin 6-state 4-state protocol

The 6-state 4-state time bin RFI-QKD protocol is a slight modification to the polarization entanglement based protocol of [70]. However, with the time bin version, one photon is converted from polarization to time bin [112]. Although we use an entanglement based approach, this scheme could easily be adapted for a prepare & measure type scheme where the sender produces 6 states while the receiver measures 4 states. However, this would require some active components (i.e. phase modulators) in the system, thus losing the "fully passive" title. For the purposes of this demonstration, the photon converted from polarization to time bin encoding will undergo the 4-state measurement, which enables the fully passive system.

Overall, the entangled state shared between Alice and Bob is

$$|\psi_{\mathrm{AB}}\rangle = \frac{1}{\sqrt{2}}\left(|H\mathscr{E}\rangle + e^{i\phi_{\mathrm{AB}}}|V\mathscr{L}\rangle\right), \tag{3.1}$$

where ϕ_{AB} is the relative phase been Alice and Bob; H,V are horizontal and vertical polarizations respectively; and $\mathscr{E}$, $\mathscr{L}$ are the early and late time-bins respectively. The particular benefit of this hybrid entangled state is that it is relatively straight forward to produce a 6-state analyzer for the polarization encoded photon, while a 4-state analyzer for time bin photons is based on a standard unbalanced interferometer. Alice performs a 6-state polarization measurement on the first qubit, measuring in the σ_{z_A}, σ_{x_A}, and σ_{y_A} bases, while Bob makes a 4-state time bin measurement on the other qubit measuring in the in the σ_{z_B} and σ_{x_B} bases. In this implementation, the computational basis is the horizontal-vertical polarization basis (σ_{z_A}) for Alice and the early-late (σ_{z_B}) basis for Bob, which are the fixed bases for the RFI protocol, and thus are used to generate the secret key. While the superposition bases are used to estimate the 6-state 4-state C-parameter.

As shown in Tannous et al.[70] and in Chap. 2.2, despite the phase drifts in the entangled state, a key can still be generated provided that strong correlations are maintained in all bases. The special part about the RFI protocols is that the correlations between the superposition coincidences of the polarization superposition bases and the time bin superposition basis may change, but a constant C-parameter can be calculated from the correlations to determine the integrity of the quantum channel. As a reminder the C-parameter is given by

$$C = \sqrt{\langle\sigma_{x_A}\otimes\sigma_{x_B}\rangle^2 + \langle\sigma_{y_A}\otimes\sigma_{x_B}\rangle^2}, \tag{3.2}$$

where as in Chap. 2.2, $0 \leq C \leq 1$ with $C = 1$ indicating a maximally entangled state or perfect channel [70]. Recall from Chap. 2.2 that the C-parameter is statistical by definition and therefore is dependent on the number of detection events used in its estimation. Typically the C-parameter is estimated over some time interval, and therefore the amount of phase drift that occurs during this time interval can also smear the observed C, as shown numerically in Chap. 2.2. Furthermore, as with the polarization based 6-state 4-state RFI protocol, there is currently no known way to use the C-parameter in a finite size key rate analysis. However, again as in Chap. 2.2, I will use the analysis done in Sheridan et al. [102] and assume the correlations of the state shared between Alice and Bob are symmetric and that $C_{66} = 2C_{64}^2$ [1].

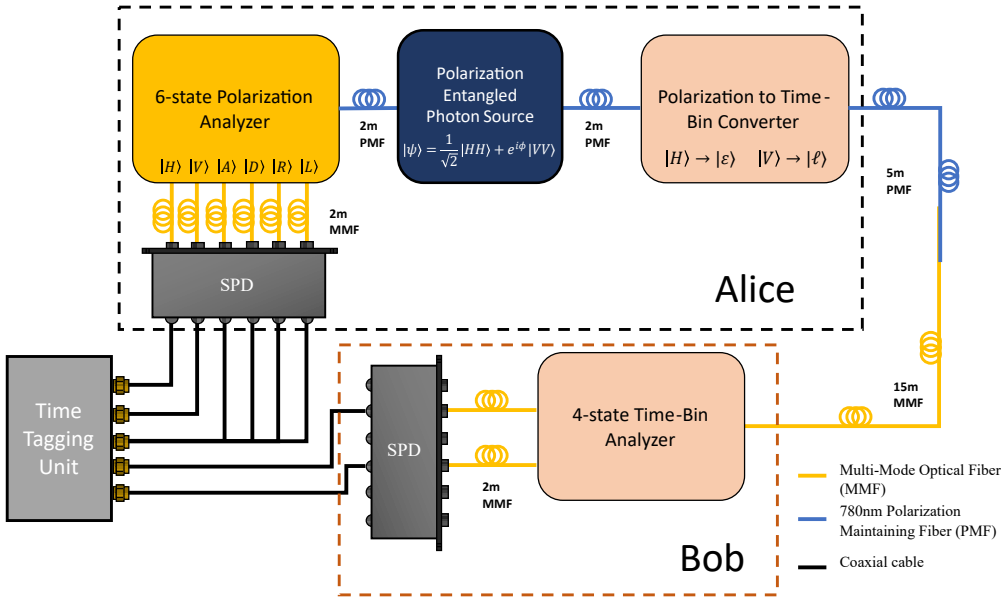

Figure 3.1: Experimental setup of the time bin RFI-QKD proof-of-principle demonstration. An entangled photon source (EPS) creates polarization entangled photon pairs at 785 nm (signal) and 842 nm (idler) via spontaneous parametric downconversion. The idler photon is measured at a local 6-state polarization analyzer, while the signal photon is converted to time bin encoding and sent across a multi mode fiber (MMF) optic channel to a receiver that performs a 4-state time bin measurement. Eight single photon detectors (SPD) are used to measure the photons. A time tagging unit is used to record detection events.

3.1.2 Experimental Details

Figure 3.1 shows a sketch of the experimental setup used for the time bin RFI-QKD proof-of-principle demonstration. where we perform the adapted 6-state 4-state protocol [70]. The experiment consists of: an entangled photon source (EPS) that was made by the SpooQy group at the National University of Singapore [99] and is the same source used in Sec. 2.2.2, a local 6-state polarization measurement, a polarization to time bin converting interferometer (Figure. 3.2a), a quantum channel, a time bin analyzing interferometer (Figure. 3.2b), and single photon detectors with time-tagging. Coincidence and correlation of the data is done on a computer during post-processing.

The EPS creates polarization entangled photon pairs that are in the two qubit state

$$|\psi_{AB}\rangle = \frac{1}{\sqrt{2}}\left(|H_A H_B\rangle + e^{i\phi_{AB^*}}|V_A V_B\rangle\right), \tag{3.3}$$

where ϕ_{AB^*} is a random phase imparted on the entangled state by the source and the collection optical fibers, similar to the behavior observed in Sec. 2.2. From each entangled pair, the idler photon is measured using the local passive 6-state polarization measurement apparatus, while the signal photon is converted to time bin encoding before being sent across the quantum channel using the polarization to time bin converter (PTC). the 6-state analyzer is the same analyzer used in Sec. 2.2. Note that the 6-state polarization measurement could also be sent across an arbitrarily long quantum channel, such as to a satellite. However, for the purposes of this demonstration it is kept as "local" and thus both the EPS and 6-state analyzer are part of Alice, though typically the EPS can be separate from Alice.

The PTC is an unbalanced Michelson interferometer and is shown in Figure 3.2c. It consists of a polarizing beam splitter and quarter-wave plates at each beam splitter output that helps maximize the signal sent to the output port of the Michelson interferometer. Here the PTC is designed such that the horizontal polarized light is takes the short path of the interferometer ($H \rightarrow \mathscr{E}$), while vertically polarized light takes the long path, ($V \rightarrow \mathscr{L}$), which creates the entangled state shown in Eq. 3.1. Thus any photon in a polarization superposition would follow a "superposition" of both interferometer paths in the PTC. The polarization information of the photons that is correlated to which path the photon took is removed at the output of the PTC with a polarizer at 45° with respect to the horizontal and vertical polarizations. Therefore, the photon polarization is no longer correlated to the time bin information and the photons are safe to send

[1] We do not follow the protocol found in Ref. [102] as it is for the symmetric 6-state 6-state protocol. Here we are making assumptions that the correlations of the state are symmetric in order to perform some key rate estimates following Eq. 2.4 that are indicative at best.

across the channel. This is in fact a quantum eraser [113, 114] and a nice practical use of one. The separation of the time-bins is given by the path difference of the PTC which is approximately 2.2 ns. The time bin separation is chosen in order for the time bins to be sufficiently separated and distinguishable given the detector and source jitters.

After passing through the PTC and being converted to the appropriate time bin state, the photons are then coupled to a polarization maintaining fiber that collects the output of the PTC. The photons are then sent across the quantum channel which, for the results presented in Sec. 3.1.3, includes, a 5 m, 10 m and 15 m MMF, a 5 m single mode fiber (SMF), and no extra channel (i.e. the output PMF directly connected to the TA). A field widened multi mode time bin analyzer (TA) is used to measure the time bin encoded photons after they pass through the quantum channel. The optical layout of the TA is shown in Figure 3.2d. It is a field widened interferometer that uses a $4f$ imaging system, the same one used in Jin et al. [76]. To truly perform the RFI-QKD, no reference optical signal is used to stabilize the relative phase between the PTC and the TA. In fact, the relative phase of the PTC (sender interferometer) and TA (receiver interferometer) were allowed to drift with ambient noise. To demonstrate the robustness of the protocol, in some experimental trials, a piezoelectric actuator is used to deliberately cause a phase change in the TA (Figure 3.9). The outputs of the field widened interferometer are coupled into multi mode fibers which are connected to single photon avalanche diodes. A time tagging unit is used to record the detection events and coincidence analysis is done during post-processing to calculate the correlations in the various bases. As mentioned in Chap. 2.2, the use of a single time tagging unit that collects all the coincidence events is not secure and two independent time tagging units (one at each party of the communication channel) are required to properly keep all signals and results secure. However, the single time tagging unit is sufficient for a proof-of-principle implementation.

On average, the overall number of coincidences measured in our proof-of-concept experiment is about 9000 coincidence/s. The EPS itself has an intrinsic pair production rate of approximately 10×10^6 pairs/s. However, this is reduced by the heralding efficiency of the source $\approx 20\%$, which includes the losses due to fiber coupling into the collection PMFs. Furthermore, there are additional losses from the PTC, TA, and the detector efficiencies. The PTC throughput is measured to be 35.4% including fiber coupling into the output PMF, however it is intrinsically reduced by 50% due to the polarizer that eliminates the polarization signature of each time-bin. Table. 3.1 shows the throughput efficiency of all the channels tested. The TA has throughput of 67.0%, including coupling into the multi mode fibers, but not including the detector efficiency. The 6-state polarization analyzer at Alice has an approximate throughput of 49.6% across all six paths, again not including the detector efficiencies. The throughput of the PTC, TA, quantum channel, and 6-state analyzer were measured using a laser and power meter. Experimentally, the total combined efficiencies, including single photon detector efficiency, are also found in Ta-

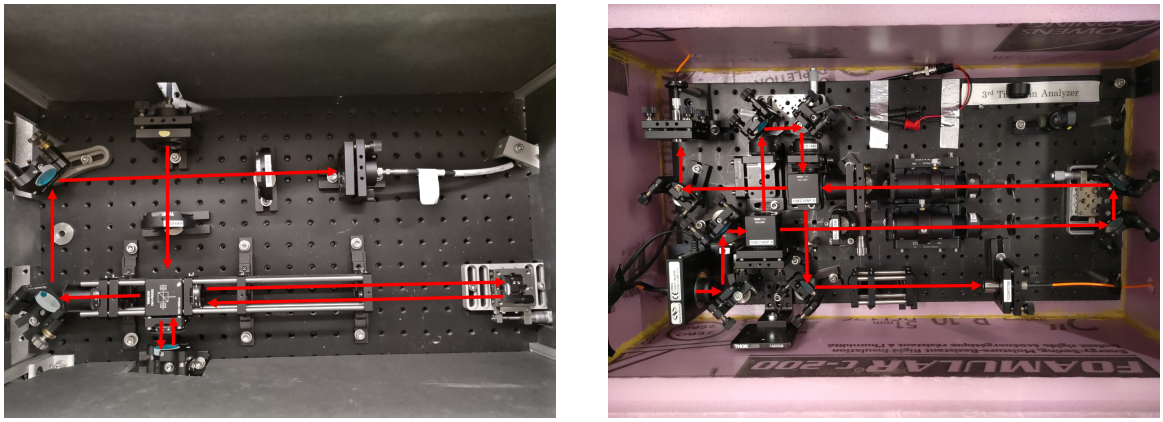

(a) (b)

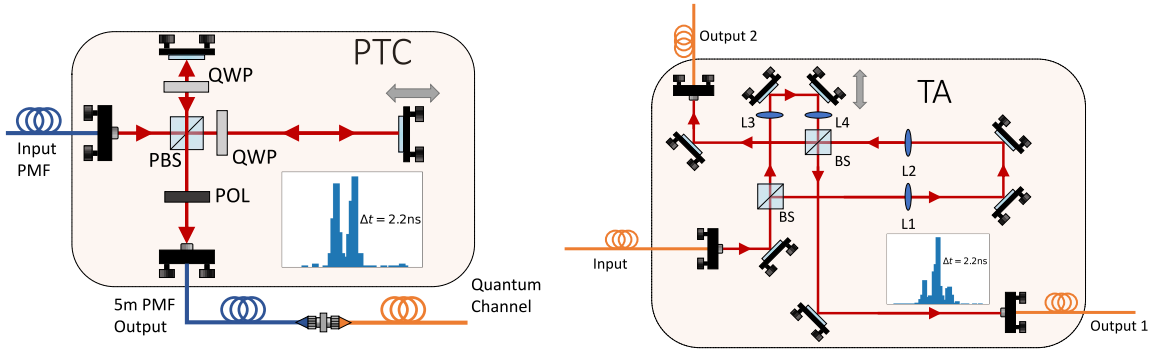

(c) (d)

Figure 3.2: (a) The polarization to time bin converter (PTC) and (b) the time bin analyzer (TA) interferometers. Both interferometers have a path separation of 2.2 ns. The TA is $4f$ field widened interferometer that has multi mode fiber inputs and outputs. No active phase compensation is used to maintain a phase reference between the two interferometers. A piezo is inserted in the TA short path to induce a phase drift. Optical schematic of the PTC (c) and TA (d). HWP: half-wave plate, QWP: quarter-wave plate, L: lens, POL: polarizer, PMF: polarization maintaining fiber, PBS: polarizing beam splitter, BS: 50:50 beam splitter.

Table 3.1: Throughput of the various quantum channels tested. η_A is the channel efficiency for the idler photons measured by the 6-state analyzer at Alice. η_B is the channel efficiency of the signal photons measured by the TA at Bob. Some variance in the transmission efficiency is due to a number of factors including but not limited to the fiber coupled heralding efficiency of the source, and the proper tuning of the laser and crystal temperatures. The error is provided on the last digit.

Channel	Transmission (%)	η_A (%)	η_B (%)
PMF	88	3.417(4)	0.983(1)
5m SMF	88	3.409(5)	0.749(1)
5m MMF	92	3.384(5)	0.854(1)
10m MMF	91	3.392(5)	0.862(1)
15m MMF	87	3.463(5)	0.835(1)

ble 3.1. These numbers are for comparison purposes only as different data sets taken on different days can have different channel efficiencies, primarily due to the source's fiber coupled heralding efficiency. For example, the PMF channel on a different day had a throughput efficiency of $\eta_B = 1.024 \pm 0.002\%$ for the signal photons and $\eta_A = 11.60 \pm 0.02\%$ for the idler photons which is higher than the PMF efficiencies shown in Table. 3.1. These changes come from different fiber coupling efficiencies at the EPS, and better alignment and coupling efficiencies of the other optical elements. The fluctuations in transmission can be mitigated by better fiber optical coupling stages or by securing the optics in a robust manner.

We use our Monte Carlo simulation to estimate the effects of a phase change for our system that measures about 3000 coincidences ($N = 3000$) in the superposition basis during a 1 s ($t_N = 1$) measurement time interval (figure 3.3). The tolerated relative phase drift is approximately $0.512\,\mathrm{rad\,s^{-1}}$ before a 5% reduction in the asymptotic key rate. This tolerance can be increased by having more coincidences per measurement time interval or by reducing the measurement time, i.e. a faster measurement system. A longer measurement time will increase the number of photon detections, but increase the smearing effect and cause a larger drop in key rate for the same phase change rate. In figure 3.3 we compare our Monte Carlo simulation to a modified version equation (17) from [102]. The modifications are necessary to match the definition of C used in the 6-state 4-state protocol [70], as discussed in Sec. 2.2.3.

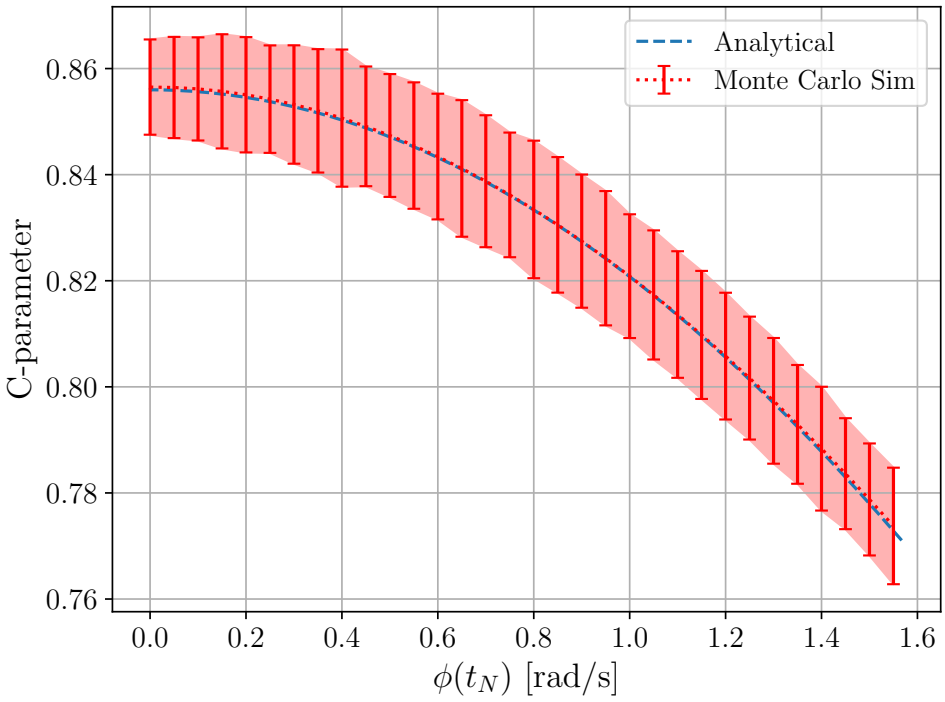

Figure 3.3: Change in the value of the C-parameter as a function of phase variation over a fixed time period ($\phi(t_N)$). The error bars are the standard deviation of the Monte Carlo distribution and demonstrate the statistical nature of the C-parameter that is not captured by equation (17) of [102] (The analytical curve). The error bars can be reduced by increasing the number of photons collected in the time $t_N = 1s$. Here $i = 300$ for each $\phi(t_N)$.

3.1.2.1 Stability of the Time Bin Analyzer

An important experimental metric for this study is to determine is the stability of the relative phase of the unbalanced interferometers. This was determined empirically for the TA by using an external cavity diode laser (Toptica DL Pro) that has long coherence length of 5 km[2]. The coherence length of the laser is significantly longer than the path difference of the interferometer and therefore interference is still observed. By measuring the optical power placing a power meter (Thorlabs PM100D) at one of output ports, the phase stability of the interferometer can be measured. If the optical power is stable and does not change over time, the phase is stable. However, if the optical power fluctuates/changes with time, then the relative phase difference

[2]Obtained from the specification sheet of the laser.

between the two paths of the interferometer is changing. The power as a function of time is shown in Figure. 3.4. From the measured results, the phase change is calculated to be approximately $0.6\,\mathrm{mrad\,s^{-1}}$ or $2.2\,\mathrm{rad\,h^{-1}}$. Comparing this to the tolerance of the C-parameter to phase change of $0.519\,\mathrm{rad\,s^{-1}}$ (Sec. 2.2.3) it appears that the 6-state 4-state RFI-QKD protocol should be able to handle the change in phase of the TA (when it is left alone and isolated from vibrational noise).

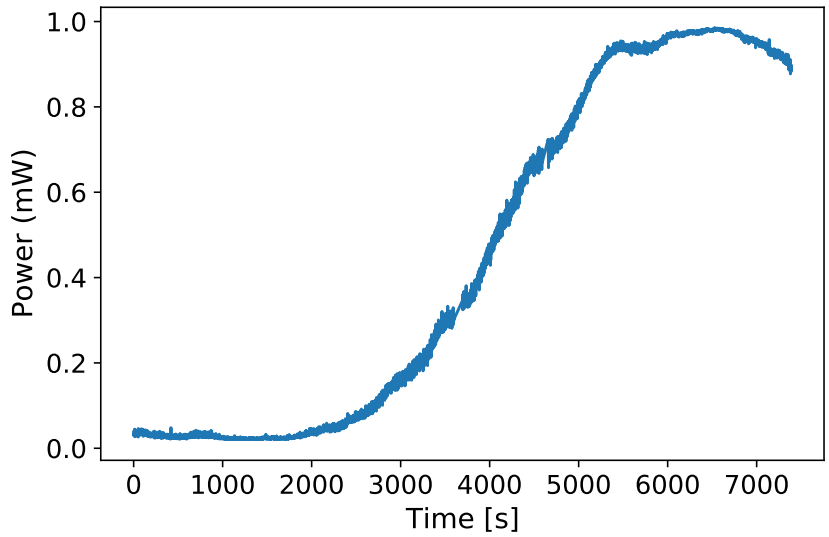

Figure 3.4: Intensity at the output of the TA showing the phase change as a function of time over two hours.

3.1.2.2 Visibility of the TA

Although in Ref. [76], it is reported that the visibility of the TA is 97%. The TA visibility during the experimental runs presented in Table. 3.5 and in Appendix B ranged from 93% to a maximum of 97%. The visibility was measured using the Toptica DL Pro, an optical power meter, and by running the piezoelectric actuator. The intensity at the output of the TA, if aligned properly, should fluctuate from a minimum to a maximum, from which an interference visibility is calculated. Figure 3.5 shows the power meter reading as a function of time and the extrema are visible.

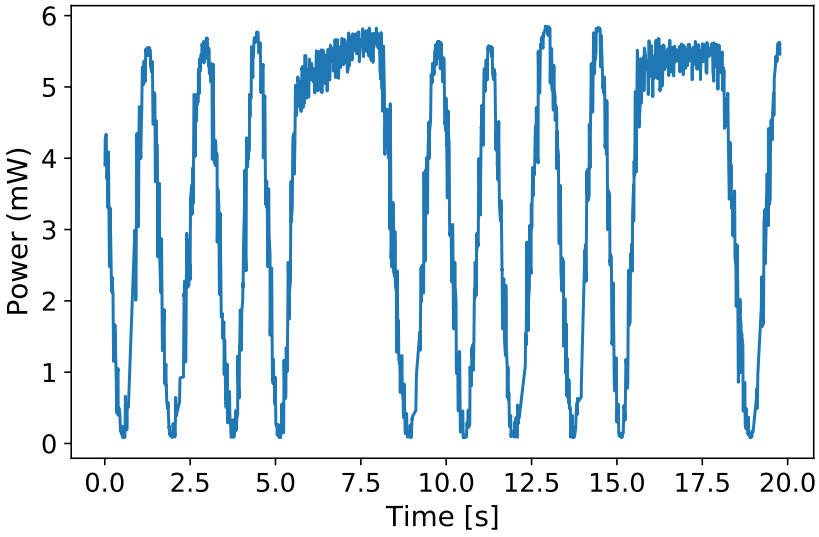

Figure 3.5: Intensity at the output of the TA with the piezoelectric actuator running at 500 Hz. Here the visibility is 96.3%. The visibility is taken by calculating the average of the visibility of the minimum and maximum pairs.

3.1.3 Results and Discussion

The results of select tests for the various quantum channels are found in Table. 3.2 and appear to be fairly similar across all quantum channels. Table. 3.2 has data describing two scenarios (i) the system and interferometers are allowed to drift due to fluctuations from the environment, (ii) a piezoelectric actuator in the TA is driven to produce a constant phase change of $0.1\,\mathrm{rad\,s^{-1}}$, which is well within phase tolerance calculated for our system. The detailed results of all the tests performed for each quantum channel can be found in the tables of Appendix. B.

For discussion purposes, two channels, the 15 m MMF and the PMF channel (i.e. no additional optical fiber), are described in detail below. Figure. 3.6 and Figure. 3.7 show the results for the PMF channel. The average visibility of the C-parameter is 0.901 ± 0.028 and 0.878 ± 0.028 for scenario (i) and (ii) respectively.

For the 15 m, MMF channel Figure 3.8 and Figure 3.9 show the results for our proof-of-principle demonstration in the two scenarios. Despite the lack of active compensation of the two interferometers' relative phase, average visibilities of 0.893 ± 0.018 and 0.876 ± 0.021 are observed in the phase-dependent superposition basis (C-parameter) for scenario (i) and (ii) respectively for the 15 m MMF channel. The more important results is that in Figures 3.8a, 3.9a

Table 3.2: Results of the RFI time bin tests over various channels. No accidental background coincidences are subtracted in obtaining these results. The piezo column indicates the presence of a change in relative phase of the interferometers due to a piezoelectric actuator. The secret bits are estimated over the entire link using the analysis of Eq. 2.4. The * indicates that the parameters of Eq. 2.4 were adjusted to differ from those in Table. 2.3, and that the entire link was not considered, see Sec. 3.1.3.1. Those with no secret bits either had too low counts or too high QBER. [1]When doubling the link, see Sec. 3.1.3.1 for details. Here the key rate estimate is taken with the block size that produced the largest key estimate.

Piezo	Channel	C Paramter	$QBER_C$	$QBER_{ZZ}$	Asymp key rate	Link length	Key rate bits
Off	PMF	0.901 ± 0.028	0.049 ± 0.014	0.030 ± 0.007	0.080	60	5918
On	PMF	0.877 ± 0.014	0.061 ± 0.007	0.023 ± 0.005	0.079	59	395*
Off	5m SMF	0.862 ± 0.033	0.069 ± 0.017	0.031± 0.008	0.0656	60	-
On	5m SMF	0.876 ± 0.027	0.062± 0.014	0.022± 0.006	0.0798	60	389*
Off	5m MMF	0.919 ± 0.019	0.040 ± 0.010	0.028 ± 0.007	0.088	59	4911
On	5m MMF	0.867 ± 0.031	0.066 ± 0.015	0.021 ± 0.006	0.078	59	-
Off	10m MMF	0.845 ± 0.021	0.078 ± 0.011	0.031 ± 0.006	0.060	59	9983
On	10m MMF	0.882 ± 0.030	0.059 ± 0.015	0.041 ± 0.007	0.063	59	-
Off	15m MMF	0.901 ± 0.017	0.049 ± 0.008	0.029 ± 0.008	0.081	30	4464[1]
On	15m MMF	0.876 ± 0.022	0.062 ± 0.011	0.021 ± 0.005	0.080	59	107*

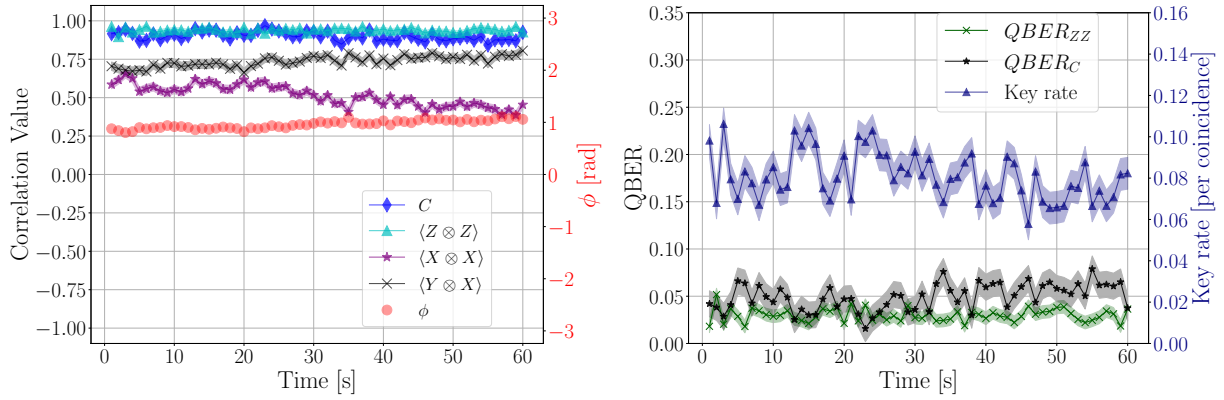

(a) (b)

Figure 3.6: (a) Measured correlation values and phase as a function of time for a 60 s link over a PMF channel (scenario (i)). The average visibility of the superposition correlations remains relatively high (0.901 ± 0.028) despite a lack of relative phase stabilization. ϕ is the relative phase difference between the two interferometers. (b) The corresponding key rate and QBER. All errors are shown as shaded regions and are approximated by Poissonian count errors.

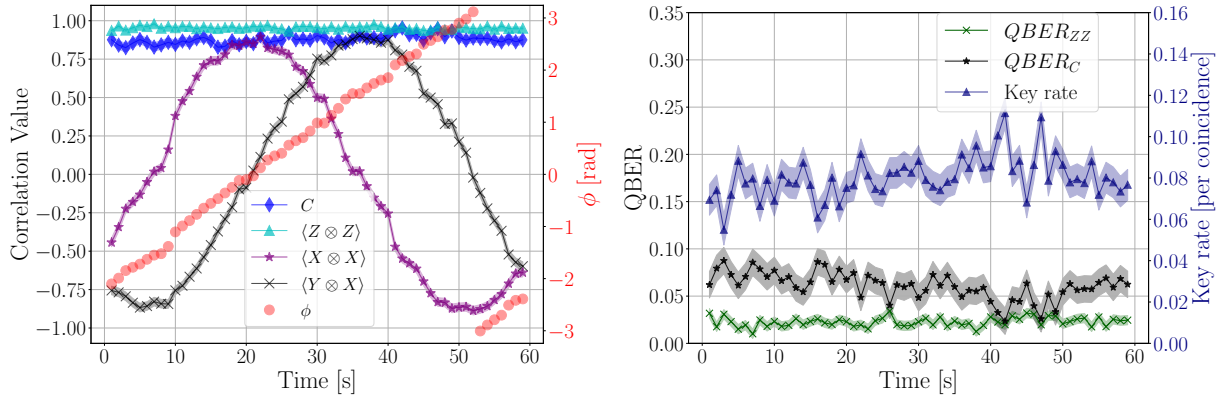

(a) (b)

Figure 3.7: (a) Measured correlation values and phase as a function of time for a 60 s demonstration over the PMF channel while a piezo actuator is inducing a phase change ($0.1\,\mathrm{rad\,s^{-1}}$) in the TA (scenario (ii)). The average visibility of the superposition correlations remains relatively high (0.878 ± 0.028) despite the relative phase variation. (b) The corresponding key rate and QBER. All errors are shown as shaded regions and are approximated by Poissonian count errors.

the C-parameter is shown to be relatively phase independent, constant, and maintains a relatively high visibility throughout the entire experiment despite the lack of relative phase stabilization and a challenging multi mode channel.

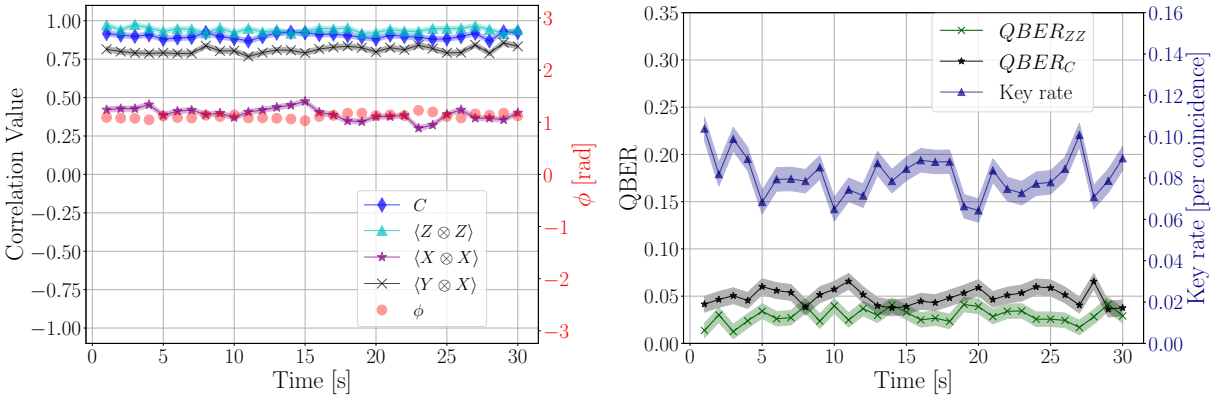

(a) (b)

Figure 3.8: (a) Measured correlation values and phase as a function of time for a 60 s link over a 15 m multi mode fiber (scenario (i)). The average visibility of the superposition correlations remains high (0.893 ± 0.18) despite a lack of relative phase stabilization. ϕ is the relative phase difference between the two interferometers. (b) The corresponding key rate and QBER. All errors are shown as shaded regions and are approximated by Poissonian count errors.

The C-parameter visibilities correspond to an average QBER in the superposition basis of scenario (i) and (ii) respectively are 0.049 ± 0.014 and 0.061 ± 0.014 for the PMF case, and 0.0533 ± 0.0089 and $0.062 \pm 0.011\%$ for the 15 m MMF case. The visibility of the superposition basis is derived from the C-parameter and is a combination of the visibility of the EPS (95%), the PTC interferometer (99%), the 6-state analyzer (99%), and the TA interferometer (93 % to 97 %). Combined, the estimated visibility for the superposition basis is 87 % to 90 % and gives a combined expected QBER of approximately 0.065 to 0.050, which agrees with the experimentally observed values. Other errors, such as wave plate errors and imperfections in the beam splitters are not accounted for but can contribute to the error in our demonstration. The average QBER in the computational basis, for scenario (i) and (ii) respectively, are 0.0298 ± 0.0067 and 0.0227 ± 0.0049 for the PMF case, 0.0220 ± 0.0060 and 0.0215 ± 0.0049 for the 15 m MMF case.

An analysis of the asymptotic key rate was done following the analysis of Tannous et al[70]. For the PMF the asymptotic key rate is 0.0801 bits/coincidence and 0.0796 bits/coincidence ((i) and (ii) respectively). For the 15 m multi mode fiber channel, the number of secret key bits per

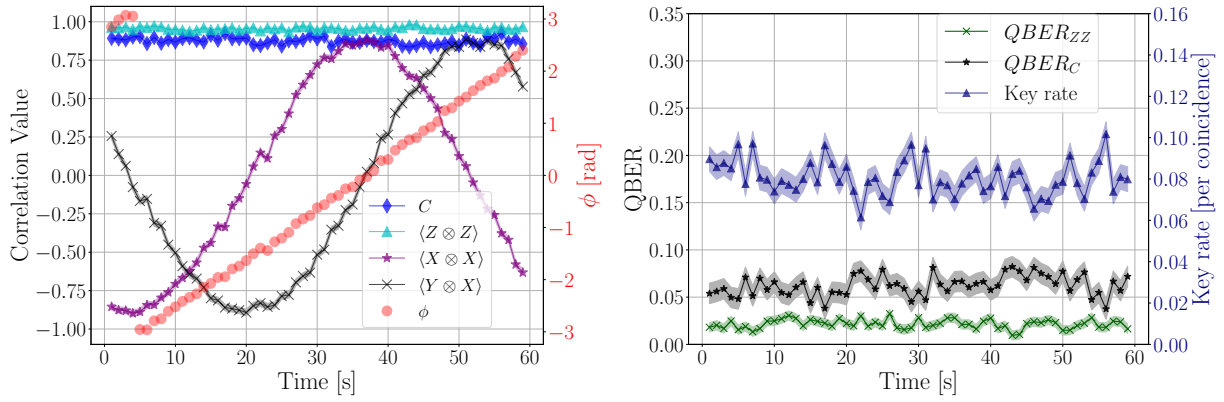

(a) (b)

Figure 3.9: (a) Measured correlation values and phase as a function of time for a 60 s demonstration over a 15 m multi mode fiber while a piezo actuator is inducing a phase change (0.1 rad s^{-1}) in the TA (scenario (ii)). The average visibility of the superposition correlations remains high (0.876 ± 0.21) despite the relative phase variation. (b) The corresponding key rate and QBER. All errors are shown as shaded regions and are approximated by Poissonian count errors.

coincidence detection is estimated to be 0.0804 bits/coincidence and 0.0802 bits/coincidence ((i) and (ii) respectively). These asymptotic key rates are compared to the maximum achievable rate for our system of 0.167 bits/coincidence. Thus there is room to improve the performance, however the results are quite promising since despite the varying phase and the challenging multi mode channel there is no drop in key rate in Figures 3.8b, 3.9b.

3.1.3.1 Key rate analysis

Recall from Sec. 2.2.4.2 that there currently no known finite size analysis for the 6-state 4-state RFI protocol. Nonetheless, a key rate estimation is done for each using the approach Eq. 2.4. For our analysis, we again make the assumption that the correlations of the entangled state shared between Alice and Bob are symmetric ($\langle X_A \otimes X_B \rangle^2 = \langle Y_A \otimes Y_B \rangle^2$ and $\langle Y_A \otimes X_B \rangle^2 = \langle X_A \otimes Y_B \rangle^2$) such that we can take the 6-state 4-state C-parameter (C_{64}) and relate it to the 6-state C_{66} as $C_{66} = 2C_{64}^2$. Results for this analysis are shown in Table. 3.2, while below we discuss the results of the PMF and 15 m MMF channels.

For the links of the PMF channel shown in Figure. 3.6 and Figure. 3.7, only scenario (i) results in a positive key fraction from Eq. 2.4. For this link, if one uses the detections collected over the entire 60 s, this gives a C_{64}-parameter and computational basis QBER of 0.898 and 0.0297

respectively. These values produced a positive key fraction of 0.0136 which from the 433406 coincidence detections gives an estimated 5918 secret bits. Note that several other experiments in Table. B.1 produce a positive key fraction. The highest positive key fraction of 0.0285 is calculated by considering the counts collected over the entire experiment of the first entry in Table. B.1. From the 484659 total coincidence detections, this produced an estimated 13827 secret bits. Here the C_{64}-parameter and computational basis QBER are 0.894 and 0.0227 respectively.

For scenario (ii), considering the entire 60 s link would not produce any key as the smearing of the C-parameter would be too great. However, shorter integration times would not produce positive key due to low photon statistics. Specifically, for an error correction factor of $f = 1.2$, no positive key is achievable. However, for an unrealistic $f = 1$, a single 13 s block of data produced a positive key fraction of 0.0036 which from the 109856 coincidence detections obtained an estimated 395 secret bits. There are other experiments within the "piezo" category in Table. B.1 that obtained positive key fractions, however these are not discussed due to the unrealistic $f = 1$.

For the 15 m MMF channel, neither of the two experimental runs that are shown in Figure. 3.8 and Figure. 3.9 were able to produce positive key. In scenario (i) of Figure. 3.8, the link is not sufficiently long enough to produce any positive key due to the low number of detections in the link. However, if the same link is extended to be twice as long, and one considers the entire 60 s link in determining the C_{64}-parameter and QBER, Eq. 2.4 does produce positive key. With a total number of coincidence counts of 395408, a computational basis QBER of 0.030, and a C_{64}-parameter of 0.8999, gave a positive key fraction of 0.01129 and an estimated 4464 secret bits. Some of the links in Table. B.5, that fall under the "no piezo" category, are able to produce positive key. Here we will show the results of the first link shown in Table. B.5. Again we considered the entire 60 s in determining the C-parameter and QBER. This gave a total number of coincidences of 402212, a computational basis QBER of 0.022 and a C_{64}-parameter of 0.8810. With these parameters and assuming perfect error correction, we calculate a key fraction of 0.0161, which amounts to an estimated 6476 secret bits from the total raw key. Note that the minor decrease in computational basis QBER has a significant increase in the estimated key.

For scenario (ii) of Figure. 3.9, as mentioned above considering the entire 60 s link or using shorter integration times would not produce any positive key for an error correction factor of $f = 1.2$. However, again for an error correction factor of $f = 1.0$, the only positive key achieved while still using the other parameter values of Table. 2.3, is from one 15 s block that has a key fraction of 0.00109 or an estimated 107 secret bits from the 99311 coincidences of the 15 s block.

From the results above, it is apparent that the coincidence count rates need to be improved in order to produce a secret key that is similar with state of the art systems reported by the literature [115, 108]. Nonetheless, the results are sufficient for a proof-of-concept experiment. In addition, further investigation into a complete finite size analysis must be conducted as there is currently no

known method to fully perform an analytical finite size analysis for the 6-state 4-state protocol.

3.1.4 Conclusions and Implications

This is the results of the first fully passive time bin RFI-QKD implementation. The results are impressive since they were obtained over a challenging channel such as a multi mode fiber. We demonstrated time bin QKD without the need for any active phase stabilization of the relative phase between sender and receiver interferometers. Furthermore there was no active spatial mode filtering or correction to overcome the distortions of the challenging MMF channels. This is particularly suitable for QKD with moving platforms where the use of multi mode interferometers are desirable compared to single mode interferometers due to better pointing requirements and optical throughput, see Sec. 3.3. With this reduced amount of overhead, our system could therefore be considered a plug-and-play QKD system (i.e. requiring no active components). This is important for quantum networks since the ability to distribute entanglement correlations with time bin encoded photons can ease the deployment of entanglement distribution experiments, and enable quantum sensing applications [87].

The next steps are to improve the performance of the system particularly in terms of photon throughput and pair generation of the source. This can be achieved by working with a source that is optimized for the apparatus wavelength and bandwidth, and increasing the EPS heralding efficiency and entanglement visibility to near unity [116]. In addition, improving the performance of the TA with a better optical design and custom optics would reduce the overall QBER of the system, for instance using a compact optical layout [88] or a new interferometer design as discussed in Chap. 4. Further theoretical studies on the robustness of the protocol are to be conducted, particularly against rapid phase fluctuations and finite size effects. Sec. 3.2 and Sec. 3.3 use this protocol in other more practical link scenarios, demonstrating the versatility of this protocol.

3.2 Time bin qubit transfer in the presence of higher order spatial modes

3.2.1 Using NIR photons in telecom networks

A major discussion of this thesis is developing time bin for free-space quantum channels. This entails overcoming the angle-of-incidence problem which also amounts to dealing with interfering multi mode signals. Although, this is high applicable for free-space applications, another

use case is through multi mode fiber optic channels. At present date, the majority of the fiber optical networks that are deployed throughout the world are single mode for what are know as telecommunication (telecom) wavelengths. Generally, this is around 1550 nm, where the losses in silica are minimal. Many quantum communication systems operate at this wavelength in order to take advantage of preexisting networks [5]. However, many single photon sources do not operate at this wavelength but rather in the near-infrared (NIR) regime (700 nm to 900 nm) [117, 118, 119, 120, 121, 122, 123, 124]. Nonetheless there are many examples of entangled photon sources operating in the telecom band and there has been a lot of development into frequency conversion devices [125, 126]. However, telecom wavelength quantum channels are challenged by the practicality of the detector systems, where cryogenic superconducting nanowire detectors are required to achieve the best detection quality at these wavelengths [127]. Conversely, near-infrared sources can take advantage of the high detection efficiency and low cost of silicon avalanche photodiode detectors. Furthermore, the telecom wavelength range is not the ideal choice for free-space channels due high absorption in the 1200 nm to 1500 nm range, though around 1550 nm the transmittance is acceptable [49]. However, due to the wavelength ranges of quantum sources and the efficiencies of the detectors, telecom wavelengths are seldom used over free-space channels, thus making integration between free-space and fiber optical networks difficult.

Given many of the aforementioned issues with telecom systems, there is a use for integrating near-infrared sources with existing telecommunication networks. However, using near-infrared photons in telecom fibers also has its challenges, mainly that several spatial modes beyond the fundamental mode of the near-infrared photons are supported by the optical fiber. As a consequence, the near-infrared photons experience modal dispersion, which in classical optical communication channels, is detrimental to the distance that data can be transmitted. This also has an effect on the quality of the quantum signal, and can result in reduced entanglement visibility quality.

Fundamentally, modal dispersion is a distortion mechanism that causes different Laguerre Gauss modes to spread out in time in an optical waveguide, typically in the context of a multi mode fiber. As a signal pulse propagates through a multi mode fiber, the different velocities of the different modes cause the pulse to spread in time, see Figure. 3.10a. In ray optics, this can be attributed to the different modes entering the waveguide (or optical fiber) at different angles and thus requiring more time to traverse the waveguide, see Figure. 3.10b. Modal dispersion occurs even with ideal monochromatic signals.

Myer-Scott et al. [128] studied the transmission of 800 nm polarization entangled photons through a standard telecom fiber channel Corning SMF-28. 800 nm photons are slightly multi mode in the telecom fiber (i.e. can occupy more than one Laguerre Gauss spatial mode), and therefore, the higher order modes will experience modal dispersion. Thus, in Ref.[128] they

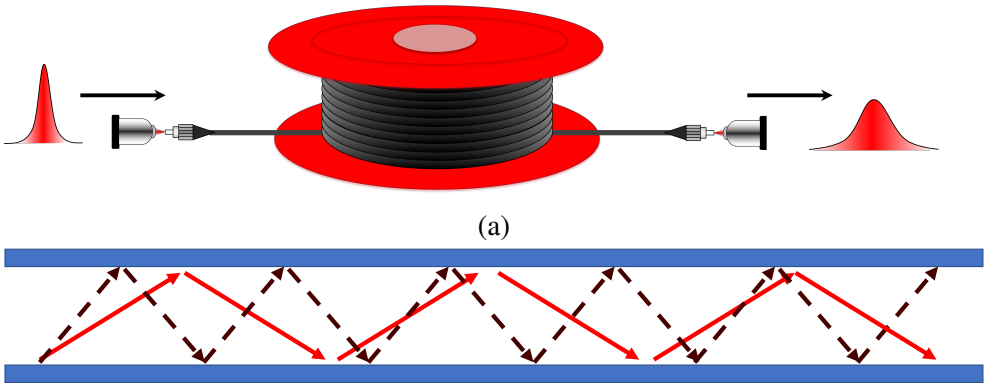

Figure 3.10: (a) Modal dispersion experience by an optical pulse. (b) Ray optics picture of modal dispersion. The darker dashed arrows represent the higher order mode.

were able to observe a high entanglement visibility in both the zeroth order mode and the first order mode despite the modal dispersion. It was shown that the entanglement visibility can be improved substantially by parallel application of spatial filtering and precise temporal filtering to select only the fundamental mode. This is an important result as it means that 800 nm photons can be transmitted through the standard telecom fibers within existing networks. However, polarization encoding is not the preferred encoding for optical fiber channels. Although in Sec. 3.1, it is shown that time bin entanglement distribution can be performed over short multi mode channels (several meters), many practical applications of entanglement distribution require longer links on the order of kilometers. Thus, the need to investigate time bin entanglement distribution in long multi-modal channels.

Modal dispersion is important for time bin entangled photons since it can cause the time bins to overlap and thus increase the error rate, Figure. 3.11a. One solution to this issue is to sufficiently separate the time bins such that modal dispersion does not pose an issue. This is highly impractical as long interferometers are very difficult to design and implement. Another, solution is to have a minimum distance for the quantum channel such that the modal dispersion is large enough that the time bins from the fundamental mode and higher order modes are completely separated, Figure. 3.11b. Here, we perform the latter as it is easier to implement and can be easily performed with the system used in Sec. 3.1. Recently there has been some experimental study relating the effects of modal dispersion on the QBER of a signal [129], however no QKD was performed.

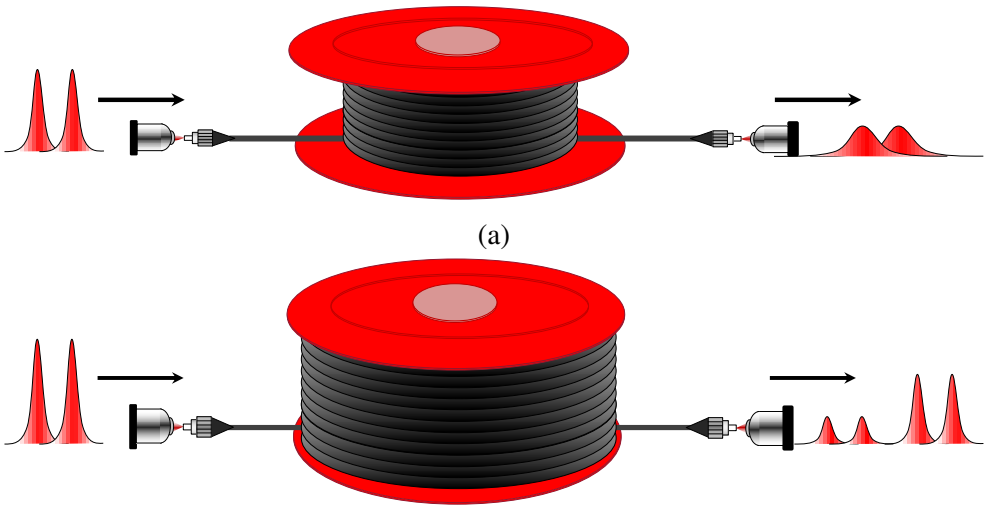

(a)

(b)

Figure 3.11: (a) Modal dispersion can cause time bins to overlap and increase the error rate of the system. (b) Long enough links can cause modal dispersion to separate the zeroth order mode from the first order mode and the time bins can be resolved with lower error rates.

3.2.2 Modal dispersion Characterization

Calculations of modal dispersion typically involve finding the propagation constants of the various modes in the optical fiber and determining the difference of the propagation constant. The calculation involves finding solutions to the Helmholtz equation, which for fibers with many modes can be a tedious calculations. For highly multi mode fibers, estimates are given to avoid such calculations and are able to provide order of magnitude approximations. Saleh and Teich [44] provide such approximate equations for both step index and graded index fibers.

For a step index fiber, the core has a refractive index of n_1 while the cladding has an index of n_2. The transition between the core and cladding is sudden like a step function, as the name implies. Step index fibers typically suffer from high amounts of modal dispersion unless the core is reduced significantly to support a single mode. The equation that approximates the modal dispersion per kilometer in a step index fiber is given by

$$\frac{\sigma_\tau}{L} \approx \frac{\Delta}{2c_1}, \tag{3.4}$$

where L is the length of the fiber in kilometers, $c_1 = c/n_1$ with c being the speed of light in

vacuum, and $\Delta \approx \frac{\mathrm{NA}^2}{2n_1^2}$. So for a typical multi mode fiber with a core index of 1.496 and an NA $= 0.2$, the modal dispersion per kilometer is $22.3\,\mathrm{ns\,km^{-1}}$.

For a graded index (GRIN) fiber, the core has an index of n_1 that is gradually changed to n_2 of the cladding. Effectively, the index of the core is gradually decreased with an increasing radial distance from the center of the core. The most commonly used profile for the core index distribution is parabolic which causes the modes to travel in a more sinusoidal path in the ray optics picture. This sinusoidal path is effectively similar to refocusing the light and thus significantly reduces the modal dispersion produced by a GRIN fiber. The equation that approximates the modal dispersion per kilometer of GRIN fiber is given by

$$\frac{\sigma_\tau}{L} \approx \frac{\Delta^2}{4c_1}, \tag{3.5}$$

which is smaller than eq. 3.4 for the same fiber parameters. For, the example fiber above, the modal dispersion per kilometer is significantly less at $99.6\,\mathrm{ps\,km^{-1}}$. The 15 m multi mode fiber used in Sec. 3.1, is a GRIN fiber and hence the low modal dispersion observed.

However, for fibers that are not highly multi mode, such as telecom fibers for 700 nm to 900 nm, one must still solve the Helmholtz equations and determine the differences in prorogation constants. For this analysis we follow the analysis done in Appendix B. of Ref.[130] and is calculated below in Sec. 3.2.3.

3.2.3 Experimental Details

The experimental details of this experiment are practically the same compared to that in Sec. 3.1. However the quantum channel is changed from a highly multi mode channel to a relatively long telecommunications optical fiber, Figure. 3.12 and Figure. 3.13. Particularly, the optical fiber used is the Corning SMF-28. This optical fiber is slightly multi mode for the 785 nm photons, and has a calculated modal dispersion at this wavelength of $2.168\,11\,\mathrm{ns/km}$, between the zeroth and first order modes. The measured modal dispersion of this optical fiber at 785 nm is $2.322\,58(15625)\,\mathrm{ns\,km^{-1}}$ which is within experimental error to the theoretically calculated value. The experimental error comes from the timing resolution of the time tagging unit used to measure the time of arrival of the photons.

Under typical operational circumstances where the output of the PTC (the PMF in Figure. 3.12) is directly connect to the telecom fiber, the zeroth order mode would be the dominant mode in which the signal propagates and very little signal would be observed in higher order modes. However, with a high enough pair rate, and a long enough count collection period, one

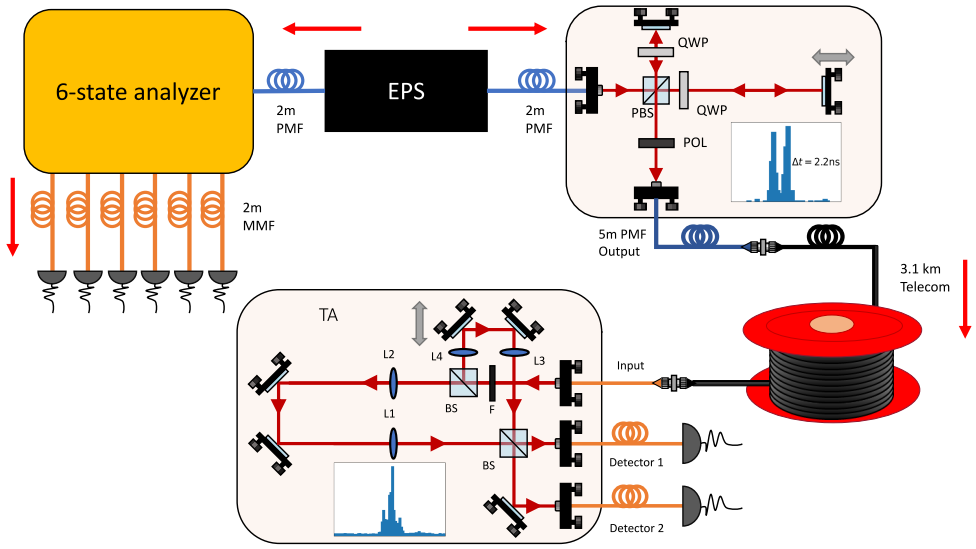

Figure 3.12: Experimental setup with the direct fiber connection between the 780PMF (5m) and the telecom fiber (3.2 km). See Figure. 3.2c and 3.2d for the part labeling convention. Here F = 785nm filter.

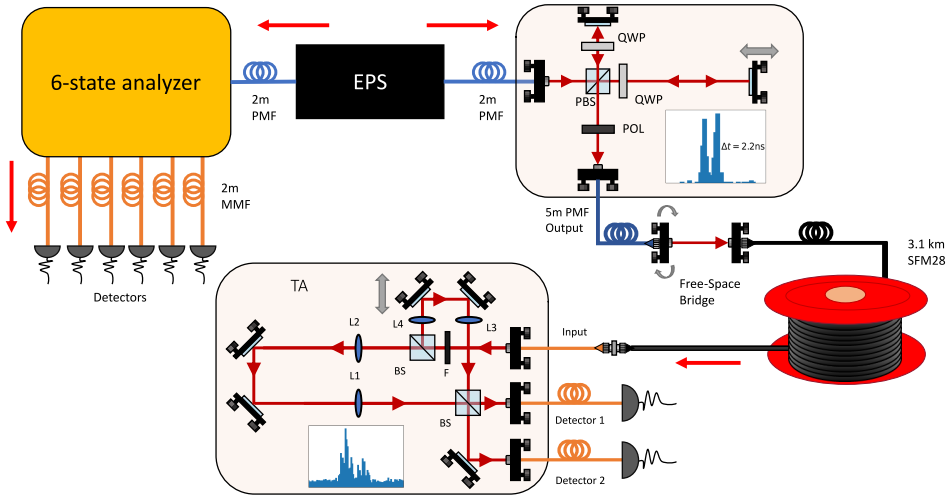

Figure 3.13: Experimental setup with the free-space bridge connection between the 780PMF (5m) and the telecom fiber (3.2 km). The free-space bridge is to increase the coupling into the higher order modes of the fiber. However, such coupling causes very poor overall photon throughput and a poor signal to noise ratio.

can possibly begin to see the contributions of these higher order modes. This was not investigated during this study.

For this particular experiment, in order to ensure that photons are coupled to both the zeroth order mode and the first order modes of the optical fiber, a free-space bridge is made such that the PMF and SMF-28 telecom fiber are slightly misaligned (Figure. 3.13). The angle of incidence between the two fibers is slightly misaligned, such that both the zeroth and first order modes are excited from the start of the 3.2 km channel. This increases the relative amount of photons that occupy the first order mode, however, it significantly reduces the total photon transmission. The photon transmission is further reduced by the increased losses in a telecom fiber for 785 nm photons (13.2% transmission through the direct fiber connection) and the filter placed in the TA (Figure3.13). The 13.2% is approximately the same as the theoretically expected loss at approximately 3 dB km^{-1}. The 3 nm bandwidth 785 nm filter is required for this experiment since the amount of modal dispersion experienced by a photon has a chromatic dependence. Hence, without the filter, the photon spectrum from the entangled photon source is too large and the time bins cannot be resolved after the 3.2 km link.

The total throughput of the direct fiber connection without including the detector efficiencies or the coupling of the entangled photons from the EPS is a function of the efficiencies of all the components, i.e. PTC (35.4%), channel (13.2%), and TA (67.0%). With these numbers total throughput is estimated to be 3.13%, again not accounting for detector efficiency or the photon collection efficiency of the source. With the those considered the efficiency of the direct fiber connection is found to be approximately $0.0613 \pm 0.0006\%$ for the signal photons measured by Bob and $7.27 \pm 0.07\%$ for the idler photons measured by Alice. However for the free-space bridge connection, the losses are even higher with a total channel efficiency of $0.0153 \pm 0.0002\%$ for the signal photons and again $7.24 \pm 0.08\%$ for the idler photons. Clearly the losses play a major role in the transmission and preventing a good signal to noise ratio.

3.2.4 Results

The results of the experiments conducted are split into a few experimental scenarios and are summarized in Table. 3.3. The first is when the signal photons are coupled to the 3.2 km telecom channel using a standard fiber mating sleeve between the PM and telecom fiber (Figure. 3.12). This results in a very small number of photons being coupled to the higher order modes. Nonetheless, some select histograms of the results are shown in Figure. 3.14. The 6-state 4-state time bin RFI-QKD protocol is used and for a 90 s photon exchange, the average C-parameter is 0.831 ± 0.023 with an average QBER in the superposition and computational basis of 0.084 ± 0.011 and 0.0792 ± 0.0070 respectively. For the case when a 90 s photon ex-

Table 3.3: 6-state 4-state protocol results for the NIR time bin entangled photons sent over a 3.2 km telecommunication fiber optic channel. Note that the zeroth and first order modes are only present in the free-space bridge case (FS Bridge). The piezoelectric actuator is inducing a relative phase change of 0.035 rad/s for the direct fiber connection and 0.015 rad/s for the free-space bridge connection.

Link Type	Piezo	C-paramter	$QBER_C$	$QBER_{ZZ}$	key rate [bit per coincidence]
Direct Fiber	Off	0.831 ± 0.023	0.084 ± 0.011	0.0792 ± 0.0070	0.0158
Direct Fiber	On	0.837 ± 0.017	0.0814 ± 0.0085	0.0761 ± 0.0073	0.0198
FS Bridge mode 0	Off	0.739 ± 0.026	0.130 ± 0.013	0.144 ± 0.013	-
FS Bridge mode 1	Off	0.595 ± 0.024	0.202 ± 0.012	0.231 ± 0.026	-
FS Bridge mode 0	On	0.771 ± 0.027	0.114 ± 0.014	0.130 ± 0.011	-
FS Bridge mode 1	On	0.652 ± 0.049	0.174 ± 0.024	0.257 ± 0.021	-

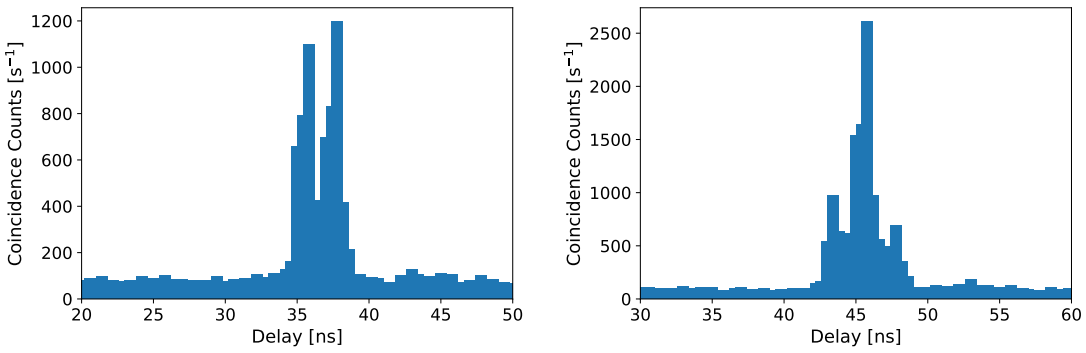

(a) (b)

Figure 3.14: Histogram of coincidences in (a) computational basis and (b) superposition basis in polarization for the direct fiber connection to the 3.2 km fiber.

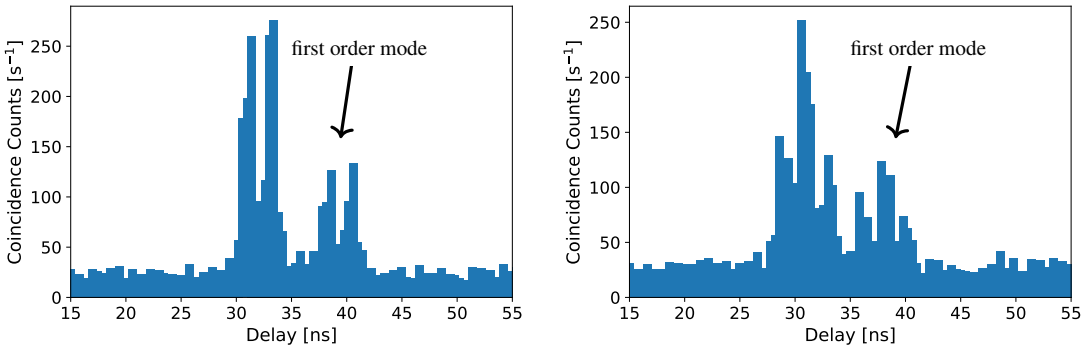

(a) (b)

Figure 3.15: Histogram of coincidences in (a) computational basis and (b) superposition basis in polarization for the free-space fiber bridge connection to the 3.2 km fiber. Note the presence of the first order mode trailing the zero order mode.

change is conducted while piezoelectric actuator is inducing a relative phase change at a rate of 0.035 rad/s, the average C-parameter is 0.837 ± 0.017 and the QBER in the superposition and computational basis are 0.0814 ± 0.0085 and 0.0761 ± 0.0073, respectively. The results for average the asymptotic key rate for the direct fiber connection for the no piezo and piezo case are 0.0158 and 0.0198 respectively for the 90 second link. The larger asymptotic key rate in the piezo case is due to the relative decrease in the overall QBER. Figure. 3.16 shows the results of both these tests.

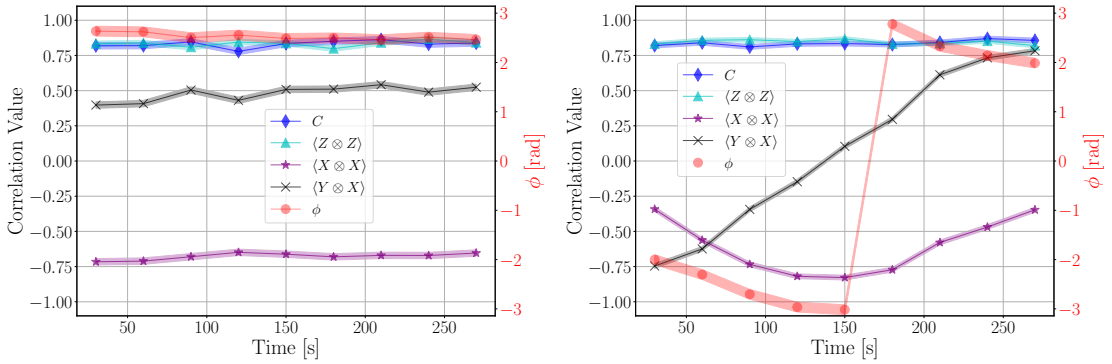

(a) (b)

Figure 3.16: The results of the case without (a) and with (a) the piezoelectric actuator for the direct fiber connection. Error values are included as the size of the point markers.

For the tests that uses a free-space fiber bridge to couple the photons from the PM fiber to the telecom fiber (Figure. 3.13), the losses produced from the slight misalignment significantly affected the signal to noise ratio and QBER. Despite the high noise, the presence of higher order mode photons is more prominent due to the misalignment of the coupling. Figure. 3.15 shows the higher order modes slightly delayed from the zeroth order modes by $7.200\,00(15625)$ ns after traversing the 3.2 km fiber optical channel. The higher order modes can still exhibit entanglement correlations with the idler photons. Thus, for these tests the C-parameter and QBER are calculated for both the zeroth order mode and first order mode. Here, for the scenario with no piezoelectric actuator, the average C-parameter is 0.739 ± 0.026 and 0.595 ± 0.024 for the zeroth and first order modes respectively. This translates to an average superposition basis QBER of 0.130 ± 0.013 and 0.202 ± 0.012 for the zeroth and first order modes respectively. The visibility in the computational basis also suffered due to the signal to noise ratio with average values of 0.144 ± 0.013 and 0.231 ± 0.026 for the zeroth and first order modes respectively. For the case when a piezoelectric actuator is run slowly at $0.015\,\mathrm{rad/s}$, the average C-parameter is 0.771 ± 0.027 and 0.652 ± 0.049 for the zeroth and first order mode respectively. While the average QBER in the superposition basis are 0.114 ± 0.014 and 0.174 ± 0.024, for the zeroth and first order modes respectively, and 0.130 ± 0.011 and 0.257 ± 0.021 for the computational basis. Figure. 3.17 shows the results of these tests. It is important to recognize that the values above for QBER and C-parameter will not produce any positive asymptotic key. However, this can be attributed to the poor signal to noise ratio of the system. Even more interesting is the fact that the entanglement correlations, although quite poor, are still present in the higher order modes as seen by the fact that the piezoelectric induced phase change is present in both the zeroth and first order modes of Figures. 3.17b and 3.17d.

The relatively high QBER's are a consequence of the low signal to noise ratio. This is especially apparent in the free-space bridge tests since the coupling losses are very significant. One method to improve the signal to noise ratio is to perform some sort of background subtraction on the signals that arrive. By removing the accidental coincidences from the signals, the visibility of the entangled state increases significantly in both the zeroth and first order modes. However, such a technique cannot be used for quantum key distribution as this assumes that the noise is uniform which cannot be assumed to be true. Nonetheless, for completeness we present the results for the asymptotic key rate and QBER with background accidental counts subtracted in Table. 3.4 and show the results in Figure. 3.18. Aside from quantum key distribution, this background subtraction technique could be used in other quantum information settings. Another contributor to the noise level is that there is a potential increase in the number of multi pair emissions due to an increased pump power as compared to the other channels. Here 48 mA is used as the laser current which has a significant pump power increase compared to the 40 mA to 43 mA used in Sec. 3.1. Nonetheless, this demonstration has the interesting implication that, provided sufficient

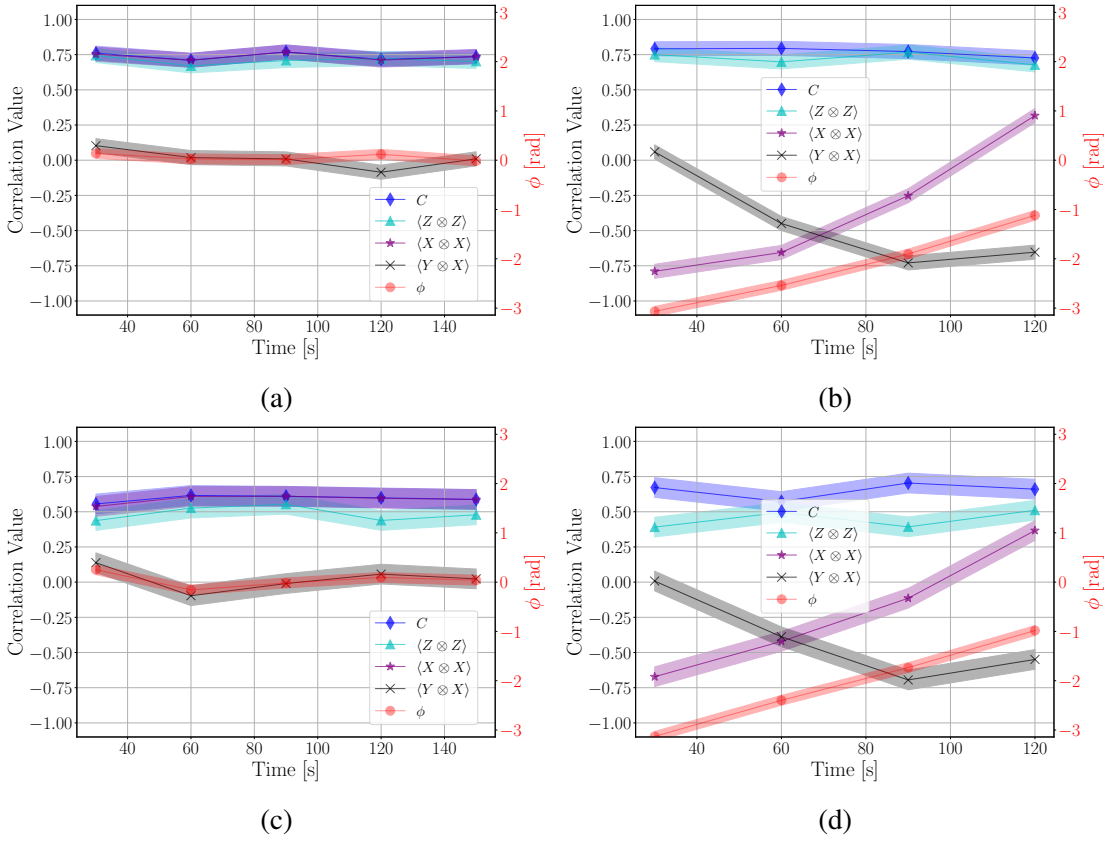

Figure 3.17: Results of the free-space bridge connection tests. (a) and (c) are the results of the zeroth and first order modes for the case without the piezoelectric actuator. (b) and (d) are the results of the zeroth and first order modes for the case with the piezoelectric actuator. Error values are included as the size of the point markers.

signal to produce secret key, one could combine the key rates between the zeroth and first order mode in order to achieve a higher key rate. No key rate analysis following Eq. 2.4 is done as the detection rates are far to low to produce any positive key fraction.

Table 3.4: 6-state 4-state protocol results for the NIR time bin entangled photons sent over a 3.2 km telecommunication fiber optic channel after background subtraction. Note that the zeroth and first order modes are only present in the free-space bridge case (FS Bridge). The piezoelectric actuator is inducing a relative phase change of 0.035 rad/s for the direct fiber connection and 0.015 rad/s for the free-space bridge connection.

Link Type	Piezo	C-parameter	QBER_C	QBER_{ZZ}	key rate [bit per coincidence]
Direct Fiber	Off	0.899 ± 0.028	0.050 ± 0.014	0.0225 ± 0.0069	0.0870
Direct Fiber	On	0.909 ± 0.018	0.0457 ± 0.0089	0.018 ± 0.013	0.0953
FS Bridge mode 0	Off	0.848 ± 0.032	0.076 ± 0.016	0.041 ± 0.014	0.0518
FS Bridge mode 1	Off	0.801 ± 0.055	0.100 ± 0.027	0.085 ± 0.021	0.0036
FS Bridge mode 0	On	0.896 ± 0.048	0.052 ± 0.024	0.029 ± 0.024	0.0791
FS Bridge mode 1	On	0.904 ± 0.021	0.048 ± 0.010	0.115 ± 0.038	0.0162

3.2.5 Discussion

The results of these experiments are quite interesting and is important for the development of quantum networks, as outlined in Sec. 3.2.1. The most important result is that the entanglement is still present in the high order modes despite the modal dispersion and does not have an adverse effect on the zeroth order mode at distances that are useful for intra-city communication channels. Thus a clever quantum network could use temporal switches and utilizes the zeroth and first order modes for different users (Figure. 3.19), creating a multi-user network. This however would require overcoming the coupling losses and a significant increase in the coincidence count rates to achieve such results. For a two party link, one could combine the key rates between the zeroth and first order mode in order to achieve a higher key rate than with temporal filtering alone.

Overall, despite the poor QBER, entanglement distribution is still achieved, albeit a very low quality. Improvements to the count rates are necessary. Nonetheless, the direct fiber connection into the telecom fiber was able to produce good entanglement distribution with sufficient visibility to produce asymptotic secret key. Such results are very promising for the use of quantum sources in the range of 700 nm to 900 nm in the existing telecommunication networks. Especially considering that most intra-city links are within a 10 km range, thus implying that creating quantum networks with entangled photons via spontaneous parametric down-conversion or quantum

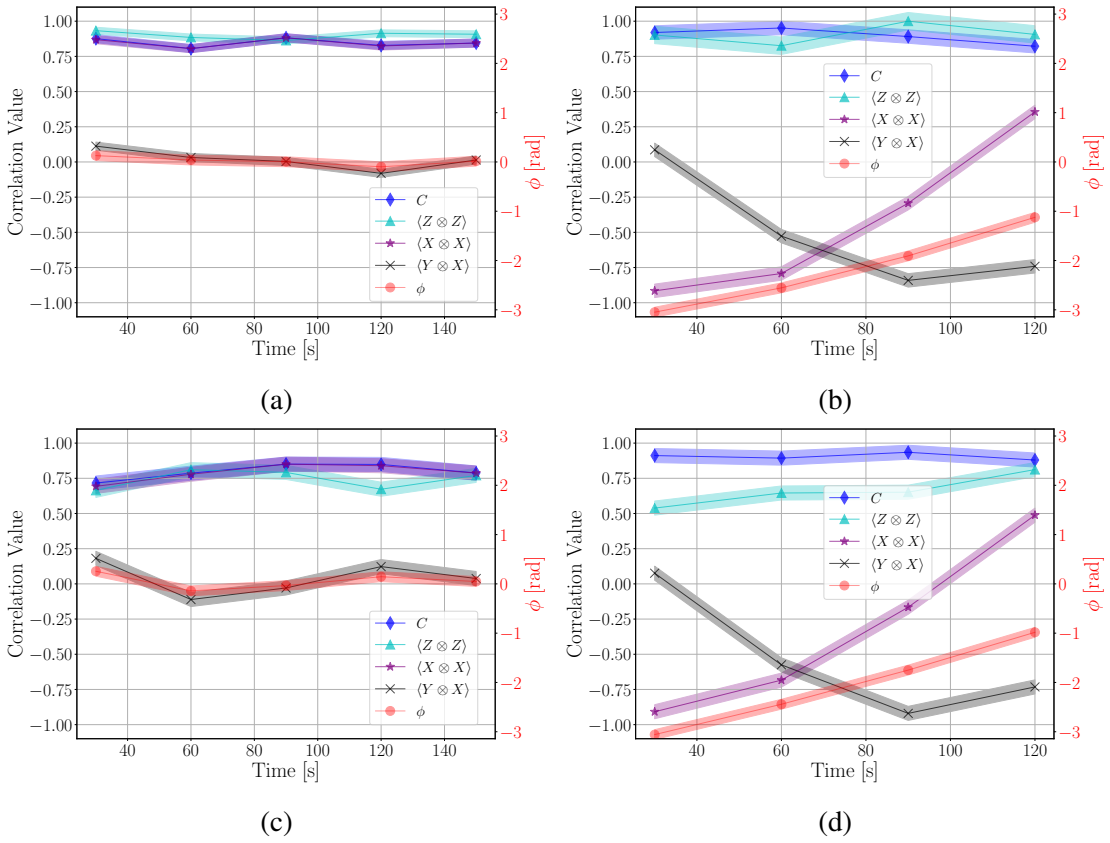

Figure 3.18: Results of the free-space bridge connection tests with the background accidental coincidences subtracted. (a) and (c) are the results of the zeroth and first order modes for the case without the piezoelectric actuator. (b) and (d) are the results of the zeroth and first order modes for the case with the piezoelectric actuator. Error values are included as the size of the point markers.

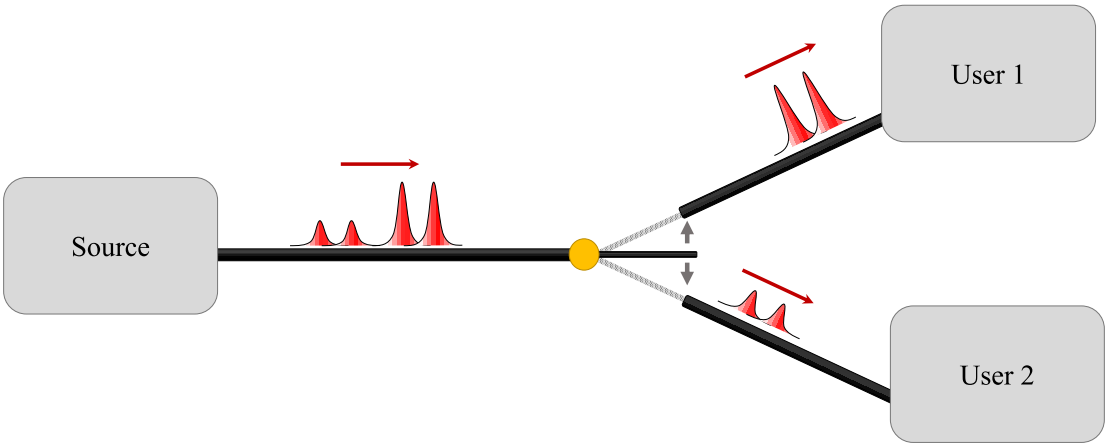

Figure 3.19: Schematic for a multi-user network switch that separates the zeroth order and first order modes between the two users.

dots is very feasible. However, the challenge of connecting these intra-city networks would require the use of satellite or free-space channels, particular moving platforms. Such an experiment is discussed in the next section and the challenges of such a goal are outlined.

3.3 Towards time bin QKD with a moving system

Free-space time bin QKD is an important step towards a global quantum network. Implementing time bin on moving platforms is a very important step in achieving this goal. Having a time bin capable satellite would be beneficial for a global quantum network as it would allow long distances to be connected beyond the fiber optical bound. Furthermore, it would remove the need for the encoding to be transferred between the optical fiber links and free-space channels.

In this section, a proof-of-concept moving free-space time bin experiment is discussed. Although the implementation is far from practical or deploy-able, this proof-of-concept experiment is progressing towards a satellite based time bin receiver. The experiment uses a lot of the systems already discussed in Chap. 2.2 and Sec. 3.1. Details of the experimental setup are found in Fig. 3.20. The protocol used is the 6-state 4-state RFI time bin scheme that is discussed in Sec. 3.1. The same entangled photon source, 6-state polarization analyzer, polarization to time bin converter (PTC), and time bin analyzer (TA) are used. The difference is that now the PMF that is used to collect the photons after the PTC is directed to the transmitter telescope of the moving free-space link rather than the multi mode fiber used in Sec. 3.1. In addition, the input of the TA is directly connected to the receiver telescope of the free-space channel.

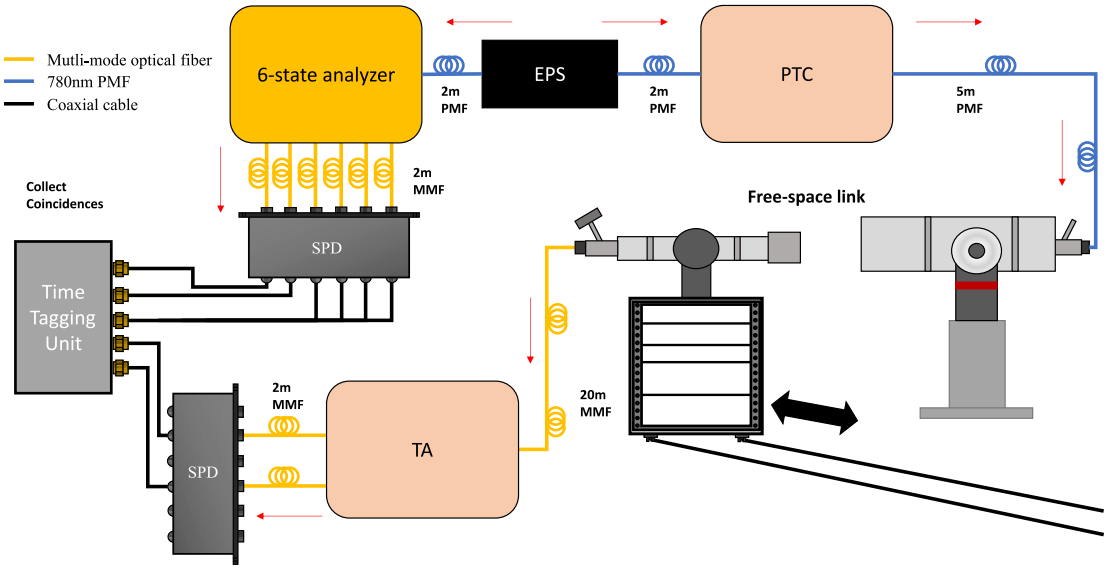

Figure 3.20: Moving time bin experimental setup. This system has the full tracking and pointing system described in Sec. 2.2.1.1. EPS: Entangled photon source. PTC: Polarization to time bin converter. TA: Time bin analyzer. SPD: Single photon detector.

The moving free-space channel includes the same transmitter and receiver telescope used in Chap. 2.2, save that only one polarization at the receive telescope is used. This unfortunately substantially increases the losses of the system as at least 50% of the photons transmitted will be lost due to the passive basis selection of APT (Sec. 2.2.1.1). To increase the photon throughput, the half-wave plate in the transmitter APT is rotated to maximize the transmission to one of the polarization states of the receiver. Then, the optical fiber associated with this polarization state is used to transmit the photons from the moving platform to the time bin analyzer, this is done through the same 15 m GRIN Infinicor 300 is used in Sec. 3.1. A proper moving platform would differ from this proof-of-principle experiment as a true moving platform would include the TA as part of the moving receiver itself. The current TA used in this experiment has a large form factor and is not sufficiently robust against vibrations to be used this way. Thus, for a viable time bin experiment to be done with a moving channel, significant improvements in the design and robustness of field widened interferometers is necessary (Chap. 4 and Chap. 5).

3.3.1 Experimental Notes

Despite the experimental challenges, some moving free-space time bin experiments were conducted. As in Chap. 2.2, the all pointing and tracking systems are used. A human is used to pull and push the moving platform from one end of the rail to the other. The goal was to achieve angular velocities of the transmitter motors up to $1.1\,^{\circ}\,\mathrm{s}^{-1}$, which is sufficient transmitter angular velocity that would be require for a LEO satellite pass (see Sec. 2.2.2.1). Figure. 3.21 shows the tracking system's recorded transmitter and receiver motor speed during the photon exchange. The maximum applied motor speed in three of the links shown in Table. 3.5 sufficiently meets the $1.1\,^{\circ}\,\mathrm{s}^{-1}$ requirement to emulate a LEO pass. The average applied motor speed is also reduced compared to the tests conducted in Sec. 2.2. this is primarily due to the caution taken to not disrupt the stability of the TA during the moving pass.

3.3.2 Experimental Challenges

There are several experimental challenges that needed to be overcome. The first is that the TA was too large to be placed on the moving platform. Thus, the 15 m multi mode fiber is used connect the TA, that is stationary, to the moving receiver. Another challenge is that the TA is not robust against vibrations. Observing the stability of the TA with a Thorlabs PM100D, one can see the instances of instability in the phase of the interferometer while the receiver is moving. The changes in the stability of the interferometer are shown in Figure. 3.22. The standard deviation in the intensity in Figure. 3.22 for the moving data is 0.023 mW, while it is 0.0098 mW for the stationary data. Clearly there is some induced phase changes in the interferometer during the movement of the receiver crate along the track that is not completely smooth and has some connection joints. These connections joints can be a source of vibrations for the TA. These external sources of error, particularly the vibrations could not be overcome during the experiment and the hope is that such a small rapid phase variation would not degrade the channel integrity substantially.

Probably the most problematic experimental challenge is the losses of the experiment. Despite the attempts to optimize the receiver setup to increase the throughput of the photons, there is still substantial losses as the system is not optimized for a time bin experiment. As mentioned above, the receiver telescope is using the polarization analyzer that is mounted on the back of the receiver APT and contributes to 50% of the losses. An optimized time bin receiver would have the polarization analyzer removed and directly couple to either a multi mode fiber or the interferometer itself. Adding to the losses is the free-space link ($\approx$ 30%, Sec. 2.2.1.1) and the other components of the system, i.e. the PTC (35.4%) and TA (67%).

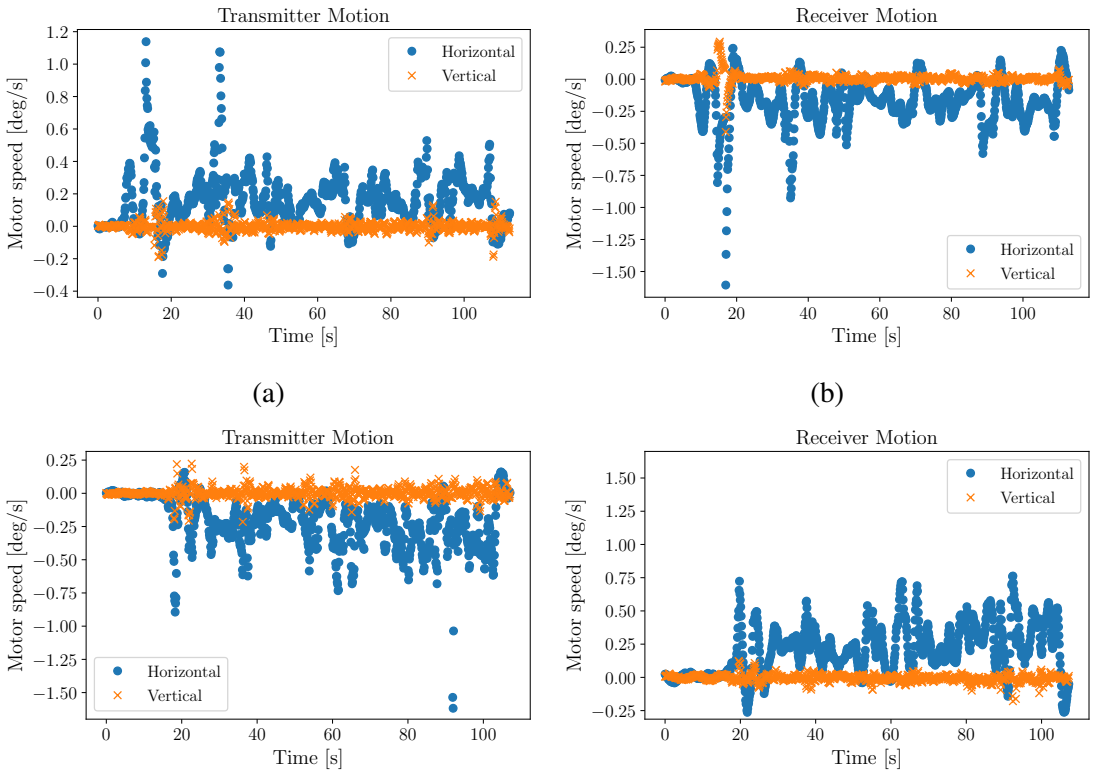

Figure 3.21: Transmitter and receiver applied motor speed for the horizontal and vertical axis. Each pair of figures shows the movement of the transmitter and receiver mount for the length of a single rail pass. For (a) and (b), the transmitter's maximum applied motor speed is $1.14\,^{\circ}\,s^{-1}$ while the average applied motor speed throughout the passes is $0.17\,^{\circ}\,s^{-1}$. For (c) and (d), the transmitter's maximum applied motor speed is $1.62\,^{\circ}\,s^{-1}$ while the average applied motor speed throughout the passes is $0.21\,^{\circ}\,s^{-1}$.

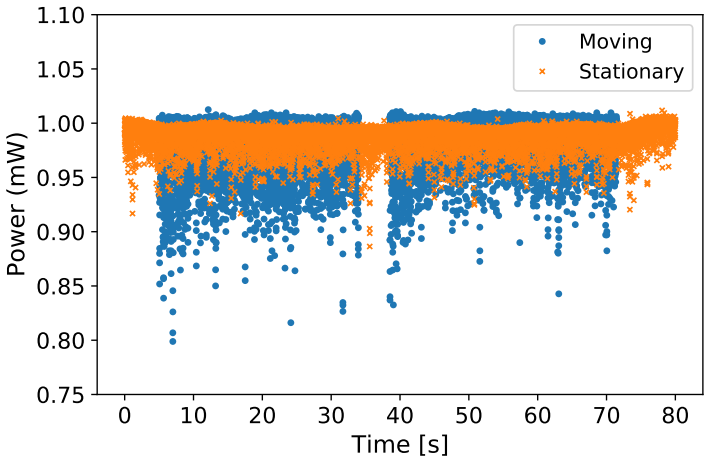

Figure 3.22: Stability of the TA while the receiver is moving along the track and while stationary. Note that the moving data is split into to sections, from 5 s to 35 s, and 38 s to 72 s, this corresponds to moving done the track in each direction. Each block of time corresponds to moving the receiver down the track in one direction.

The total throughput of the system is found by calculating the channel efficiencies from the coincidence and single photon statistics (as done in Sec.3.1 with Table. 3.1). As a reminder to the reader, the signal photons of the entangled pairs are sent over the free-space channel. For a stationary free-space link the total channel efficiency, including detector efficiencies is $\eta_B = 0.0113 \pm 0.0002\%$ for the signal photons and $\eta_A = 5.05 \pm 0.07\%$ for the idler photons. For the moving link, the total efficiency of the channel could change depending on the pass and how well the coarse and fine pointing system are able to maintain the link. Nonetheless the average total channel efficiency is calculated to be $\eta_B = 0.014 \pm 0.001\%$ for the signal and $\eta_A = 4.89 \pm 0.04\%$ for the idler photons.

The losses are a significant issue as larger blocks of data will be required to estimate the C-parameter and error rate. This makes the link susceptible to the relative phase stability of the interferometers involved and can decrease the quality of the channel. Thus, increasing the brightness of the photon source and the efficiency of the free-space channel would significantly improve the signal to noise ratio and by consequence the other experimental parameters.

3.3.3 Results and Discussion

Table. 3.5 shows the results for five separate free-space moving tests. As with the free-space bridge telecom fiber optical link, the losses of the system dominated the signal to noise ratio and significantly increased the QBER such that no positive asymptotic key is achieved. Furthermore, as in Sec. 3.2, key rate analysis following Eq. 2.4 is done as the detection rates are to low to produce any positive key fraction. Despite this, correlations are still found during the photon transmission to the moving receiver. From the results in Table. 3.5 we will discuss the results of experiment 3 and 4 as shown in Figure. 3.23. For experiment 3, achieved an average C-parameter value of 0.808 ± 0.028 despite the average applied motor speed of the transmitter telescope of $0.173\,^{\circ}\,\mathrm{s}^{-1}$ and a maximum transmitter speed of $1.14\,^{\circ}\,\mathrm{s}^{-1}$. The QBER in both the superposition and computation basis are 0.096 ± 0.014 and 0.118 ± 0.023 respectively, which are quite high due to the low signal to noise ratio and low photon throughput. As a result, no positive asymptotic key is calculated. Similarly for experiment 4, the C-parameter visibility of 0.768 ± 0.038 is quite poor. The QBER in both the superposition and computational basis are also poor at 0.116 ± 0.019 and 0.125 ± 0.022 respectively. As with experiment 3, no positive asymptotic key is calculated due to the low photon throughput and signal to noise ratio. It is clear that significant improvements to the entire moving free-space time bin system are required for any practical applications.

Table 3.5: Results of the moving free-space time bin demonstration. No accidental background coincidences are subtracted in obtaining these results. In each experiment the source pump laser was set to 48 mA or approximately 900 μW.

Experiment	Average motor speed [deg/s]	Max motor speed [deg/s]	C	$QBER_C$	$QBER_{ZZ}$	Asymp key rate [per coincidence]	Link time [s]
1	0.270	0.95	0.782 ± 0.030	0.109 ± 0.015	0.097 ± 0.016	-	80
2	0.230	1.17	0.778 ± 0.016	0.1109 ± 0.028	0.126 ± 0.015	-	100
3	0.173	1.14	0.808 ± 0.028	0.096 ± 0.014	0.118 ± 0.023	-	120
4	0.214	1.61	0.768 ± 0.038	0.116 ± 0.019	0.125 ± 0.022	-	120
5	0.187	0.79	0.779 ± 0.060	0.111 ± 0.030	0.1106 ± 0.029	-	100
All	0.214	1.61	0.787 ± 0.012	0.1063 ± 0.0062	0.1211 ± 0.0086	-	-

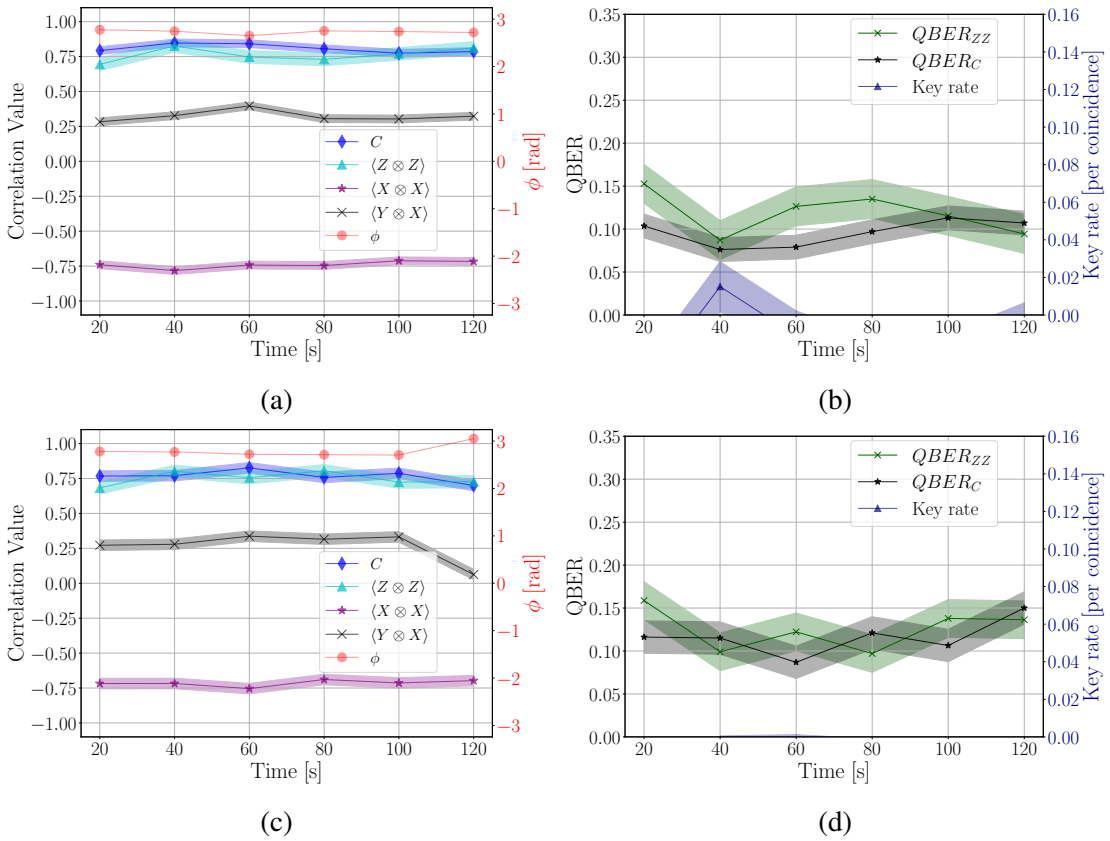

Figure 3.23: Results of two moving time bin receiver experiments. Specifically, experiment 3 and 4 found in Table. 3.5.

As done in Sec. 3.2, accidental coincidence noise is subtracted from the results, shown in Figure. 3.24 for experiment 3 and 4, while Table. 3.6 has the results of all the passes. Again, although the visibility increase significantly, these result cannot be used for quantum key distribution. The QBER and asymptotic key rate results are to be viewed as the potential performance of the current system. Furthermore, Figure. 3.25 shows the results of using multiple moving receiver passes together to attempt to create a positive key, a method that can be employed by any free-space link. Despite combining all the counts from each experiment, there is still no positive key fraction. However, an interesting results is the relative phase stability of the TA and PTC across all five passes, indicating that more passes are possible where eventually sufficient detections are collected to produce a positive key fraction. The current study does not dive into this investigation since it is not a practical approach, while improving the source and link hardware is much more desired.

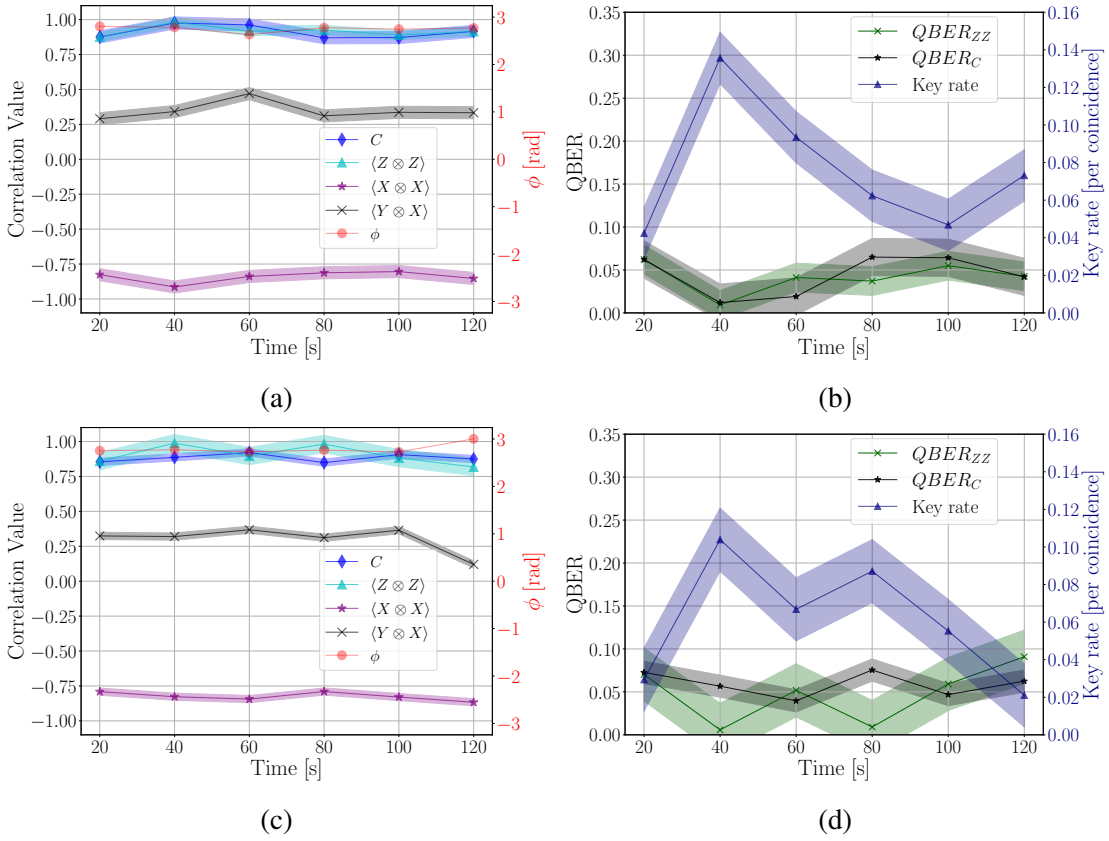

Figure 3.24: Results of two moving time bin receiver experiments when the accidental background counts are subtracted. These two tests are the same ones shown in Figure. 3.24, experiment 3 and 4 of Table. 3.6.

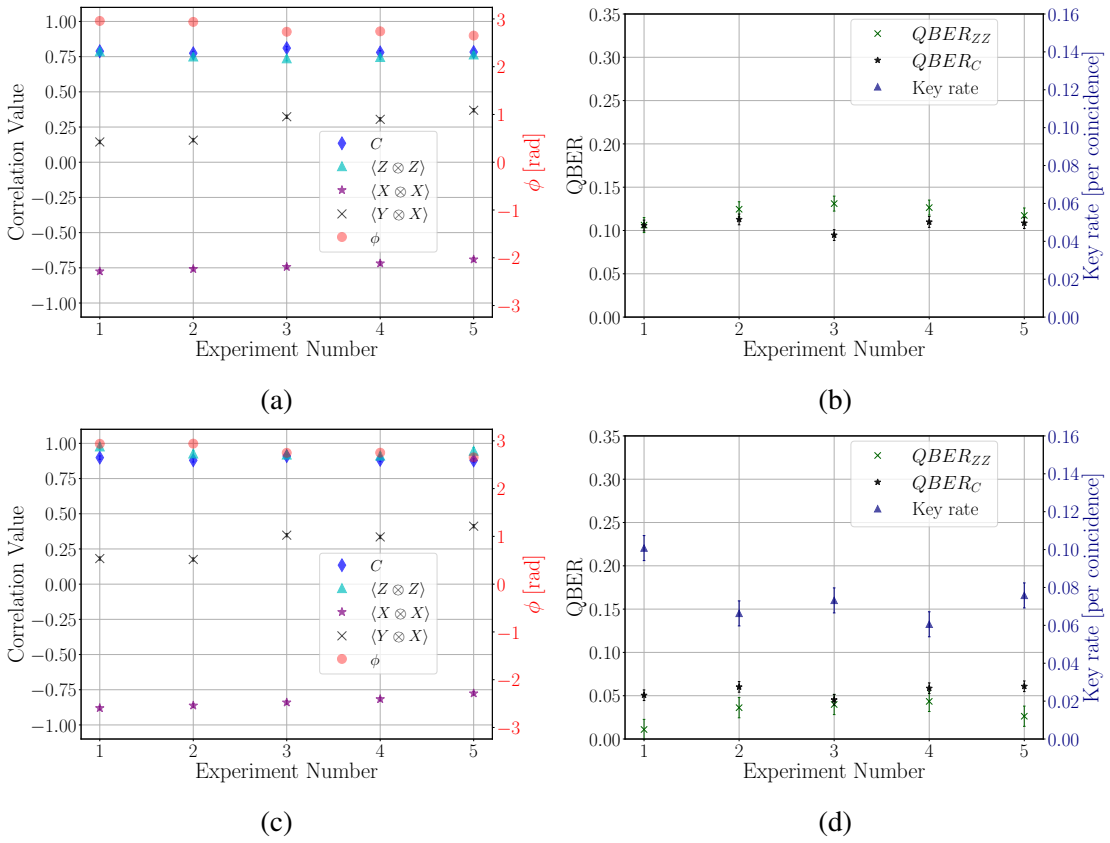

Figure 3.25: Results of the time bin moving receiver tests where each data point is calculated by combining the detections over the entire link. (a) and (b) have no background accidental subtraction. (c) and (d) are the results with the background accidental counts subtracted. In (b) the key rate is negative and thus does not appear in the plots range.

Table 3.6: Time bin moving test results when accidental background counts are subtracted. In each experiment the source pump laser current was set to 48 mA.

Experiment	C	$QBER_C$	$QBER_{ZZ}$	Asymp key rate [per coincidence]
1	0.889 ± 0.055	0.055 ± 0.027	0.013 ± 0.011	0.0946
2	0.889 ± 0.033	0.055 ± 0.016	0.038 ± 0.025	0.0679
3	0.912 ± 0.043	0.044 ± 0.021	0.041 ± 0.017	0.0728
4	0.882 ± 0.026	0.059 ± 0.013	0.048 ± 0.031	0.0564
5	0.875 ± 0.056	0.062 ± 0.028	0.0202 ± 0.028	0.0815
All	0.890 ± 0.012	0.0551 ± 0.0061	0.031 ± 0.012	0.0745

3.3.4 Discussion

Although, the losses and photon detection rates were too low, this experiment serves as a proof-of-concept demonstration how time bin with moving receivers is feasible. For a better time bin moving test, the receiver system would have to be modified in order to remove the inherent 50% loss from the 4-state analyzer. A truly optimized moving time bin receiver would couple all the collected photons into one multi mode fiber or directly to the interferometer. Furthermore, as mentioned in Sec. 2.2.1.1 the link throughput is approximately 30% and could be optimized further by changing the transmitter telescope. Table. 3.7 summarizes all the experimental throughput and identifies realistic improvements to the systems. The EPS heralding efficiency, the 6-state analyzer throughput, and the PTC throughput can be improved with better collection optics and alignment. The TA throughput can be improved using an alternate interferometer design such as the Offner relay interferometer of Chap. 4. The receiver telescope can be optimized by removing the passive beam splitter and adjusting the aperture size (here a conservative value is provided). With these improvements, a factor of six increase in the coincidence counts can be observed which would increase the signal to noise ratio and thus the quality of the link.

Another important result from theses proof-of-concept tests is that the concept of a moving time bin link needs a modular and very stable field widened interferometer. We were not able to attempt placing the TA on the moving receiver due to both its size and stability issues. The former must be solved before one can conclusively conclude that the latter is an issue. In light of this, future and current research activities have focused on reducing the form factor of the field widened interferometer (Chap. 4) and increases its robustness (Chap. 5).

Table 3.7: Elements of the free-space whose photon throughput can be improved.

Element	Efficiency	Improvement
EPS heralding	20	25
PTC	35.4	40
TA	67	87.5
6-state analyzer	49.6	80
Receiver telescope	30	60

3.4 Summary

In this chapter, a fully passive time bin RFI-QKD protocol is tested over several channels. Of particular interest is the results of using time bin over multi mode channels, such as GRIN fibers, NIR sources in telecom, and over moving free-space channels. These channels are particularly challenging and have real practical applications that could have an impact on the deployment of quantum networks. Particularly the work done in Sec. 3.2 as many quantum sources produce photons in the NIR regime, while the existing fiber optic network is for the telecom band. In addition, an improved field widened time bin interferometer that can be placed on a moving receiver would enable a quantum network that uses only one encoding type, which reduces the overhead of implementation. Future works can improve on the performance by improving the source brightness and entanglement visibility, as well as improve the time bin hardware (i.e. PTC and TA). Improving the visibility and robustness of the TA is discussed in Chap. 4 and Chap. 5.

Chapter 4

Towards a compact and practical field widened interferometer

Creating field deploy-able quantum information devices for quantum sensing and quantum communication applications is of particular interest. For optical qubits, time bin encoding has been shown to be useful for quantum sensing and developed for free-space quantum key distribution. To use time bin encoding with free-space optical channels, one needs to use a field widened interferometer (Sec. 1.6.1) The goal of the work presented in this chapter is to build an field widened unbalanced interferometer that has a long time delay with a small form factor and is practical in the sense that it does not have a chromatic dependence. The novel field widened interferometer design uses what is called a folded Offner relay imaging system which allows for a small form-factor, is relatively achromatic, and has a high interference visibility (greater than 0.97) for both single mode and multi mode signals.

Statement of contributions Prof. Thomas Jennewein and I conceived the conceptual design of the Offner relay interferometer. I refined the optical design and performed the verification simulations. I constructed with experimental prototype and conducted the data collection with some assistance from Tabitha Arulpragasam and Dogan Sinar. I performed the data analysis of the results.

4.1 Introduction

In Chap. 3, it is shown that active stabilization of the interferometers is not needed when using RFI-QKD protocols. However, the interferometers used in the experiments suffered due to their bulky size. This affected the stability of the interferometer, particularly in the free-space moving tests as seen in Figure. 3.22. Furthermore, in the experiments of the first free-space time bin QKD experiment [76], it was found that the interferometers were unstable and susceptible to thermal and vibrational noise. Thus, creating a practical unbalanced interferometer for time bin is an important and ongoing effort of development. In addition to quantum key distribution, creating practical time bin interferometers offers a near term field deploy-able quantum device that can be used in a variety of settings, such as quantum sensing [87].

Some recent efforts have reported improvements of the thermal stability of the interferometers [88]. However, the imaging system used to make the interferometer to be field widened are highly wavelength dependent and thus not ubiquitously practical. This is because the path length in an optically dense material is highly wavelength dependent and thus the imaging condition cannot be easily satisfied for all wavelengths. With the 4f lens system[1], chromatic aberrations from the lenses can contribute to some loss in the interference visibility. Anecdotally, these systems are quite difficult and tedious to align.

In this chapter, work done to develop a field widened interferometer that uses only simple optics that have a limited chromatic dependence is presented. The results show that the design is able to improve the robustness of the interferometer. Furthermore, by being useful over a wide wavelength range, the interferometer is more practical for real-world applications since quantum sources vary widely in operating wavelength.

4.2 Optical Design

The optical design of the field widened interferometer in this work was developed with a few goals in mind:

1. The first goal is to reduce the physical footprint of the system, i.e. creating an optical path such that a relative path delay between the two arms of the interferometer is much longer than the physical footprint it takes up.

2. The second goal is to have the ability to use off-the-shelf, simple optical components that are easy to use and align.

[1] Here the 4f refers to a system that has two lens that form a one-to-one imaging system.

3. The third goal is to reduce the chromatic dependence of the system. Due to chromatic aberrations, chromatic dispersion and spherical aberrations, we avoided refractive optics and instead focused on using reflective optics such a spherical and flat mirrors for the imaging system.

The third goal is difficult to achieve for many field widened interferometer systems, particularly those that rely on proper tuning of the refractive index between the two interferometer arms. To meet all three requirements, the one-to-one imaging system in our field widened interferometer is created using a folded Offner relay-like configuration [131], see Figure 4.1. We call it an Offner relay-like system because in a normal Offner relay, both mirrors in the system have a curved reflective surface whereas here, only the larger, primary mirror is a spherical mirror. The curved mirrors emulate lenses as the curved geometry focuses any beam incident on the mirror to a fixed point. The spherical mirrors do not have a chromatic dependence and the imaging quality of the system is purely a geometric problem. With repeated reflections between the spherical mirror and the flat mirror found in Figure. 4.1, one can achieve the desired one-to-one imaging system. Since our novel interferometer design uses an Offner relay-like imaging system, we refer to this type of interferometer as an Offner relay interferometer (ORI).

Adjusting the distances appropriately between the curved mirror and the flat mirror, a cavity-like configuration can be used to further reduce the footprint of the one-to-one Offner relay imaging system. Creating such a cavity-like configuration with lenses would require multiple lenses that are custom built, further increasing the alignment problem. Furthermore, a standard Offner relay would not easily allow for multiple reflections in a cavity-like configuration and hence the use of a flat mirror in the ORI. The ORI design allows for long focal length mirrors to be used with a small physical footprint. Comparing this to imaging systems that require lens, the ORI allows much smaller physical footprint for the same or longer time delays between the two interferometer arms (Table. 4.3 and Table. 4.4). The overall relative delay between the two paths of the ORI can be altered by either switching the spherical mirrors used to those with shorter or longer focal lengths, or by changing the distance in the Offner relay cavity (effectively changing the number of reflections on the spherical mirror), thus offering a wide range of configurations and time delays, see Table. 4.3 and 4.4. Practically speaking, any time delay can be made provided that the spherical mirrors have a custom radius of curvature. The ones presented in Table. 4.3 and 4.4 are for configurations that use standard off-the-shelf optics.

The ORI design has several advantages over previous works. First, the folded, cavity-like design permits a small form factor that permits relatively longer time delays in a smaller space. When compared to a Michelson and Mach Zehnder interferometer with a similar time delay (Table. 4.3 and more convincingly Table. 4.4), it becomes apparent that the design of the ORI is advantageous for reducing the form factor of the field widened interferometer system for longer

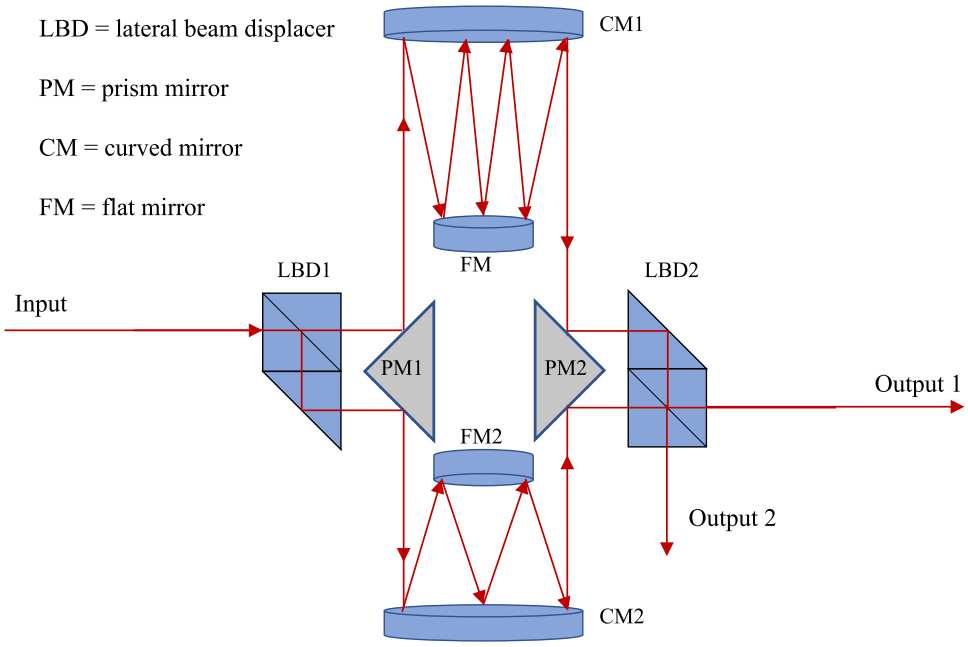

Figure 4.1: Conceptual design of the optical layout for the modular quantum time bin analyzer. The folded configuration allows for multiple passes between the curved mirrors and the flat mirrors. The red arrows indicate the optical path.

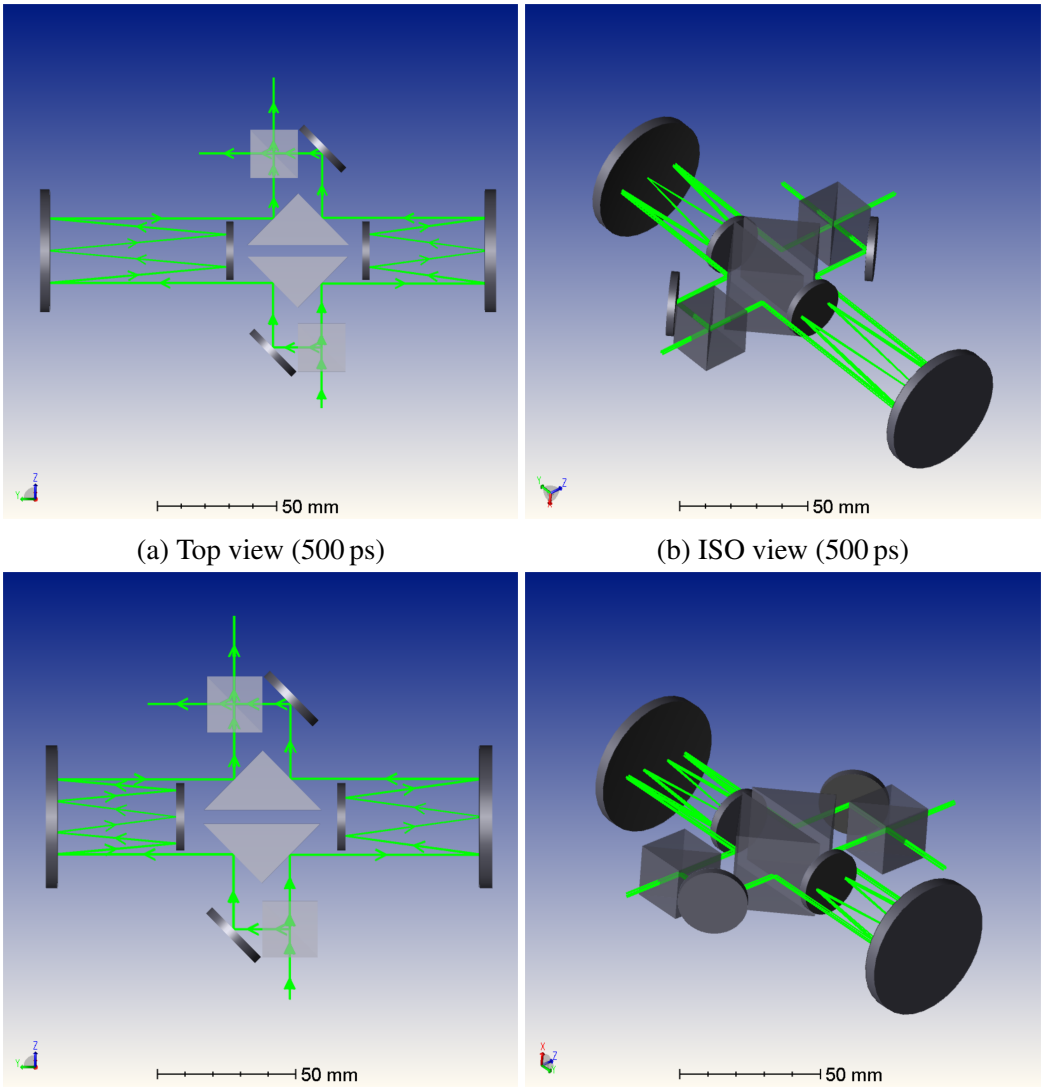

(a) Top view (500 ps)

(b) ISO view (500 ps)

(c) Top view (715 ps)

(d) ISO view (715 ps)

Figure 4.2: Schematic of the optical design of the Offner relay interferometer. The one-to-one imaging system consists of a curved, spherical mirror (CM) and a flat mirror (FM) in folded a Offner relay cavity-type configuration. (a) and (b) shows a 500 ps delay unbalanced interferometer. Multiple reflections in the cavity-like configuration between the CM and FM in each path allows for a reduce physical footprint of the system as seen in (c) and (d), however the delay is increased (715 ps). Here the CM are the larger circular optical elements.

delays. The very long time delays are advantageous as they relax the measurement requirements of time bin systems. If the time delay is too short, for many applications, the distinguishability of the time bins will be reduced and thus affect the performance of the system. In addition, commercially available avalanche photodiodes have typical time resolutions of on the order of hundreds of picoseconds. Thus, longer time delays are beneficial for using off-the-shelf and cost efficient detector systems. The smaller form factor of the ORI can also reduce the costs associated with manufacturing an enclosure for the system. The smaller enclosure can help in increasing the thermal and vibrational robustness of the interferometer. Furthermore, the reduced form-factor enables the use additive manufacturing to create a monolithic optomechanical enclosure for the system as discussed in Chap. 5.

Another advantage is the use of off-the-shelf spherical mirrors in the imaging system that has no chromatic dependence, thus making the ORI an achromatic interferometer. In fact, the only chromatic dependent optical elements in the ORI are the beam splitters used in the interferometer, nonetheless these devices are typically functional over a broad range of wavelengths. Furthermore, most implementations of interferometers will suffer from a similar chromatic dependence of the beam splitter. In fact, to our knowledge there is no achromatic solution for beam splitters beyond polarization optics and knife-edge right angle prisms. Aside from removing the chromatic effects, the use of spherical mirrors also reduces the alignment degrees of freedom compared to using parabolic mirrors. Regardless, it is difficult to employ parabolic mirrors in a cavity-like configuration and thus would be difficult to use in an ORI setup.

The overall optical design of the ORI is shown in Figure. 4.1. It resembles a unbalanced interferometer with two beam splitters. However, in this conceptual design, lateral beam displacers (LBD) are used in place of a beam splitter and mirror to separate the optical beams of the two paths. The light then strikes the two reflective surfaces of a prism mirror (PRM), which sends the beam of each path towards the curved mirror, thus entering the cavity-like Offner relay configuration, i.e. the one-to-one imaging system. Upon exiting the one-to-one imaging system, the optical beam of each path is again incident on a PRM, that redirects the beam towards the output LBD,, where the two paths are recombined and interference occurs. We will call the LBD, and PRM, the central optics, while the Offner relay cavity-like configuration as the ORI-imaging system. The path difference of the central optics portion of the ORI must be minimized, this is due to the glass portion of the lateral beam displacer. Hence in Figure. 4.1, we can see that the paths through each LBD, is made symmetric in order to avoid unwanted chromatic phase dependence. This implies that the entire difference in path length occurs in the ORI-imaging system of each path and therefore it is the critical component of the ORI. An algebraic system of equations is derived to determine the path length differences below.

4.2.1 Algebraic Path Analysis

To start, the various elements of both the short and long path will be derived. All distances will be measured from a global origin in the very center of the ORI optical setup. The optical elements from here are then placed at the appropriate points and a optical path through the ORI is calculated for both the short and long path.

To perform this calculation we first need to calculate the total optical path traveled by the light in each interferometer path. First, we define the starting point that the two paths deviate from each other. The difference in the two interferometer path length begins from the reflection from each prism mirror and is defined horizontally from the center point of the system as

$$d_x = \frac{x_{ps}}{2} + x_p \left(1 - \frac{s_b}{2h_p}\right), \tag{4.1}$$

where x_{ps} is the distance between the two prism mirrors, x_p is the horizontal thickness of each PRM,, s_b is the beam displacer offset, and h_p is half the height of the prism mirror. Thus the starting point of the difference in optical path is $(-d_x,s_b)$. The next distance in the optical path is the path length from the prism mirror to the large curved mirror, i.e. the first time the beam path strikes the curved mirror. This is given by

$$y(d_x,R)_{curv} = \sqrt{R^2 - d_x^2} - \left[R - \left(d_{CM} - \frac{s_b}{2}\right)\right], \tag{4.2}$$

where R is the radius of curvature of the spherical mirror and d_{CM} is the distance from the origin to the curved mirror's origin. The latter is found when undergoing the optical design optimizations in Zemax [132]. Recall that in the ORI, there is a cavity-like configuration so multiple reflections will occur and the Eq. 4.2 represents the path to the first reflection from the curved mirror and the path after the last reflection from the curved mirror. These points are defined as $(-d_x, y(d_x,R))$ and $(d_x, y(d_x,R))$. A visual definition of the various distances is shown in Figure. 4.3.

Next in the optical path is the cavity-like configuration in the ORI, which includes the hypotenuse-like distances from the curved mirror to the flat mirror. The derivation of this equation starts with the simple distance formula $d = \sqrt{(x_1 - x_2)^2 + (y_1 - y_2)^2}$. Then we define a point on the spherical mirror (CM) and one on the flat mirror (FM). These points are determined using geometry as shown in Figure. 4.4 for the case of $B = 4$, where B is the total number of angled paths taken by the light in the cavity-like configuration.

Using the distance formula and the geometric analysis to define the optical path of the rays in the ORI cavity-like configuration, the distance between the points where the light strikes the CM and the FM can be generalized to arbitrary B and R by

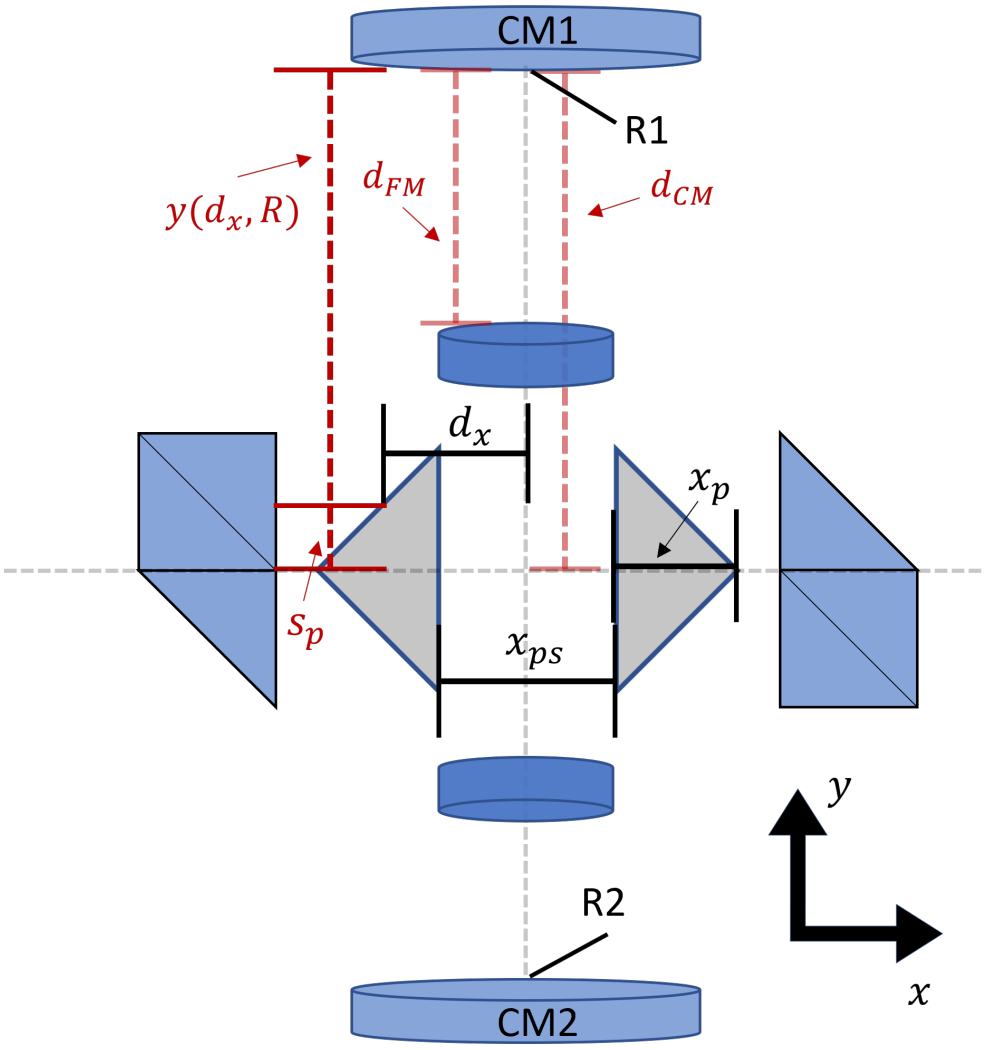

Figure 4.3: Definition of the distances for the algebraic calculations of the ORI optical path.

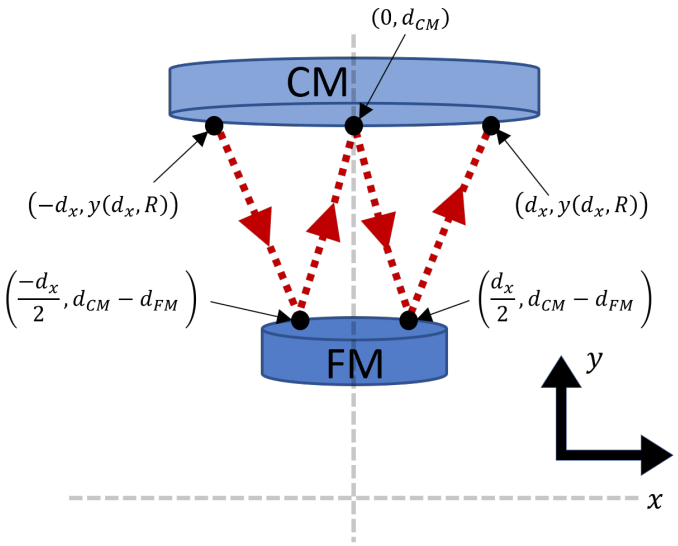

Figure 4.4: Definition of the distances for the algebraic calculations of the ORI optical path.

$$hyp(d_x,B,R)_n = \begin{cases} \left[\left(\sqrt{R^2-\left(d_x-\frac{2d_xn}{B}\right)^2}-(R-d_{CM})-(d_{CM}-d_{FM})\right)^2+\left(\frac{2d_x}{B}\right)^2\right]^{\frac{1}{2}} & n \text{ even} \\ \left[\left(\sqrt{R^2-\left(d_x-\frac{2d_x(n+1)}{B}\right)^2}-(R-d_{CM})-(d_{CM}-d_{FM})\right)^2+\left(\frac{2d_x}{B}\right)^2\right]^{\frac{1}{2}} & n \text{ odd} \end{cases} \tag{4.3}$$

where B is the total number of paths taken by the light (i.e. $B = 2,4,6\ldots$) in the cavity-like configuration, d_{FM} is the distance from the center of CM to FM at $x = 0$, and $n = 0,1,\ldots,\frac{B}{2}-1$ is an index for the specific "bounce" path taken by the light. The difference between the odd an even path accounts for the change in direction the light takes when it strikes each mirror. Eq. 4.3 only calculates half the optical path in the ORI cavity-like configuration. The total path length taken by a photon in the cavity-like Offner relay is given by,

$$hyp(d_x,B,R)_{tot} = 2\sum_{n=0}^{\frac{B}{2}-1} hyp(d_x,B,R)_n. \tag{4.4}$$

Note that the factor of 2 is due to the symmetry in the optical path of the ORI cavity-like configuration and without it the sum would only account for half of the total path length. Now the

full path length without accounting for thermal expansion (see Sec. 5.2.2) can be obtained from know design quantities and is found by combining Eq. 4.2 and Eq. 4.4 which gives

$$d(d_x,B,R)_{full} = 2y(d_x,R)_{curv} + hyp(d_x,B,R)_{tot}. \tag{4.5}$$

As in Eq. 4.4, the factor 2 is needed to account for the entire optical path length. Thus, an expression for the full path of one arm of the ORI is given and the difference in path length and time delay of various ORI configurations can be easily calculated as $\Delta d = |d(d_x,B_1,R_1)_{full} - d(d_x,B_2,R_2)_{full}|$. Various time delays for several configurations are shown in Table. 4.1 and Table. 4.4. However, the distances of d_{CM}, and d_{FM} must be determined for each configuration (Tables 4.1 and 4.2), while other values such as x_{ps}, s_b and R are determined by the components selected. For the calculations of the results of Table. 4.1 and Table. 4.4, $x_{ps} = 16.645$mm while $s_b = 20$mm.

4.2.2 ORI design considerations

As mentioned above, the use of off-the-shelf components is desired so only certain candidate spherical mirrors are considered for the ORI imaging system. The dimensions of the ORI-imaging system are specific to the spherical curved mirror used. The distance from the curved mirror (CM) to the flat mirror (FM) is dependent on the configuration but is generally given by $d_{FM} \approx R/B$, where $B = 2,4,6,\ldots$ is determined by the number of reflections from the curved mirror in the given configuration. There must be an even number of reflections from the curved mirror in order to properly create a one-to-one imaging system. The exact distance between the CM and FM is determined by the Zemax ray tracing software and is optimized to produce the one-to-one imaging system. Various configurations and distances are shown in Table. 4.1. Note that the distance from the CM to the origin is simply a fixed offset from the CM to FM distance. In the cases presented in Table. 4.2 the offset is approximately 30 mm.

Table 4.1: Distance from the center of the CM to the FM. All distances, including the radii of curvature, are in millimeters.

Bounces	R=100	R=150	R=200	R=300
2	49.600	74.750	99.712	149.886
4	24.779	37.367	49.861	74.962
6	14.442	21.838	29.189	43.898
8	9.340	14.192	18.997	28.590

Table 4.2: Distances of the CM to the origin of the ORI. All dimensions are in millimeters.

Bounces	R=100	R=150	R=200	R=300
2	80	105	130	180
4	55	65	80	105
6	45	55	60	75
8	40	45	50	60

Table 4.3: Time delays and form factors of various ORI configurations using a $R_1 = 0.20$m and $R_2 = 0.30$m. The form factor includes the length and width of the optical component setup, with no consideration given to the height. A comparison is made to a reasonable form factor required for a field widened Michelson interferometer that uses optics with 25 mm aperture size and a 10 mm short path distance. The time delays are calculated using both the Zemax ray tracing and the algebraic analysis presented in Sec. 4.2.1

CM1 Radius [m]	CM2 Radius [m]	CM1 Reflections	CM2 Reflections	Time Delay [ps]	ORI Size [mm^2]	Michelson Size [mm^2]	Mach Zehnder Size [mm^2]
0.20	0.30	8	6	537.64	3937.00	3709.57	5895.15
0.20	0.30	8	4	859.02	4699.00	4934.02	8344.03
0.20	0.30	8	2	1358.77	6604.00	6838.06	12152.11
0.20	0.30	6	4	715.46	4953.00	4387.05	7250.10
0.20	0.30	6	2	1215.20	6858.00	6291.09	11058.18
0.20	0.30	4	4	501.34	5461.00	3571.25	5618.49
0.20	0.30	4	2	1001.08	7366.00	5475.29	9426.57
0.20	0.30	2	2	667.82	8636.00	4205.55	6887.10

Table 4.4: Time delays and form factors of ORI configurations that provide a time delay of >1 ns.

CM1 Radius [m]	CM2 Radius [m]	CM1 Reflections	CM2 Reflections	Time Delay [ps]	ORI Size [mm^2]	Michelson Size [mm^2]	Mach Zehnder Size [mm^2]
0.10	0.20	8	2	1014.11	5080.00	5524.93	9525.87
0.10	0.30	8	4	1182.19	4445.00	6165.28	10806.57
0.10	0.30	8	2	1681.93	6350.00	8069.32	14614.65
0.10	0.30	6	4	1109.96	4572.00	5890.12	10256.24
0.10	0.30	6	2	1609.71	6477.00	7794.16	14064.32
0.10	0.30	4	4	1002.13	4826.00	5479.29	9434.58
0.10	0.30	4	2	1501.88	6731.00	7383.33	13242.66
0.15	0.30	8	4	1020.22	4572.00	5548.18	9572.36
0.15	0.30	8	2	1519.96	6477.00	7452.22	13380.44
0.15	0.30	6	2	1395.45	6731.00	6977.81	12431.62
0.20	0.30	8	2	1358.77	6604.00	6838.06	12152.11

4.3 Numerical Simulations

4.3.1 Visibility

After optimizing the imaging system of the ORI for each curved mirror, the interference performance of the ORI is calculated, particularly with multi mode signals. The ORI design is validated by using the coherence and interference features, offered by the non-sequential mode in the Zemax ray tracing software[2]. A custom script was made using the Zemax API to study the field widened capabilities of the ORI by analyzing the interference quality of optical fields that are input at various different small angles of incidence. The interference quality of their overlap at the output of the ORI is analyzed after travelling through the two interferometer paths. These results are shown in Fig. 4.5 for the minimum intensity output (top) and for a maximum intensity output (bottom). For these simulations, a collimated 1 µm wavelength light source with an infi-

[2]A very important note to make is that the coherence length feature in Zemax is not a timing coherence length but rather changes the spectral bandwidth of the light. Basically the bandwidth is calculated given the coherence length and a random distribution of frequencies within that bandwidth is assigned to each ray. Thus if you have an interferometer with two equal paths but provide Zemax a small coherence length, the results will have poor visibility. To achieve good interference simulations with pulsed light, one can ask Zemax to determine the phase of the light assuming it is infinitely coherent and then deal with the pulse timing on the side.

nite coherence length, and a spot diameter of 3 mm is used. Although a light source with infinite coherence is used, a setup that is appropriately balanced in time can work for light sources with various coherence lengths. Regardless, the key features of Fig. 4.5 are that the five spots all share the same intensity values and are all in phase relative to each other. Having all five spots in phase is an important characteristic in confirming that the ORI is field widened. However, we must quantify the ORI's ability to interfere signals. The main merit of measure of the performance of an interferometer is the interference visibility defined as

$$V = \frac{I_{max} - I_{min}}{I_{max} + I_{min}}, \tag{4.6}$$

where $I_{max(min)}$ are the maximum (minimum) intensities of the interference fringes produced by the interferometer. Here, $1 \geq V \geq 0$ with $V = 1$ being a perfect interferometer. The visibility for the ORI configuration was calculated using the results of the numerical simulation. The sum of the intensity across the entire detection surface in Fig. 4.5 top and bottom, are used to calculate a visibility of 0.9978 for both angular deviations. In Figure. 4.5a the Gaussian beams are given an input angle of 0.05°, while it was found that with standard SM1 (1 inch) optics, a maximum input angle was found to be 0.2° after which beam clipping occurred, Figure. 4.5b. These input angles are for a collimated Gaussian source that is place 1 cm away from the input aperture of the ORI. This would emulate something similar to a multi mode signal that is emerging from a fiber optical cable. Nonetheless, given these angular deflections of the incident beam, the visibility did not decrease substantially, see Figure. 4.6. The beam input angle is varied from 0° to 0.225°. As seen in Figure. 4.6, the visibility remains high with an average visibility of 0.996 for horizontal tilts and 0.994 for vertical tilts. Comparing these results with the fine pointing system used in the Sec. 2.2 and Sec. 3.3, that has a pointing accuracy of 50 µrad which is 0.0028°, significantly smaller than the deflections investigated. Thus, the ORI can be used with pointing systems that exist today.

Another quantitative test of the ORI performance was to observe the visibility as the input field is laterally shifted across the input aperture. Since the ORI has one-to-one imaging systems in both paths of the interferometer, the laterally displaced input beam is directly imaged to the output aperture. The visibility of the laterally displaced beam is plotted as a function of displacement from the center in Figure. 4.7. During these simulations a Gaussian with a 2 mm beam waist is displaced from 0 mm to 0.9 mm. The average visibility for the horizontal displacement is 0.995, and 0.994 for vertical displacements.

Overall these results indicates that the ORI is an excellent field-widened interferometer since the high visibility is achieved despite the changes in angle of incidence and lateral displacement. Furthermore, these results are consistent for all the ORI configurations shown in Table. 4.3 and Table. 4.4, further pointing the practicality of the ORI system.

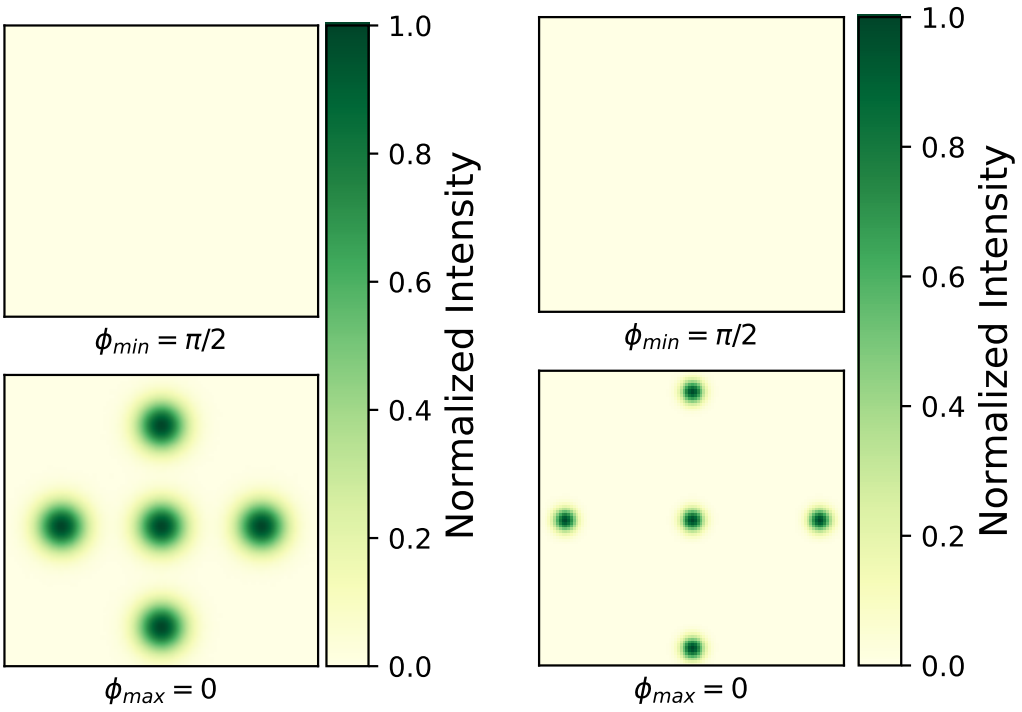

(a) (b)

Figure 4.5: Simulated coherent interference maxima (bottom) and minima (top) using Zemax non-sequential ray tracing. (a) Input fields are offset by 0.05°. (b) Input fields are offset by 0.2°, after which beam clipping occurs. The calculated visibility across the entire detector aperture is 0.9978 for both cases.

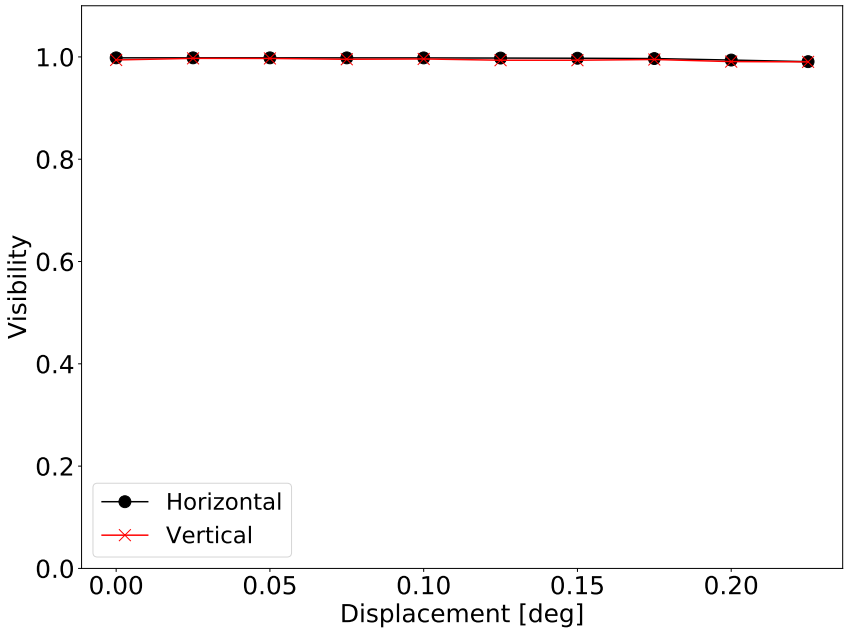

Figure 4.6: Numerical simulation of visibility as a function of beam incident input angle for the ORI. The average visibility over the test range is remains high at 0.996 in the horizontal and 0.994 in the vertical direction.

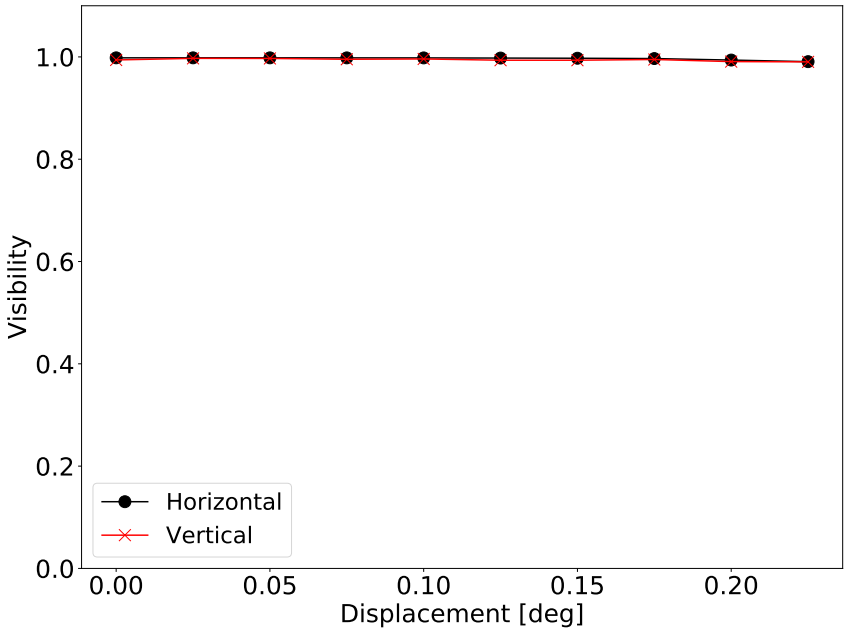

Figure 4.7: Numerical simulation of visibility as a function of lateral displacement of the beam incident input beam for the ORI. The average visibility over the test range is remains high at 0.995 in the horizontal and 0.994 in the vertical direction.

4.3.2 Chromatic Investigation

One of the main design features of the ORI is the use of reflective optics in the one-to-one imaging system. Since the spherical mirrors use geometry to focus the signal rather than refraction, the ORI could be used with a broadband source. This means that the ORI is effectively achromatic, within the range of the beam splitter's function. Thus, to investigate the achromatic capabilities of the ORI, a numerical simulation using Zemax was performed with a simulated white light source. For the simulation, the source consists of several monochromatic sources that are passed through an unbalanced Michelson then the ORI with the intensity of each wavelength is measured at the output. In this simulation the chosen range is 600 nm to 1000 nm, however any range can be selected based on the coating of the beam splitters. The results in Figure 4.8 indicate that despite the broad wavelengths of the signal, the intensity at the output of the ORI is constant as a function of wavelength since the total relative phase of the combined Michelson and ORI setup is the same across the broad wavelength range. By contrast, any chromatic dependence in the one-to-one imaging system would show up as a phase difference and thus the black line in Figure 4.8 would appear more sinusoidal. However, since the black line is relatively flat over the range of 600 nm to 1000 nm, one can conclude that the ORI can easily be used with a broadband source, and can be used with signals of many different wavelength. This is in contrast to typical dispersion based field widened interferometers that rely on refractive optics which are highly wavelength dependent, as see in Figure 4.8.

The results of the chromatic simulations have quite a significant impact for the practicality of the ORI. In comparison, the results of a field widened interferometer using optically dense materials (e.g. glass) similar to that found in [84] and [88] is the opposite. As expected, due to the dispersion the relative phase of the output of the system has chromatic dependence.

4.4 Implementation

Table 4.5: Parameters used for the table-top ORI setup.

CM1 Radius [m]	CM2 Radius [m]	CM1 Reflections	CM2 Reflections	Time Delay [ps]
0.20	0.30	4	4	501.34

Although the ORI footprint can be substantially reducing by using small optical components, the experimental implementation of the ORI was built using standard SM1 (1 inch) and SM2 (2

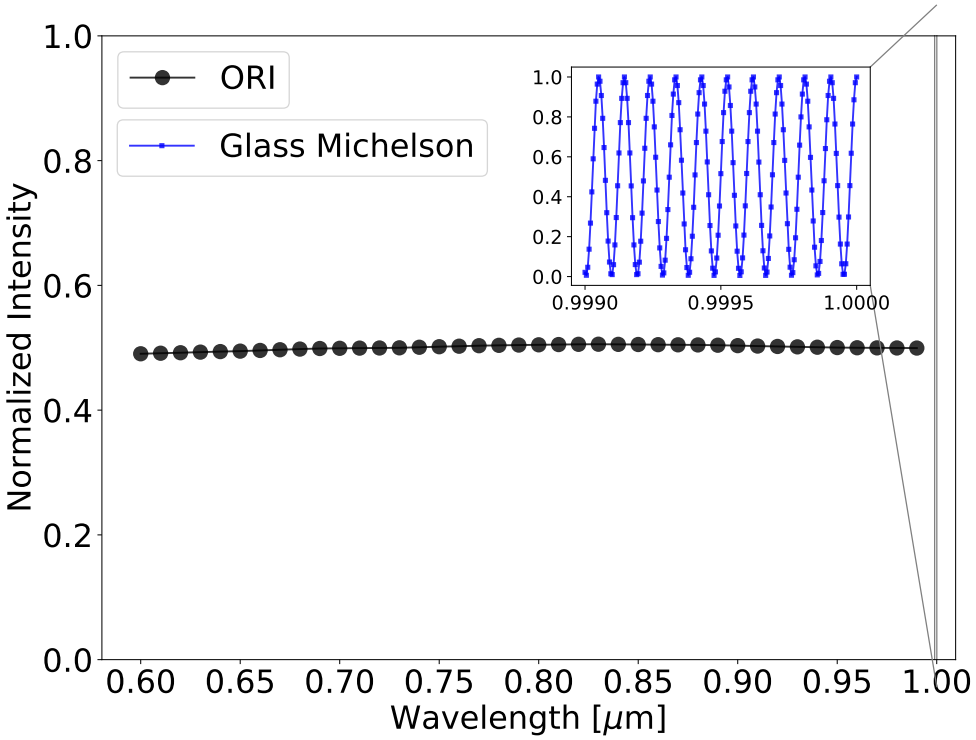

Figure 4.8: The main graph shows the intensity of one of the outputs of the ORI as a function of wavelength, demonstrating very good achromatic behaviour across the large range of 600 nm to 1000 nm. For comparison, the inset shows the intensity of the output of a field widened glass Michelson interferometer similar to those used in [88] over a short wavelength range. Clearly there is a high chromatic dependence.

inch) optics and standard optomechanical components from Thorlabs. The design selected to be build has the dimensions outlined in Table. 4.5. The choice of the B1=4, B2=4 configuration is due to the simplicity of the system, while at the same time showcasing the folded cavity-like configuration of the ORI design. Several modifications and iterations were done in order to get to a good performing system. The experimental and design issues are discussed in Sec. 4.4.1.

4.4.1 Design Issues

Although the ORI performed very well in the numerical simulations, the realities of manufacturing capabilities limited the performance of the system as designed in Figure. 4.1. In the original ORI design, the only optical element with any degrees of freedom is the CM. Translating the CM could easy correct any translational and in-plane angular beam misalignment. However, any out of plan angular deviations could not be corrected by simply translating the CM. Thus, all the central optics had to be manufactured with very tight tolerances. Unfortunately, the realities of off-the-shelf components are that the tolerances for these components are typically not sufficient for such a system. Particularly, it was measured that both the LBD, and the PRM, had significant out of plane angular deviations that could not easily be correct by the translation of the CM ($\pm$ 2° for some optical elements). The reality is that these deviations are within the manufacturing tolerances for these components. Furthermore, adding tip-tilt translations to the FM also could not correct the out of plane angular deviations. Full visibility was not achieved and interferometric shearing fringes were observed.

To correct this issue, the LBD,s were removed and replaced by a beam splitter and a flat mirror that has tip-tilt capabilities. The angular deviations of the PRM, are still present but the additional flat mirror in each path allows for the angular deviations to be corrected and maximal interference visibility can be observed. Therefore, for all the results presented in Sec. 4.4.2, the modified version of the ORI is show in Figure. 4.2a and Figure. 4.2c.

This table top experimental demonstration of the ORI (Figure. 4.9) has a much larger physical footprint than necessary. Nonetheless, the results in Sec. 4.4.2 are indicative of the overall performance of the optical design. Chap. 5 discusses some work towards reducing the physical footprint of the system. However, this remains as a future work.

4.4.2 Experimental Optical performance

The visibility of the ORI is tested using both single mode and multi mode signals from a continuous wave 785 nm external cavity diode laser (Toptica DLPro) and is measured as the difference

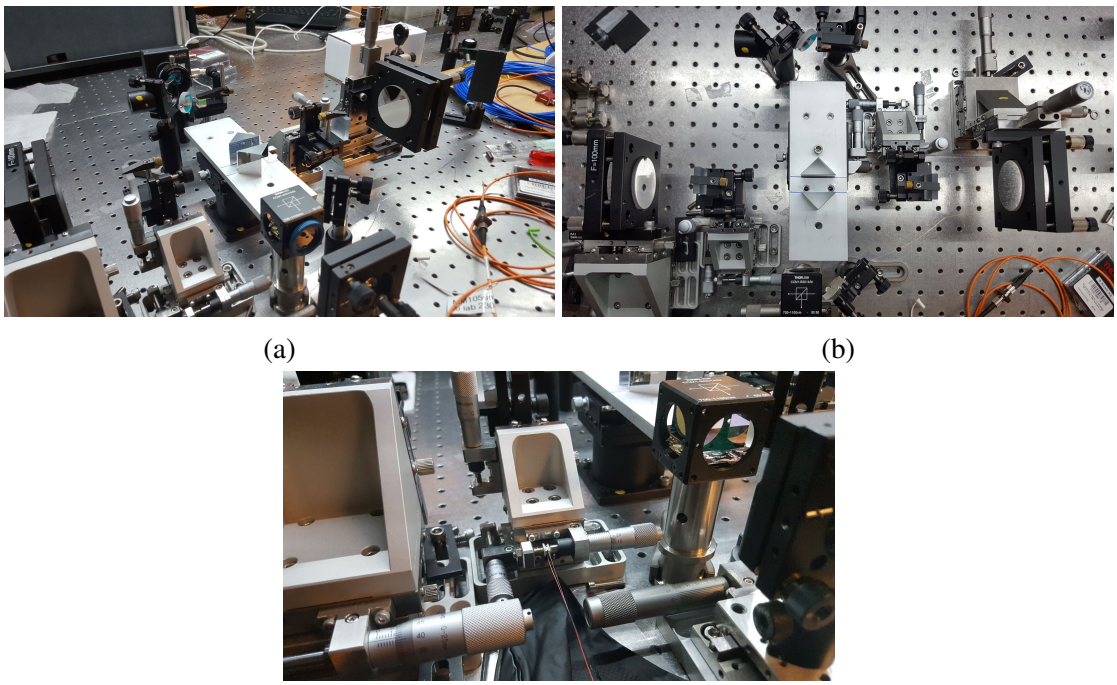

(a) (b)

(c)

Figure 4.9: (a) ORI table top implementation. (b) Top view of the ORI table top setup. (c) Location of the piezoelectric actuator that is adjusting the phase for the visibility measurements.

between the maximum and minimum intensity observed on a camera (WinCamD-UCD12 – $\frac{1}{2}$" CCD). A piezoelectric actuator is used to change the relative phase between the two paths of the ORI to reach the intensity minima and maxima (Figure. 4.9c). The visibility for the single mode signal is approximately 0.977 ± 0.016 for the Offner relay interferometer (ORI). This is in good agreement with the simulated results shown in Fig. 4.5. The single mode result is indicative of the experimental maximum that the interferometer can achieve with a multi mode signal if the imaging system functions as expected. However, with single mode signals such high visibilities are easily achievable with standard interferometers such as a Michelson interferometer, which in comparison had a single mode visibility of 0.997 ± 0.022 (Figure. 4.11a). The visibility here is calculated from the data by taking the visibility of each minimum and maximum pair, and then averaging over these values. The error bars are obtained via appropriate error propagation due to the sensitivity of the camera.

The true value of the ORI is when it is used with multi mode signals. In general for corrected interferometers, the visibility of the multi mode signal may suffer compared to the single-mode signal due to many factors such as, optical aberrations that cause deviations from an ideal imaging system. Nonetheless, the performance of the ORI with multi mode signals was quite good with a visibility of 0.979 ± 0.022, as seen in Figure 4.10. This maximum is achieved after careful alignment of the optical setup and spot size matching. The optical design in consistently achieved visibilities of 0.9 or greater with little to no alignment effort. However, the remaining boost to the theoretical maximum required very careful alignment. Future work will be done to improve the ease of alignment by reducing the number of optical elements involved, see Sec. 4.5. The multi mode visibility of the ORI greatly exceeded that of an uncorrected unbalanced Michelson interferometer (Figure 4.11b) which saw a visibility of 0.536 ± 0.023. To further demonstrate the capabilities of the ORI, we compared its performance to that of the field widened interferometers used in [76]. It was tested using the same sensor and laser source as the ORI visibility tests and resulted in a multi mode signal visibility of 0.931 ± 0.02, Figure. 4.12. In [76] the visibility was reported to be 0.97 and recall that in Sec. 3.1.2.2 the visibility of this interferometer ranged from 0.93 to 0.97, which is still comparable to the ORI setup. Regardless, the multi mode performance of the ORI is comparable to other field widened interferometers. Furthermore, the optical throughput of the experimental implementation of the ORI is measured to be 87.5%. Which when compared to the throughput of the time bin analyzer (67%), it is clear that the reduced number of optics in the ORI is advantageous.

To demonstrate the achromatic ability of the field-widened ORI, a broad pulsed source was sent through both the Michelson and the ORI. The broad pulses were at 810 nm with a bandwidth of approximately 1 nm. Using a fast powermeter the visibility of sending the pulsed signal through both the Michelson, a multi mode quantum channel (multi mode fiber) and the ORI, was measured to be 0.48 ± 0.03, see Figure.4.13a. Using the powermeter, the maximum achievable

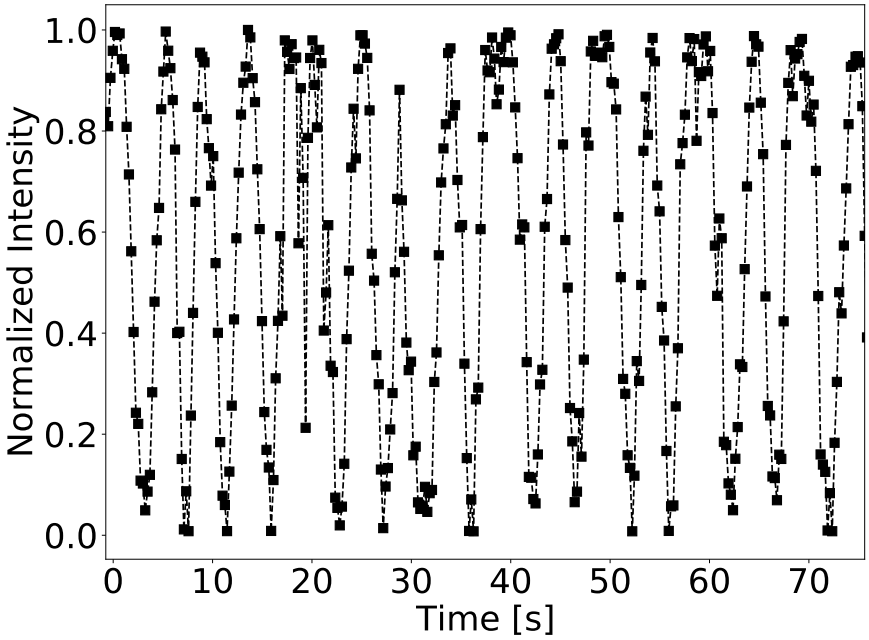

Figure 4.10: Normalized intensity at the output of the ORI for a multi mode input signal. The interference visibility is 0.979 ± 0.022. All intensity fluctuations are induced by a piezo electric actuator. The intensity is normalized such that the maximum recorded value is 1 and the detector background is 0. Measurement errors of the intensity are included in the plots and are represented by the size of the plot markers.

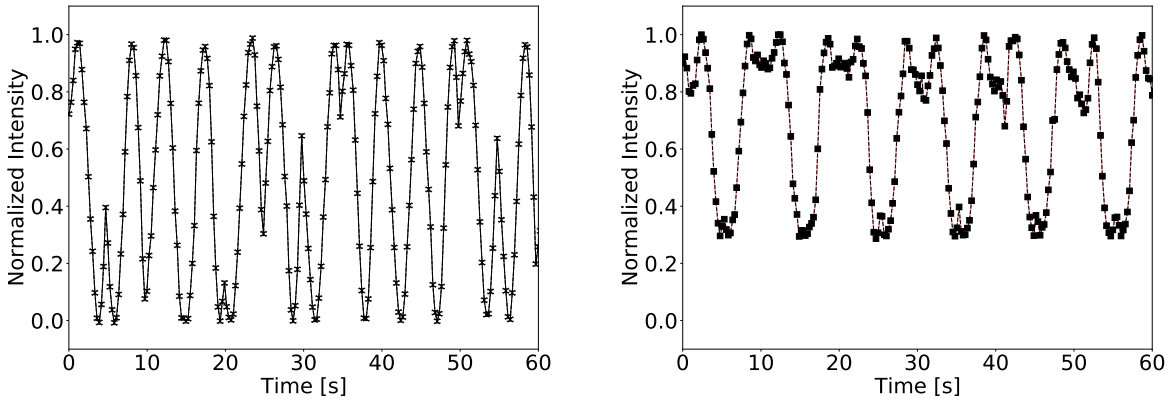

(a) Single mode input

(b) Multi mode input

Figure 4.11: Relative intensity of the output of an unbalanced Michelson interferometer that has a delay of approximately 500 ps. **(a)** shows the relative intensity of the output using single mode input with an interference visibility of 0.997 ± 0.022. **(b)** shows the relative intensity of the output using a multi mode input with an interference visibility of 0.536 ± 0.023. Note that unlike the corrected interferometer (Figure 4.10), the multi mode visibility suffers substantially. Both signals were taken using a continuous wave laser at 785 nm. The intensity fluctuations are induced by a piezo electric actuator. The intensity is normalized such that the maximum recorded value is 1 and the measurement camera background is 0. Measurement errors of the intensity are included in the plots and are represented by the size of the plot markers.

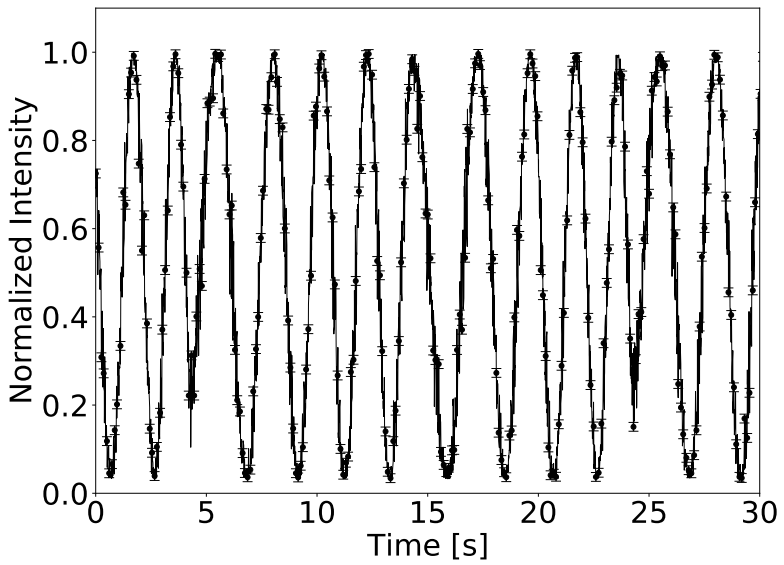

Figure 4.12: Normalized intensity of a multi mode signal passing through a field widened unbalanced Mach Zehnder interferometer that employs lenses as its imaging system. These are the inteferometers used in [76]. The visibility was obtained using a 785 nm continuous-wave laser and a camera. The intensity fluctuations are induced by a piezo electric actuator. An interference visibility of 0.931 ± 0.006 is obtained and found to be comparable to the ORI multi mode signal results. For clarity, every fifth data point is plotted, though all data points are considered when calculating the visibility.

visibility is 0.5, this is due to the satellite (side peak) pulses not having an interfering components but only the central peak is interfering. The central peak interference visibility is thus approximately 0.96 ± 0.06 thus indicating similar performance to the 780 nm source. The large error in the visibility is due to the uncertainty in the powermeter measurements. Nonetheless, the results indicate that the visibility with a source at a different wavelength from the design wavelength (780 nm) is quite high, which would not be easily achievable with a standard field widened interferometer due to the chromatic dependence of dispersion. It is again important to note the consequences of such a result as integrating many different quantum sources to a quantum network can be difficult if the hardware of the network is design for specific wavelengths.

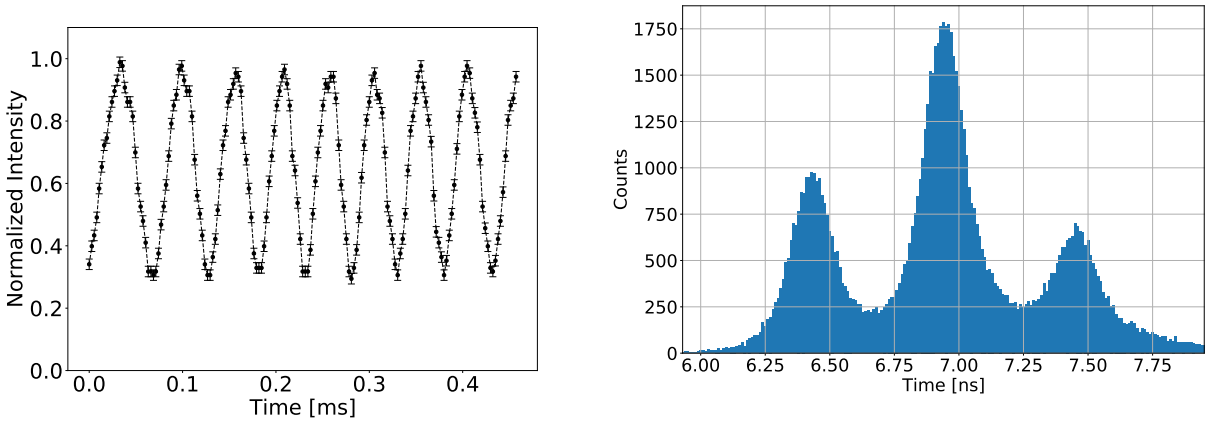

(a) (b)

Figure 4.13: **(a)** Relative intensity of the output of the Offner relay interferometer when using a broad pulsed source at 810 nm measured using a powermeter. The pulses are first passed through the Michelson interferometer then through a multi mode fiber and are measured using the Offner relay interferomter. The visibility is measured to be 0.48 ± 0.03 which when compared to the maximum achievable of 0.5. The large error in the visibility is due to the uncertainty in the powermeter measurements. Measurement errors of the intensity are included in the plots and are represented by the error bars. For clarity every 10^{th} point of data is plotted here, however all points were considered when calculating the visibility. **(b)** Histogram of the Offner relay interferometer combined with a Michelson interferometer of the same delay, approximately 500 ps. Bin sizes are 10 ps.

4.4.3 Imaging demonstration

To demonstrate the practicality of the ORI, a small imaging demonstration along the lines of those demonstrated in quantum imaging experiments was performed [87], see Figure 4.14. A target in the shape of a ψ that is 6 mm horizontally by 7 mm vertically is illuminated by a continuous wave laser and the scattered light was imaged through the ORI. The ORI was able to image the target and measure the interference of the signals after passing both arms of the interferometer. In contrast, an uncorrected Michelson would not be able to show any interference of the signals, hence any quantum information stored in the signals would be lost [87].

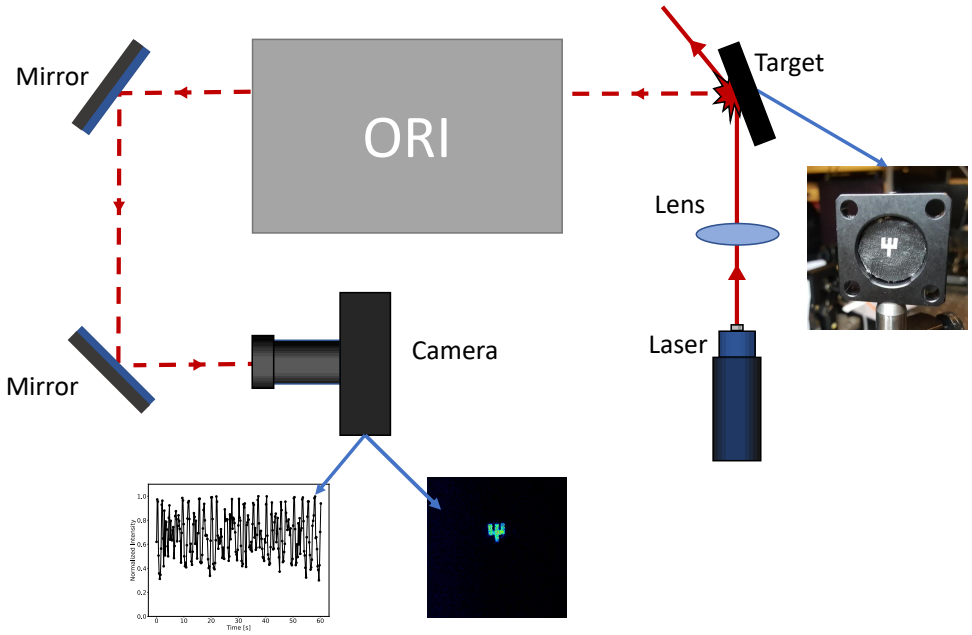

Figure 4.14: Quantum sensing demonstration using the ORI system. A target is illuminated using a continuous wave 785 nm laser. The signal is scattered off the target and directed through the two paths of the ORI. The relative path difference of the ORI is being changed using a piezo electric actuator which allows for coherence properties of the signals to be measured. The intensity at one of the outputs of the ORI is measured using a camera. The image of the illuminated target is recovered by the camera while at the same time interference fringes are observed.

As shown in Figure 4.14, the practical imaging setup was performed such that the target was facing away from the ORI such that scattered light is measured rather than a first order reflection of the illuminating beam. The results of the demonstration, shown in Figure 4.15, are very promising and can be extended to be used in a quantum enhanced LiDAR setting. The

interferometer system combined with a camera was able to image the target while at the same time measure the phase information of the signals as interference was observed from the signal after it passed through the two arms of the interferometer. This is especially important since it demonstrates that the one-to-one imaging system of the interferometer is functional and that the interferometer works with multi mode signals and with true scattered light. This point is further stressed in Figures 4.15 where results for the intensity of the signal after passing through the ORI are shown for the two scenarios, passing through both ORI paths, and blocking one ORI path. In both scenarios a piezo electric actuator is being driven to produce intensity fringes. The visibility of this interference was found to be around 0.49 ± 0.03 for the full interferometer scenario, compared to the 0.11 ± 0.04 observed when blocking one path of the interferometer. This is to indicates that the visibility with both arms unblocked is real and that the signals are in fact interfering. The relatively reduced visibility in the imaging scenario can be attributed to a number of reasons including; poor alignment of the system, higher exposure time of the camera needed to see the image which can cause smearing of the interference visibility. Nonetheless the results show a potential application for the ORI as an effective field widened interferometer.

4.5 Future Considerations

Although the concept of the ORI performed well under simulation, the manufacturing tolerances of optical components required modifications to the system in order to experimentally achieve the same performance. In addition, the physical footprint of the ORI implementation is quite large. Reducing the footprint of the system is an important objective. As mentioned above, the alignment of the system is not relatively easy and thus another future step is to reduce the required number of optical elements in the system. Such a configuration could be similar to that found in Figure. 4.16.

Another interesting avenue to explore is the possibility of using what are know as Herriott cells [133]. These cells can satisfy the imaging condition and can create relatively long path delays with a very small physical footprint. Although this is a deviation from the ORI design, it is still an interesting topic to investigate as one must ensure that the interference quality is sufficient and that it is achromatic.

4.6 Summary

In summary, this chapter discusses the work in developing a novel optical design for a field widened time bin interferometer that can easily integrate with current free-space and fiber optical

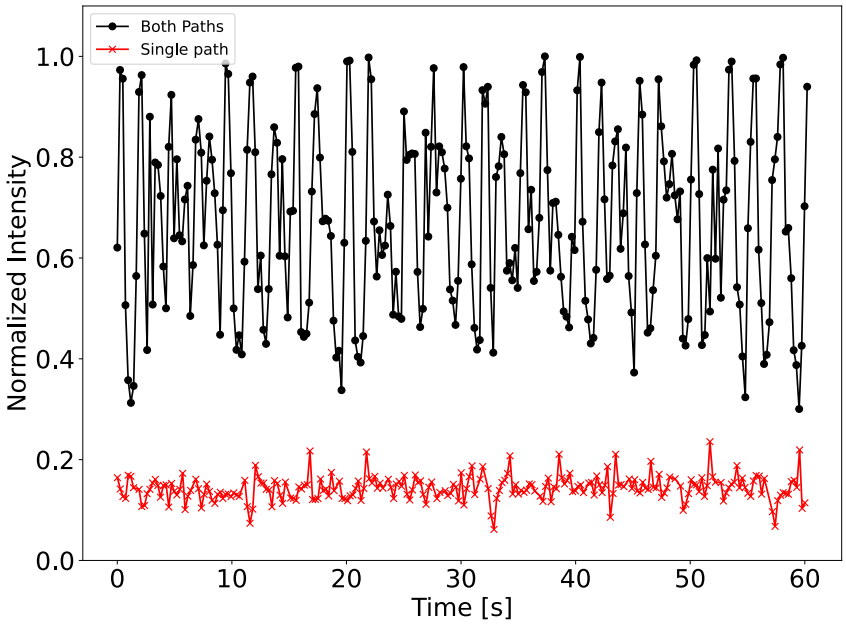

Figure 4.15: Intensity of the psi target image, as imaged through the ORI. The black circles are the intensity pattern of the scattered light from the target when allowed to pass through both arms of the interferometer. The relative intensity of the light is seen to have a periodic interference pattern. A piezo electric actuator is used to produce these patterns. Here the visibility is 0.49 ± 0.03. The red crosses show the stable intensity when only one arm is used, and the other arm is blocked. This has a visibility of 0.11 ± 0.04. The intensity is normalized to the maximum value of the data set for both paths (black circles). The single path data (red crosses) are lowered by 0.3 to increase the clarity of the plot.

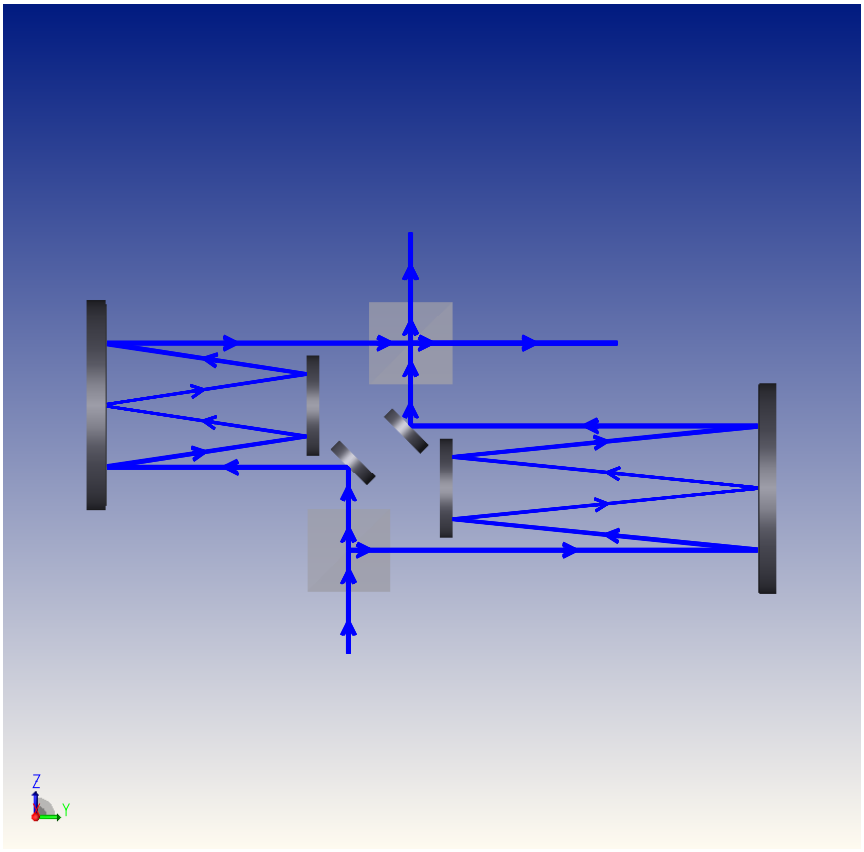

Figure 4.16: New ORI design with fewer optical elements.

networks. The interferometer was designed to have a small form factor and uses reflective optics for the imaging system which allows for the use of a broad range of wavelengths, in fact showing promise of being able to perform white light interferometry. We experimentally demonstrated that the optical design performs well with a multi mode interference visibility of greater than 0.97. Furthermore, the ORI design is capable of producing long relative path delays with a relatively reduced form factor compared to a standard Michelson or Mach Zehnder approach. The next steps are to investigate the limits of our design in terms of optical relative path delay and form factor, and test our device in a practical field setting such as with many different quantum sources (Sec. 3.2) or a moving free-space time bin experiment (Sec. 3.3).

Chapter 5

Monolithic Chassis for Quantum Sensing Interferometer

In this chapter, a monolithic chassis is created for the Offner relay interferometer (ORI) design (see Chap. 4). The goal is to create a chassis that experiences very little thermal expansion and has a small physical footprint. Furthermore, the optomechanical components necessary for the optical alignment of the system are build into the monolithic structure using flexures. The resulting enclosure, that was built using additive manufacturing, combined with the ORI is called the Printed Offner relay interferometer (PORI). This work is done in collaboration with the Multi-scale additive manufacturing lab (MSAM) team from the Department of Mechanical and Mechatronics Engineering. The project was funded with a Defense Research and Development Canada IDEAS grant and had a duration of six months.

Statement of contributions Prof. Thomas Jennewein and I conceived the idea of the monolithic structure with alignment flexures. I calculated and created the theoretical study of functionally graded materials for an athermal enclosure. Dogan Sinar and I designed and tested of the prototype flexure components. For the monolithic chassis, I performed most of the mechanical design work with a lot of guidance from Mark Kirby. Dogan Sinar performed the thermal finite element analysis of the final system. I tested the final structure with contributions from Tabitha Arulpragasam and Dogan Sinar. Sagar Patel, Vlad Parserin, Mark Kirby, Issa Rishmawi, and Prof. Mihaela Vlassae conducted the material selection, adjusted the parameters of the manufacturing, and coordinated the construction of the enclosure. Tabitha Arulpragasam, Dogan Sinar and I tested the mechanical stability of the flexure devices in the final structure.

5.1 Practical Time Bin Interferometer

Creating a practical time bin interferometers for free-space moving platforms such as satellites and airplanes has several challenges. First, long optical time delays allow for better distinction between the various time bins. Increasing the time delay allows for a relaxation of the detection and timing electronics. Time delays of >1 ns are ideal since relatively inexpensive single photon detectors (such as SiAPDs) can be used in combination with "slower" timing electronics. State of the art systems today could distinguish time bin separations on the order of 10 ps, however such systems have large cost, power, and physical footprint requirements that make them infeasible for small moving platforms.

The major side effect of having long time delays is the stability of the interferometer. Vibrations and thermal expansion of the materials that compose the interferometer will create challenges for the stability of the interferometer. Vibrations can be solved by applying epoxy to the components once in place. However, this is a procedure that requires specialized manufacturing and technicians which is not always readily available for university research labs. Thermal expansion can be solved by isolating and insulating the interferometer or by actively stabilizing the interferometer temperature. Such options are feasible, however they can be challenging for platforms that have power and space limitations, particularly satellites. With such a small physical footprint, commercial optomechanical components are not feasible as they are often designed for general-purpose use and may not be appropriate for a compact interferometer design due to their bulky form. Therefore custom optomechanical structures are typically designed and integrated for such platforms. For this study, the tool used to build the custom optomechanical components is Additive manufacturing (AM).

Several studies have been conducted over the last decade, investigating potential uses of AM for optomechanical components. Discreet optical mounts and flexures were manufactured using polymer filament 3D printers [134, 135, 136, 137]. A common theme among these studies is the use of traditional optomechanical designs. Consequently, several components had to be manufactured in pieces and later assembled. Single piece flexure mounts have been printed from metal using electron beam melting and were mounted on other conventional mounts during tests [138]. Finally, a quasi-monolithic system where a low power laser system was 3D printed as a single monolithic piece, except for the adjustable pump mirror which was assembled post-printing [139]. Furthermore, there is recently a fully monolithic interferometer that was used for a trapped atom system [140]. However, this monolithic system did not have any optomechanical components in the monolithic portion of the interferometer.

In this chapter, the challenge of building and designing a monolithic athermal enclosure for an interferometer is studied. The thermal expansion effects are considered and simulated to find

the materials required to create an athermal system. A monolithic structure is designed to house the optics of the interferometer with a small physical footprint and provide alignment tools for the system using custom designed optomechanical flexures. These optomechanical structures are embedded into the monolithic structure. This chapter discusses the research involved in the design and manufacturing of the first monolithic interferometer chassis created using AM that includes the optomechanical components.

5.2 Thermal Expansion Simulations

Thermal expansion of materials is an important consideration for highly sensitive equipment such as interferometers where typically a substantial effort is put forth to reduce the effects of thermal expansion [141]. In designing a practical time bin interferometer the thermal expansion of both the optical components and the enclosure must be considered. For optical components, birefringent stresses[1], and small changes in index of refraction can have detrimental effects on the performance of the interferometer. This is of particular concern for field widened interferometers that rely on optically dense materials to form the corrective imaging system [84, 88] as discussed in Chap. 4. The optical design must be carefully considered in order to avoid such effects, for example the use of reflective optics in theORI setup (Chap. 4) avoids the birefringence issue. There is a large amount of literature on the stress tensors due to thermal effects, the physical mechanisms behind thermal expansion, and the treatment of non-isotropic materials [142, 143]. However, here only the thermal expansion of linear[2] isotropic materials is considered and discussed.

5.2.1 Theoretical Framework

The relative thermal expansion of materials has been studied for several decades and is an important characteristic to consider in manufacturing. The 3-dimensional linear thermal expansion of a material can be described by

$$\frac{\Delta V}{V_0} = \alpha_V \Delta T, \tag{5.1}$$

[1] stemming from thermal expansion among other things

[2] Thermal expansion can be exponential depending on the temperature range and regime, this study will remain in the linear regime.

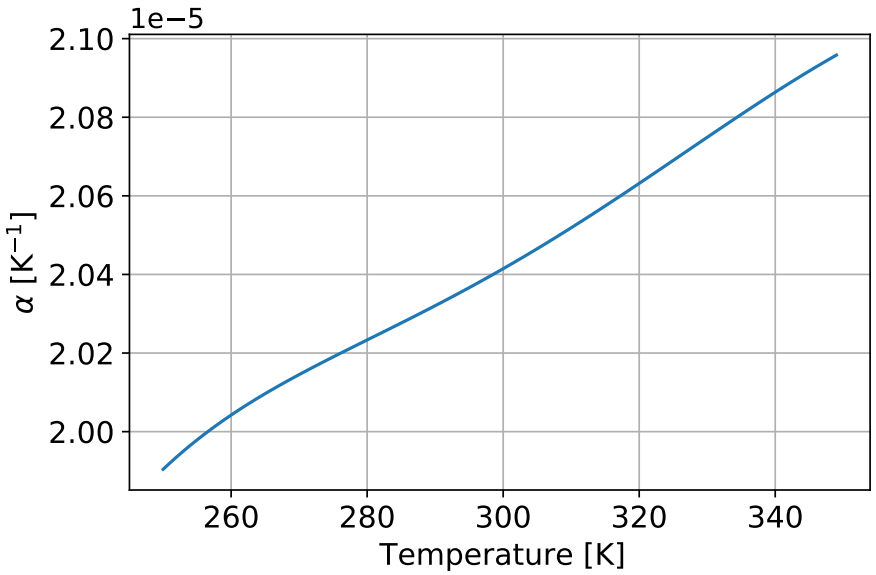

Figure 5.1: $\alpha(T)$ for Aluminum alloy AL 2014.

where V_0 is the initial volume of the material at the initial temperature T_0, $\Delta T = T_f - T_0$ is the change in temperature, and α_V is the 3-dimensional coefficient of thermal expansion. For isotropic materials, which is what will be considered in this work, the thermal expansion is the same in every direction such that

$$\alpha_V = 3\alpha_l, \tag{5.2}$$

where α_l is the coefficient thermal expansion (CTE) in one dimension. From now on α_l will be written as α for brevity. Now the CTE is temperature dependent such that $\alpha(T)$ as is typically represented as the Taylor expansion

$$\alpha(T) = A_0 + A_1 T + A_2 T^2 + \ldots \tag{5.3}$$

where the A_i are typically determined empirically and found in the literature [144, 145]. The A_i are usually defined for a specific temperature range and not valid for all temperatures. Figure. 5.1 shows $\alpha(T)$ for an Aluminum alloy between 250 K to 350 K. α is typically on the order of $10^{-5}\mathrm{K}^{-1}$ as seen for Aluminum (Table 5.1) and Steel alloys (Table 5.2).

Table 5.1: A_i of various Aluminum alloys. The first column is the order of A_i found in Eq. 5.3.

i	AL 2014	AL X2020	AL 2219	AL 5456	AL 7075	AL 7079	Aluminum
0	-2.35E-04	1.32E-03	-1.32E-03	-1.33E-04	2.60E-03	7.82E-04	3.77E-02
1	3.56E-06	-2.44E-05	2.71E-05	2.05E-06	-5.18E-05	-1.66E-05	7.84E-04
2	-1.85E-08	1.86E-07	-2.26E-07	-9.22E-09	4.27E-07	1.47E-07	-6.77E-06
3	3.96E-11	-7.39E-10	9.89E-10	9.12E-12	-1.85E-09	-6.83E-10	3.11E-08
4	-9.91E-15	1.61E-12	-2.40E-12	4.67E-14	4.44E-12	1.74E-12	-8.00E-11
5	-8.19E-17	-1.84E-15	3.07E-15	-1.37E-16	-5.62E-15	-2.33E-15	1.10E-13
6	8.54E-20	8.49E-19	-1.61E-18	1.06E-19	2.93E-18	1.28E-18	-6.23E-17

Table 5.2: A_i Steel alloys. The first column is the order of A_i found in Eq. 5.3.

i	FE 17-7PH	A286	20-CB	301	347	410	InconelX	RonHI
0	-3.70E-04	9.51E-04	8.95E-04	-8.16E-04	3.04-E04	-1.06E-03	1.54E-03	-3.58E-04
1	6.91E-06	-1.74E-05	-1.65E-05	1.62E-05	-6.16E-06	2.07E-05	-2.99E-05	7.01E-06
2	-5.16E-08	1.31E-07	1.27E-07	-1.29E-07	5.19E-08	-1.65E-07	2.38E-07	-5.51E-08
3	2.03E-10	-5.12E-10	-5.13E-10	5.45E-10	-2.24E-10	6.91E-10	-9.98E-10	2.29E-10
4	-4.40E-13	1.11E-12	1.15E-12	-1.27E-12	5.28E-13	-1.60E-12	2.31E-12	-5.29E-13
5	5.01E-16	-1.26E-15	-1.37E-15	1.57E-15	-6.44E-16	1.95E-15	-2.82E-15	6.41E-16
6	-2.34E-19	5.85E-19	6.70E-19	-7.98E-19	3.19E-19	-9.78E-19	1.42E-18	-3.19E-19

Overall, the final expression that we will be dealing with is

$$\frac{\Delta L}{L_0} = \alpha(T)\Delta T, \tag{5.4}$$

where L is the length of one-dimension of the material.

The analysis that is to follow will conduct a study on the materials required to make an enclosure that induces the least amount of phase shift between the long and short arm of an interferometer. The naive solution is to find a single material that exhibits very little to no thermal expansion, e.g. ZeroDur or Invar. However, even these materials require some form of insulation or active temperature regulation since a small difference in the relative path length is still created though they reduce the requirements. An ideal solution would be an enclosure that maintains the relative path length difference between all the optical components. Such a solution would require two materials of differing thermal expansion be in one of the paths. The reason for this is that the absolute change in path in the short and long path will be different since Eq. 5.4 represents the relative change. Thus, a larger initial path will exhibit a larger absolute change in length. Thus if the entire enclosure was made of the same material, the relative path length difference between the short and long path will not be maintained. Effectively the condition to satisfy is

$$\begin{aligned}
&L_l(T) - L_s(T) = L_l(0) - L_s(0), \\
&\alpha_l(T)\Delta T L_l(0) + L_l(0) - (\alpha_s(T)\Delta T L_s(0) + L_s(0)) = L_l(0) - L_s(0), \\
&\alpha_l(T)\Delta T L_l(0) - \alpha_s(T)\Delta T L_s(0) = 0, \\
&\alpha_l(T) L_l(0) = \alpha_s(T) L_s(0).
\end{aligned} \tag{5.5}$$

The final condition of Eq. 5.5 demonstrates that if $\alpha_l = \alpha_s$ it is impossible to create an enclosure that does not exhibit some thermal expansion effects. However, slightly adjusting the materials that make up each path will allow for this condition to be satisfied. Figure 5.2 depicts how to materials can be used in an enclosure that houses an interferometer.

The problem of creating a zero thermal expansion enclosure for an interferometer is reduced to a simple expression. Knowing the initial optical path lengths and optical element positions, one can calculate the required CTE needed to satisfy the condition in Eq. 5.5. More practically, one would choose two materials and calculate the required thickness of each material in each path that satisfies Eq. 5.5. Following this concept, the use of "expansion" joints, or a smaller area of a different material that behaves similar to the expansion joints used in bridges, can be used to buffer the effects of thermal expansion. Typically, this would mean a material with a larger $\alpha(T)$ than the base material if placed in the shorter path, and a material with a smaller $\alpha(T)$ compared to the base material for the longer path.

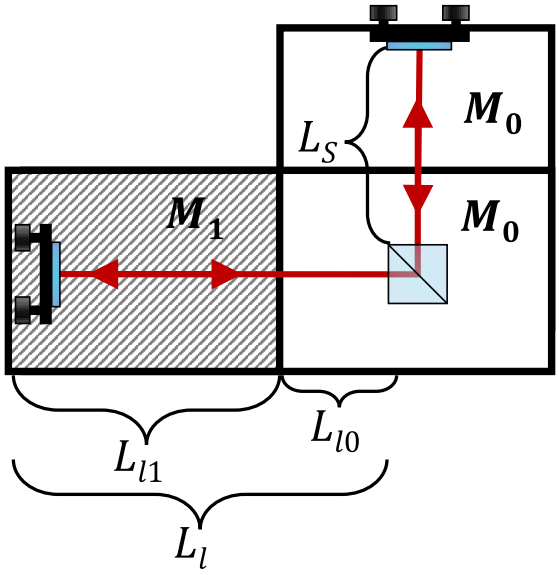

Figure 5.2: Two materials can be used to create a condition where the path difference of the interferometer is stable over a large temperature range.

There are some non-trivial considerations that need to be accounted for when actually manufacturing a device with such expansion joints. First, the means by which the expansion joint is attached is highly important as the thermal expansion occurs in three dimensions so the stresses could potentially be quite large at the material boundary. Second, the thickness of this material must be within the range of the devices used in the manufacturing process. For example, if the expansion joint requires to be in the sub-millimeter regime while the manufacturing technology's accuracy is reliably in the millimeter regime, then the manufacturing of such an expansion joint is not feasible.

5.2.2 Analysis with ORI setup

TheORI setup has complex path lengths that require some calculations in order to fully get to the conditions of Eq. 5.5. For theORI we will have a base system that houses most of the optical elements in of the system similar to the situation in Figure. 5.2. The type of materials to use for M_1 and M_0, and the relative amounts of each material are the variables that need to be calculated in order to satisfy the condition in Eq. 5.5.

In Sec. 4.2.1, the total path length of each path of theORI is established. Thermal expansion is now considered and included in the model in order to satisfy the conditions of Eq. 5.5. For

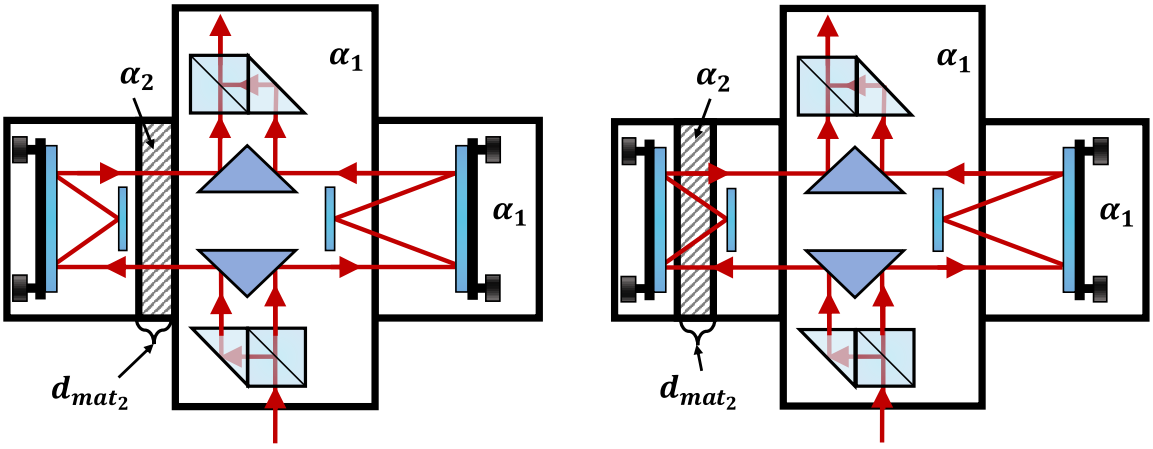

(a) Scenario 1 (b) Scenario 2

Figure 5.3: The two expansion joint scenarios considered in the thermal calculations. The white areas are made of the same material with a CTE of α_0, while the striped area represents the expansion joints with a CTE of α_1. Note the difference of the relative location of the FM and the expansion joint between scenario 1 and scenario 2.

this analysis, the consideration is for enclosures that have a change in material at some point in either the short or long path in order to compensate for the differences in relative change in path length. There are two scenarios to account for:

1. The change in material occurs at $\frac{sb}{2} < |y| < d_{CM} - d_{FM}$ thus only the paths of Eq. 4.2 are affected.

2. The change in material occurs at $d_{CM} - d_{FM} < |y| < d_{CM}$ thus the total path length of Eq. 4.5 is affected.

Both scenarios are illustrated in Figure. 5.3. For scenario 1, one side of Eq. 5.5 becomes,

$$\sum_{i=1}^{2} \alpha_i(T) L_i = 2\left(\alpha_1(y(d_x,R)_{curv} - d_{mat_2}) + \alpha_2 d_{mat_2}\right) + \alpha_1 hyp(d_x,B)_{tot}, \tag{5.6}$$

where α_i is the coefficient of thermal expansion for the material. In this example of scenario 1, only two materials are considered, however any number of materials can be used. For scenario 2, one side of Eq. 5.5 becomes,

$$\sum_{i=1}^{2} \alpha_i(T)L_i = 2\left(\alpha_1\left(y(d_x,R)_{curv} - d_{mat_2}\right) + \alpha_2 d_{mat_2}\right) + \alpha_1 hyp(d_x,B)_{tot} + B\frac{d_{mat_2}}{\sin\left(\arctan\left(\Omega\right)\right)}\left(\alpha_2 - \alpha_1\right),) \tag{5.7}$$

where again more than two α_i may be considered, and Ω is the angle with respect to the vertical made by the cavity-like bounces in the Offner relay, and is defined as,

$$\Omega = \frac{B\sqrt{R^2 - d_x^2} - (R - d_{CM}) - (d_{CM} - d_{FM})}{2d_x}. \tag{5.8}$$

Eq. 5.6 5.7 can be applied to either the short path or long path in order to satisfy the condition in Eq. 5.5. Knowing which path to apply to which scenario is highly dependent on the available materials and the desired time delay of the interferometer. Therefore with these two scenarios, a simulation with known quantities is conducted to find realistic expansion joint lengths for various combinations of materials, curved mirror radii of curvature, and number of diagonal paths taken in the Offner relay. This numerical simulation finds the distance of d_{mat_2} (the expansion joint thickness) that satisfies the condition in Eq. 5.5. This is done over a temperature range ΔT and a solution for each temperature is found. An average of d_{mat_2} value is calculated with a standard deviation. The thermal expansion of the optical elements is not considered in this simulation since it is much smaller compared the metallic materials investigated. The metal combinations of interest are steel and aluminum, and Invar and Titanium64. The steel and aluminum combination is investigated because of the availability of these materials in standard manufacturing techniques. The Invar and Titanium64 combination is investigated due to the availability of these metals with additive manufacturing. These are discussed further in Sec. 5.3.

5.2.3 Results of Algebraic Simulations

The results for the numerical simulation where material1 is Ti64-100 and material2 is Invar36 for both scenario 1 and 2 over a temperature range of $\Delta T = 10$ is given in Table 5.3 and Table 5.4 respectively.The 10 K temperature range is chosen as a baseline for the thermal expansion simulations and are indicative of the temperature stability capable with some thermal insulation or reduced thermal stabilization. The results are displayed such that R1 and R2 is the radius of curvature of the curved mirror in the long path and short path of the interferometer respectively. The long path contains the expansion joint made of material2 (Invar36 for Table 5.3 and Table 5.4) and is given by d_{mat_2}. Note that there are more possible configurations for scenario 2

since many of the results for scenario 1 were not physically possible. Nonetheless, these results show that the expansion joint technique is a viable solution for the thermal expansion problem. The main challenge is to manufacture such an enclosure that includes expansion joints. This is difficult as wielding different materials and joining the expansion joints can prove difficult with conventional manufacturing techniques. Furthermore, using screws, or other joining devices would complicate the thermal properties of the enclosure and more proper simulations would need to be done. A promising solution is to use additive manufacturing to create such an enclosure since gradient materials can be manufactured or joined, this is called a functionally graded material [146, 147, 148]. However, there are drawbacks to using additive manufacturing and the realities of creating such an enclosure using additive manufacturing are discussed in Sec.5.3.4.2. Results for more metals and more interferometer configurations are provided in long tables in Appendix D.

Table 5.3: Simulation results for the Titanium64-100 and Invar as metal 1 and metal 2 respectively. These results are for scenario 1, that is solving for d_{mat_2} of Eq. 5.6 where B = Bounce 2 and the the other interferometer path has no expansion joint. The simulation is done over a 10 °C temperature range ($\Delta T = 10$). The standard deviation is for the average of the distribution of solutions for d_{mat_2}. Here only configurations with time delays of greater than 0.5 ns and solutions with realistic values of d_{mat_2} (i.e. those that satisfy the condition in scenario 1) are considered.

R1 [m]	R2 [m]	Bounce 1	Bounce 2	Time Delay [ns]	d_{mat_2} [mm]	std (10^{-14}) [mm]
0.3000	0.2000	6	8	0.5376	38.1443	0.6939
0.3000	0.2000	4	8	0.8590	31.6307	0.6939
0.3000	0.2000	2	8	1.3588	19.4839	0.3469
0.3000	0.2000	2	6	1.2152	38.0316	0.6939

5.3 Additive Manufacturing

Additive manufacturing (AM) is an exciting field that enables researchers and industry to create structures that are otherwise expensive or difficult to create with conventional techniques. Furthermore, the advent of design for AM has drastically opened up the potential to high-complex geometries [149], and has unlocked the potential to obtain performance superior to conventional manufacturing processes [150]. Compared to conventional machining, AM is capable of producing very complex shapes and geometries that are light weight but structurally robust. Furthermore, AM has the ability to produce unique material densities and compositions that are

Table 5.4: Simulation results for the Titanium64-100 and Invar as metal 1 and metal 2 respectively. These results are for scenario 2, that is solving for d_{mat_2} of Eq. 5.7 where B = Bounce 2 and the the other interferometer path has no expansion joint. The simulation is done over a 10 °C temperature range ($\Delta T = 10$). The standard deviation is for the average of the distribution of solutions for d_{mat_2}. Here only configurations with time delays of greater than 0.5 ns are considered.

R1 [m]	R2 [m]	Bounce 1	Bounce 2	Time Delay [ns]	d_{mat_2} [mm]	std (10^{-14}) [mm]
0.3000	0.2000	6	8	0.5376	12.9940	0.0000
0.3000	0.2000	4	8	0.8590	34.0244	0.6939
0.3000	0.2000	4	6	0.7155	28.1854	0.3469
0.3000	0.2000	4	4	0.5013	18.4057	0.0000
0.3000	0.2000	2	8	1.3588	96.4726	0.0000
0.3000	0.2000	2	6	1.2152	87.3027	1.3878
0.3000	0.2000	2	4	1.0011	71.9438	1.3878
0.3000	0.2000	2	2	0.6678	43.3042	0.0000

not possible with conventional machining, such as functionally graded materials. AM can also reduce manufacturing waste when compared to conventional machining since the structures are built layer by layer rather than being cut from a larger piece. Although AM is a fast changing and expansive field, for this thesis, only laser powder bed fusion is discussed, though there are many types of additive manufacturing [151].

Laser powder bed fusion (LPBF) is the leading metal AM technologies used for industrial part production for several industrial applications [152, 153, 154, 155, 156, 157]. Briefly, LPBF creates structures by applying a layer of powdered material (typically metal) and melting/fusing the structure together using a high powered, well focused laser beam. The powder is applied onto a base plate and precise movements of the laser beam begin to form the component. Subsequent layers of powder are introduced and at each layer, the laser beam is applied at the necessary location to grow the component from the sea of metal powder, as seen in Figure 5.4 and Figure. 5.5. Several important parameters are adjusted to properly create a structure that has the same properties as the bulk material. These include but are not limited to; the power level laser power, the laser beam spot size, the exposure time, the powder layer thickness, amongst others. LPBF currently has the highest industrial uptake amongst all the other AM technologies[151]. The are several practical reasons for the advancement of LPBF. First, amongst all the AM technique, fine features can easily be resolved due to the ability to manipulate the laser beam spot sizes. These spot sizes are generally being between 50-100 µm [158]. Second, there is a wide range of materials compatible with the technology [159] and of particular interest for this project, low

thermal expansion materials such at Invar36.

5.3.1 Designing for Additive Manufacturing

Designing components for additive manufacturing is not as straightforward as taking a design and trying to print it. There are many things to consider when designing for additive manufacturing and a few lessons learned during this study will be outlines.

First and foremost, one must take advantage of the fact that additive manufacturing creates structures that conventional manufacturing cannot. For example, creating complex lattices, or hollow chambers in an otherwise solid piece are unheard of in conventional machining and even molding techniques. Such complex structures can be used to lightweight while strengthening the component. Building monolithic multilayered structures is easy and cannot be done with conventional machining. AM cannot create everything and is not good at everything, it is analogous to quantum computing in that it can solve certain problems that is difficult for other manufacturing techniques. One certainly would not print a large block on metal but rather cut a bulk piece to the appropriate size.

Second, design your part such that it will require the least amount of supports. As discussed, the AM process starts with a blank metal build plate. Material deposited onto this build plate achieves attachment without additional post-processing. AM can create very complex structures, however with the current technology, overhangs or "hanging" features are problematic. Any overhang that is $>45^\circ$ from the vertical will require the addition of support beams. These support structures are cumbersome to properly place such that the structure does not fail and to remove once the device is manufactured. Therefore, care and consideration must be taken in the design to ensure that overhangs are $<45^\circ$ from the vertical. Figure 5.6a and Figure 5.6b illustrates overhanging structures and the potential location for supports. Figure. 5.7 shows a part that was built that needed supports and the tedious process of removing these support structures. Thus, in order to avoid tedious removal steps, a design has to avoid hanging edges and planes where support structures cannot be deposited. In general, hanging parts must be supported from underneath by existing structures in the design. Nonetheless there are several techniques to avoid using overhanging structures. First, rather than having a sudden overhang, using 45° chamfer[3]. as seen in Figure 5.6c. This chamfer technique can be used in a variety of situations and is the main tool in eliminating overhangs. Another technique is to build your device such that it requires the least supports possible. This can be as simple as reorienting the direction from which the part is grown. Finally, being mindful that AM can create structures that are otherwise difficult

[3] A chamfer can refer to the process of adding a beveled edge or corner to a 3D printed part. They can be used to improve the overall quality of the part, reduce sharp edges, and make assembly easier i.e. reduce overhangs

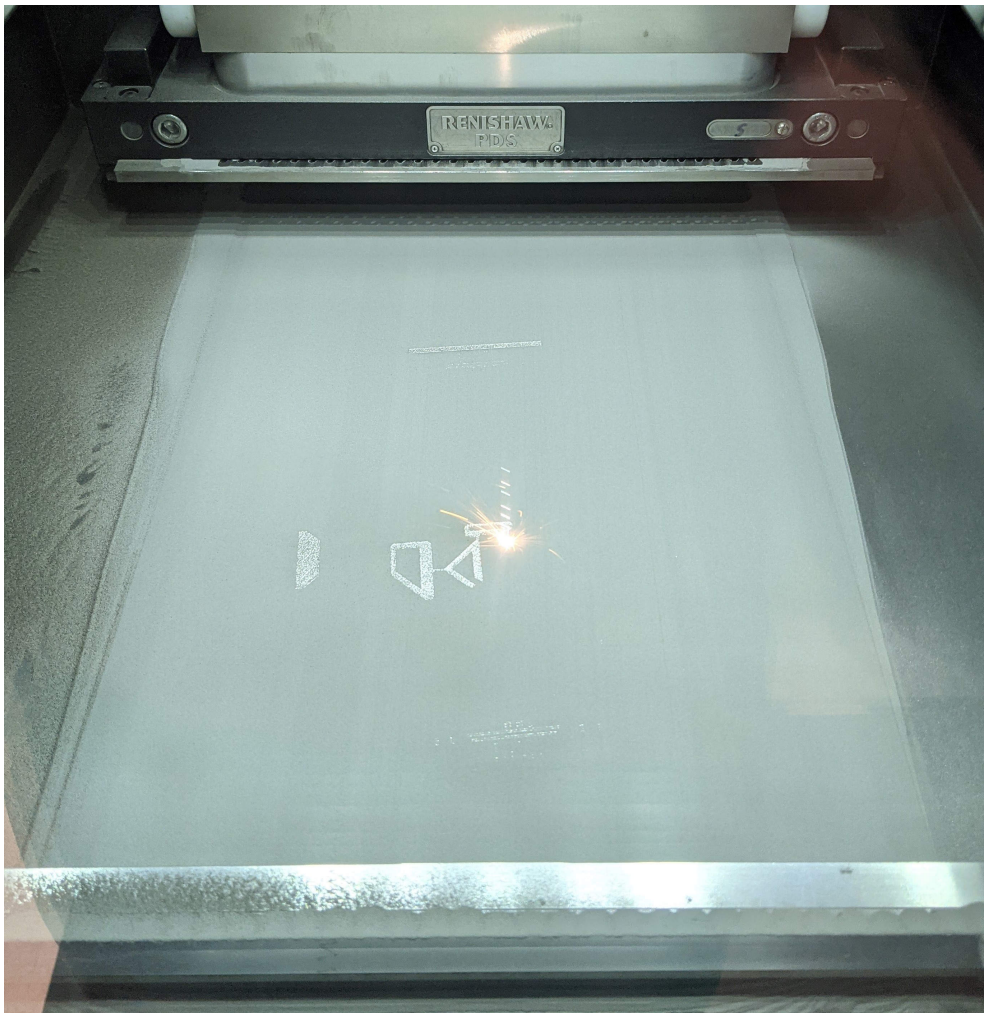

Figure 5.4: Focused laser beam striking the metallic powder. The structure being built can be seen among the layer of powder. Photo taken by Dr. Sagar Patel of the MSAM group.

Figure 5.5: Completed structure in a sea of powder. This powder must be removed prior to use as it poses a health risk. Photo taken by Dr. Sagar Patel of the MSAM group.

for standard manufacturing, and can allow for all overhangs to be greater than 45° with respect to the horizontal. Thus, all overhangs needing supports are removed. All the techniques to reduce the number of supports are used in the final design of the flexures in the monolithic chassis as see in Sec. 5.3.3.5 and Sec. 5.3.4.2.

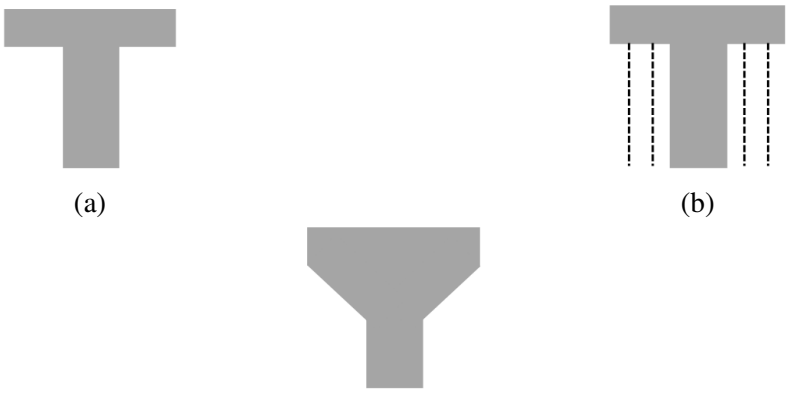

(a) (b) (c)

Figure 5.6: Eliminating the need for temporary support structures. (a) The overhang can cause the build structure to collapse under its own weight during the build process. (b) The typical and wasteful solution is to use thin support structures that printed and removed after the build process. (c) Chamfers built into the design can reduce or completely remove the need for support structures.

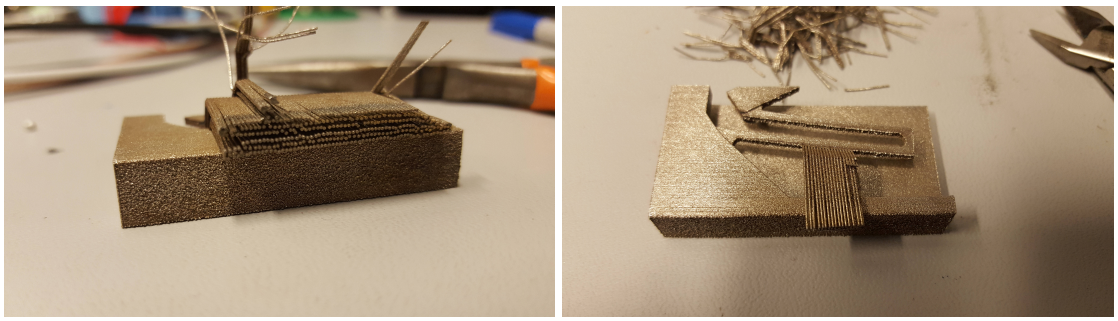

(a) (b)

Figure 5.7: The process of removing support structures is tedious and takes a lot of time. Thus a design that is considering using additive manufacturing should try to remove the need for any support structures.

Lastly, additive manufacturing is still in its infancy. Perhaps by the time you are reading this

there may be several advances in AM that expand its capabilities and usefulness. Some things that are currently being studied and worked on are printing of optical components, so potentially in the future full optical systems can be printed. For metal AM, combining materials (functionally graded materials [146, 147, 148]) and direct fusing or welding of these mixed structures are being studied and can be used to create athermal enclosures, as studied in Sec. 5.2.

5.3.2 Material Selection

The selection of the material for this project is highly motivated by two factors, a low Coefficient of thermal expansion (CTE) and a relatively high yield strength; the former having a higher influence when considering the material selection. The thermal expansion is important since it plays an important role in reducing the thermal instability of an interferometer. Completely eliminating the thermal instabilities over a typical outdoor temperature range (i.e. 0 °C to 30 °C) with only passive compensation via the enclosure design is ideal. However, this requires the use of expansion joints and composite materials to counteract any expansion that is exhibited by the material used, see Sec. 5.2.3. Despite the promising calculations and the potential of creating a zero thermal expansion interferometer enclosure, functionally graded material (FGM) technologies are currently not within the capabilities of the MSAM group and are therefore not pursued during the manufacturing portion of this project. For context, a functionally graded material is a material that exhibits a gradual variation in composition, structure, or other properties over its volume [146, 147, 148]. In the context of this work it can be used to create a highly thermally stable structure.. However, FGM are subject of further research and can potentially be implemented in future applications.

Despite the limitations of using a single alloy, thermal stability analysis indicated that the alloy must exhibit a very low coefficient of thermal expansion of less than 0.6 ppm/K in order to keep the interferometer thermally stable. This required CTE is substantially lower than that exhibited by most metal alloys that are commercially available. Nonetheless, two materials are considered for the construction of the optomechanical structures, Ti6Al4V and Invar36. Ti6Al4V has a high yield strength of approximately 900 MPa, but relatively high CTE (≈8.6 ppm/K at 20 °C). Furthermore, it has been used extensively by the MSAM group in printing structures so the manufacturing parameters are well know. The high yield strength makes Ti6Al4V an attractive option for the flexures, as this allows for larger ranges of motion to be achieved with smaller bending leg lengths. However, only one type of flexure is built and tested (orthoplanar springs) using Ti6Al4V in order to investigate its possible use for flexures. However, due to the relatively higher CTE of Ti6Al4V, it was not used to print other flexures or structures, and was not considered in the final build of the enclosure.

Invar36 is an iron-nickel based alloy that has a very low coefficient of thermal expansion ($\approx$1.2 ppm/K at 20 °C). In fact, it has one of the lowest CTE for metals. There are some special variants of Invar alloys that have even lower CTEs (as low as 0.01 ppm/K) [160]. Invar36 is a variant that is available in powder form (necessary for LPBF) and was studied and characterized for the additive manufacturing process by the MSAM group. Compared to Ti6Al4V, Invar36 has a lower yield strength of 276 MPa. However, the low CTE of Invar36 makes it a very interesting candidate. By using Invar36 and the additive manufacturing approach, one can minimize dimensional changes due to thermal expansion and at the same time reduce the number of different components used to make the interferometer. The latter is important for understanding the thermal and vibrational characteristics of the device. Although the CTE of Invar36 is larger than the required 0.6 ppm/K, the use of Invar36 is still studied as it is nonetheless considerable an improvement compared to conventional optomechanical structures typically made of aluminum or other metals. Furthermore, temperature changes are typically on the order of several tens of seconds to hours, and thus the small expansion produced by the Invar36 can be compensated with a relatively cheap feedback system, or by using the appropriate scheme (Chap. 3). In a practical application, such as on a satellite, the interferometer could be properly insulated such that the temperature variations are reduced further. Therefore, the Invar36 was selected to print the flexure structures and the enclosure. In fact, Invar baseplates were purchased such that the chassis can be manufactured on Invar as well as the standard stainless steel plates typically used.

5.3.3 Flexure Design

With the selected materials, an investigation into the possible flexure actuators is conducted in order to create a monolithic chassis that includes the optomechanical components. For proper alignment and use of theORI, small optomechanical mounts are needed to make fine adjustments to the position of the curved mirror. Stable fine adjustments can be achieved using flexure mounts[89, 137]. Flexures, unlike conventional optomechanical mounts, can provide fine adjustment movements with minimal components [89]. Furthermore, the single piece nature of flexures allows for a reduced size and ease of integration, since the flexure can be manufactured into the monolithic enclosure. In addition, flexures are pursued over conventional optomechanical structures, which are typically bulky and made of high CTE materials. The lack of conventional springs makes modeling the thermal expansion of the optomechanical components simpler.

Below several candidate flexure designs that are produced using additive manufacturing are discussed. It was determined during the optical design phase that the most important degree of freedom is the motion of theCM and only a small range of motion is needed, on the order of a few mm. In addition, all the components that are presented in this section enable the system to achieve a small form factor and are less than 80 mm x 80 mm x 5 mm in footprint. Furthermore,

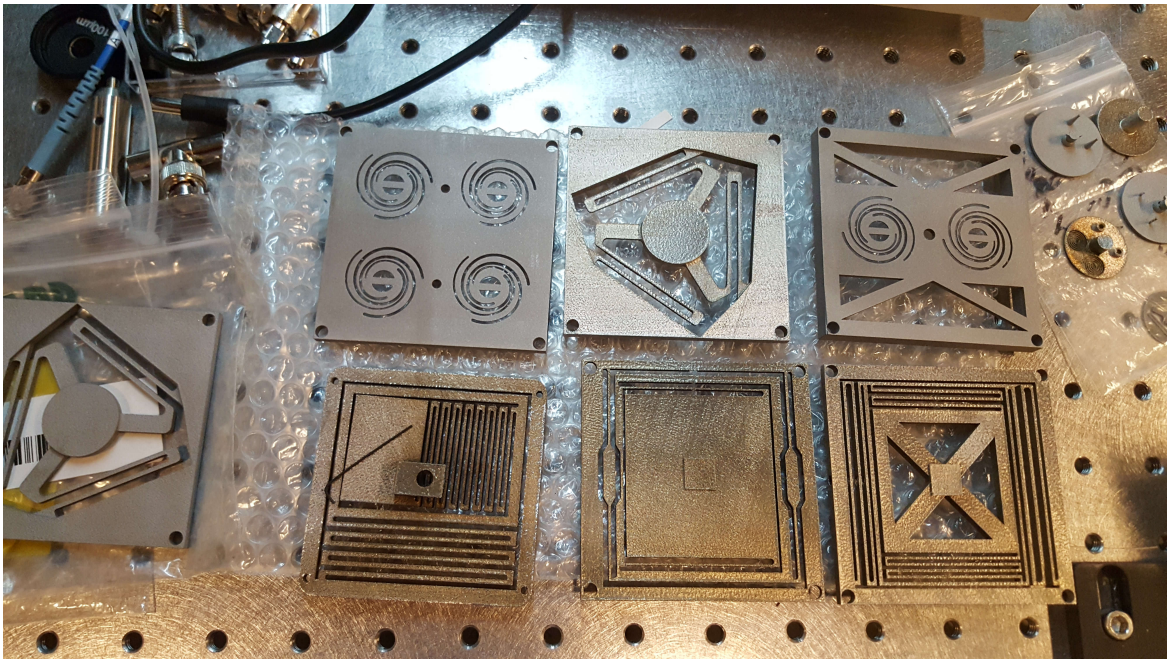

Figure 5.8: Flexure prototypes. Clockwise from top left: fourOxford, triangleRD, twoOxford, 4armRadiatorTS, singleArmTS, flexure designed by Dr. Dogan Sinar (TS1001), triangleRD.

the use of Invar36 (CTE $\approx$1.2 ppm/K at 20 °C range) as the material for the optomechanical components reduces thermal effects to the system compared to other materials (e,g, Ti6-4 alloy has CTE $\approx$8.6 ppm/K at 20 °C).

Several candidate designs have been thoroughly investigated, first using finite element modeling to establish candidate components to be printed. The printed components are then physically tested to ensure their performance, verify and measure the stress and fatigue induced to the components under their nominal conditions (Sec. 5.3.3.4). Figure 5.8 shows a photo of a selection of the printed flexure prototypes that are tested.

5.3.3.1 One-Dimensional Translation

The basic concept of the one-dimensional translation stages are to provide a range of motion along one axis. For the particular optical design of theORI, the axis normal to the center of the curved mirror is the degree of freedom that is the most important for alignment. Thus, one-dimensional flexures are considered. Here flexure springs that are well established in the literature are studied, the orthoplanar [161] and Oxford spring [162], see Figure. 5.9. The one-

(a) (b)

Figure 5.9: (a) The Oxford spring, note the complex and small features involved. (b) The Ortho-planar spring, note the three flexure arms.

dimensional translation stages (twoOxford and fourOxford), shown in Figure 5.10, are structures that embed an Oxford spring to a rigid body to create a linear translation. The desired range of motion is to provide a few millimeters of translation (approximately 2 mm). These devices would ideally be attached to one of the multidimensional stages and would thus be required to hold some transverse, or gravitational load.

5.3.3.2 Multi-dimensional translation stages

Multi-dimensional flexure translation stages were investigated to provide proper alignment of theCM inORI. Recall that the alignment of theCM can be reduced to three axes of translation, since for a spherical mirror, the act of translation and tilting have a similar effect. Conceptually there are two types of translations that are studied; multi-dimensional linear translation stages, and multi-dimensional angular translation stages.

The multi-dimensional linear translation stage creates linear translations in the plane of the optical component, i.e. horizontal and vertical translation. This can be achieved in several ways. Here the use of a radiative design (4armRadiatorTS) and a single leg design (singleArmTS) are pursued, as seen in Figure. 5.11. The 4armRadiatorTS design (Figure. 5.11a) produces a large displacement in both the horizontal and vertical direction. The long flexure beams that are stacked in a radiator design reduce the total stress experienced by each individual leg and reduces the stiffness of the overall flexure, thus increasing its range of motion. The expected range of

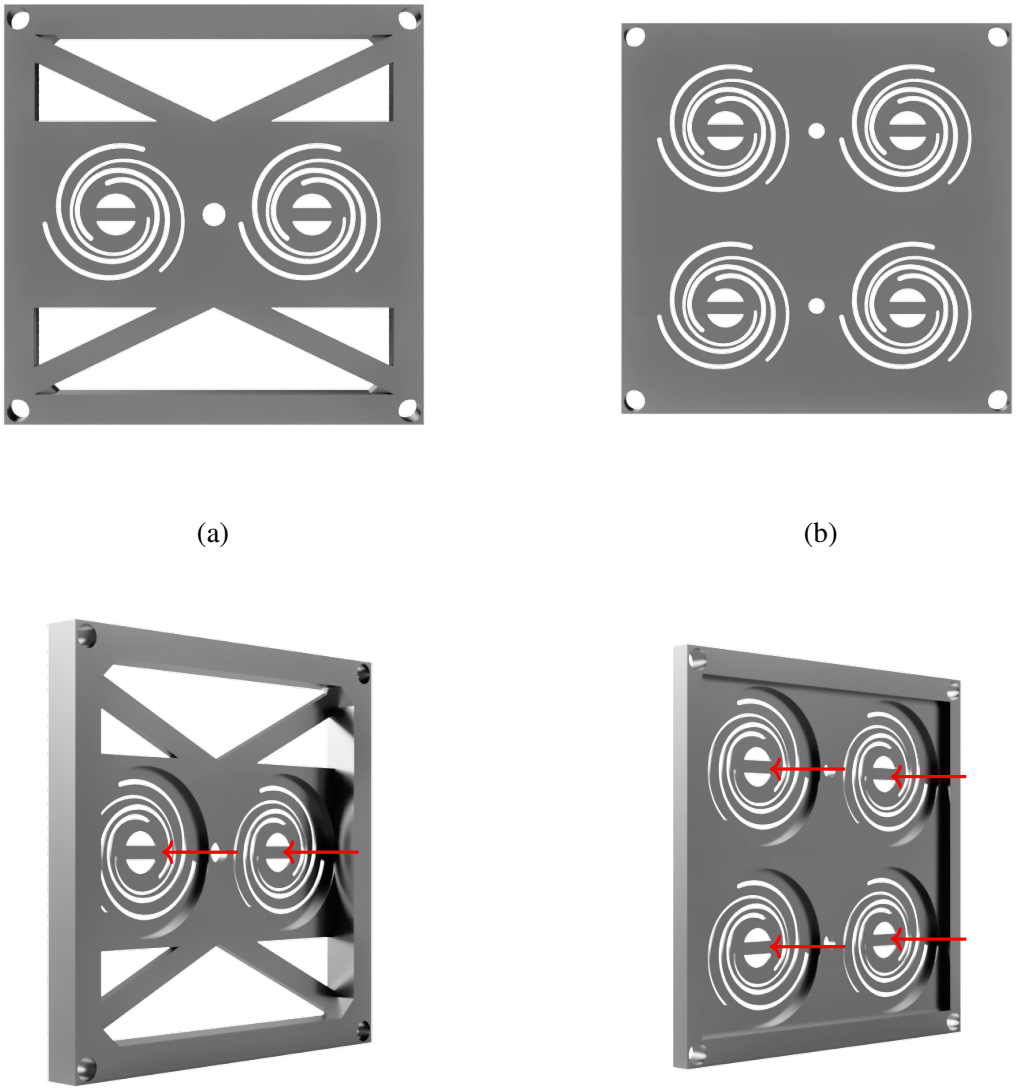

(a) (b)

(c) (d)

Figure 5.10: (a) The twoOxford translation stage. (b) The fourOxford translation stage. (c) and (d) the red arrows indicate the direction a force would be applied to create the translation.

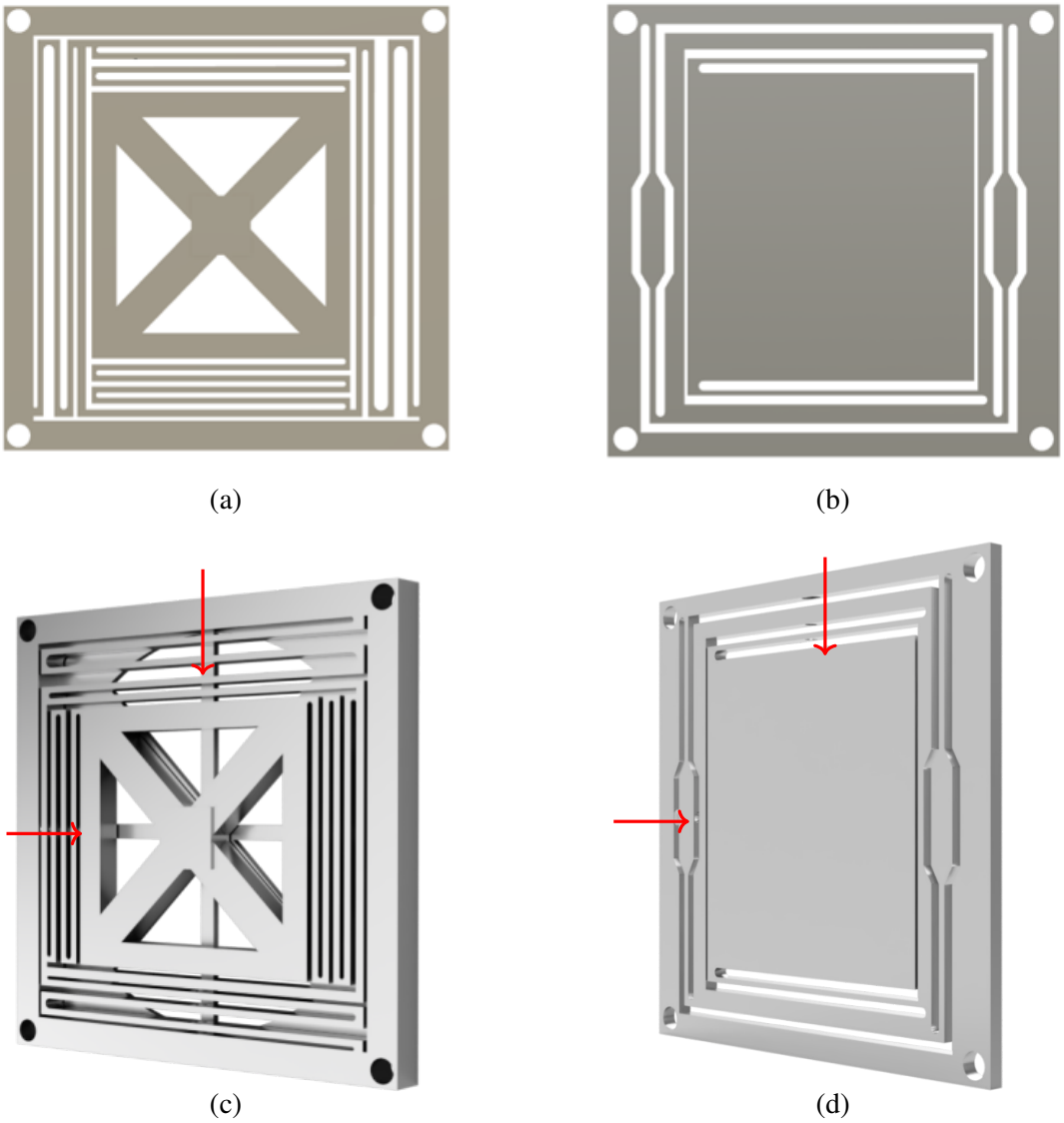

Figure 5.11: (a) The fourArmRadiator x-y translation stage. (b) The singleArmTS x-y translation stage. (c) and (d) the red arrows indicate the direction a force would be applied to create the translation.

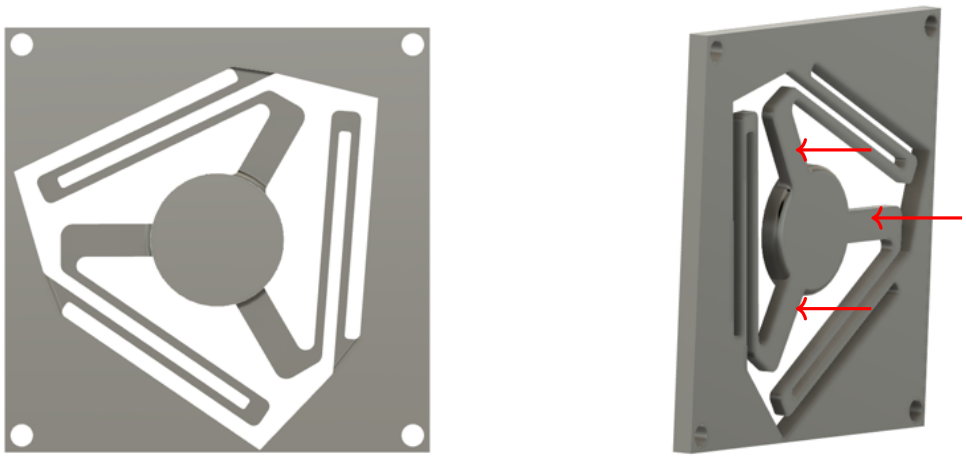

(a) (b)

Figure 5.12: (a) The triangleRD tip-tilt translation stage. (b) the red arrows indicate the direction a force would be applied to create the translation.

motion for the design show in Figure. 5.11 is 2.35 mm in the horizontal direction and 1 mm to 1.5 mm in the vertical direction. Although it produces a large range of motion, the radiator design can suffer from out of plane motion that can be detrimental to the performance of the flexure.

In contrast, the singleArmTS flexure (Figure. 5.11b) is much more stable and therefore does not suffer from out-of-plane motion. However, the length of the flexure beams in the single leg design need to be optimized to provide the desired large range of motion. The design shown in Figure. 5.11 has a range of motion of 750 µm in the horizontal direction and 600 µm in the vertical direction. In both designs the linear translation is produced by applying a force on the appropriate contact surfaces as shown by red arrows in Figure. 5.11. This can be achieved by using set screws, piezo actuators, or linear stepper motors.

The second type of multi-dimensional flexure design produces angular deflections about given axes, i.e. provides what is known colloquially as a tip-tilt motion. The triangleRD design shown in Figure. 5.12 produces angular deflections about three axes and emulates what is colloquially known in optics as a tip-tilt stage. This action on a spherical mirror produces the same results to a beam as the linear translation stages discussed above. The specific design shown in Figure. 5.12 utilizes a large Orthoplanar spring embedded into a metal mount plate. The angular deflections are created by applying a normal force directly to the larger portion of the flexure arms. As with the linear translation stages, the motion can be achieved by using a set screw, piezo actuators, linear stepper motors, or some combination of the three. The expected

range of motion of this design is greater than 1 mm of deflection from each arm.

5.3.3.3 Finite Element Simulations

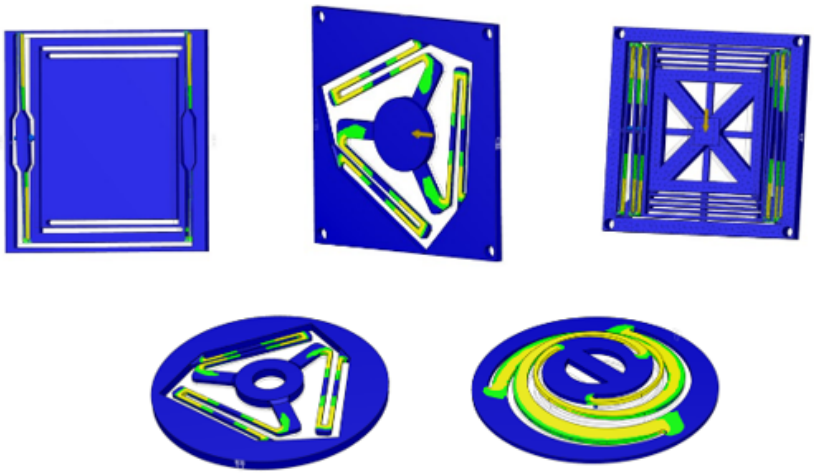

Figure 5.13: Graphics of the simulation results of various flexures. The numbers for the results are provided in the text and in Table. 5.5. Here we can see that most flexures experience stresses along the bending legs or beams, this is expected. Yellow indicates high amounts of stress while blue indicates no stress.

Prior to printing and physically testing the flexure structures, finite element analysis simulations were conducted to confirm the expected range of motion. The simulations were conducted to determine the flexures range of motion and the expected safety factors the flexure will exhibit when placed under stress (example graphics of the simulation results for stresses and safety factors are shown in Figure. 5.13). Results of the simulations for each flexure are shown in Table 5.5.

The goal with the simulations was to calculate the resulting safety factor (SF) and stress that results from meeting the displacement requirements of at least 500 µm with a safety factor of 1.2 or greater[4]. The SF is given by,

[4]Typically in engineering the acceptable safety factor is dependent on the industry but a general rule is 3 or greater for consumer use. For prototyping anything about 1 is acceptable with 1.2 accounting for inaccuracies in the finite element simulations.

$$SF = \frac{(\text{Yield stress})}{(\text{Working Stress})}. \tag{5.9}$$

The simulated translation capabilities of the orthoplanar spring is quite limited as it is quite stiff and a 30 mm diameter spring is only capable of achieving the desired displacement if its material is Ti6Al4V, (displacement 1.5 mm, max stress 686.5 MPa and a SF of 1.3). However, the Invar 30 mm spring can only produce 0.4 mm displacement with a max stress of 222.3 MPa with a SF of 1.1. The orthoplanar spring, although quite stiff, is resistive to radial forces. However, to be practical for this application it must have a relatively larger diameter (i.e. 60 mm vs 30 mm) or be made out of a high yield strength, but high thermal expansion material such as Ti6Al4V. Nonetheless, the triangleRD is based on an orthoplanar spring and performed reasonably in the simulations. The results in Table 5.5, are for a 65 mm orthoplanar spring made of Invar and has a displacement of 2 mm when the force is applied to the center but 2.5 mm when applied to one of the legs of the spring cause a tilting action. These meet the displacement requirement and have reasonable safety factors of 1.1 and 1.5, respectively.

The simulated Oxford spring linear displacement capabilities exceed those of the orthoplanar spring. For a 30 mm diameter spring made of Invar, it can produce a displacement of 1.2 mm with a max stress of 203.1 MPa and a SF of 1.2. Therefore it meets the displacement requirements and is used in the fourOxford and twoOxford flexures.

The translation stages based on radiator arm bending actions performed quite well in the simulations. The 4armRadiatorTS achieved a maximum displacement of 3.5 mm and 1.2 mm for the horizontal (X) and vertical (Y) axis, respectively. The SF of the 4armRadiatorTS is 1.6 and 1.5 for the X and Y axis respectively. The singleArmTS as met the requirements for displacement, having a simulated displacement of 1.78 mm and 1.17 mm in the X and Y axes, respectively. Again, the SF is suitable in each axis, 1.5 and 1.4, for X and Y, respectively.

5.3.3.4 Testing and Results

The flexures are tested within their nominal range of motion and stiffness[5]. Nonetheless, the results of these tests are useful to assist with the decisions required for selecting final flexure components. The test apparatus used to conduct the load testing of the flexures is shown schematically in Figure 5.14 with photos taken during testing shown in Figure 5.15. It consists of a direct current stepper motor, that rotates the lead screw of a linear translation stage. The

[5] Some of the flexure devices are heat treated prior to testing which will reduce the intrinsic stresses present in the flexures. However, the final monolithic chassis could not be heat treated and therefore many of the flexures tested are not heat treated.

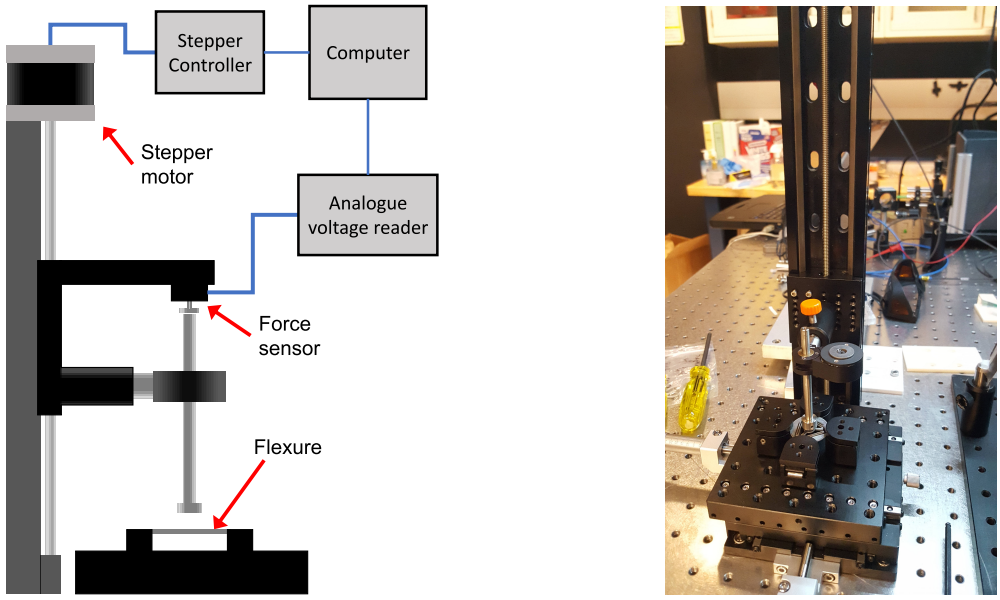

(a) (b)

Figure 5.14: (a) Schematic of the load test setup. A stepper motor is used to move a rod down towards the flexure which resists the motion, this applies a force that is measured by the force sensor. The stepper motor moves to set displacements and the force sensor records the force as an analogue voltage at the given distances. A computer interprets the voltages and converts it to force values. (b) Photo of test setup in lab.

linear translation stage is equipped with holders that can apply a force to the desired flexure. The force is read by a modular load cell placed within the holding system. The force sensor provides a voltage as a readout which was collected and logged using a National Instruments USB-6211 DAQ. The stepper motor actuated translation stage has a calculated step size of approximately 2 µm which allows highly precise control over the applied displacement. Using the steps/mm constant, the force vs displacement relationship can be calculated. This in turn can be used to calculate the spring constant of the flexure, given by Hooke's Law,

$$k = |F|/|x|, \tag{5.10}$$

where $|F|$ is the magnitude of the force and $|x|$ is the magnitude of the displacement. From this relation k has units of N/m and is indicative of the stiffness of the flexure.

Results of the load testing are summarized in Table 5.5, selected force versus displacement curves shown in Figure 5.16. The simulation results from the finite element analysis are also

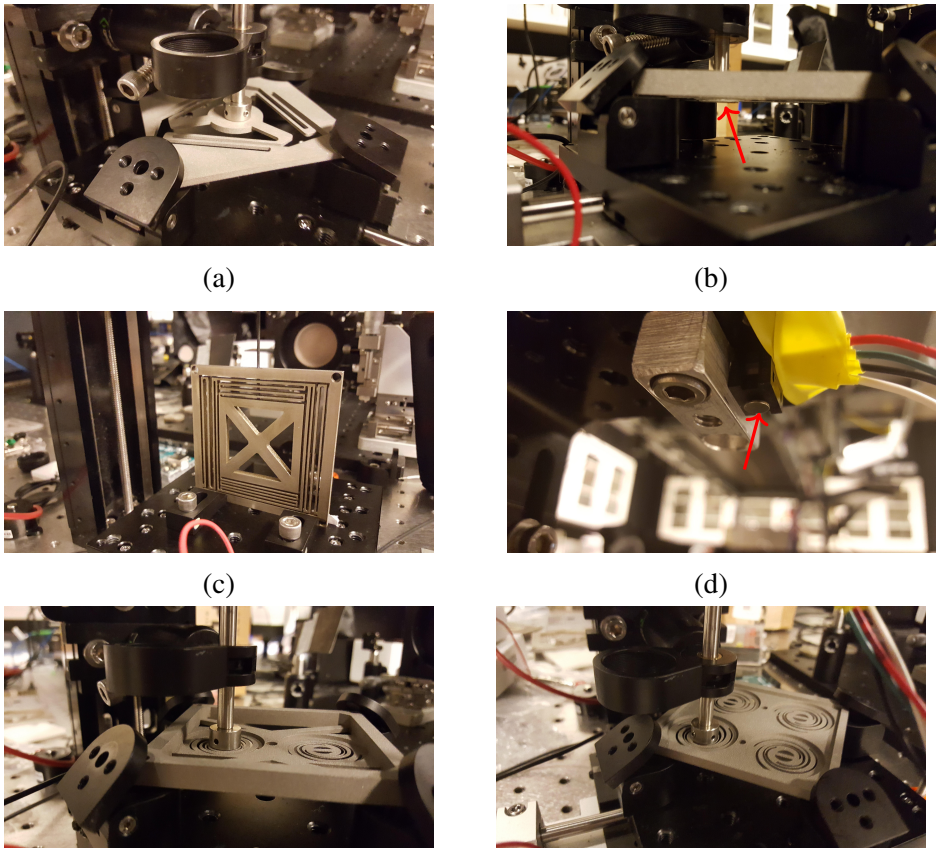

(a) (b) (c) (d) (e) (f)

Figure 5.15: (a) triangleRD under load test. (b) twoOxford under load test showing flexure displacement as indicated by the red arrow. (c) 4armRadiatorTS under load test. (d) The force sensor used, indicated by the red arrow. (e) twoOxford under load test. (f) fourOxford under load test.

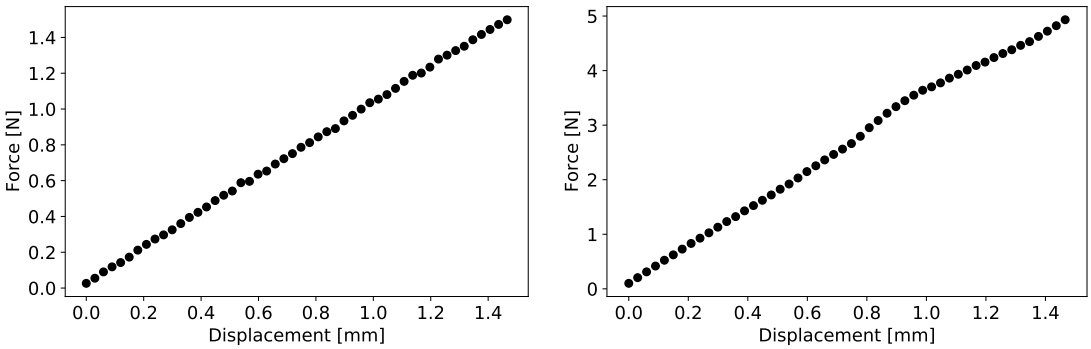

(a) (b)

Figure 5.16: Force measured by the force sensor based on the displacement of the flexure for up to 1.5 mm translation of the twoOxford (a) and 1.5 mm tilt of the triangleRD (b).

provided in Table 5.5 for direct comparison. The maximum force is calculated from the output voltage of the sensors. Note that some of the flexures (indicated with an asterisk) were not tested in their proper configuration. Specifically, flexures that have displacement in the horizontal plane were not designed to resist or compensate for the load of gravity. Hence some of the flexures displacement range appears smaller than the simulation due to the starting position already having been slightly displaced due to gravity.

The results in Table 5.5 indicate that the printed flexures agree with the simulation results in terms of possible displacement. Therefore, confirming that the printed materials behave similarly to the simulation of bulk material. Thus, the simulations can be used to modify and validate the designs without the need for creating several testing prototypes beyond some final candidate structures. More importantly, the results in Table 5.5 allow for the performance of each flexure to be directly compared, which facilitates the decision of which flexures to pursue. It should be noted that only two flexures experienced plastic deformation due to errors were the stepper motor drove the applicator rod too far beyond the intended range of motion (orthoplanar-Invar). While the other flexure had plastic deformation already present due to the manufacturing process (singleArmTS). Furthermore, the singleArmTS was printed thinner than the design and thus experienced poor performance. Beyond these incidents, there were no visible effects or observable plastic deformations present in any of the flexures tested. This indicates that the printing parameters for the Invar36 powder are satisfactory to emulate the bulk material. In Table 5.6, a qualitative evaluation of each flexure is presented listing the advantages and disadvantages of each design, with some additional comments for the reason behind their selection choice.

Table 5.5: Quantitative results for the flexure tests. The simulation displacement, minimum safety factor, and simulation max stress are results obtained from the finite element analysis. The max applied force, real displacement, and spring constant are obtained from the experimental data.

Flexure Name	Simulated Displacement [mm]	Minimum Safety Factor	Simulation Max Stress [MPa]	Max Applied Force [N]	Real Displacement [mm]	Spring Constant [N/m]
Orthoplanar-Ti (30mm diameter)	1.5	1.286	686.5	8.7	1.0	5300
Orthoplanar-Invar (30mm diameter)	0.4	1.08	222.3	0.28	0.5	630
Oxford-Invar (30mm diameter)	1.2	1.184	203.1	0.88	1.2	770
triangleRD (60mm diameter)	Center = 2.0 Tilt = 2.5	Center = 1.125 Tilt = 1.510	Center = 202.3 Tilt = 160.5	Center = 9.94 Tilt = 4.93	Center = 2.0 Tilt = 1.5	Center = 5260 Tilt = 3360
fourOxford (30 mm diameter)	1.2	1.184	203.1	1.45	1.5	1007
twoOxford (30mm diameter)	1.2	1.184	203.1	1.49	1.5	1010
singleArmTS	x= 1.78 y= 1.17	x= 1.493 y= 1.442	x= 160.8 y= 166.5	x= 0.5* y= 0.88	x=0.62* y= 0.65	x=760 y=520
4armRadiatorTS	x=3.5 y=1.2	x=1.589 y=1.524	x=151.5 y=157.2	x=0.88* y=1.6	x=1.8* y=1.5	x=530 y=1070

Table 5.6: Qualitative analysis and comments on each of the flexure types discussed.

Flexure Name	Pros	Cons	Selection
Orthoplanar Spring	Good range of motion. Little effects from radial forces.	Can be stiff, creating extra stress on the material large spring constant (needing robust set screw)	Can be difficult to build vertically, not pursued
Oxford Spring	Smaller spring constant. Large range of motion. Less material stress.	Small restoring force so it is sometimes too easily displaced. Radial forces can have a grave effect.	Complex shape is difficult to manufacture vertically, not pursued.
fourOxford	Provides large range of motion with little force. Four springs reduces effect of radial forces (gravity).	Only one-dimensional motion. Large radial forces can cause sagging issues.	Complex shape makes it difficult to manufacture vertically, not pursued
twoOxford	Large range of motion with little force	Only one-dimensional motion. Effects of radial forces are significant.	Complex shapes, not pursued
4armRadiatorTS	Large range of motion. Motion in two dimensions. Low spring constant.	Sagging occurs slightly in the vertical direction though can be prevented with set screws	Multiple overhangs make it difficult to manufacture with AM, thus not pursued
singleArmTS	Good range of motion. Little to no out of plane motion.	Small arms can be easily plastically deformed	Pursued due to ease of manufacturing
triangleRD	Good range of motion (3axis). Robust and stable. Not affected by radial forces.	Stiffness Large force	Pursued

In addition to the single load tests, some flexures were chosen to undergo repeated cycle testing in order to infer a lifetime performance of the components. The lifetime cycles of each component may vary, and depending on the printing parameters used, may vary over the same device. The same setup (Figure 5.14) is also capable of performing repeated load tests where the maximum load is repeatedly applied to the flexure. This is conducted on select flexures with varying number of cycles per test. Results for these tests are shown in Figure 5.17. Although the repeated load tests are interesting, no conclusions were drawn from the results because in practice, the flexures would not be used under repeated maximum load. Furthermore, typically devices manufactured using AM are heat treated after the build process, this was skipped for these structures and therefore residual stresses from the manufacturing process might still be present in the material. The residual stresses are a possible explanation for the drop then leveling of the restoring force in Figure 5.17. Nonetheless, further investigation into the repeated load results are beyond the scope of this study and for future research.

5.3.3.5 Final Flexure Design

The optomechanical flexures presented in the above functioned well and performed appropriately. However, the designs are not easily manufacturable using additive manufacturing techniques. The reason is that there are several locations with overhanging features in the designs that need to be supported during the manufacturing process. Particularly, in laser powder bed fusion (LPBF), any overhang that is at an angle less than 45° to the horizontal must be supported by solidified material, or support structures, underneath it for facilitating heat transfer, for avoiding part warping or curling, and for ensuring mechanical anchoring to the substrate. For instance, the 4armRadiatorTS and singleArmTS designs have several arms that are not supported by any support structures underneath and thus would not be suitable for creating a monolithic design as many temporary support pillars would need to be created during the build process (Figure 5.6). However, the other flexure designs presented also had similar overhanging material or very small intricate structures that are not easy to consistently produce. Thus a new design was required and is inspired by the singleArmTS and the 4armRadiatorTS.

The final solution for the flexure is a device that is to be built upright and have a range of motion that is sufficient to align theCM of Offner relay. The range of motion was determined using Zemax simulations and was found to be at most 3 mm translation along the optical axis of the curved mirror and 1.5 mm in each of the two orthogonal axes that are perpendicular to the optical axis. If placement of the fixed optics in theORI is sufficiently accurate than the requirements for the range of motion of theCM is reduced. With these requirements considered a final flexure design is implemented utilizes a similar design to the singleArmTS and 4armRadiatorTS.

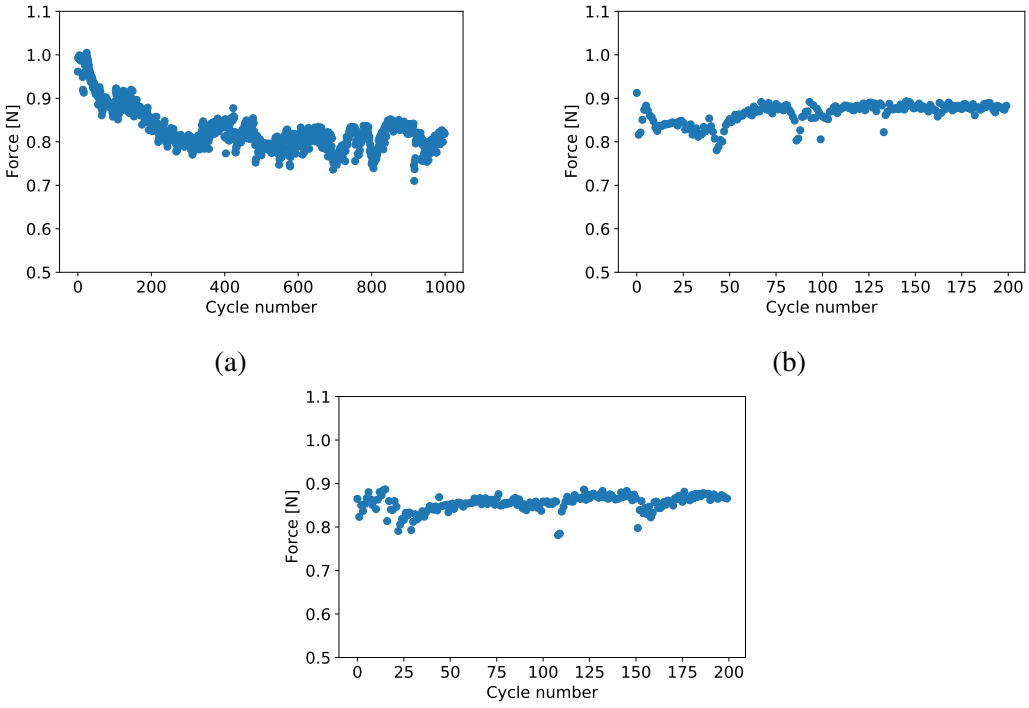

Figure 5.17: Repeated cycle tests on the fourOxford translation stage. Note the drop in the restoring force seen in (a). This could be caused by the release of residual stresses that were present in the material after the manufacturing process. (b) and (c) are tests taken at a later and do not show a further drop in the restoring force, but rather a convergence of the restoring force value.

The finalCM flexure design (called TSK-45) takes the concept of the singleArmTS and rotates it by 45° such that none of the flexure arms are at an angle that is less than 45° with the horizontal (Figure 5.21). This eliminated the need for a significant number of support structures as none of the long flexure arms needed to be supported directly during the build. The rotated singleArmTS provides the required motion in the plane perpendicular to the optical axis of theCM. Two set screws are used to induce the translation in this plane by pushing against the center plate while the bending beams act like springs. The translation along the optical axis is provided by four arms that are attached to the stationary backplate of the TSK-45 and the other side is attached to the rotated singleArmTS. The rotated singleArmTS is effectively floating, save for the four attachment flexure arms. The stiffness of these arms dictates the relative range of motion of along the optical axis. COMSOL® [163] simulations were used to predict mechanical stress at maximum displacement. Considering the yield strength of bulk Invar36 (276 MPa), a safety factor of no less than 1.3 was targeted in order to remain within the elastic regime of the flexure.

The motion along the optical axis is controlled by five set screws that need to be adjusted in unison. The five set screws are located with four placed one at each corner diamond shape, while the fifth set screw is placed at the center of the backplate. The five set screws can provide both a linear translation by the "master" set screw in the center, and angular "tip-tilt' motion by the four set screws on the corners (Figure. 5.18).

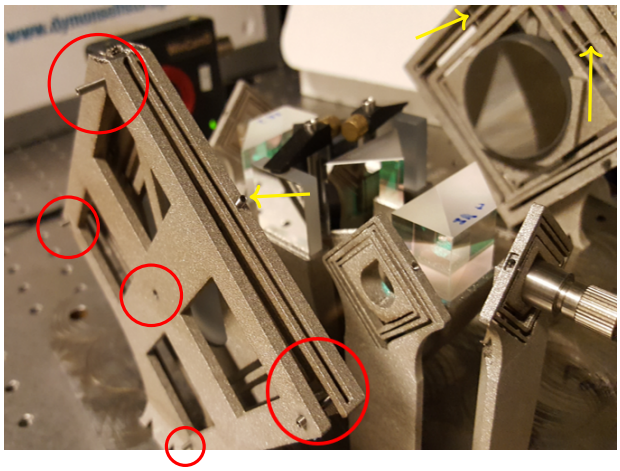

Figure 5.18: Set screws that provide the motion for the TSK-45. The four on each corner and "master" screw on the back are indicated with the red circles. The yellow arrows indicates location of the set screw that move the TSK-45 in the plane perpendicular to the optical axis of theCM.

TheCM is supported by a slot that extrudes from the center plate of the TSK-45 and is secured

by in place by set screw as shown by the red arrow in Figure. 5.19. The extrusion is supported during the build by a chamfer and a small number of temporary supports Figure. 5.20. These supports are attached strategically in order to allow access for the minimal supports that are required for the base of the rotated singleArmTS portion of the TSK-45. The base of the moving portion of the TSK-45 is modified to ease the placement of supports while at the same time reducing the number of temporary support structures required. This is achieved by a triangular notch cut out of the base that created two flat pieces that the supports were attached to Figure. 5.20a. These supports were angled such that they protruded forward from the center plate and did not interfere with the rest of the structure. Other design considerations that influenced the shape of the TSK-45 are to reduce the amount of material used in the build process, and the reduction of excessive heating of the structure. To reduce the amount of material used, sections in the back plate of the TSK-45 are left empty, see Figure 5.21b, and material was removed where deemed unnecessary. To decrease the amount of excess heating, the base of the TSK-45 has a saw-tooth shape which reduces the heating effects that occur at the junction with the base plate.

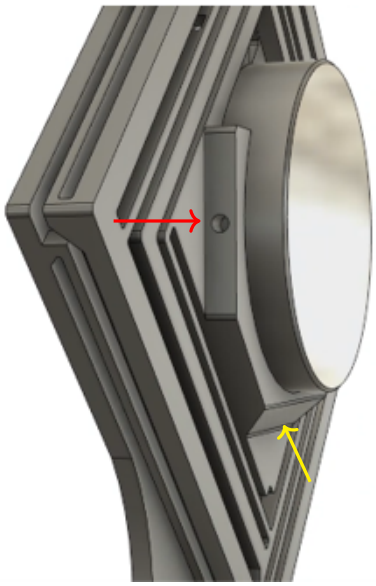

Figure 5.19: Set screw to hold the curved mirror in place (red arrow). The chamfer that allows the extrusion to be built is also visible (yellow arrow).

Overall the monolithic flexure device TSK-45, shown in Fig. 5.21, although ultimately designed considering the advantages and limitations provided by additive manufacturing, still provides at minimum the required 3 mm translation along the optical axis of the curved mirror and 1.5 mm in each of the two orthogonal axes that are perpendicular to the optical axis. The flex-

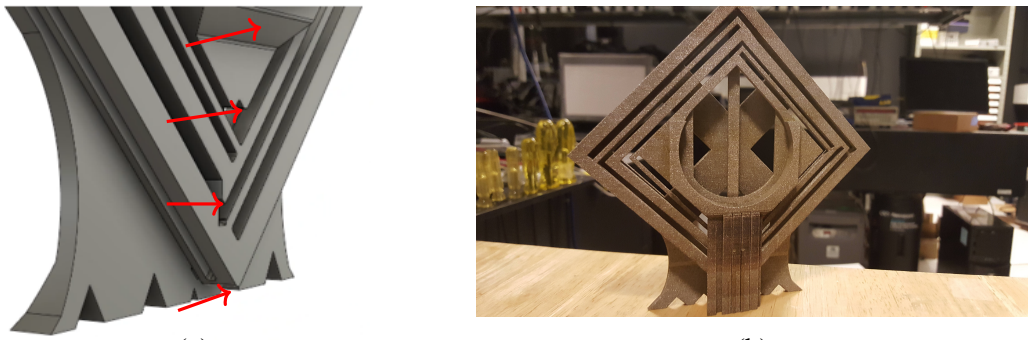

(a) (b)

Figure 5.20: (a) Support attachment points for the TSK-45. (b) Supports shown on a prototype TSK-45.

ures surprisingly had a much larger range of motion $>$ 5mm along the optical axis while still remaining in the elastic (flexure) regime. This can be explained by a difference in the bulk material properties compared to the fused powdered version of the same material used in AM. This suggests that yield strength of the material is a function of powdered metal properties and AM process parameters.

The range of motion is measured experimentally and in each axis the motion is reproducible. Figure. 5.22 shows the displacement and some movement data of the TSK-45. Note that the range of motion tested is well under the specified range of motion of the flexure, maximum tests were not conducted due to the risk of damaging the flexure. However, despite the small displacements, the TSK-45's range of motion was more than enough to properly align the interferometer.

The long-term stability of the TSK-45 is tested using the setup shown in Figure. 5.23. A laser beam is sent to strike a mirror being held by the TSK-45 and is directed to a camera that records an image of the spot as a function of time. The images are taken over twelve hours. The centroid of the laser spot on the camera is determined by fitting a 3D-Gaussian function to the intensity data of each image. The centroids of these Gaussian functions are then analyzed for the standard deviation and maximum displacement of the spot. The standard deviation is indicative of how stable the spot was over the twelve hours, while the maximum displacement indicates range of motion of the displacement.

A stand-alone TSK-45 (i.e. not a part of a monolithic chassis) made via AM using Invar36, shows a standard deviation of 0.9012 µm and 2.6395 µm in the horizontal and vertical plane respectively. Compared to a standard Thorlabs optomechanical mount (KM200PM) that experience a standard deviation of 0.7625 µm and 1.1491 µm in the horizontal and vertical plane. It should be noted that the TSK-45 is not fixed to any structure but held in place by standard

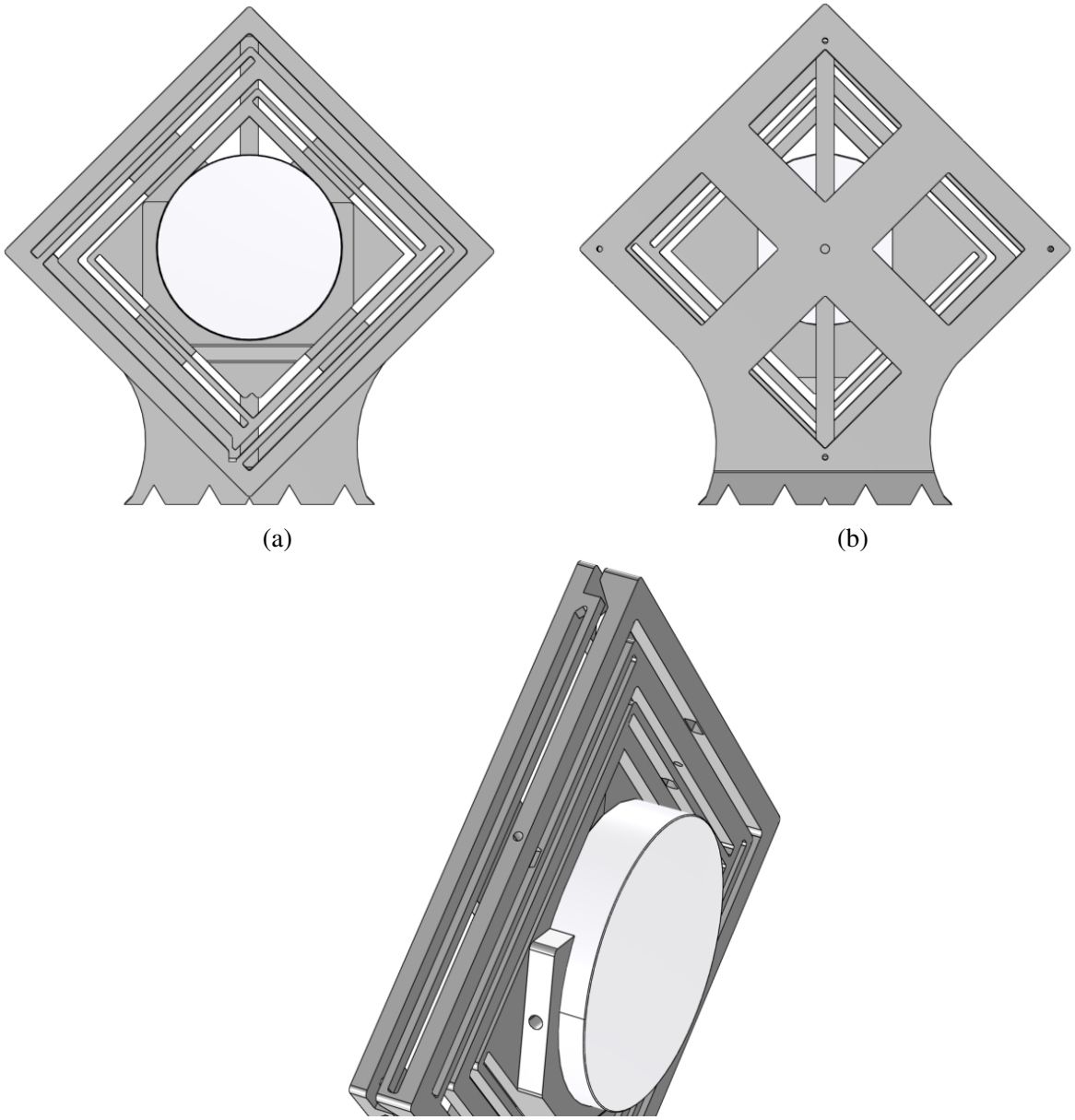

(a) (b)

(c)

Figure 5.21: Monolithic TSK-45 for alignment of the folded Offner relay. The curved mirror rests in the TSK-45 device and set screws push on the structure that is held by the flexure arms. The close up image (c) shows the single beam connection between back plate and the front of the TSK-45.

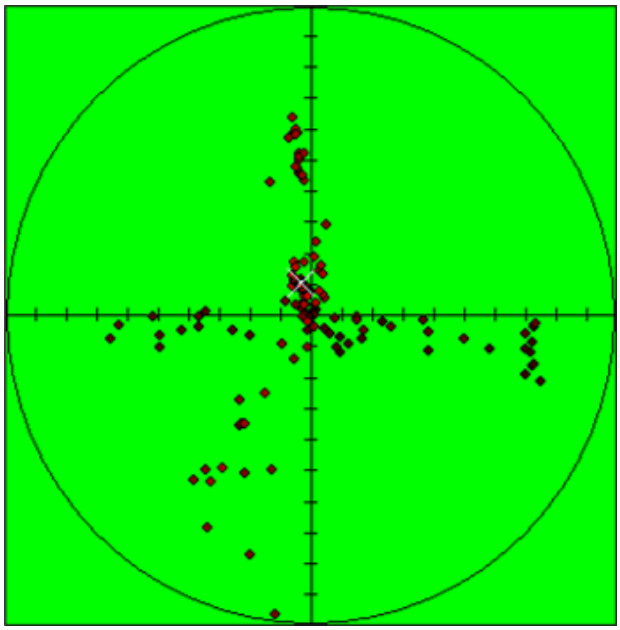

Figure 5.22: Results of the TSK-45 stability tests. The circle radius is 280 µm which each dot representing a location where the optical beam's center was recorded. The largest displacement recorded here is 274 µm, however, larger displacements are easily achievable. These displacements are done by adjusting the setscrew on the back of the TSK-45 by hand. The maximum possible displacement achievable by the TSK-45 was not recorded in order to avoid the risk of damaging the system prior to the completion of the other tests.

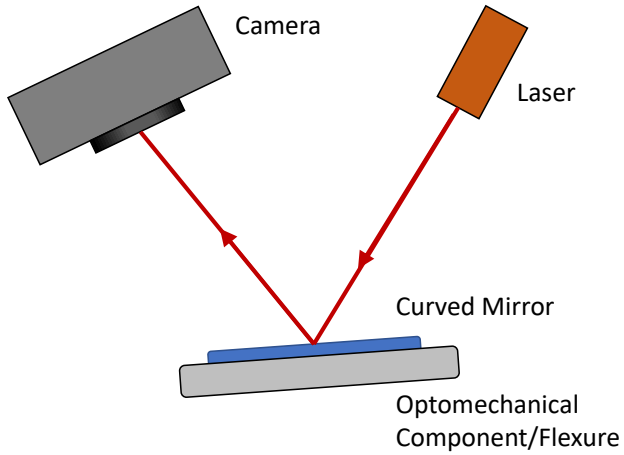

Figure 5.23: Long term stability test setup. The reflection of a laser source off of the curved mirror is measured using a camera. The centroid of the measured beam spot is tracked as a function of time to determine the long-term stability.

Table 5.7: Data of 12 hour stability tests. Here x indicates the horizontal plane while y indicates the vertical plane. All values are in micrometers.

Part	STD-x	STD-y	Displacement-x	Displacement-y
KM200PM	0.7625	1.1491	4.4670	6.6543
TSK-45	0.9012	2.6395	3.3354	9.9608

optomechanical clamps and thus the larger deviations could be due to slipping of the clamps. Additionally, the range of motion of the TSK-45 was larger than expected, meaning that the stiffness of the flexure arms is reduced compared to the bulk material. Thus, the TSK-45 could experience much more sagging than expected as a result of the reduced stiffness. In fact, the centroid of the spot did move down over the course of the twelve hour test, thus pointing to the reduced stiffness as a plausible cause for the high displacement. Nonetheless, the results are quite promising since the TSK-45 is made of a low thermal expansion material using AM, and is a monolithic structure, yet still performs similar to a standard optomechanical part. A summary of the results is provided in Table. 5.7, including the maximum displacement in each plane.

5.3.4 Monolithic Chassis (PORI)

The Printed Offner relay interferometer (PORI) is the combination of theORI design, the optomechanical flexures, and a monolithic structure for holding the optics. This combination went through several iterative designs and failures before a final design was achieved. Figure. C.1 shows the final dimensions of the PORI. Some offsets were introduced into the dimensions as to allow for printing accuracy errors to be corrected by the range of motion of the flexures. For example, the TSK-45's that hold theCM in place were placed 500 µm further back from their ideal position. The ideal position would then be found by displacing the TSK-45 flexure. Some tolerances were also provided in the pocket dimensions as well as for most dimensions of the PORI. Dimensions that needed tighter tolerances given a 0.25 mm tolerance, while those with looser tolerances have a 0.3 mm tolerance. Those familiar with computer numerical control lathes will note that these tolerances are quite large. However, this is due to the resolution of the LPBF machine (Renishaw AM 400) that is around 100 µm. In addition, optical elements can also have minor manufacturing tolerances that will need to be compensated for when placing the optics. Input and output flexures for fiber coupling the input and output of theORI were designed based on the TSK-45, as seen in Figure. 5.29. These flexures however, only needed to provide motion in the plane perpendicular to the optical axis, i.e. xy-plane.

The structure that holds the stationary optics and supports the pockets for the central optical elements is also build using AM and is part of the monolithic structure. This structure also provides support for the input and output flexures. The original proposed design was to use a flat tabletop with the pockets build into the surface. As discussed in Sec. 5.3.1, a flat tabletop would require structural support underneath in order to avoid a build failure.

The first proposed design is to build a lattice structure that supports the flat top. This would take advantage of the capabilities of AM by building a structure that standard manufacturing techniques could not produce. In addition lattices ease the depowdering of the structure after the build. A Voronoi lattice design is shown in Figure. 5.24a. The Voronoi structures have the potential to help with vibration damping [164]. Although the build setup was simulated in Fusion 360 using relevant LPBF process parameters, it is difficult to simulate lattices accurately in large and complex structure due to challenges related to computational time and accuracy involved. Therefore it was not feasible to properly simulate the Voronoi lattice structure. Additionally, since AM latticing software do not readily incorporate LPBF design guidelines while generating lattices structures, there were numerous areas with large overhanging regions. These regions lead to a build failure as shown in Figure. 5.24b, and a shift from pursuing Voronoi lattices as a viable support solution.

The second lattice structure considered is known as a Gyroid lattice [164] as seen in Figure. 5.25. The Gyroid lattice has less complex structures though could still not be properly

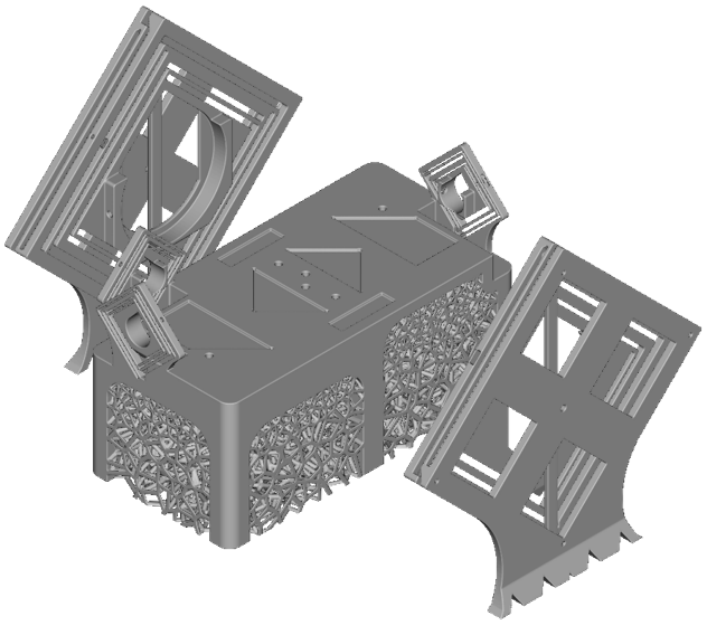

(a)

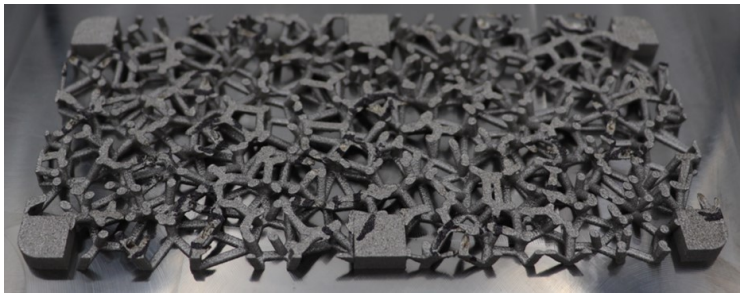

(b)

Figure 5.24: (a) Voronoi lattice supporting the central tabletop. (b) Failed build attempt of the Voronoi lattice.

generated by the AM software and thus there were still regions with large overhangs. Although the build was more successful that with the Voronoi lattice, it still failed since the large top structure of the flat top is quite a significant area to build using AM as seen in Figure. 5.25b and Figure. 5.25c.

The second proposed solution for supporting the flat tabletop is to use the typically temporary support structures as permanent supports. The choice of support structure is important since most auto-generated structures produced by the specialized additive manufacturing software (Renishaw QuantAM) are meant to be temporary. Nonetheless, thick grid supports are used and placed under the flat top. The use of the grid support structure ensured that the plinth setup printed successfully as shown in Figures. 5.26. The overall volume of the supports reduced the required number of layers and thus the build time. However, there were issues with powder accumulation and storage on the Renishaw AM 400 LPBF system which led to a print failure as can be seen Figure. 5.26b and Figure. 5.26c. Since the plinth design created transition from printed layers of low cross-sectional area to layers with a high cross-sectional area suddenly, while being manufactured, it was challenging to control the powder dosage and flow in the system during the 36-hour print, as it can only be done manually. This resulted in powder dosing shortage and ultimately a build failure.

5.3.4.1 Loft Island Design

After the failures of the three previous prints a complete redesign of the chassis was done. Since all the previous designs involved the use of a plinth structure that resembles a tabletop, which has a severe jump in surface area from the supporting structures underneath, it created a major challenge of monitoring and changing the powder dosage and flow. This challenge supersedes all benefits of the lattice or grid support design. The team hence decided on pursuing a approach to merge the worlds of what had been designed and what would be easily manufactured using AM. This led to a complete overhaul of the entire central plinth design. The result is called the loft island design shown in Figure. 5.27. Effectively, the loft island design is inspired by the lessons learned from the previous failures. The lessons learned are as follows; first, the structures that require a large amount of powder are more likely to cause issues during the build. Second, large transition in surface area, e.g. supports to a tabletop, can cause issues with powder flow and thus a build failure. Finally, altering the design to suit additive manufacturing is important, see Sec. 5.3.1.

The loft island design takes advantage of the abilities of AM. In order to reduce the required powder of the tabletop the loft islands has three main design features that achieve this. The first is that the the top surface area is redesigned such that it is just sufficient to hold each optical element

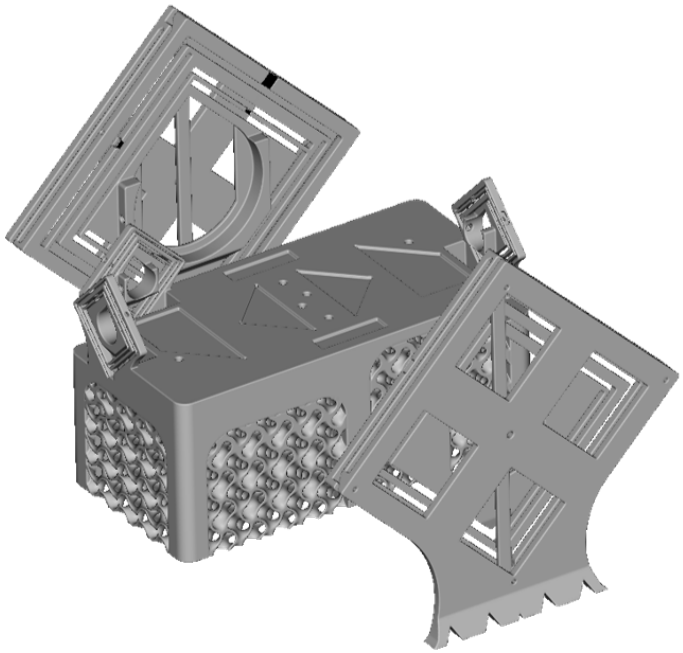

(a)

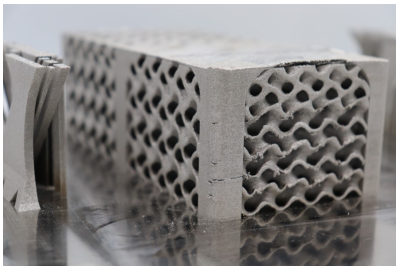

(b)

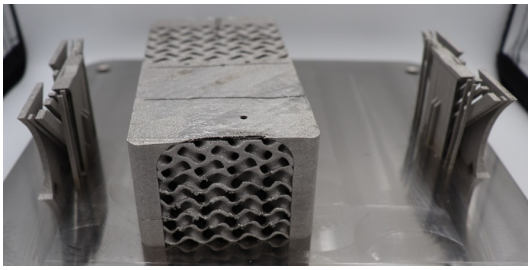

(c)

Figure 5.25: (a) Gyroid lattice supporting the central tabletop. (b) and (c) Failed build attempt of the Gyroid lattice.

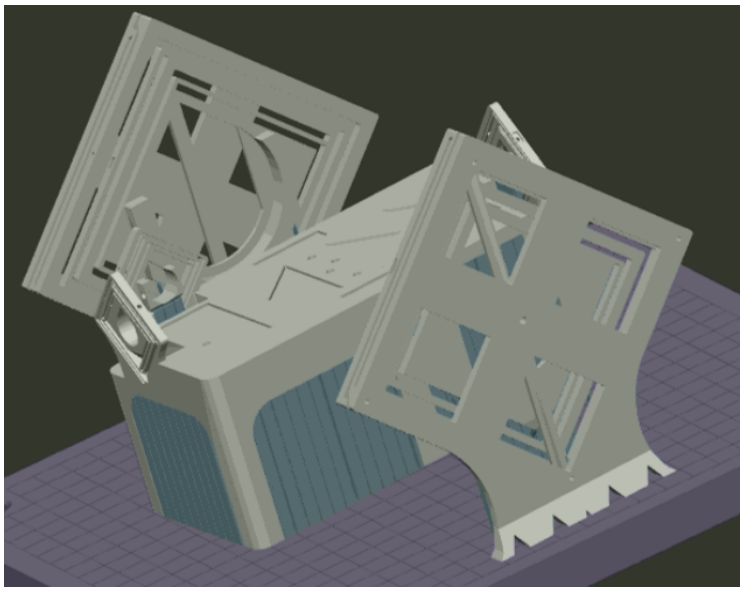

(a)

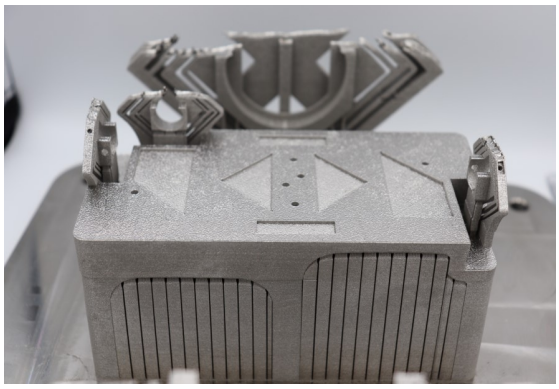

(b)

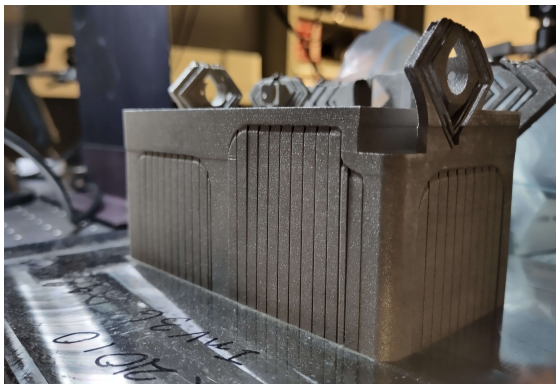

(c)

Figure 5.26: (a) Grid supports used to support the central tabletop. (b) and (c) Failed build attempt of the grid support tabletop system.

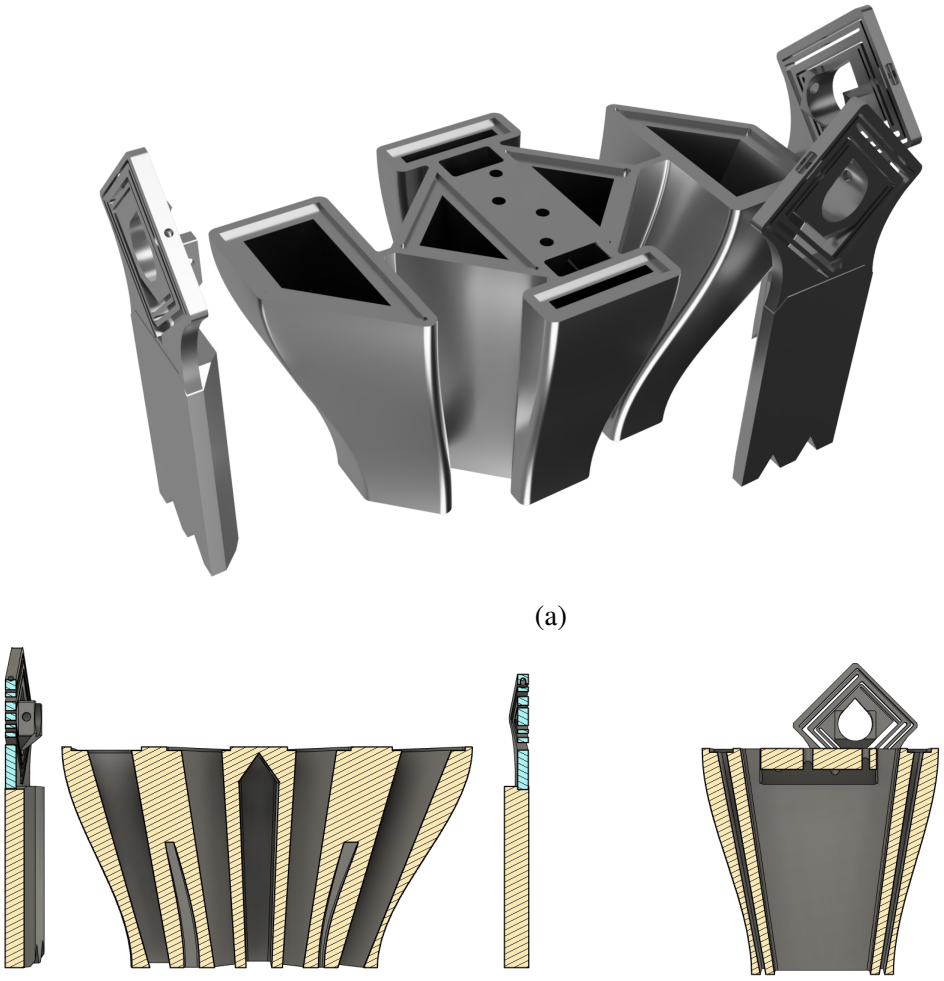

(a)

(b) (c)

Figure 5.27: Loft island conceptual schematics. (a) Render of the loft island design that supports the central optics, including the input and output flexures. (b) and (c) Cross sectional view of the loft island design showing the hollow core of each support structure.

or flexure and no longer has a large amount of additional surface area that is not functional. Second a tapered design is used such that from the top surface of each island, the cross sectional area is continuously scaled down towards the connection with the base plate, except for the ones used for the input and output flexures. Finally, each loft island is hollow except for the ones used for the input and output flexures. This helps with removing the residual powder from the structure as compared to the other lattice techniques.

The center of the loft island design still had a small tabletop component that is necessary to include the holes required to secure the flat mirrors and prism mirrors in place. To avoid any build failures, a chamfer is grow from the loft island walls at an angle of 35° with respect to the vertical, thus well inside the capabilities of AM, that supports the central table top, see Figure. 5.27b. This central portion can be eliminated if the optical elements are epoxied in place and thus not a critical element of the loft island design.

Comments on Design Process Overall the design process that took place to make it to the loft island design is not lost on me. There is certainly a lot of lessons learnt along the way that are not mentioned in this thesis. However, one of the most paramount comments is that designing for additive manufacturing is different than for conventional machining, and furthermore trying to create a monolithic structure in one print presented its challenges. Figure. 5.28 shows the progression of the design process from a concept on the white board to a final design that looks completely different.

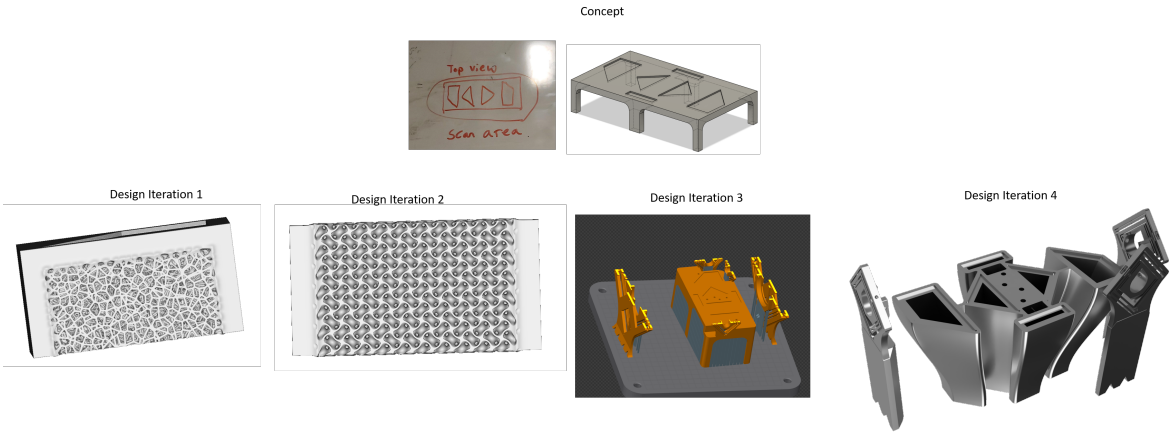

Figure 5.28: Iterations of the design process to achieve a solution that is design for additive manufacturing.

5.3.4.2 Final Structure

The combination of the TSK-45 and the loft island design (Figure. 5.29) is the final design attempted during the timeline of the project. It had a much more successful build as shown in Figure. 5.30. However, despite the attempts at creating a design that countered most difficulties experienced in the previous build failures, the last few layers of the print were not successfully built as shown in Figure. 5.31. This is again due to a similar issue of powder dosage and flow which is challenging to control manually even when the print time is reduced to 20 hours. I have been told from the MSAM team that this last issue, although unexpected, is trivial to address. Unfortunately, due to the project timeline (6 months), budget constraints, and the availability of the LPBF machine, it was not feasible to attempt another build. Nonetheless, despite the missing last few layers, the resulting build was relatively functional, though it did have a noticeable impact on the testing results as is discussed in Sec. 5.5.3. Nonetheless, the loft island chassis presents a promising candidate for manufacturing monolithic chassis with additive manufacturing. Particularly the inclusion of the flexures in the monolithic design, something that has not been previously achieved in the literature and would not be possible to make using standard manufacturing techniques.

5.4 PORI Thermal Results

As mentioned in Sec.5.2, it is paramount for unbalanced interferometers to exhibit thermal stability. Although insulation can partially address impact of thermal fluctuations, allowed temperature tolerance is often much smaller than common engineering materials can achieve. To limit the effects of thermal expansion a low thermal expansion material must be chosen for the additive manufacturing of the monolithic chassis. This material needs to have a low thermal expansion with reasonable elastic properties in order to be used as flexures. The material chosen is Invar36. The reported thermal expansion of the Invar36 is 1.44×10^{-6}. Ideally the entire interferometer, chassis and base-plate would all be composed of Invar. However, due to higher cost of Invar, alternative base plate options were also investigated to see the effect of such configurations.

In order to assess operational feasibility in a thermally fluctuating environment, the thermal stability of the monolithic structure was investigated with steady-state COMSOL® simulations for a temperature range of 20 °C. The relative change in interferometer paths between points of interests (Figure 5.32) and accumulation of mechanical stress was analyzed for three device combinations, Invar36 flexures/Invar36 base, Invar36 flexures/stainless steel base, and Invar36 flexures/aluminum 6061 base.

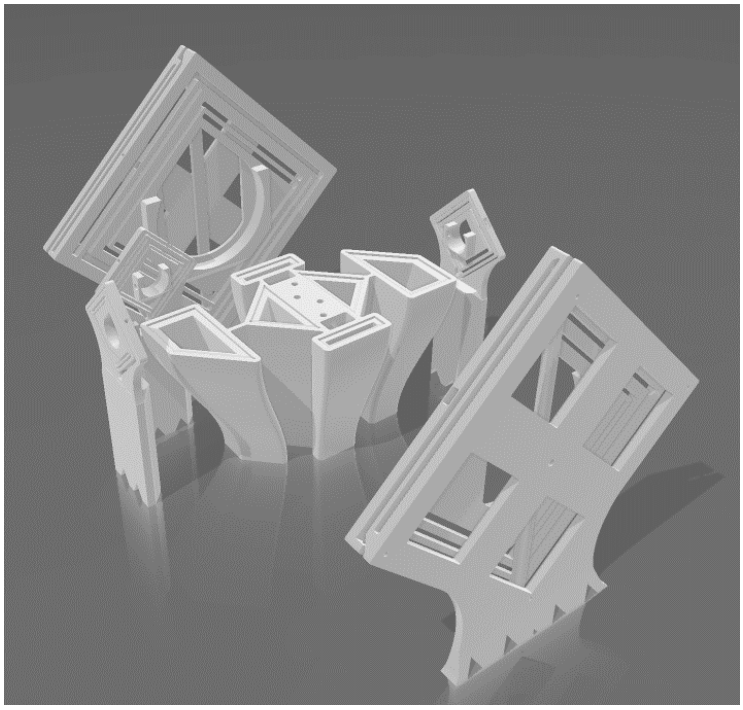

Figure 5.29: CAD image of the final PORI device. The whole design is to be printed in a single pass without any assembly steps beyond taping of the set screw holes. Center island and the flexures are built directly onto the rectangular build plate.

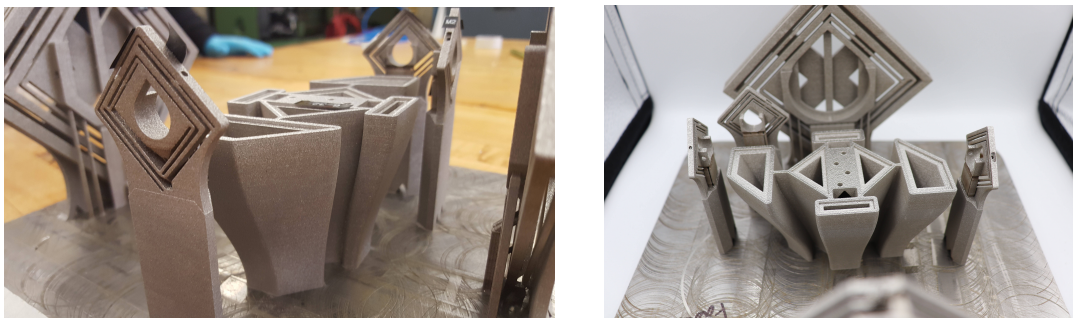

(a) (b)

Figure 5.30: (a) and (b) Loft island design successfully printed in combination with TSK-45.

(a) (b)

Figure 5.31: (a) and (b) TSK-45 incomplete on the final PORI build. The print failed with approximately 4 cm remaining. No further builds were attempted due to the project budget, timeline, and availability of the Renishaw AM 400.

The thermal stability was quantified by measuring the distance a light ray travels for each path of the interferometer (ΔL) compared to design parameters, as well as overall distance change between the two large flexures housing the curved mirrors (Figure 5.32). The path deviations were calculated with a horizontally aligned beam. Hence, only the length in Z and X axis were considered (see Figure. 5.32). In addition to stress buildup at assembly points at the intersection of the base plate and flexures, the overall out of plane deformations were also investigated. The results are summarized in Table. 5.8.

The steady-state simulation revealed that ΔL of the Invar36 base plate setup experiences approximately 3.19 and 12.53 um optical path change for 5 °C and 20 °C temperature change of the chassis, respectively. This deviation from the design parameters corresponds to 1.27 (4.8λ @ 800nm, 2.5λ @ 1500nm) and 4.18 (15.6λ @ 800nm, 8.3λ @ 1500nm) fs increase in the path delay for 5 °C and 20 °C temperature change, respectively. No out of plane deformations were observed as expected. Mechanical stress build up was present but trivial due to matching expansion coefficients of the base and flexures. The mechanical stress at the base plate-flexure joints was in the millipascal range even for the 20 °C temperature change.

In the case of stainless steel (SS) base plate, divergence from design parameters, stress buildup, and warping was significant. The δL of the interferometer was approximately 29.4 and 95.9 µm for 5 °C and 20 °C temperature change, respectively. This corresponded to a deviation in the difference in the path delay corresponding to 9.79 (36.7λ @ 800nm, 19.6λ @ 1500nm) and 31.95 (119.8λ @ 800nm, 63.9λ @ 1500nm) fs for 5 °C and 20 °C temperature change, respectively. Out of plane deformations were also significant, causing 0.80 µm relative

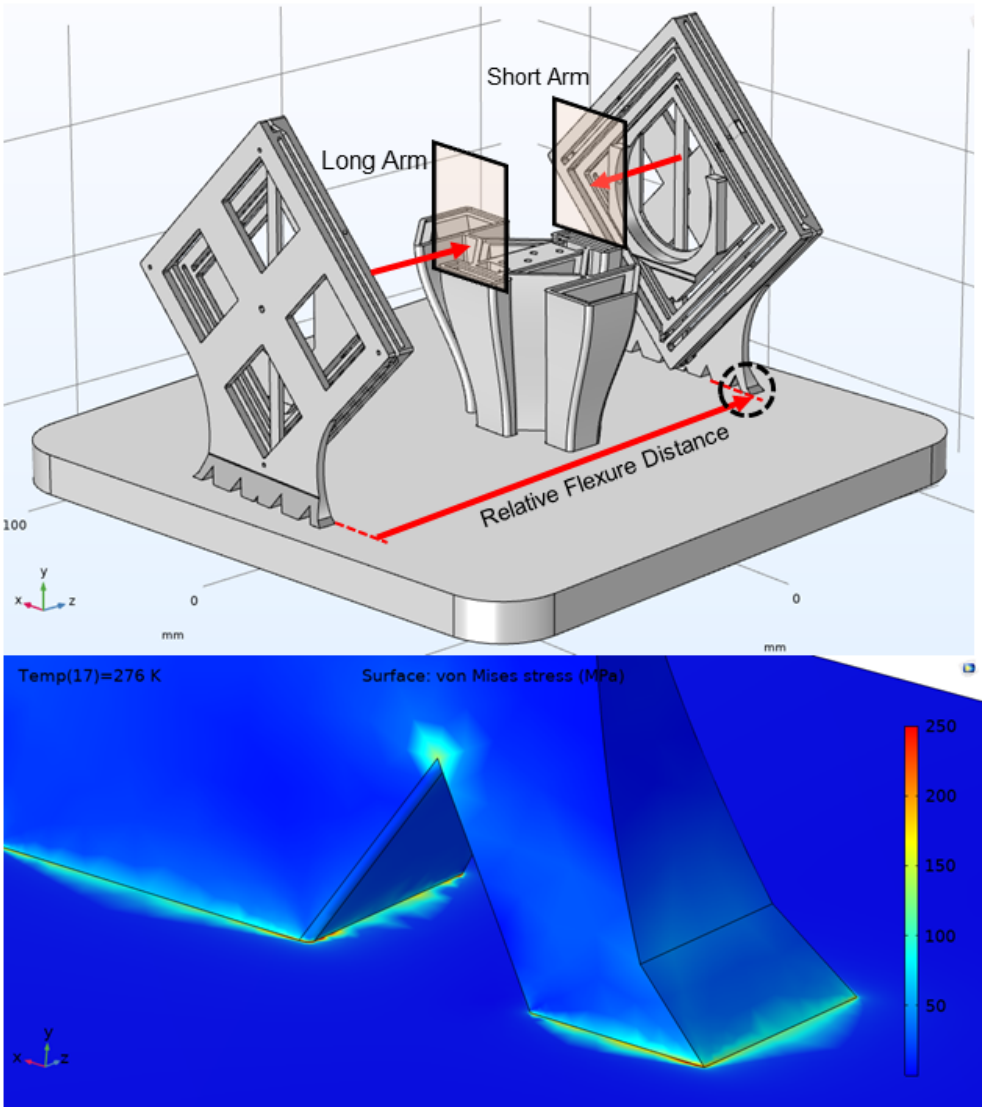

Figure 5.32: Dimensional stability of the PORI chassis under changing temperature conditions was quantified by measuring the change in distance at the long arm, short arm, and between the large flexure (top). The stress buildup at the base plate/printed TSK-45 joint (indicated by the dashed circle in the top image) can surpass materials yield strength at sufficiently high temperature changes (26 °C) (bottom). Figure created by Dr. Dogan Sinar and used with permission.

Table 5.8: Results of the thermal expansion simulations of the PORI for an Invar, stainless steel (SS), and aluminum base plate. The resulting phase shift is represented in terms of the number of wavelengths at 800 nm and at 1550 nm.

Metal	Δ T [°C]	Δ L [μm]	Delay change [fs]	λ @ 800nm	λ @ 1500nm
Invar	5	3.19	1.27	4.8	2.5
Invar	20	12.53	4.18	15.6	8.3
SS	5	29.4	9.79	36.7	19.6
SS	20	95.9	31.95	31.95	63.9
Aluminum	5	93.8	31.26	117.2	62.5
Aluminum	20	303.5	101.18	379.4	202.4

warping between the lateral beam displacers and approximately 0.63 µm warping for the large flexures compared to initial base plate plane, for a 5 °C temperature change.

To compare the above two base plate alloys to a standard optical breadboard, aluminum (6061 alloy) is investigated. The ΔL of the interferometer was calculated to be approximately 93.8 and 303.5 µm for 5 °C and 20 °C temperature change, respectively. The change in the difference in the path delay is 31.26 (117.2λ @ 800nm, 62.5λ @ 1500nm) and 101.18 (379.4λ @ 800nm, 202.4λ @ 1500nm) fs for a 5 °C and 20 °C temperature change, respectively. Out of plane deformations were 1.67 µm relative warping between the beam displacers and approximately 0.93 µm warping for the large flexures compared to initial base plate plane, for a 5 °C temperature change. Evidently, the path length deviations for stainless steel and aluminum base plates are too large to preserve the phase stability of the interferometer, while warping would cause the beam to go out of alignment. As expected from the warping behavior, stress buildup at the attachment boundary layer between the SS (aluminum) base plate and Invar36 flexures were high, reaching approximately 98.8 MPa (148.7 MPa) at the attachment points for only a 5 °C temperature change. For a larger change in temperature (17 °C), the stress buildup reaches the yield strength of Invar36 (276 MPa) which would lead to a failure of the system. Considering the imperfect joint between the base plate and the 3D printed structures, the chassis would be expected to fail before a temperature change that reaches this magnitude.

5.5 PORI Optical Results

5.5.1 Visibility

The combination of the monolithic printed enclosure and the Offner relay interferometer (Fig. 5.33) were tested together. To our knowledge, this is the first monolithic interferometer enclosure that includes optomechanical flexures that allow for the alignment of the system. The performance of the combined monolithic system is quantified using a metric called interference visibility. The system was tested with two types of signals, single-mode laser light and multi-mode laser light. The multi-mode light is more representative of the performance of the system during a quantum sensing application because any signal scatters off of the target surface and thus behaves similar to the effect of light passing through a multimode fiber. For both experiments, a continuous wave 785 nm laser was passed through a single-mode or multi-mode fiber before passing through the PORI. A piezo-ceramic actuator was used to vary the path length of one of the PORI paths to observe intensity changes in order to measure the interference visibility. However, in both scenarios the results were difficult interpret due to the vibrational instabilities of the flexure mounts of the curved mirror and therefore the relative phase between the two paths of the PORI rapidly fluctuated during the measurement. Nonetheless, there were periods of relatively stable interference and thus the measured visibility for both the single-mode and multi-mode signals are 0.874 ± 0.026 and 0.894 ± 0.037 respectively, see Fig. 5.34a and Fig. 5.34b. In Fig. 5.34b, the region from 25 s to 30 s is when one of the paths of the PORI is blocked in order to show that the intensity fluctuations are a result of interference and not the laser source. The relatively low visibility performance can be attributed to the flexure instabilities. Nonetheless, the visibility with the multi-mode signals are much greater than with results obtained using a non-field widened unbalanced Michelson interferometer (0.536 ± 0.023, see Chap. 4).

5.5.2 Imaging Demonstration

To demonstrate the practicality of the interferometer, a small imaging demonstration along the lines of those demonstrated in quantum imaging experiments was performed [87], see Fig. 5.35 and Figure. 5.36. A target was illuminated by a continuous wave laser and the scattered light was imaged through the system. The printed Offner relay setup was used to image the target or object while at the same time measure the interference of the signals after passing both arms of the interferometer. This demonstration is of particular importance because it indicates that the system can be used in various scenarios that an uncorrected interferometer could not, because an uncorrected interferometer would not be able to recover the interference. Particularly, an

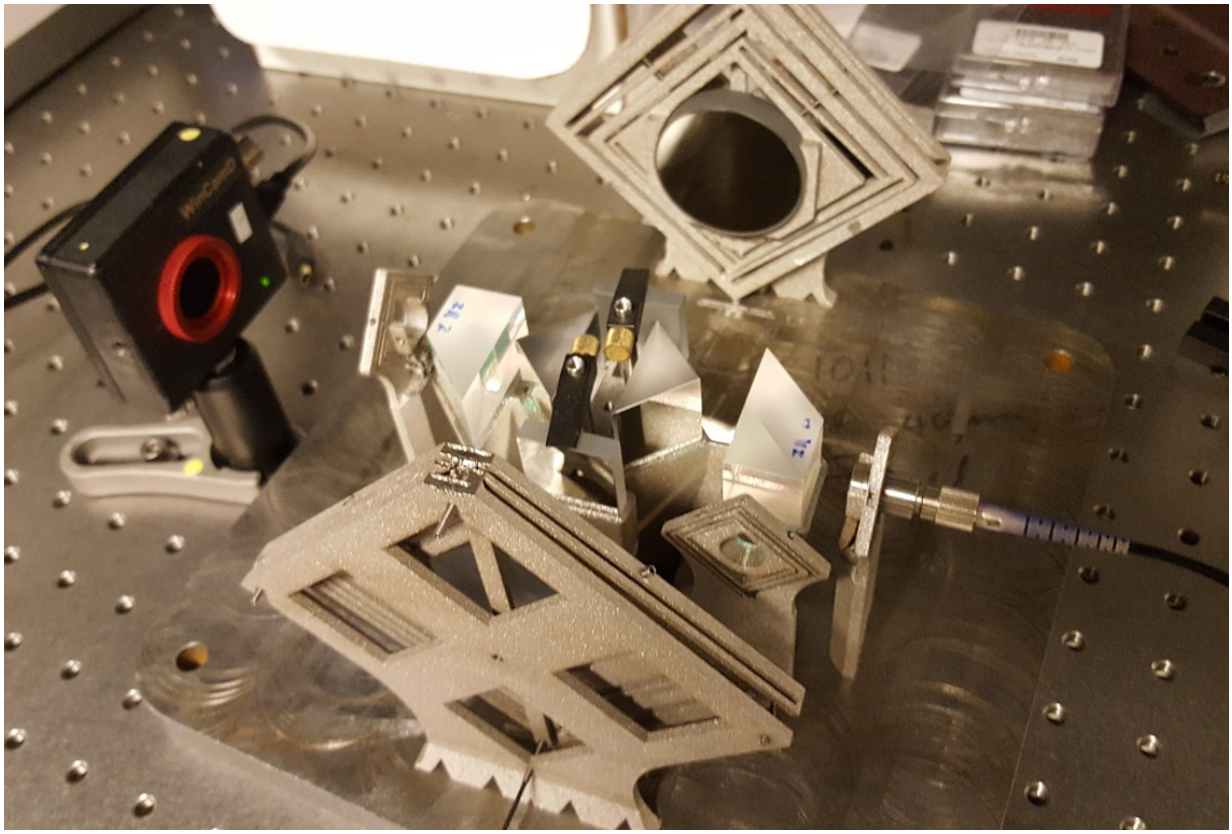

Figure 5.33: The Offner relay interferometer monolithic chassis with the optics in place. Note that the entire chassis including the optomechanical stages are a single monolithic piece. The flexures and optical supports are constructed using Invar36 while the baseplate is composed of stainless steel.

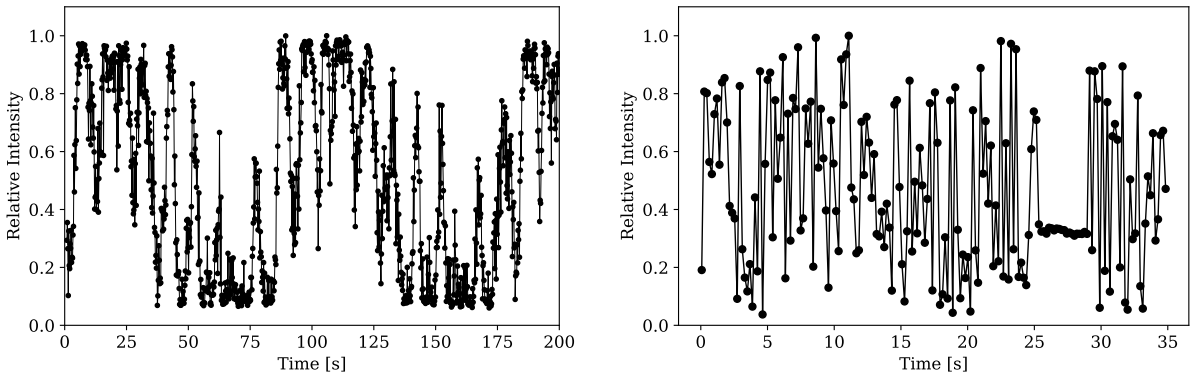

(a) Single-mode signal

(b) Multi-mode signal

Figure 5.34: The relative intensity of the PORI for both the single-mode case (a) and the multi-mode case (b). A continuous wave 785 nm laser fiber coupled laser is passed through a single-mode/multi-mode fiber then passed through the PORI and a camera is used to measure the intensity at one of the PORI outputs. The noisy and non-periodic fluctuations in the intensity are due to a combination of the flexure instabilities and a piezo-ceramic actuator. The visibility for the single-mode and multi-mode signals are calculated to be 0.874 ± 0.026 and 0.894 ± 0.037 respectively. The reduced visibility can be attributed to the flexure instability that make it difficult to properly align the system. Here, the relative intensity values are normalized to the maximal value of the data set. The zero intensity level is the background level of the camera.

uncorrected Michelson would not be able to show any interference of the signals, hence any quantum information stored in the signals would be lost.

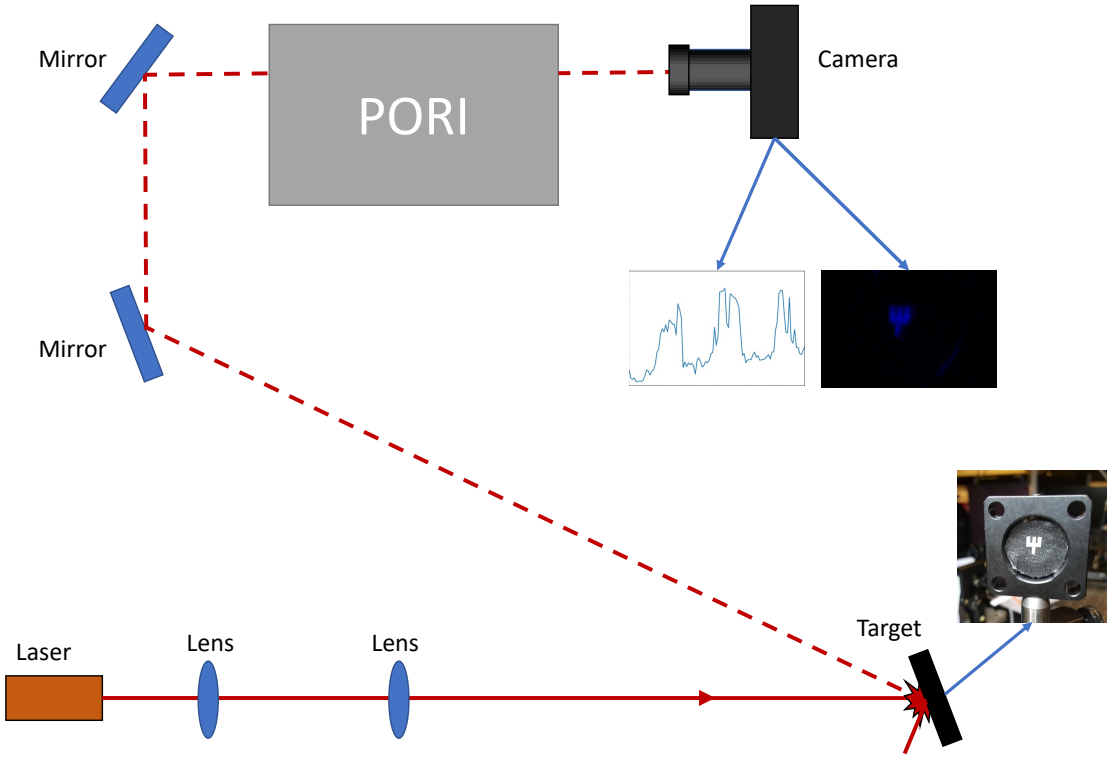

Figure 5.35: Diagram of a LiDAR imaging demonstration of the PORI. A target is was illuminated using a 785 nm laser source. The light scattered off of the target was collected using two flat mirrors and passed through the PORI where interference effects were could be measured by a camera located at one of the outputs of the PORI. The results are shown in Fig. 5.37. A non-field widened unbalanced Michelson interferometer would not show little to no interference effects and would not be useful for this type of application.

As shown in Fig. 5.37, the results of the demonstration are very promising and can be extended to be used in a quantum enhanced LiDAR setting. The PORI system combined with a camera was able to image the target despite using scattered light as the signal.

The intensity of the image of the target also contained phase information as interference was observed from the signal after it passed through the two arms of the interferometer, Figure 5.37. This is especially important since it clearly demonstrates that the one-to-one imaging system of the interferometer is functional and that the interferometer works with multi-mode signals and with true scattered light (target looking away from the interferometer). This point is further

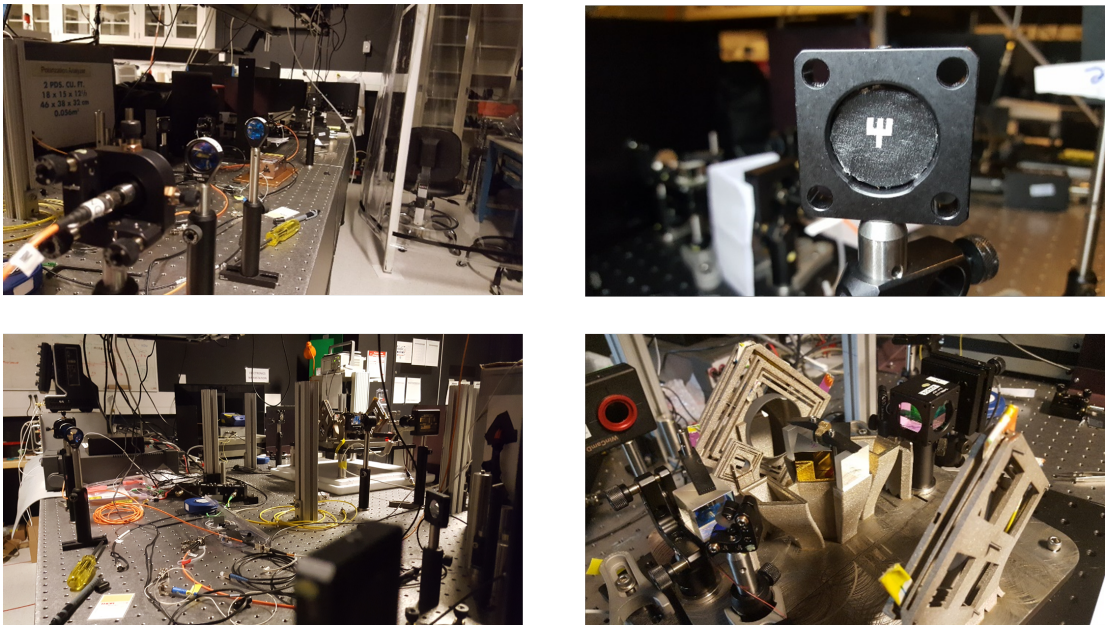

Figure 5.36: Photos of the PORI practical imaging setup. Clockwise from top left: Laser source directed towards the target. A close up of the Psi target. The PORI the camera that is used to image the target. A view from the target towards the PORI.

stressed in Figures 5.37 where the signal is passed through both arms for approximately 40 s where interference occurs and then only one arm after 40 s where no interference is seen. This is to demonstrate that the fluctuations in Figure 5.37 are caused by real interference and thus the coherence properties of the signal light that is scattered from the target can be recovered. The visibility of this interference in Figure. 5.37 is found to be around 0.28 ± 0.03 for both the looking towards and away scenarios which is very promising compared to the 0.09 ± 0.01 observed when blocking one path of the interferometer.

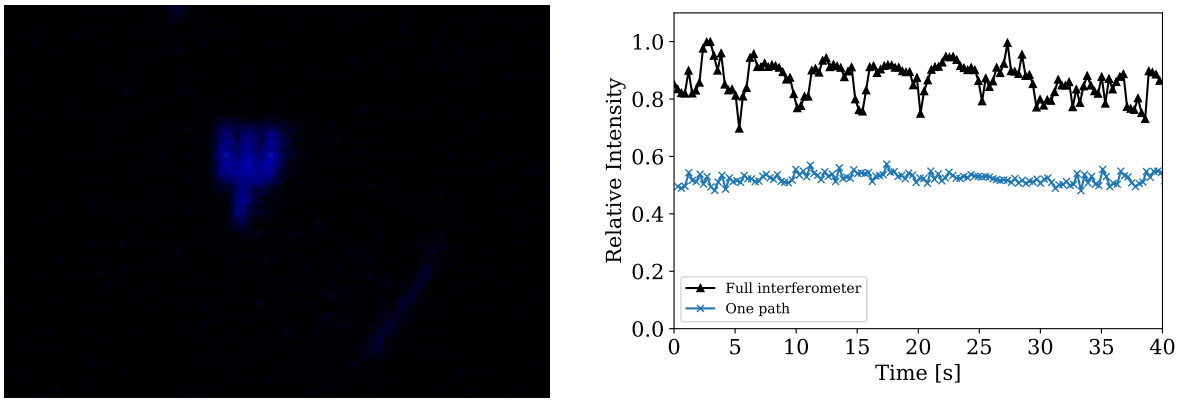

(a) (b)

Figure 5.37: Results of the PORI being used in a practical imaging scenario. (a) Image of the psi target taken with the signals that pass through the PORI. The entire target surface is illuminated uniformly. (b) Relative intensity of the scattered light from the target after passing through the PORI. Intensity pattern that shows both the interference from both arms of the interferometer and the stable intensity when only one arm is used, e.g. one of the interferometer arms is blocked. Triangles, the intensity pattern shown when the light can pass through both arms of the PORI. A piezo electric actuator is driven at 200 mHz to produce these patterns with a visibility of 0.28 ± 0.03. Despite having the light scatter off of the target, coherence properties of the signal can still be recovered. Crosses, isolation of the one arm intensity shown in the left to further demonstrate that there is no periodic interference despite the piezo actuator still running, this has a visibility of 0.09 ± 0.01. The intensity is normalized such that the intensity of one path produces a relative intensity of 0.5. The intensity for the full interferometer is offset by 0.3 for clarity.

5.5.3 Investigation of issues

Although the final loft island design had significantly reduced the build time, the final layers did not complete. This was due to a similar issue of powder dosage and flow which is challenging to control manually even when the print time is reduced to 20 hours. This issue, although unexpected, is trivial to address for future builds. Nonetheless, despite the missing last few layers, the resulting build was functional, though it did have some negative effects on the testing results. Particularly, the final few layers are crucial in connecting on the of the bending arms of the optical axis translation in the TSK-45. The removal of this connection significantly changed the behaviour and stiffness of the TSK-45. Particularly, the action of the master set screw was no longer along the optical axis but rather at an angle. As discussed in Sec. 5.5.3.1, the stability and resonance frequency of the TSK-45 was greatly affected and made it difficult to align the PORI. Unfortunately, due to the project's short timeline (6 months), limited budget, and availability of the 3D printer, the build with the missing final layers is the final assembly for this project and it was not possible to fabricate a revised PORI model. Thus, an investigation was done to characterize the issues of the TSK-45's in the final PORI chassis.

5.5.3.1 Mechanical Stability

The vibration characteristics of flexures are determined by the elastic strength of the beams and the stiffness of the entire structure. A high stiffness would increase the resonance frequency of the system and the stability of the flexure. On the other hand, increased stiffness results in a limited range of motion. In contrast, low stiffness would result in a flexure susceptible to low frequency vibrations. Since, flexures can be fixed with adhesives, the TSK-45 is designed to provide a wide range of motion while still providing sufficient vibrational stability, with what was assumed to be enough to conduct the necessary experiments. Nevertheless, stability of the flexures, particularly the TSK-45, can be important for alignment and temporary preservation of alignment prior to fixing of the mount. Hence, short and long-term stability (12 hour) of the mounts were investigated and compared to a conventional optomechanical mount[6]. The tests below are conducted on the TSK-45's that are in the monolithic PORI chassis. Recall that both of the TSK-45's in the final PORI were not built to completion and hence the results of the tests below are indicative of an incomplete TSK-45 structure. Nonetheless, the results below are indicative of the performance issues of the final PORI and can explain the poor performance relative to theORI (see Chap. 4).

[6]In Sec. 5.3.4.2 only the 12 hour stability is tested because there was no indication at the time that the acoustic noise in the laboratory would present an issue

Short Term Stability: The short-term flexure stability of the TSK-45 is investigated to quantify impact of background noise and dampening behavior to external stimuli. In a typically laboratory environment, several common vibration sources can be expected. Acoustic and mechanical vibration from nearby fans or pedestrian traffic can couple into resonance frequencies of a mechanical system. In the case of mechanical systems with low stiffness, these low frequency disturbances can contribute to uncontrolled vibrations. Due to sensitivity of optical interferometers, it is paramount that the TSK-45 provide enough stability to perform basic alignment procedures prior to application of permanent fixing methods (adhesives).

To perform the stability tests, a piezoceramic stack is placed inside the TSK-45, between two beams, to measure the mechanical motion of the system in the lateral plane as a voltage output. This voltage output is measured on an oscilloscope and frequency components of the signal are determined using Fast Fourier transform (FFT) analysis. First, the EM background noise was investigated and found to be centered around 50-60 Hz. The FFT analysis revealed that the 3D printed TSK-45 is sensitive to low frequency vibration modes, as predicted from the low stiffness of the structure. Low frequency components were observed at 32, 56 (EM noise), 120, 176, and 296 Hz. These frequency components are very similar to the predicted resonance frequencies by the COMSOL® eigenfrequency analysis, where the differences can be attributed to the bulk material properties versus the printed material properties. The COMSOL® analysis was done with the same missing portion at the top of the TSK-45.

The dampening behaviour of the TSK-45 was also experimentally measured. The dampening is defined as the time it takes for the oscillations to completely diminish after an initial disturbance as shown in Figure. 5.38. For the disturbance, a metal bar is dropped from a 10 cm height and allowed to strike the baseplate of theORI. The bar is then stopped immediately before falling and producing more disturbances. The TSK-45 exhibited an average dampening time of 1.55 s without any of the composite dampeners. As mentioned above, the 3D printed Invar36 was significantly more malleable, indicating that 3D printed material has different yield strength and elastic modulus compared to bulk material. With the dampeners in place, the observed low frequency components were 56 (EM noise) and 296 Hz. Therefore, many of the low frequency components were removed and the average dampening time was reduced to 0.85 s. For comparison, the low frequency components in the control optical mount (ThorLabs KM200PM) are practically absent, with an average dampening time of 0.58 s. Overall, this indicates that an investigation into the use of adhesive to fix the optomechanical components after the initial alignment is necessary for the practical deployment of the current version of the TSK-45. If adhesive use is not desired, further studies would be required to optimize flexure stiffness in order to combat vibrational noise.

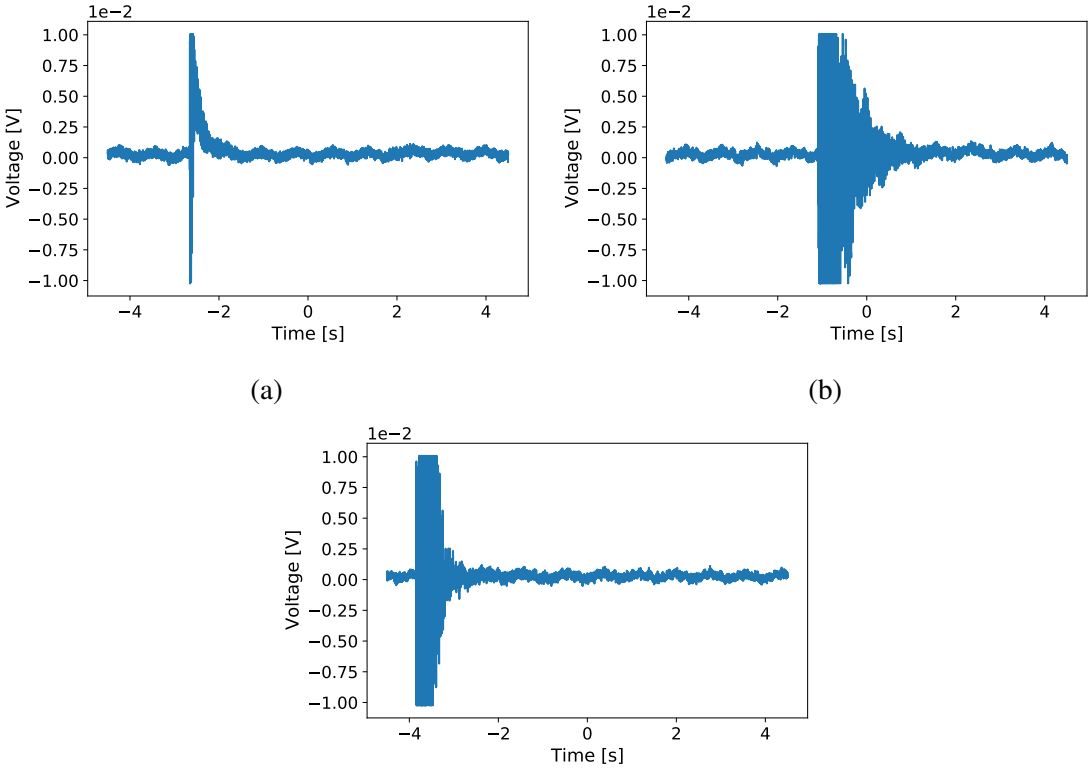

Figure 5.38: (a) Thorlabs KM200PM response after the drop test. (b) TSK-45 drop test response with no dampeners. (c) TSK-45 drop test response with the dampeners.

Twelve Hour Stability: The twelve hour stability of the TSK-45 flexures in the monolithic PORI chassis is tested by keeping the flexures under load over 12 hours and monitoring a reflected spot from the curved mirror, employing a similar technique to that shown in Figure 5.23. Despite the lacking layers and flexure beam connection, the TSK-45 mounts exhibited a performance on par with conventional optomechanical mounts. The standard deviation (STD) of the control and TSK-45 mounts were 0.7625 and 0.8625 µm in the horizontal axis, and 1.149 and 5.891 um, in the vertical axis. The stability of the TSK-45 in the vertical axis was impacted by the low stiffness and resulted in a higher STD value. The low stiffness also impacted the change in absolute vertical position of the beam spot, which over the 12 hour span was 6.6543 and 9.1236 um for the control and TSK-45, while the change in horizontal position was 4.4670 and 3.6303 um for the control and TSK-45. The composite dampeners were not used during these tests. Interestingly, the final position of the beam spot after the 12 hour test is elevated compared to initial position for the TSK-45. This suggests that low stiffness of the flexures and vibrations from the room may have contributed to a random shift in final spot position. The 0.1 nm precision in both the stability measurement and error is obtained from the DataRay software accuracy in determining the centroid position of the beam.

5.5.3.2 Optical Element Tolerances

As discussed in Chap. 4 and Sec. 4.4.1, the original optical design of theORI relies on very tight manufacturing tolerances of the lateral beam displacers and the prism mirrors. These optical elements unfortunately have manufacturing tolerances that make them not suitable for theORI as they displace the optical paths in a way that cannot be corrected by only moving the large curved mirror of one path.

The solution provided in Sec. 4.4.1 is to remove the lateral beam displacers and replace them with the combination of a beam splitter and a flat mirror. The flat mirror in this combination is adjustable and allows for the necessary degrees of freedom in order to compensate for the manufacturing tolerances of the prism mirrors. This was used during the imaging demonstration and in the visibility tests. Adding this degree of freedom to the PORI requires adding two small flexures that are inspired by the TSK-45 but specialize in tip-tilt motion. This configuration is shown in Figure. 5.39 with the tabletop design, however it can easily be adapted to the loft island design. Such a design should be strongly considered for future builds.

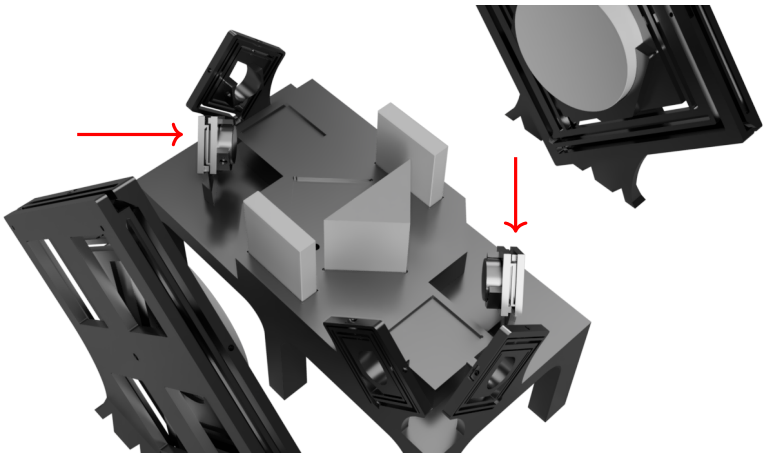

Figure 5.39: PORI design that removes the dependence on the lateral beam displacer manufacturing tolerances and introduces a flexure to align a flat mirror in each path (shown with red arrows), easing the alignment procedures. Although shown here with the tabletop design, it can be easily modified for the loft island design.

5.6 Future Considerations

Despite the short timeline for the PORI project, several achievements were made towards bringing the exciting world of additive manufacturing to quantum information. Nonetheless, I present some of my thoughts and considerations for improving any future PORI or optomechanical flexure. First, one goal of the project was to reduce the physical footprint of the interferometer. This was achieved using theORI design but can be further achieved by the use of smaller optics that are commercially off-the-shelf. This will not only reduce the physical footprint of the PORI but also reduce the height and in consequence the number of printing layers required to make the PORI. A decreased number of layers can reduce the build time and the risk of build failure. Furthermore, custom optical elements can be used to further reduce the height of the PORI.

Second, reducing the range of the flexures and increasing the stiffness of the TSK-45 would be very beneficial. The accuracy of AM is improving and the range of motion provided by the TSK-45 is currently much larger than necessary. Furthermore, flexures are used only to compensate for the accuracy of AM in creating the pockets for the optics of the loft islands. In light of this, I strongly advise that in the future the loft islands be manufactured with no pockets, but rather have the pockets added after the build using standard machining techniques that can be significantly more accurate. It would also be ideal to increase the stiffness of the TSK-45's as to assist in dampening resonance noise. The design of the TSK-45 should be thoroughly reviewed

for the application by using the psuedo-rigid body model to fine tune its stiffness and range of motion [89]. I would also advise investigating the resonance frequencies of the flexures during the design process, especially compared to its operating conditions. This is particularly important during the design process and before the structure is built.

Another future consideration is the investigation of functionally graded materials. As I have mentioned several times, the use of functionally graded materials would be beneficial in creating an athermal interferometer chassis. Thus, experimental confirmation of the analysis done in Sec. 5.2.2 would be very interesting and potentially lead to a highly robust and practical unbalanced interferometer.

5.7 Summary

In this chapter, an interferometer chassis is build using additive manufacturing and is the first monolithic chassis for a field widened interferometer that includes the optomechanical alignment tools embedded in the structure. Using additive manufacturing allowed for a monolithic design of the chassis optomechanical flexure components that would be otherwise impossible to create using standard machining or manufacturing techniques. Furthermore, the chassis was printed using low thermal expansion materials which increases the thermal stability of the device. This work leads to new avenues of combining the possibilities of additive manufacturing with quantum devices.

Chapter 6

Conclusion and Outlook

6.1 Conclusion

The work presented in this thesis demonstrates several advances towards quantum networks for both free-space and optical fiber channels. Two topics towards the advancement of QEYSSat were investigated. We discussed the development of an improved polarization modulation system for the weak coherent pulse source of the QEYSSat mission. Moving receiver tests were conducted to confirm the feasibility of the 6-state 4-state protocol for QEYSSat. The 6-state 4-state protocol was modified for time bin encoding and used to demonstrate the robustness of time bin encoding over several challenging channels. From the challenges faced in the time bin experiments, the design of a more compact and practical interferometer was investigated. To accompany the new design, a study into the design and manufacturing of a robust chassis was conducted.

In Chapter 2, two components of the QEYSSat ground station were advanced. A new design for the polarization modulation setup of the weak coherent pulse source is conceived and tested. The new inline design increases the robustness of the system, creating a plug-and-play module that requires little to no alignment. The current system achieves a polarization visibility of 97% which corresponds to an intrinsic QBER of 1.5%. Nonetheless, the current system is not fully optimized and work is being done to improve the system. In parallel to the WCPS development. Moving receiver tests were conducted to test the feasibility of the 6-state 4-state protocol to remove the need for an active polarization alignment system. The indoor receiver is moved to emulate a low Earth satellite pass. Despite the lack of an active polarization alignment system, the performance of the quantum channel is unchanged compared to a static link with no movement. The visibility of the C-parameter remained unchanged at > 0.90 in both the moving and static

tests. Maintaining such a visibility during a moving pass is not possible without the use of RFI protocols or an active polarization alignment system. These results can reduce the overhead of the QEYSSat ground station and any free-space polarization quantum channel.

In Chapter 3, three major experiments were conducted. The first is a demonstration of a fully passive plug-and-play time bin scheme. Time bin encoded photons are sent over challenging multi mode channels without any active phase compensation to maintain the relative phase difference between the sender and receiver interferometers. Visibilities of approximately 0.90 are obtained for various fiber channels. The fully passive scheme is then used in a demonstration of distributing near-infrared time bin photons over a telecommunication fiber channel. Although the photon throughput of the system is sub-optimal, the results indicate that for short metropolitan links, near-infrared photons can be directly injected into telecommunication fibers without any need for frequency conversion. Finally, the passive time bin scheme is used in the first proof-of-principle moving time bin experiment. With the removal of all the active components, no timing components are required creating a plug-and-play system for moving free-space time bin. The feasibility of moving time bin quantum channels was demonstrated, however, significant system improvements, particularly the development of a robust and compact interferometer, are required to perform genuine moving time bin QKD.

In Chapter 4, a novel design for a field widened interferometer is conceived and prototyped. The imaging system employed uses only reflective optics and is thus achromatic. The cavity-like design allowed for a smaller physical footprint, particularly for relatively long time delays. The simulated and experimental performance of the system for both single mode and multi mode signals is shown to be excellent with visibilities of greater than 97%, which is comparable to current field widened interferometer designs. The potential practicality of this design could potentially be part of a future space mission or deployed in a local near-infrared over telecom quantum network.

In Chapter 5, a study of the thermal and vibrational stability of a monolithic chassis for the Offner relay interferometer is conducted. The study tested the feasibility of manufacturing a low thermal expansion, monolithic structure. Optomechanical flexure devices were built into the chassis and provided the necessary movements for optical alignment. The performance of the system was limited due to build failures, however, visibilities of approximately 90% were obtained. This pioneering work tested the limits of the capabilities of additive manufacturing and has opened many avenues for future research.

Overall, this thesis has focused on improving the robustness of both polarization and time bin encoding hardware. Particularly advancing the development of satellite deploy-able time bin interferometers that can be used for not only quantum key distribution, but quantum sensing as well. The various experiments and studies are a small part in a long line of progress towards the

realization a global quantum network.

6.2 Publications

The work presented in this thesis has been published in the following:

1. Ramy Tannous, Wilson Wu, Stéphane Vinet, Chithrabhanu Perumangatt, Dogan Sinar, Alexander Ling, and Thomas Jennewein. Towards fully passive plug-and-play time-bin quantum key distribution over multi-mode channels. arXiv:2302.05038 (2023) [165]

2. Ramy Tannous, Dogan Sinar, Tabitha D. Arulpragasam, Thomas Jennewein. All reflective, small form-factor field widened interferometer for quantum sensing and communication applications. *In preparation*

3. Ramy Tannous, Stéphane Vinet, Wilson Wu, Kimia Mohammadi, Chithrabhanu Perumangatt, Brendon Higgins, Alexander Ling, and Thomas Jennewein. Reference frame independent quantum key distribution to a moving receiver. *In preparation*

4. Ramy Tannous*, Dogan Sinar*, Sagar Patel, Tabitha D. Arulpragasam, Issa Rishmawi, Mark Kirby, Vlad Paserin, Mihaela Vlasea, and Thomas Jennewein. 3D Printed monolithic time bin interferometer for quantum information processing applications. *In preparation* * equally contributed

5. Anindya Banerji*, Ramy Tannous*, Rui Wang, Thomas Jennewein, and Alexander Ling. High quality entanglement distribution through telecommunication fiber using near-infrared non-degenerate photon pairs. *In preparation* * equally contributed

This list is not fully comprehensive of the work done during my Ph.D. as I was involved in several other studies that are not part of this work, the reader can see the latest and full list of publications here.

6.3 Outlook

6.3.1 Enhancements for the QEYSSat ground to space link

6.3.1.1 Development of the weak coherent photon source for the QEYSSat mission

In Section 2.1.2.3, an upgraded version of the Inline polarization modulation system (IPMS) is tested with the Weak coherent pulse source (WCPS) laser setup. This system is currently being upgraded to have better PMF length matching and a reduced number of fiber to fiber connects. Each connection introduces additional errors to the system, thus increasing the intrinsic QBER. Furthermore, the phase modulators of the IPMS are going to be driven by an arbitrary waveform generator at a rate of 400 MHz. This requires a substantial amount of data and random numbers. This is currently being developed by QPL members in parallel to the IPMS progress.

Once the intrinsic error is minimized and the WCPS is fully operational with an intrinsic QBER below the 1% threshold, some interesting experiments can be conducted. Since the IPMS is completely fiber-based, it can be easily employed to work in space limited environments, such as on a satellite. In fact, a similar concept of crossing two PMFs will be employed for the QEYSSat downlink source [67, 68]. Overall, the IPMS promises to create a model for a plug-and-play weak coherent pulse source that can be used for a variety of experiments with the QEYSSat mission and beyond. Although WCPS in general are not true single photon sources, they will still play a very important role in building quantum networks, particularly because of their robustness and relatively low cost.

6.3.1.2 Indoor Moving 6-state 4-state Demonstration

In Section 2.2, the 6-state 4-state protocol is tested over a moving channel similar to a QEYSSat pass. Reducing the need for a polarization compensation significantly decreases the ground station overhead and will increase the photon throughput of the transmitter telescope. The immediate next steps are to conduct further feasibility studies with both the QEYSSat WCPS and entangled photon source [94]. As it is currently implemented, the QEYSSat ground station will still require to have a polarization alignment system to account for the roll of the satellite. For future satellites, this problem can be eliminated by putting a quarter-wave plate at the transmitter telescope to convert the slow and fast axis (computational basis) polarizations to the rotationally invariant circular basis. The satellite receiver would then have to measure in the circular basis and one linear basis and no polarization alignment system would be needed. This is not a new concept and comes from the original RFI-QKD work [71].

6.3.2 Fully passive time bin quantum key distribution

6.3.2.1 Plug and play time bin network

In Section 3.1, a fully passive time bin scheme is demonstrated over multiple challenging channels. The reduction in the need for a relative phase stabilization of the two interferometers is an important result for quantum networks. The use of this scheme can relax the thermal and vibrational stability requirements of the interferometers used in the communication link, something that will be received well by engineers (Chap. 5). The major benefit of this scheme is to be used in free-space moving links (Section 3.3). To date there has been no genuine free-space moving time bin demonstration due to the difficulties in establishing a stable relative phase and a high interference visibility. The latter due to the lack of adoption of field widened interferometers by the community[1]. Thus, a genuine moving free-space time bin demonstration can be performed if the stability of the time bin analyzer is improved such that it can be placed on the moving receiver. In addition, optimizing the photon throughput of the moving receiver is necessary. Additionally, using a data collection system that is fully integrated and optimized for time bin communication can be used to reduce the overhead of the receiver system [166]. Ultimately, with this fully passive scheme, a time bin analyzer or source could be placed on a satellite, simplifying quantum networks by directly interfacing optical fiber and free-space quantum channels using time bin encoded photons.

6.3.2.2 Near-infrared single photon quantum network

Many of the single photon sources available today emit photons in the visible or Near-infrared (NIR) regime [117, 118, 119, 120, 121, 122, 123, 124]. By contrast, the majority of the deployed optical fiber networks are in the telecommunications regime. However, in Section 3.2 we successfully demonstrated that time bin encoded NIR photons can be distributed in a telecommunications optical fiber over short distances. This implies that many of the quantum sources can be employed immediately for small local networks without the need for frequency conversion nodes or development of alternate sources that emit in the telecommunications regime. Although, telecom fibers are multi mode for NIR photons, the passive time bin scheme is suitable for this application since the higher order modes of the NIR photons in the telecommunications fiber can be used for key generation. Furthermore, for sources that emit in the visible range, many modes will be present, thus a field widened interferometer is even more important. Regardless, near-term experiments and demonstrations could be conducted with several different photon sources

[1] Which seems much more interested in using adaptive optics, yet this unnecessarily increases the overhead of the system.

including quantum dots [121, 122, 123], and other material based sources [118, 124]. Ultimately, this would ease the requirements for quantum networks to be strictly in the telecom regime, which can reduce costs and the need for additional hardware, i.e. frequency converters. In fact, some quantum links can be simplified by directly interfacing the signal from a satellite into the metropolitan network. Thus, not limiting the free-space channels to areas close to a ground station[2].

6.3.3 Improving the Offner relay interferometer

In Chapter 4, a novel design for a field widened interferometer is investigated. Creating long time delay, compact, and robust time bin interferometers is an important piece for building a quantum network. Reducing the form factor of the Offner relay interferometer would enable it to be suitable for satellite payloads, moving platforms, and quantum sensing platforms. This could be achieved by investigating one of the alternate designs found in Table. 4.4 or by employing a similar yet alternate design, e.g. using Herriott cells [133]. Another application of the Offner relay interferometer is using it in the experiments for NIR time bin encoding in telecommunication fibers. This is an especially good fit since quantum photon sources span a broad spectral range and the Offner relay performance is achromatic over a broad spectral range. Ultimately, the progress towards modular, robust, and practical time bin interferometers is important for free-space channels as it could lead to the possibilities of translating fiber-based quantum protocols to long-distance free-space channels, such as the coherent-one-way and differential-phase-shift protocols [167, 168].

6.3.4 Uses of additive manufacturing for quantum information

In Chapter 5, we explored the use of additive manufacturing for enhancing the robustness of a time bin interferometer. Building a robust interferometer enclosure is still an active area of development that requires further investigation. Beyond this challenge, the outlook for the use of additive manufacturing is promising as it is still in its infancy. As the technology progresses, so do the applications. As eluded to many times in Chapter 5, functionally graded materials would be very beneficial for creating a thermally robust housing for a time bin interferometer [146, 147, 148]. Furthermore, alignment flexures can be specifically tuned to maximize the elasticity of certain regions while maintaining a low thermal expansion. Another promising technology that is emerging from the field of additive manufacturing, is the direct manufacturing of refractive

[2] A particularly interesting use case is a ground station that is located outside of a dense metropolitan area but has access to the telecommunications network.

and reflective optical elements [169, 170]. This would truly be revolutionary, as complex optical devices can be manufactured into monolithic structures containing all the necessary components.

6.3.5 Final thoughts

Overall, the use of both time bin and polarization encoding over free-space channels is important for the development of a global quantum network. There are many space missions that are being developed [26, 171, 172], and with the technologies becoming more mature a global network is closer to realization. The next steps are to deploy many sub-networks that are interconnected with long distance free-space links as either trusted or untrusted nodes. The work presented in this thesis, along with many subsequent years of study and development, will provide a great technological and scientific baseline for achieving the quantum network goals of Canada [32] and the scientific community.

References

[1] C. H. Bennett and G. Brassard, "Quantum cryptography: Public key distribution and coin tossing," arXiv preprint arXiv:2003.06557, 2020.

[2] H.-K. Lo, M. Curty, and B. Qi, "Measurement-device-independent quantum key distribution," Physical review letters, vol. 108, no. 13, p. 130503, 2012.

[3] U. Vazirani and T. Vidick, "Fully device-independent quantum key distribution," Phys. Rev. Lett., vol. 113, p. 140501, Sep 2014.

[4] M. Lucamarini, Z. L. Yuan, J. F. Dynes, and A. J. Shields, "Overcoming the rate–distance limit of quantum key distribution without quantum repeaters," Nature, vol. 557, no. 7705, pp. 400–403, 2018.

[5] S. Pirandola, U. L. Andersen, L. Banchi, M. Berta, D. Bunandar, R. Colbeck, D. Englund, T. Gehring, C. Lupo, C. Ottaviani, et al., "Advances in quantum cryptography," Advances in optics and photonics, vol. 12, no. 4, pp. 1012–1236, 2020.

[6] P. W. Shor and J. Preskill, "Simple proof of security of the bb84 quantum key distribution protocol," Physical review letters, vol. 85, no. 2, p. 441, 2000.

[7] C. Portmann and R. Renner, "Security in quantum cryptography," Reviews of Modern Physics, vol. 94, no. 2, p. 025008, 2022.

[8] W. K. Wootters and W. H. Zurek, "A single quantum cannot be cloned," vol. 299, p. 802, 1982.

[9] L. Lydersen, C. Wiechers, C. Wittmann, D. Elser, J. Skaar, and V. Makarov, "Hacking commercial quantum cryptography systems by tailored bright illumination," Nature photonics, vol. 4, no. 10, pp. 686–689, 2010.

[10] N. Lütkenhaus and M. Jahma, "Quantum key distribution with realistic states: photon-number statistics in the photon-number splitting attack," New Journal of Physics, vol. 4, no. 1, p. 44, 2002.

[11] R. Gallager, "Low-density parity-check codes," IRE Transactions on information theory, vol. 8, no. 1, pp. 21–28, 1962.

[12] D. J. C. MacKay and R. M. Neal, "Near shannon limit performance of low density parity check codes," Electronics Letters, vol. 33, pp. 457–458, Mar 1997.

[13] M. C. Davey, Error-correction using low-density parity-check codes. PhD thesis, University of Cambridge, 2000.

[14] O. Maroy, M. Gudmundsen, L. Lydersen, and J. Skaar, "Error estimation, error correction and verification in quantum key distribution," IET Information Security, vol. 8, pp. 277–282(5), September 2014.

[15] G. Brassard and L. Salvail, "Secret-key reconciliation by public discussion," in Advances in Cryptology—EUROCRYPT'93: Workshop on the Theory and Application of Cryptographic Techniques Lofthus, Norway, May 23–27, 1993 Proceedings 12, pp. 410–423, Springer, 1994.

[16] T. Sugimoto and K. Yamazaki, "A study on secret key reconciliation protocol," IEICE transactions on fundamentals of electronics, communications and computer sciences, vol. 83, no. 10, pp. 1987–1991, 2000.

[17] M. Hayashi and T. Tsurumaru, "More efficient privacy amplification with less random seeds via dual universal hash function," IEEE Transactions on Information Theory, vol. 62, no. 4, pp. 2213–2232, 2016.

[18] B. Yan, Q. Li, H. Mao, and N. Chen, "An efficient hybrid hash based privacy amplification algorithm for quantum key distribution," Quantum Information Processing, vol. 21, no. 4, p. 130, 2022.

[19] M. N. Alenezi, H. Alabdulrazzaq, and N. Q. Mohammad, "Symmetric encryption algorithms: Review and evaluation study," International Journal of Communication Networks and Information Security, vol. 12, no. 2, pp. 256–272, 2020.

[20] J. Thakur and N. Kumar, "Des, aes and blowfish: Symmetric key cryptography algorithms simulation based performance analysis," International journal of emerging technology and advanced engineering, vol. 1, no. 2, pp. 6–12, 2011.

[21] S. Wengerowsky, S. K. Joshi, F. Steinlechner, H. Hübel, and R. Ursin, "An entanglement-based wavelength-multiplexed quantum communication network," Nature, vol. 564, no. 7735, pp. 225–228, 2018.

[22] S. K. Joshi, D. Aktas, S. Wengerowsky, M. Lončarić, S. P. Neumann, B. Liu, T. Scheidl, G. C. Lorenzo, Ž. Samec, L. Kling, et al., "A trusted node–free eight-user metropolitan quantum communication network," Science advances, vol. 6, no. 36, p. eaba0959, 2020.

[23] J.-P. Chen, C. Zhang, Y. Liu, C. Jiang, W. Zhang, X.-L. Hu, J.-Y. Guan, Z.-W. Yu, H. Xu, J. Lin, et al., "Sending-or-not-sending with independent lasers: Secure twin-field quantum key distribution over 509 km," Physical review letters, vol. 124, no. 7, p. 070501, 2020.

[24] J.-P. Chen, C. Zhang, Y. Liu, C. Jiang, D.-F. Zhao, W.-J. Zhang, F.-X. Chen, H. Li, L.-X. You, Z. Wang, et al., "Quantum key distribution over 658 km fiber with distributed vibration sensing," Physical Review Letters, vol. 128, no. 18, p. 180502, 2022.

[25] S. Wang, Z.-Q. Yin, D.-Y. He, W. Chen, R.-Q. Wang, P. Ye, Y. Zhou, G.-J. Fan-Yuan, F.-X. Wang, W. Chen, et al., "Twin-field quantum key distribution over 830-km fibre," Nature Photonics, vol. 16, no. 2, pp. 154–161, 2022.

[26] J. S. Sidhu, S. K. Joshi, M. Gündoğan, T. Brougham, D. Lowndes, L. Mazzarella, M. Krutzik, S. Mohapatra, D. Dequal, G. Vallone, et al., "Advances in space quantum communications," IET Quantum Communication, vol. 2, no. 4, pp. 182–217, 2021.

[27] D. Stucki, M. Legré, F. Buntschu, B. Clausen, N. Felber, N. Gisin, L. Henzen, P. Junod, G. Litzistorf, P. Monbaron, L. Monat, J.-B. Page, D. Perroud, G. Ribordy, A. Rochas, S. Robyr, J. Tavares, R. Thew, P. Trinkler, S. Ventura, R. Voirol, N. Walenta, and H. Zbinden, "Long-term performance of the swissquantum quantum key distribution network in a field environment," New Journal of Physics, vol. 13, p. 123001, dec 2011.

[28] M. Sasaki, M. Fujiwara, H. Ishizuka, W. Klaus, K. Wakui, M. Takeoka, S. Miki, T. Yamashita, Z. Wang, A. Tanaka, K. Yoshino, Y. Nambu, S. Takahashi, A. Tajima, A. Tomita, T. Domeki, T. Hasegawa, Y. Sakai, H. Kobayashi, T. Asai, K. Shimizu, T. Tokura, T. Tsurumaru, M. Matsui, T. Honjo, K. Tamaki, H. Takesue, Y. Tokura, J. F. Dynes, A. R. Dixon, A. W. Sharpe, Z. L. Yuan, A. J. Shields, S. Uchikoga, M. Legré, S. Robyr, P. Trinkler, L. Monat, J.-B. Page, G. Ribordy, A. Poppe, A. Allacher, O. Maurhart, T. Länger, M. Peev, and A. Zeilinger, "Field test of quantum key distribution in the tokyo qkd network," Opt. Express, vol. 19, pp. 10387–10409, May 2011.

[29] T.-Y. Chen, J. Wang, H. Liang, W.-Y. Liu, Y. Liu, X. Jiang, Y. Wang, X. Wan, W.-Q. Cai, L. Ju, et al., "Metropolitan all-pass and inter-city quantum communication network," Optics express, vol. 18, no. 26, pp. 27217–27225, 2010.

[30] C. Monroe, M. G. Raymer, and J. Taylor, "The us national quantum initiative: From act to action," Science, vol. 364, no. 6439, pp. 440–442, 2019.

[31] B. Sussman, P. Corkum, A. Blais, D. Cory, and A. Damascelli, "Quantum canada," Quantum Science and Technology, vol. 4, no. 2, p. 020503, 2019.

[32] S. Innovation and E. D. Canada. https://ised-isde.canada.ca/site/national-quantum-strategy/en, 2023.

[33] M. Bloch, S. W. McLaughlin, J.-M. Merolla, and F. Patois, "Frequency-coded quantum key distribution," Optics letters, vol. 32, no. 3, pp. 301–303, 2007.

[34] E. Knill, R. Laflamme, and G. J. Milburn, "A scheme for efficient quantum computation with linear optics," nature, vol. 409, no. 6816, pp. 46–52, 2001.

[35] M. Mafu, A. Dudley, S. Goyal, D. Giovannini, M. McLaren, M. J. Padgett, T. Konrad, F. Petruccione, N. Lütkenhaus, and A. Forbes, "Higher-dimensional orbital-angular-momentum-based quantum key distribution with mutually unbiased bases," Physical Review A, vol. 88, no. 3, p. 032305, 2013.

[36] J. Brendel, N. Gisin, W. Tittel, and H. Zbinden, "Pulsed energy-time entangled twin-photon source for quantum communication," Phys. Rev. Lett., vol. 82, pp. 2594–2597, Mar 1999.

[37] I. Marcikic, H. de Riedmatten, W. Tittel, H. Zbinden, M. Legré, and N. Gisin, "Distribution of time-bin entangled qubits over 50 km of optical fiber," Phys. Rev. Lett., vol. 93, p. 180502, Oct 2004.

[38] F. Bouchard, A. Sit, F. Hufnagel, A. Abbas, Y. Zhang, K. Heshami, R. Fickler, C. Marquardt, G. Leuchs, E. Karimi, et al., "Quantum cryptography with twisted photons through an outdoor underwater channel," Optics express, vol. 26, no. 17, pp. 22563–22573, 2018.

[39] F. Hufnagel, A. Sit, F. Grenapin, F. Bouchard, K. Heshami, D. England, Y. Zhang, B. J. Sussman, R. W. Boyd, G. Leuchs, et al., "Characterization of an underwater channel for quantum communications in the ottawa river," Optics express, vol. 27, no. 19, pp. 26346–26354, 2019.

[40] K. Azuma, S. E. Economou, D. Elkouss, P. Hilaire, L. Jiang, H.-K. Lo, and I. Tzitrin, "Quantum repeaters: From quantum networks to the quantum internet," arXiv preprint arXiv:2212.10820, 2022.

[41] A. Boaron, G. Boso, D. Rusca, C. Vulliez, C. Autebert, M. Caloz, M. Perrenoud, G. Gras, F. Bussières, M.-J. Li, D. Nolan, A. Martin, and H. Zbinden, "Secure quantum key distribution over 421 km of optical fiber," Phys. Rev. Lett., vol. 121, p. 190502, Nov 2018.

[42] J.-P. Chen, C. Zhang, Y. Liu, C. Jiang, W. Zhang, X.-L. Hu, J.-Y. Guan, Z.-W. Yu, H. Xu, J. Lin, M.-J. Li, H. Chen, H. Li, L. You, Z. Wang, X.-B. Wang, Q. Zhang, and J.-W. Pan, "Sending-or-not-sending with independent lasers: Secure twin-field quantum key distribution over 509 km," Phys. Rev. Lett., vol. 124, p. 070501, Feb 2020.

[43] A. G. Alkholidi, K. S. Altowij, et al., "Free space optical communications—theory and practices," Contemporary Issues in Wireless Communications, pp. 159–212, 2014.

[44] Fiber Optics, ch. 8, pp. 272–309. John Wiley & Sons, Ltd, 1991.

[45] R. Ursin, F. Tiefenbacher, T. Schmitt-Manderbach, H. Weier, T. Scheidl, M. Lindenthal, B. Blauensteiner, T. Jennewein, J. Perdigues, P. Trojek, et al., "Entanglement-based quantum communication over 144 km," Nature physics, vol. 3, no. 7, pp. 481–486, 2007.

[46] J. Yin, Y. Cao, Y.-H. Li, J.-G. Ren, S.-K. Liao, L. Zhang, W.-Q. Cai, W.-Y. Liu, B. Li, H. Dai, M. Li, Y.-M. Huang, L. Deng, L. Li, Q. Zhang, N.-L. Liu, Y.-A. Chen, C.-Y. Lu, R. Shu, C.-Z. Peng, J.-Y. Wang, and J.-W. Pan, "Satellite-to-ground entanglement-based quantum key distribution," Phys. Rev. Lett., vol. 119, p. 200501, Nov 2017.

[47] C.-Y. Lu, Y. Cao, C.-Z. Peng, and J.-W. Pan, "Micius quantum experiments in space," Reviews of Modern Physics, vol. 94, no. 3, p. 035001, 2022.

[48] P. Chaiwongkhot, S. Hosseini, A. Ahmadi, B. L. Higgins, D. Dalacu, P. J. Poole, R. L. Williams, M. E. Reimer, and T. Jennewein, "Enhancing secure key rates of satellite qkd using a quantum dot single-photon source," arXiv preprint arXiv:2009.11818, 2020.

[49] J. Bourgoin, E. Meyer-Scott, B. L. Higgins, B. Helou, C. Erven, H. Huebel, B. Kumar, D. Hudson, I. D'Souza, R. Girard, et al., "A comprehensive design and performance analysis of low earth orbit satellite quantum communication," New Journal of Physics, vol. 15, no. 2, p. 023006, 2013.

[50] C. Erven, B. Heim, E. Meyer-Scott, J. Bourgoin, R. Laflamme, G. Weihs, and T. Jennewein, "Studying free-space transmission statistics and improving free-space quantum

key distribution in the turbulent atmosphere," New Journal of Physics, vol. 14, no. 12, p. 123018, 2012.

[51] F. G. Smith, "Atmospheric propagation of radiation," The infrared and electro-optical systems handbook-IR/EO systems handbook, 1993.

[52] E. J. McCartney, "Optics of the atmosphere: scattering by molecules and particles," New York, 1976.

[53] R. Good, R. Beland, E. Murphy, J. Brown, and E. Dewan, "Atmospheric models of optical turbulence," in Modeling of the Atmosphere, vol. 928, pp. 165–186, SPIE, 1988.

[54] A. Rafalimanana, C. Giordano, A. Ziad, and E. Aristidi, "Prediction of atmospheric turbulence by means of wrf model for optical communications," in International Conference on Space Optics—ICSO 2020, vol. 11852, pp. 1856–1866, SPIE, 2021.

[55] M. Azouit and J. Vernin, "Optical turbulence profiling with balloons relevant to astronomy and atmospheric physics," Publications of the Astronomical Society of the Pacific, vol. 117, no. 831, p. 536, 2005.

[56] J. Chabé, E. Aristidi, A. Ziad, H. Lantéri, Y. Fanteï-Caujolle, C. Giordano, J. Borgnino, M. Marjani, and C. Renaud, "Pml: a generalized monitor of atmospheric turbulence profile with high vertical resolution," Applied optics, vol. 59, no. 25, pp. 7574–7584, 2020.

[57] R. K. Tyson and B. W. Frazier, Principles of adaptive optics. CRC press, 2022.

[58] J. Osborn, M. J. Townson, O. J. Farley, A. Reeves, and R. M. Calvo, "Adaptive optics precompensated laser uplink to leo and geo," Optics Express, vol. 29, no. 4, pp. 6113–6132, 2021.

[59] A. Rukosuev, A. Kudryashov, A. Lylova, V. Samarkin, and Y. V. Sheldakova, "Adaptive optics system for real-time wavefront correction," Atmospheric and oceanic optics, vol. 28, pp. 381–386, 2015.

[60] C. J. Pugh, J.-F. Lavigne, J.-P. Bourgoin, B. L. Higgins, and T. Jennewein, "Adaptive optics benefit for quantum key distribution uplink from ground to a satellite," Advanced Optical Technologies, vol. 9, no. 5, pp. 263–273, 2020.

[61] C. J. Pugh, P. Kolenderski, C. Scarcella, A. Tosi, and T. Jennewein, "Towards correcting atmospheric beam wander via pump beam control in a down conversion process," Optics Express, vol. 24, no. 18, pp. 20947–20955, 2016.

[62] J.-P. Bourgoin, "Experimental and theoretical demonstration of the feasibility of global quantum cryptography using satellites," 2014.

[63] C. Pugh, "Free space quantum key distribution to moving platforms," 2017.

[64] T. Jennewein, J. Bourgoin, B. Higgins, C. Holloway, E. Meyer-Scott, C. Erven, B. Heim, Z. Yan, H. Hübel, G. Weihs, et al., "Qeyssat: a mission proposal for a quantum receiver in space," in Advances in photonics of quantum computing, memory, and communication VII, vol. 8997, pp. 21–27, SPIE, 2014.

[65] A. Scott, T. Jennewein, J. Cain, I. D'Souza, B. Higgins, D. Hudson, H. Podmore, and W. Soh, "The qeyssat mission: on-orbit demonstration of secure optical communications network technologies," in Environmental Effects on Light Propagation and Adaptive Systems III, vol. 11532, pp. 71–76, SPIE, 2020.

[66] H. Podmore, I. D'Souza, J. Cain, T. Jennewein, B. L. Higgins, Y. S. Lee, A. Koujelev, D. Hudson, and A. McColgan, "QKD terminal for Canada's Quantum Encryption and Science Satellite (QEYSSat)," in International Conference on Space Optics — ICSO 2020 (Z. Sodnik, B. Cugny, and N. Karafolas, eds.), (Online Only, France), p. 17, SPIE, June 2021.

[67] Q. T. News. https://www.insidequantumtechnology.com/news-archive/u-of-strathclyde-canadas-qyessat-glasgows-refq-developing-quantum-encryption-scheme-to-be-tested-on-satellite/, 2023.

[68] C. Prospect. https://craftprospect.com/craft-prospect-spearheads-novel-commercial-quantum-source-development-in-uk-canada-bilateral-collaboration/, 2023.

[69] C. H. Bennett, G. Brassard, and N. D. Mermin, "Quantum cryptography without bell's theorem," Physical review letters, vol. 68, no. 5, p. 557, 1992.

[70] R. Tannous, Z. Ye, J. Jin, K. B. Kuntz, N. Lütkenhaus, and T. Jennewein, "Demonstration of a 6 state-4 state reference frame independent channel for quantum key distribution," Applied Physics Letters, vol. 115, no. 21, p. 211103, 2019.

[71] A. Laing, V. Scarani, J. G. Rarity, and J. L. O'Brien, "Reference-frame-independent quantum key distribution," Physical Review A, vol. 82, no. 1, p. 012304, 2010.

[72] C. J. Pugh, S. Kaiser, J.-P. Bourgoin, J. Jin, N. Sultana, S. Agne, E. Anisimova, V. Makarov, E. Choi, B. L. Higgins, and T. Jennewein, "Airborne demonstration of a

quantum key distribution receiver payload," Quantum Sci. Technol., vol. 2, p. 024009, June 2017. arXiv:1612.06396 [quant-ph].

[73] P. E. Ciddor, "Refractive index of air: new equations for the visible and near infrared," Appl. Opt., vol. 35, pp. 1566–1573, Mar 1996.

[74] L. Kral, I. Prochazka, and K. Hamal, "Optical signal path delay fluctuations caused by atmospheric turbulence," Optics letters, vol. 30, no. 14, pp. 1767–1769, 2005.

[75] F. Quelle, "Thermal distortion of diffraction-limited optical elements," Applied optics, vol. 5, no. 4, pp. 633–637, 1966.

[76] J. Jin, J.-P. Bourgoin, R. Tannous, S. Agne, C. J. Pugh, K. B. Kuntz, B. L. Higgins, and T. Jennewein, "Genuine time-bin-encoded quantum key distribution over a turbulent depolarizing free-space channel," Optics express, vol. 27, no. 26, pp. 37214–37223, 2019.

[77] J. A. Zielińska, F. A. Beduini, N. Godbout, and M. W. Mitchell, "Ultranarrow faraday rotation filter at the rb d 1 line," Optics letters, vol. 37, no. 4, pp. 524–526, 2012.

[78] W. T. Buttler, R. J. Hughes, S. K. Lamoreaux, G. L. Morgan, J. E. Nordholt, and C. G. Peterson, "Daylight quantum key distribution over 1.6 km," Physical Review Letters, vol. 84, no. 24, p. 5652, 2000.

[79] H. Ko, J.-S. Choe, B.-S. Choi, K.-J. Kim, J.-H. Kim, Y. Baek, and C. J. Youn, "Daylight operation of a high-speed free-space quantum key distribution using silica-based integration chip and micro-optics-based module," in 2019 Optical Fiber Communications Conference and Exhibition (OFC), pp. 1–3, IEEE, 2019.

[80] M. Avesani, L. Calderaro, M. Schiavon, A. Stanco, C. Agnesi, A. Santamato, M. Zahidy, A. Scriminich, G. Foletto, G. Contestabile, et al., "Full daylight quantum-key-distribution at 1550 nm enabled by integrated silicon photonics," npj Quantum Information, vol. 7, no. 1, p. 93, 2021.

[81] F. Basso Basset, M. Valeri, J. Neuwirth, E. Polino, M. B. Rota, D. Poderini, C. Pardo, G. Rodari, E. Roccia, S. Covre da Silva, et al., "Daylight entanglement-based quantum key distribution with a quantum dot source," Quantum Science and Technology, 2022.

[82] H. Chen, J. Wang, B. Tang, Z. Li, B. Liu, and S. Sun, "Field demonstration of time-bin reference-frame-independent quantum key distribution via an intracity free-space link," Opt. Lett., vol. 45, p. 3022, June 2020.

[83] Y. Cao, Y.-H. Li, K.-X. Yang, Y.-F. Jiang, S.-L. Li, X.-L. Hu, M. Abulizi, C.-L. Li, W. Zhang, Q.-C. Sun, et al., "Long-distance free-space measurement-device-independent quantum key distribution," Physical Review Letters, vol. 125, no. 26, p. 260503, 2020.

[84] J. Jin, S. Agne, J.-P. Bourgoin, Y. Zhang, N. Lütkenhaus, and T. Jennewein, "Demonstration of analyzers for multimode photonic time-bin qubits," Physical Review A, vol. 97, no. 4, p. 043847, 2018.

[85] J. G. Hirschberg, "Field Widened Michelson Spectrometer with No Moving Parts," Applied Optics, vol. 13, p. 233, Feb. 1974.

[86] S. Mahadevan, J. Ge, S. W. Fleming, X. Wan, C. DeWitt, J. C. van Eyken, and D. McDavitt, "An Inexpensive Field-Widened Monolithic Michelson Interferometer for Precision Radial Velocity Measurements," Publications of the Astronomical Society of the Pacific, vol. 120, pp. 1001–1015, Sept. 2008. arXiv: 0809.3721.

[87] S. Sajeed and T. Jennewein, "Observing quantum coherence from photons scattered in free-space," arXiv:2103.00298 [quant-ph], Feb. 2021.

[88] C. Cahall, N. T. Islam, D. J. Gauthier, and J. Kim, "Multi-mode Time-delay Interferometer for Free-space Quantum Communication," Physical Review Applied, vol. 13, p. 024047, Feb. 2020.

[89] L. L. Howell, S. P. Magleby, and B. M. Olsen, eds., Handbook of compliant mechanisms. Chichester, West Sussex, United Kingdom ; Hoboken: John Wiley & Sons, Inc, 2013.

[90] S. T. Smith, Flexures: elements of elastic mechanisms. Crc Press, 2000.

[91] L. L. Howell, "Compliant mechanisms," in 21st Century Kinematics: The 2012 NSF Workshop, pp. 189–216, Springer, 2013.

[92] N. Lobontiu, Compliant mechanisms: design of flexure hinges. CRC press, 2002.

[93] Z. D. Jastrzebski, "Nature and properties of engineering materials," 1976.

[94] Y. S. Lee, M. Xie, R. Tannous, and T. Jennewein, "Sagnac-type entangled photon source using only conventional polarization optics," Quantum Science and Technology, vol. 6, no. 2, p. 025004, 2021.

[95] A. Duplinskiy, V. Ustimchik, A. Kanapin, V. Kurochkin, and Y. Kurochkin, "Low loss qkd optical scheme for fast polarization encoding," Optics Express, vol. 25, 09 2017.

[96] M. Jofre, A. Gardelein, G. Anzolin, G. Molina-Terriza, J. Torres, M. Mitchell, and V. Pruneri, "100 mhz amplitude and polarization modulated optical source for free-space quantum key distribution at 850 nm," Journal of Lightwave Technology, vol. 28, no. 17, pp. 2572–2578, 2010.

[97] I. Lucio-Martinez, P. Chan, X. Mo, S. Hosier, and W. Tittel, "Proof-of-concept of real-world quantum key distribution with quantum frames," New Journal of Physics, vol. 11, no. 9, p. 095001, 2009.

[98] H. Jones, "The recent large reduction in space launch cost," 48th International Conference on Environmental Systems, 2018.

[99] A. Lohrmann, C. Perumangatt, A. Villar, and A. Ling, "Broadband pumped polarization entangled photon-pair source in a linear beam displacement interferometer," Applied Physics Letters, vol. 116, no. 2, p. 021101, 2020.

[100] P. J. Godin, W. Wu, R. Tannous, B. Moffat, and T. Jennewein, "Birefringence compensation from polarization maintaining fiber pairs," in CLEO: Applications and Technology, pp. AM2D–6, Optica Publishing Group, 2022.

[101] J. C. McDowell, "The low earth orbit satellite population and impacts of the spacex starlink constellation," The Astrophysical Journal Letters, vol. 892, no. 2, p. L36, 2020.

[102] L. Sheridan, T. P. Le, and V. Scarani, "Finite-key security against coherent attacks in quantum key distribution," New Journal of Physics, vol. 12, no. 12, p. 123019, 2010.

[103] J. R. Johansson, P. D. Nation, and F. Nori, "Qutip: An open-source python framework for the dynamics of open quantum systems," Computer Physics Communications, vol. 183, no. 8, pp. 1760–1772, 2012.

[104] J. Johansson, P. Nation, and F. Nori, "Qutip 2: A python framework for the dynamics of open quantum systems," Computer Physics Communications, vol. 184, no. 4, pp. 1234–1240, 2013.

[105] I. George, J. Lin, and N. Lütkenhaus, "Numerical calculations of the finite key rate for general quantum key distribution protocols," Physical Review Research, vol. 3, no. 1, p. 013274, 2021.

[106] A. Boaron, G. Boso, D. Rusca, C. Vulliez, C. Autebert, M. Caloz, M. Perrenoud, G. Gras, F. Bussières, M.-J. Li, D. Nolan, A. Martin, and H. Zbinden, "Secure quantum key distribution over 421 km of optical fiber," Phys. Rev. Lett., vol. 121, p. 190502, Nov 2018.

[107] F. Bouchard, K. Bonsma-Fisher, K. Heshami, P. J. Bustard, D. England, and B. Sussman, "Measuring ultrafast time-bin qudits," arXiv preprint arXiv:2302.03045, 2023.

[108] B.-Y. Tang, H. Chen, J.-P. Wang, H.-C. Yu, L. Shi, S.-H. Sun, W. Peng, B. Liu, and W.-R. Yu, "Free-running long-distance reference-frame-independent quantum key distribution," npj Quantum Information, vol. 8, pp. 1–8, Sept. 2022. Number: 1 Publisher: Nature Publishing Group.

[109] J. Jin, S. Agne, J.-P. Bourgoin, Y. Zhang, N. Lütkenhaus, and T. Jennewein, "Demonstration of analyzers for multimode photonic time-bin qubits," Phys. Rev. A, vol. 97, p. 043847, Apr. 2018. Publisher: American Physical Society.

[110] H.-Y. Liu, X.-H. Tian, C. Gu, P. Fan, X. Ni, R. Yang, J.-N. Zhang, M. Hu, J. Guo, X. Cao, et al., "Drone-based entanglement distribution towards mobile quantum networks," National science review, vol. 7, no. 5, pp. 921–928, 2020.

[111] S.-K. Liao, W.-Q. Cai, W.-Y. Liu, L. Zhang, Y. Li, J.-G. Ren, J. Yin, Q. Shen, Y. Cao, Z.-P. Li, F.-Z. Li, X.-W. Chen, L.-H. Sun, J.-J. Jia, J.-C. Wu, X.-J. Jiang, J.-F. Wang, Y.-M. Huang, Q. Wang, Y.-L. Zhou, L. Deng, T. Xi, L. Ma, T. Hu, Q. Zhang, Y.-A. Chen, N.-L. Liu, X.-B. Wang, Z.-C. Zhu, C.-Y. Lu, R. Shu, C.-Z. Peng, J.-Y. Wang, and J.-W. Pan, "Satellite-to-ground quantum key distribution," Nature, vol. 549, pp. 43–47, Sept. 2017.

[112] X.-s. Ma, A. Qarry, J. Kofler, T. Jennewein, and A. Zeilinger, "Experimental violation of a bell inequality with two different degrees of freedom of entangled particle pairs," Physical Review A, vol. 79, no. 4, p. 042101, 2009.

[113] T. J. Herzog, P. G. Kwiat, H. Weinfurter, and A. Zeilinger, "Complementarity and the quantum eraser," Physical Review Letters, vol. 75, no. 17, p. 3034, 1995.

[114] Y.-H. Kim, R. Yu, S. P. Kulik, Y. Shih, and M. O. Scully, "Delayed "choice" quantum eraser," Physical Review Letters, vol. 84, no. 1, p. 1, 2000.

[115] B. Feng, Z. Zhao, S. Yang, T. Dou, Z. Li, J. Wang, Z. Sun, F. Zhou, Y. Han, Y. Huang, and H. Ma, "Four-state reference-frame-independent quantum key distribution using heralded pair-coherent sources with source flaws," Optoelectronics Letters, vol. 17, pp. 636–640, Oct. 2021.

[116] A. Anwar, C. Perumangatt, F. Steinlechner, T. Jennewein, and A. Ling, "Entangled photon-pair sources based on three-wave mixing in bulk crystals," Review of Scientific Instruments, vol. 92, no. 4, p. 041101, 2021.

[117] R. Ikuta, T. Kobayashi, S. Yasui, S. Miki, T. Yamashita, H. Terai, M. Fujiwara, T. Yamamoto, M. Koashi, M. Sasaki, et al., "Frequency down-conversion of 637 nm light to the telecommunication band for non-classical light emitted from nv centers in diamond," Optics express, vol. 22, no. 9, pp. 11205–11214, 2014.

[118] T. T. Tran, C. Elbadawi, D. Totonjian, C. J. Lobo, G. Grosso, H. Moon, D. R. Englund, M. J. Ford, I. Aharonovich, and M. Toth, "Robust multicolor single photon emission from point defects in hexagonal boron nitride," ACS nano, vol. 10, no. 8, pp. 7331–7338, 2016.

[119] S. Castelletto, "Silicon carbide single-photon sources: challenges and prospects," Materials for Quantum Technology, vol. 1, no. 2, p. 023001, 2021.

[120] Y. Arakawa and M. J. Holmes, "Progress in quantum-dot single photon sources for quantum information technologies: A broad spectrum overview," Applied Physics Reviews, vol. 7, no. 2, p. 021309, 2020.

[121] C.-Y. Lu and J.-W. Pan, "Quantum-dot single-photon sources for the quantum internet," Nature Nanotechnology, vol. 16, no. 12, pp. 1294–1296, 2021.

[122] F. Basso Basset, M. Valeri, E. Roccia, V. Muredda, D. Poderini, J. Neuwirth, N. Spagnolo, M. B. Rota, G. Carvacho, F. Sciarrino, et al., "Quantum key distribution with entangled photons generated on demand by a quantum dot," Science advances, vol. 7, no. 12, p. eabe6379, 2021.

[123] A. Ahmadi, A. Fognini, and M. E. Reimer, "Toward on-demand generation of entangled photon pairs with a quantum dot," in Recent Advances in Nanophotonics-Fundamentals and Applications, IntechOpen, 2020.

[124] R. Al Maruf, S. S. Venuturumilli, D. Bharadwaj, P. Anderson, J. Qiu, Y. Yuan, B. Semnani, S. Malik, M. Zeeshan, D. Dalacu, et al., "Single-photon source based on a quantum dot emitting at cesium wavelength," in Optical and Quantum Sensing and Precision Metrology II, vol. 12016, pp. 239–246, SPIE, 2022.

[125] A. Dréau, A. Tchebotareva, A. El Mahdaoui, C. Bonato, and R. Hanson, "Quantum frequency conversion of single photons from a nitrogen-vacancy center in diamond to telecommunication wavelengths," Physical review applied, vol. 9, no. 6, p. 064031, 2018.

[126] G. Moody, V. J. Sorger, D. J. Blumenthal, P. W. Juodawlkis, W. Loh, C. Sorace-Agaskar, A. E. Jones, K. C. Balram, J. C. Matthews, A. Laing, et al., "2022 roadmap on integrated quantum photonics," Journal of Physics: Photonics, vol. 4, no. 1, p. 012501, 2022.

[127] I. Esmaeil Zadeh, J. Chang, J. W. Los, S. Gyger, A. W. Elshaari, S. Steinhauer, S. N. Dorenbos, and V. Zwiller, "Superconducting nanowire single-photon detectors: A perspective on evolution, state-of-the-art, future developments, and applications," Applied Physics Letters, vol. 118, no. 19, p. 190502, 2021.

[128] E. Meyer-Scott, H. Hübel, A. Fedrizzi, C. Erven, G. Weihs, and T. Jennewein, "Quantum entanglement distribution with 810 nm photons through telecom fibers," Applied Physics Letters, vol. 97, no. 3, p. 031117, 2010.

[129] A. Lee, A. T. Castillo, C. Whitehill, and R. Donaldson, "Quantum bit error rate timing jitter dependency on multi-mode fibers," Opt. Express, vol. 31, pp. 6076–6087, Feb 2023.

[130] E. Meyer-Scott, "Experimental quantum communication in demanding regimes," Master's thesis, University of Waterloo, 2011.

[131] A. J. Monson and M. J. Pierce, "BIRCAM: A Near-Infrared Camera for The University of Wyoming Red Buttes Observatory," Publications of the Astronomical Society of the Pacific, vol. 121, pp. 728–734, July 2009.

[132] "Zemax opticsstudio." https://www.zemax.com/, 2023.

[133] D. R. Herriott and H. J. Schulte, "Folded optical delay lines," Applied Optics, vol. 4, no. 8, pp. 883–889, 1965.

[134] L. J. Salazar-Serrano, J. P. Torres, and A. Valencia, "A 3d printed toolbox for opto-mechanical components," PloS one, vol. 12, no. 1, p. e0169832, 2017.

[135] B. J. Winters and D. Shepler, "3d printable optomechanical cage system with enclosure," HardwareX, vol. 3, pp. 62–81, 2018.

[136] C. Zhang, N. C. Anzalone, R. P. Faria, and J. M. Pearce, "Open-source 3d-printable optics equipment," PloS one, vol. 8, no. 3, p. e59840, 2013.

[137] Z. Zhang, B. Liu, P. Wang, and P. Yan, "Design of an additive manufactured XY compliant manipulator with spatial redundant constraints," in 2016 35th Chinese Control Conference (CCC), pp. 9149–9154, July 2016. ISSN: 1934-1768.

[138] P. V. Mammini, D. Ciscel, and J. Wooten, "3d-additive manufactured optical mount," in Optomechanical Engineering 2015, vol. 9573, p. 957309, International Society for Optics and Photonics, 2015.

[139] F. Kranert, J. Budde, M. Hinkelmann, A. Wienke, J. Neumann, D. Kracht, and R. Lachmayer, "Quasi-monolithic laser system based on 3d-printed optomechanics," in Components and Packaging for Laser Systems VII, vol. 11667, p. 116670L, International Society for Optics and Photonics, 2021.

[140] S. Madkhaly, L. Coles, C. Morley, C. Colquhoun, T. Fromhold, N. Cooper, and L. Hackermüller, "Performance-optimized components for quantum technologies via additive manufacturing," arXiv preprint arXiv:2102.11874, 2021.

[141] J. Aasi, B. Abbott, R. Abbott, T. Abbott, M. Abernathy, K. Ackley, C. Adams, T. Adams, P. Addesso, R. Adhikari, et al., "Advanced ligo," Classical and quantum gravity, vol. 32, no. 7, p. 074001, 2015.

[142] O. Sigmund and S. Torquato, "Composites with extremal thermal expansion coefficients," Applied Physics Letters, vol. 69, no. 21, pp. 3203–3205, 1996.

[143] G. D. Barrera, J. A. O. Bruno, T. Barron, and N. Allan, "Negative thermal expansion," Journal of Physics: Condensed Matter, vol. 17, no. 4, p. R217, 2005.

[144] F. Kroeger and C. Swenson, "Absolute linear thermal-expansion measurements on copper and aluminum from 5 to 320 k," Journal of Applied Physics, vol. 48, no. 3, pp. 853–864, 1977.

[145] J. James, J. Spittle, S. Brown, and R. Evans, "A review of measurement techniques for the thermal expansion coefficient of metals and alloys at elevated temperatures," Measurement science and technology, vol. 12, no. 3, p. R1, 2001.

[146] B. Zhang, P. Jaiswal, R. Rai, and S. Nelaturi, "Additive manufacturing of functionally graded material objects: a review," Journal of Computing and Information Science in Engineering, vol. 18, no. 4, 2018.

[147] C. Zhang, F. Chen, Z. Huang, M. Jia, G. Chen, Y. Ye, Y. Lin, W. Liu, B. Chen, Q. Shen, et al., "Additive manufacturing of functionally graded materials: A review," Materials Science and Engineering: A, vol. 764, p. 138209, 2019.

[148] S. A. Tyagi and M. Manjaiah, "Laser additive manufacturing of titanium-based functionally graded materials: A review," Journal of Materials Engineering and Performance, vol. 31, no. 8, pp. 6131–6148, 2022.

[149] M. K. Thompson, G. Moroni, T. Vaneker, G. Fadel, R. I. Campbell, I. Gibson, A. Bernard, J. Schulz, P. Graf, B. Ahuja, et al., "Design for additive manufacturing: Trends, opportunities, considerations, and constraints," CIRP annals, vol. 65, no. 2, pp. 737–760, 2016.

[150] Y. M. Wang, T. Voisin, J. T. McKeown, J. Ye, N. P. Calta, Z. Li, Z. Zeng, Y. Zhang, W. Chen, T. T. Roehling, et al., "Additively manufactured hierarchical stainless steels with high strength and ductility," Nature materials, vol. 17, no. 1, pp. 63–71, 2018.

[151] A. Khorasani, I. Gibson, J. K. Veetil, and A. H. Ghasemi, "A review of technological improvements in laser-based powder bed fusion of metal printers," The International Journal of Advanced Manufacturing Technology, vol. 108, no. 1, pp. 191–209, 2020.

[152] T. DebRoy, T. Mukherjee, J. O. Milewski, J. W. Elmer, B. Ribic, J. J. Blecher, and W. Zhang, "Scientific, technological and economic issues in metal printing and their solutions," Nature Materials, vol. 18, pp. 1026–1032, 10 2019. number: 10 publisher: Nature Publishing Group.

[153] G. Electric, "3d printing in aerospace & aviation | ge additive." https://www.ge.com/additive/additive-manufacturing/industries/aviation-aerospace, 2021. (Accessed on 06/13/2021).

[154] M. McGregor, S. Patel, S. McLachlin, and M. Vlasea, "Architectural bone parameters and the relationship to titanium lattice design for powder bed fusion additive manufacturing," Additive Manufacturing, vol. 47, p. 102273, 2021.

[155] CSIRO, "World-first surgery saves cancer patient's leg." https://www.csiro.au/en/research/health-medical/biomedical/titanium-heel, 1 2021. (Accessed on 06/13/2021).

[156] P. Whittaker, "Fraunhofer ilt and concept laser develop additive manufacturing for the automotive industry." https://www.pm-review.com/fraunhofer-ilt-and-concept-laser-develop-additive-manufacturing-for-the-automotive-industry/, 11 2012. (Accessed on 06/13/2021).

[157] L. Brock, I. Ogunsanya, H. Asgari, S. Patel, and M. Vlasea, "Relative performance of additively manufactured and cast aluminum alloys," Journal of Materials Engineering and Performance, vol. 30, no. 1, pp. 760–782, 2021.

[158] S. Patel and M. Vlasea, "Melting modes in laser powder bed fusion," Materialia, vol. 9, p. 100591, 2020.

[159] S. L. Sing, J. An, W. Y. Yeong, and F. E. Wiria, "Laser and electron-beam powder-bed additive manufacturing of metallic implants: A review on processes, materials and designs," Journal of Orthopaedic Research, vol. 34, no. 3, pp. 369–385, 2016.

[160] R. Roy, D. K. Agrawal, and H. A. McKinstry, "Very low thermal expansion coefficient materials," Annual Review of Materials Science, vol. 19, no. 1, pp. 59–81, 1989.

[161] J. J. Parise, L. L. Howell, and S. P. Magleby, "Ortho-planar linear-motion springs," Mechanism and Machine Theory, vol. 36, pp. 1281–1299, Nov. 2001.

[162] W. Zhou, L. Wang, Z. Gan, R. Wang, L. M. Qiu, and J. Pfotenhauer, "The performance comparison of Oxford and triangle flexure bearings," (Spokane, Washington, USA), pp. 1149–1156, 2012.

[163] "Comsol multphysics." https://www.comsol.com/, 2023.

[164] C. Pan, Y. Han, and J. Lu, "Design and optimization of lattice structures: A review," Applied Sciences, vol. 10, no. 18, p. 6374, 2020.

[165] R. Tannous, W. Wu, S. Vinet, C. Perumangatt, D. Sinar, A. Ling, and T. Jennewein, "Towards fully passive plug and play time-bin quantum key distribution over multi-mode channels," arXiv preprint arXiv:2302.05038, 2023.

[166] S. Carrier, M. Labrecque-Dias, R. Tannous, P. Gendron, F. Nolet, N. Roy, T. Rossignol, F. Vachon, S. Parent, T. Jennewein, et al., "Towards a multi-pixel photon-to-digital converter for time-bin quantum key distribution," Sensors, vol. 23, no. 7, p. 3376, 2023.

[167] D. Stucki, N. Brunner, N. Gisin, V. Scarani, and H. Zbinden, "Fast and simple one-way quantum key distribution," Applied Physics Letters, vol. 87, no. 19, p. 194108, 2005.

[168] K. Inoue, E. Waks, and Y. Yamamoto, "Differential phase shift quantum key distribution," Physical review letters, vol. 89, no. 3, p. 037902, 2002.

[169] F. Alam, M. Elsherif, B. AlQattan, M. Ali, I. M. G. Ahmed, A. Salih, D. S. Antonysamy, A. K. Yetisen, S. Park, and H. Butt, "Prospects for additive manufacturing in contact lens devices," Advanced Engineering Materials, vol. 23, no. 1, p. 2000941, 2021.

[170] K. Zhang, H. Qu, H. Guan, J. Zhang, X. Zhang, X. Xie, L. Yan, and C. Wang, "Design and fabrication technology of metal mirrors based on additive manufacturing: A review," Applied Sciences, vol. 11, no. 22, p. 10630, 2021.

[171] D. K. Oi, A. Ling, J. A. Grieve, T. Jennewein, A. N. Dinkelaker, and M. Krutzik, "Nanosatellites for quantum science and technology," Contemporary Physics, vol. 58, no. 1, pp. 25–52, 2017.

[172] A. Belenchia, M. Carlesso, Ö. Bayraktar, D. Dequal, I. Derkach, G. Gasbarri, W. Herr, Y. L. Li, M. Rademacher, J. Sidhu, et al., "Quantum physics in space," Physics Reports, vol. 951, pp. 1–70, 2022.

[173] I. Hussain and P. Nath, "Design of a 3d printed compact interferometric system and required phone application for small angular measurements," Review of Scientific Instruments, vol. 89, no. 10, p. 103111, 2018.

[174] F. Kranert, J. Budde, P. Neef, R. Bernhard, M. Lammers, K. Rettschlag, T. Grabe, A. Wienke, J. Neumann, H. Wiche, et al., "3d-printed, low-cost, lightweight optomechanics for a compact, low-power solid-state amplifier system," in Components and Packaging for Laser Systems VI, vol. 11261, p. 1126105, International Society for Optics and Photonics, 2020.

[175] P. McVey-White, P. Besson, M. Baudrit, H. P. Schriemer, and K. Hinzer, "Effects of lens temperature on irradiance profile and chromatic aberration for cpv optics," in AIP Conference Proceedings, vol. 1766, p. 040004, AIP Publishing LLC, 2016.

[176] L. Cohen, E. S. Matekole, Y. Sher, D. Istrati, H. S. Eisenberg, and J. P. Dowling, "Thresholded quantum lidar: exploiting photon-number-resolving detection," Physical Review Letters, vol. 123, no. 20, p. 203601, 2019.

[177] J. F. Haase, S. Grollius, S. Grosse, A. Buchner, and M. Ligges, "A 32x24 pixel spad detector system for lidar and quantum imaging," in Photonic Instrumentation Engineering VIII, vol. 11693, p. 116930M, International Society for Optics and Photonics, 2021.

[178] H. Liu, A. Helmy, and B. Balaji, "Inspiring radar from quantum-enhanced lidar," in 2020 IEEE International Radar Conference (RADAR), pp. 964–968, IEEE, 2020.

[179] A. Salmi, F. Calignano, M. Galati, and E. Atzeni, "An integrated design methodology for components produced by laser powder bed fusion (l-pbf) process," Virtual and Physical Prototyping, vol. 13, no. 3, pp. 191–202, 2018.

[180] P. C. Priarone, V. Lunetto, E. Atzeni, and A. Salmi, "Laser powder bed fusion (l-pbf) additive manufacturing: On the correlation between design choices and process sustainability," Procedia CIRP, vol. 78, pp. 85–90, 2018.

[181] H. Saito, Physics and applications of invar alloys. Maruzen, 1978.

[182] H. Asgari, M. Salarian, H. Ma, A. Olubamiji, and M. Vlasea, "On thermal expansion behavior of invar alloy fabricated by modulated laser powder bed fusion," Materials & Design, vol. 160, pp. 895–905, 2018.

[183] S. Patel, H. Chen, M. Vlasea, and Y. Zou, "The influence of divergent laser beams on the laser powder bed fusion of a high reflectivity aluminium alloy," arXiv preprint arXiv:2105.07920, 2021.

[184] J. Brendel, N. Gisin, W. Tittel, and H. Zbinden, "Pulsed energy-time entangled twin-photon source for quantum communication," Phys. Rev. Lett., vol. 82, pp. 2594–2597, Mar 1999.

[185] A. Muller, T. Herzog, B. Huttner, W. Tittel, H. Zbinden, and N. Gisin, ""plug and play" systems for quantum cryptography," Applied Physics Letters, vol. 70, no. 7, pp. 793–795, 1997.

[186] D. Stucki, N. Gisin, O. Guinnard, G. Ribordy, and H. Zbinden, "Quantum key distribution over 67 km with a plug&play system," New Journal of Physics, vol. 4, no. 1, p. 41, 2002.

[187] W. Zhang, T. van Leent, K. Redeker, R. Garthoff, R. Schwonnek, F. Fertig, S. Eppelt, W. Rosenfeld, V. Scarani, C. C.-W. Lim, et al., "A device-independent quantum key distribution system for distant users," Nature, vol. 607, no. 7920, pp. 687–691, 2022.

[188] T. van Leent, M. Bock, F. Fertig, R. Garthoff, S. Eppelt, Y. Zhou, P. Malik, M. Seubert, T. Bauer, W. Rosenfeld, et al., "Entangling single atoms over 33 km telecom fibre," Nature, vol. 607, no. 7917, pp. 69–73, 2022.

[189] W. S. Rabinovich, R. Mahon, M. S. Ferraro, P. G. Goetz, M. Bashkansky, R. E. Freeman, J. Reintjes, and J. L. Murphy, "Free space quantum key distribution using modulating retro-reflectors," Optics Express, vol. 26, no. 9, pp. 11331–11351, 2018.

[190] X. Wang, W. Liu, T. Wu, C. Guo, Y. Zhang, S. Zhao, and C. Dong, "Free space measurement device independent quantum key distribution with modulating retro-reflectors under correlated turbulent channel," Entropy, vol. 23, no. 10, p. 1299, 2021.

[191] G. Ribordy, J.-D. Gautier, N. Gisin, O. Guinnard, and H. Zbinden, "Fast and user-friendly quantum key distribution," Journal of Modern Optics, vol. 47, no. 2-3, pp. 517–531, 2000.

[192] E. MacQuarrie, C. Chartrand, D. Higginbottom, K. Morse, V. Karasyuk, S. Roorda, and S. Simmons, "Generating t centres in photonic silicon-on-insulator material by ion implantation," New Journal of Physics, vol. 23, no. 10, p. 103008, 2021.

[193] G. Hao and X. He, "Designing a monolithic tip-tilt-piston flexure manipulator," Archives of Civil and Mechanical Engineering, vol. 17, pp. 871–879, Sept. 2017.

[194] N. Lobontiu, J. S. N. Paine, E. Garcia, and M. Goldfarb, "Corner-Filleted Flexure Hinges," Journal of Mechanical Design, vol. 123, pp. 346–352, Oct. 2000.

[195] T. Lu, D. C. Handley, Y. Kuan Yong, and C. Eales, "A three-DOF compliant micromotion stage with flexure hinges," Industrial Robot, vol. 31, pp. 355–361, Aug. 2004.

[196] P. V. Mammini, D. Ciscel, and J. Wooten, "3D-additive manufactured optical mount," p. 8.

[197] S.-K. Liao, W.-Q. Cai, W.-Y. Liu, L. Zhang, Y. Li, J.-G. Ren, J. Yin, Q. Shen, Y. Cao, Z.-P. Li, et al., "Satellite-to-ground quantum key distribution," Nature, vol. 549, no. 7670, pp. 43–47, 2017.

[198] J. Yin, Y.-H. Li, S.-K. Liao, M. Yang, Y. Cao, L. Zhang, J.-G. Ren, W.-Q. Cai, W.-Y. Liu, S.-L. Li, et al., "Entanglement-based secure quantum cryptography over 1,120 kilometres," Nature, vol. 582, no. 7813, pp. 501–505, 2020.

[199] K. Mohammadi, "Design and characterization of a transceiver telescope for quantum communications with satellites," Master's thesis, University of Waterloo, 2021.

[200] M. A. Nielsen and I. L. Chuang, "Quantum computation and quantum information (cambridge series on information and the natural sciences)," 2010.

APPENDICES

Appendix A

Additional 6-state 4-state moving experiment results

The results for each moving test of Sec. 2.2 are in the tables below. In each table, the experimental details column provides the laser current used, and the experiment number.

Table A.1: Results of the moving tests across the indoor free-space channel. Pass 12 did not record any data due to a recording error. Passes with no motion data had an error in recording the trasnmitter motor data.

Laser current - Pass	Mean speed [deg/s]	Max speed [deg/s]	C	$\langle ZZ \rangle$	QBER_C	QBER_{ZZ}	Asym key rate [per coincidence]	Coin per second	Link time [s]
46mA - 1	0.42 ± 0.24	1.19	0.918 ± 0.010	0.918 ± 0.007	0.041 ± 0.005	0.041 ± 0.004	0.076	17487	59
46mA - 2	0.44 ± 0.35	1.29	0.917 ± 0.010	0.918 ± 0.009	0.041 ± 0.005	0.041 ± 0.005	0.075	16369	26
46mA - 3	0.41 ± 0.30	2.36	0.923 ± 0.018	0.907 ± 0.016	0.039 ± 0.009	0.047 ± 0.008	0.072	13214	9
46mA - 4	0.52 ± 0.35	1.42	0.903 ± 0.018	0.917 ± 0.008	0.049 ± 0.009	0.042 ± 0.004	0.069	14880	14
46mA - 5	-	-	0.919 ± 0.024	0.916 ± 0.020	0.040 ± 0.012	0.042 ± 0.010	0.075	10977	10
46mA - 6	0.34 ± 0.24	1.10	0.907 ± 0.024	0.922 ± 0.012	0.047 ± 0.012	0.039 ± 0.006	0.073	15722	31
46mA - 7	0.67 ± 0.56	1.96	0.923 ± 0.030	0.920 ± 0.016	0.038 ± 0.015	0.040 ± 0.008	0.078	15162	25
46mA - 8	0.51 ± 0.36	1.31	0.927 ± 0.018	0.927 ± 0.012	0.036 ± 0.009	0.037 ± 0.006	0.083	14729	44
46mA - 9	0.34 ± 0.31	1.42	0.934 ± 0.013	0.924 ± 0.008	0.033 ± 0.006	0.038 ± 0.004	0.084	15460	47
46mA - 10	0.46 ± 0.32	1.42	0.938 ± 0.023	0.926 ± 0.011	0.031 ± 0.011	0.037 ± 0.005	0.087	14883	37

Continued on next page

Laser current - Pass	Mean speed [deg/s]	Max speed [deg/s]	C	$\langle ZZ \rangle$	QBER_C	QBER_{ZZ}	Asym key rate [per coincidence]	Coin per second	Link time [s]
46mA - 11	0.54 ± 0.30	1.06	0.914 ± 0.021	0.924 ± 0.013	0.043 ± 0.010	0.038 ± 0.006	0.076	12475	12
46mA - 13	0.32 ± 0.27	1.87	0.926 ± 0.028	0.924 ± 0.012	0.037 ± 0.014	0.038 ± 0.006	0.081	12022	24
46mA - 14	0.38 ± 0.32	1.93	0.925 ± 0.013	0.917 ± 0.011	0.037 ± 0.006	0.042 ± 0.005	0.078	10918	27
46mA - 15	0.72 ± 0.18	2.10	0.875 ± 0.023	0.894 ± 0.019	0.062 ± 0.012	0.053 ± 0.009	0.050	7523	25
46mA - 16	0.34 ± 0.34	2.033	0.878 ± 0.026	0.884 ± 0.034	0.061 ± 0.013	0.058 ± 0.017	0.046	5055	14
39mA - 17	0.08 ± 0.05	0.1	0.939 ± 0.022	-0.949 ± 0.012	0.030 ± 0.011	0.025 ± 0.006	0.099	3083	439
39mA - 18	0.4 ± 0.31	1.42	0.952 ± 0.019	-0.954 ± 0.010	0.024 ± 0.009	0.023 ± 0.005	0.107	2863	146
41mA - 19	0.21 ± 0.19	1.83	0.938 ± 0.035	-0.941 ± 0.091	0.031 ± 0.018	0.030 ± 0.046	0.094	2654	473
39mA - 20	0.42 ± 0.24	1.15	0.938 ± 0.029	-0.962 ± 0.013	0.031 ± 0.015	0.019 ± 0.017	0.106	1599	208
48mA - 21	0.27 ± 0.20	1.60	0.870 ± 0.022	-0.906 ± 0.013	0.065 ± 0.011	0.047 ± 0.017	0.053	4030	286
39mA - 22	0.32 ± 0.22	1.05	0.952 ± 0.021	-0.952 ± 0.011	0.024 ± 0.011	0.024 ± 0.016	0.106	2731	277

Continued on next page

Laser current - Pass	Mean speed [deg/s]	Max speed [deg/s]	C	$\langle ZZ \rangle$	QBER_C	QBER_{ZZ}	Asym key rate [per coincidence]	Coin per second	Link time [s]
39mA - 23	0.35 ± 0.21	1.20	0.950 ± 0.017	-0.954 ± 0.013	0.025 ± 0.008	0.023 ± 0.016	0.107	2634	79
40mA - 24	0.33 ± 0.25	1.15	0.986 ± 0.036	-0.959 ± 0.012	0.007 ± 0.018	0.021 ± 0.016	0.127	1965	250
40mA - 25	-	-	0.889 ± 0.044	-0.965 ± 0.012	0.055 ± 0.022	0.018 ± 0.013	0.089	1540	280
39mA - 26	0.37 ± 0.25	1.23	0.916 ± 0.038	-0.969 ± 0.013	0.042 ± 0.019	0.016 ± 0.007	0.101	1427	263
39mA - 27	0.47 ± 0.25	1.17	0.955 ± 0.123	-0.830 ± 0.494	0.022 ± 0.061	0.085 ± 0.087	0.056	1186	57
39mA - 28	0.19 ± 0.17	1.04	0.923 ± 0.035	-0.905 ± 0.326	0.038 ± 0.017	0.048 ± 0.063	0.071	1322	144
39mA - 29	0.31 ± 0.20	1.11	0.921 ± 0.036	-0.961 ± 0.015	0.039 ± 0.018	0.020 ± 0.017	0.098	1481	286
48mA - 30	0.26 ± 0.1892	1.00	0.891 ± 0.017	-0.913 ± 0.012	0.054 ± 0.008	0.044 ± 0.016	0.063	4081	313

Table A.2: Key estimation results of the moving tests across the indoor free-space channel based on Eq. 2.4. The key estimation is for the block size that produced the largest key. Entries with * are for an experiment that pass is artifitially lengthened to produce positive key. Pass 12 did not record any data due to a recording error.

Laser current - Pass	Key rate bits	Block size [s]	Link time [s]
46mA - 1	47357	59	59
46mA - 2	38258*	52	26
46mA - 3	-	-	9
46mA - 4	35743*	56	14
46mA - 5	12004*	40	10
46mA - 6	11922	31	31
46mA - 7	10393	20	25
46mA - 8	31260	44	44
46mA - 9	33122	40	47
46mA - 10	56640*	74	37
46mA - 11	26067*	69	12
46mA - 13	-	-	24
46mA - 14	62583 *	108	27
46mA - 15	1523*	50	25
46mA - 16	-	-	14
39mA - 17	117102	129	439
39mA - 18	39640	146	146
41mA - 19	169575	235	473
39mA - 20	25708	111	208
48mA - 21	68937	286	286
39mA - 22	114978	253	277
39mA - 23	138424*	316	79
40mA - 24	484003*	960	250
40mA - 25	36539	152	280

Continued on next page

Laser current - Pass	Key rate bits	Block size [s]	Link time [s]
39mA - 26	30644	187	263
39mA - 27	5672*	102	57
39mA - 28	15221	133	144
39mA - 29	30325	286	286
48mA - 30	142324	205	313

Table A.3: Results of the static tests across the indoor free-space channel.

Laser current - Pass	C	$\langle ZZ \rangle$	QBER_C	QBER_{ZZ}	Asym key rate [per coincidence]	Coin per second	Link time [s]
46mA - static-1	0.892 ± 0.016	0.902 ± 0.010	0.054 ± 0.008	0.049 ± 0.005	0.059	13101	29
46mA - static-2	0.909 ± 0.023	0.906 ± 0.009	0.045 ± 0.011	0.047 ± 0.004	0.066	14230	29
41mA - static-3	0.936 ± 0.018	-0.934 ± 0.012	0.032 ± 0.009	0.033 ± 0.006	0.090	3262	220
41mA - static-4	0.934 ± 0.018	-0.939 ± 0.013	0.033 ± 0.009	0.031 ± 0.006	0.092	3269	355
39mA - static-5	0.885 ± 0.038	0.877 ± 0.034	0.058 ± 0.019	0.061 ± 0.017	0.046	9495	550
39mA - static-6	0.940 ± 0.023	-0.956 ± 0.012	0.030 ± 0.011	0.022 ± 0.006	0.103	2868	171
39mA - static-7	0.938 ± 0.021	-0.957 ± 0.010	0.031 ± 0.010	0.021 ± 0.005	0.103	3066	181
48mA - static-8	0.916 ± 0.017	-0.915 ± 0.008	0.042 ± 0.009	0.042 ± 0.004	0.073	8856	70

Table A.4: Key estimation results of the static tests across the indoor free-space channel based on Eq. 2.4. Entries with * are for an experiment that pass is artifitially lengthened to produce positive key.

Laser current - Pass	key rate bits	Block size [s]	Link time [s]
46mA-static-1	64508*	116	29
46mA - static-2	31724*	58	29
41mA - static-3	97346	220	220
41mA - static-4	152216	182	355
39mA - static-5	389565	157	550
39mA - static-6	15506	47	171
39mA - static-7	52546	121	181
48mA - static-8	55436	70	70

Appendix B

Additional RFI time bin experiment results

For each quantum channel of Sec. 3.1, several experiments were conducted and the results are in the tables below. In each table, the experimental details column provides the laser current used, the experiment type (i.e. with a piezoelectric actuator inducing a phase change), and the presence of a 3 nm 785 band pass filter. In the tables, p indicates the presence of the piezoelectric actuator inducing a relative phase change, while np indicates that there is no piezoelectric actuator induced phase change. The presence of the band pass filter is indicated by BPF.

Table B.1: Results of the RFI time bin tests across polarization maintaining fiber channel. This channel is when the output PMF of the PTC is coupled directly to the input of the TA. No accidental background coincidences are subtracted in obtaining these results. In the experimental details p indicates the presence of the piezoelectric actuator, while np is no piezoelectric actuator. Entries with * are for an experiment that is double in length.

Experiment details	C	$\langle ZZ \rangle$	QBER_C	QBER_{ZZ}	Asym key rate [per coincidence]	Coin per second	Link time [s]	Key rate bits
40mA, np	0.879 ± 0.016	0.958 ± 0.009	0.060 ± 0.008	0.021 ± 0.005	0.082	7719	20	8044*
40mA, p	0.866 ± 0.024	0.961 ± 0.010	0.067 ± 0.012	0.020 ± 0.005	0.079	7094	20	-
40mA, np	0.874 ± 0.014	0.954 ± 0.009	0.063 ± 0.007	0.023 ± 0.004	0.078	8630	20	7168*
40mA, np	0.877 ± 0.014	0.954 ± 0.010	0.061 ± 0.007	0.023 ± 0.005	0.079	8356	60	13474
40mA, np, BPF	0.846 ± 0.039	0.975 ± 0.021	0.077 ± 0.019	0.012 ± 0.011	0.082	1279	60	-
40mA, np, BPF	0.852 ± 0.031	0.972 ± 0.021	0.074 ± 0.015	0.014 ± 0.011	0.082	1344	30	-
40mA, p	0.865 ± 0.023	0.957 ± 0.009	0.068 ± 0.011	0.022 ± 0.004	0.077	7953	20	-
40mA, p	0.878 ± 0.028	0.955 ± 0.010	0.061 ± 0.014	0.023 ± 0.005	0.080	8212	60	-
40mA, p	0.871 ± 0.018	0.955 ± 0.008	0.065 ± 0.009	0.023 ± 0.004	0.077	8518	20	-

Continued on next page

Experiment details	C	$\langle ZZ \rangle$	$QBER_C$	$QBER_{ZZ}$	Asym key rate [per coincidence]	Coin per second	Link time [s]	Key rate bits
40mA, p, BPF	0.864 ± 0.033	0.976 ± 0.017	0.068 ± 0.016	0.012 ± 0.009	0.088	1790	30	-
40mA, p, BPF	0.864 ± 0.042	0.969 ± 0.018	0.068 ± 0.021	0.015 ± 0.009	0.084	1837	30	-
43mA, np	0.887 ± 0.020	0.934 ± 0.010	0.056 ± 0.010	0.033 ± 0.005	0.072	12754	20	9773*
43mA, np, BPF	0.897 ± 0.020	0.941 ± 0.011	0.052 ± 0.010	0.030 ± 0.006	0.079	6888	60	4043
43mA, np, BPF	0.901 ± 0.028	0.940 ± 0.013	0.049 ± 0.014	0.030 ± 0.007	0.080	7343	60	5738
43mA, p	0.865 ± 0.018	0.938 ± 0.010	0.067 ± 0.009	0.031 ± 0.005	0.067	12662	20	-
43mA, p	0.848 ± 0.016	0.936 ± 0.010	0.076 ± 0.008	0.032 ± 0.005	0.061	12575	20	-
43mA, p, BPF	0.883 ± 0.023	0.940 ± 0.012	0.059 ± 0.011	0.030 ± 0.006	0.074	6880	30	-
43mA, p, BPF	0.892 ± 0.018	0.942 ± 0.011	0.054 ± 0.009	0.029 ± 0.006	0.078	7550	30	-
44mA, p, BPF	0.875 ± 0.018	0.917 ± 0.013	0.062 ± 0.009	0.042 ± 0.006	0.060	7747	60	-

Table B.2: Results of the RFI time bin tests across a 5 m single mode fiber channel. No accidental background coincidences are subtracted in obtaining these results. In the experimental details p indicates the presence of the piezoelectric actuator, while np is no piezoelectric actuator.

Experiment details	C	$\langle ZZ \rangle$	QBER$_C$	QBER$_{ZZ}$	Asym key rate [per coincidence]	Coin per second	Link time [s]	Key rate bits
40mA, p	0.876 ± 0.027	0.956 ± 0.013	0.062± 0.014	0.022± 0.006	0.0798	6276	60	-
40mA, p, BPF	0.885 ± 0.035	0.973 ± 0.020	0.058± 0.018	0.014± 0.010	0.0928	1834	30	-
40mA, p, BPF	0.919 ± 0.028	0.973 ± 0.020	0.040± 0.014	0.014± 0.010	0.1052	1945	15	-
40mA, np, BPF	0.899 ± 0.043	0.976 ± 0.015	0.051± 0.022	0.012± 0.008	0.0996	1863	60	-
43mA, p	0.854 ± 0.023	0.931 ± 0.012	0.073± 0.012	0.034± 0.006	0.0599	8983	30	-
43mA, p, BPF	0.877 ± 0.029	0.940 ± 0.017	0.062± 0.014	0.030± 0.009	0.0714	4885	30	-
43mA,np, BPF	0.862 ± 0.033	0.938 ± 0.016	0.069 ± 0.017	0.031± 0.008	0.0656	4896	60	-

Table B.3: Results of the RFI time bin tests across a 5 m multi mode fiber channel. No accidental background coincidences are subtracted in obtaining these results. In the experimental details p indicates the presence of the piezoelectric actuator, while np is no piezoelectric actuator. Finite size secret bit entries with * are for an experiment that is double in length.

Experiment details	C	$\langle ZZ \rangle$	QBER_C	QBER_{ZZ}	Asym key rate [per coincidence]	Coin per second	Link time [s]	Key rate bits
40mA, np	0.875 ± 0.017	0.956 ± 0.011	0.062 ± 0.008	0.022 ± 0.005	0.079	7148	20	7321*
40mA, np, BPF	0.890 ± 0.023	0.974 ± 0.013	0.055 ± 0.012	0.013 ± 0.007	0.095	2089	60	-
40mA, np, BPF	0.902 ± 0.016	0.984 ± 0.013	0.049 ± 0.008	0.008 ± 0.006	0.106	2137	30	-
40mA, p	0.867 ± 0.031	0.957 ± 0.011	0.066 ± 0.015	0.021 ± 0.006	0.078	7114	60	-
40mA, p	0.883 ± 0.024	0.958 ± 0.009	0.059 ± 0.012	0.021 ± 0.004	0.083	7135	20	-
40mA, p	0.861 ± 0.021	0.958 ± 0.010	0.069 ± 0.011	0.021 ± 0.005	0.076	7090	20	-
40mA, p	0.885 ± 0.020	0.958 ± 0.013	0.057 ± 0.010	0.021 ± 0.007	0.084	6684	30	-
40mA, p, BPF	0.910 ± 0.030	0.979 ± 0.011	0.045 ± 0.015	0.011 ± 0.006	0.105	2067	30	-
40mA, p, BPF	0.900 ± 0.031	0.969 ± 0.014	0.050 ± 0.016	0.015 ± 0.007	0.095	2146	30	-
43mA, np, BPF	0.919 ± 0.019	0.944 ± 0.014	0.040 ± 0.010	0.028 ± 0.007	0.088	5829	60	4911

Continued on next page

Experiment details	C	$\langle ZZ \rangle$	$QBER_C$	$QBER_{ZZ}$	Asym key rate [per coincidence]	Coin per second	Link time [s]	Key rate bits
43mA, np, BPF	0.920 ± 0.015	0.941 ± 0.012	0.040 ± 0.008	0.029 ± 0.006	0.087	6164	30	6387
43mA, p	0.870 ± 0.013	0.936 ± 0.013	0.065 ± 0.006	0.032 ± 0.006	0.067	10350	20	-
43mA, p, BPF	0.889 ± 0.028	0.944 ± 0.014	0.056 ± 0.014	0.028 ± 0.007	0.078	5827	30	-
43mA, p, BPF	0.870 ± 0.025	0.942 ± 0.013	0.065 ± 0.013	0.029 ± 0.006	0.070	5894	30	-
44mA, p, BPF	0.854 ± 0.053	0.918 ± 0.014	0.073 ± 0.027	0.041 ± 0.007	0.054	7404	60	-

Table B.4: Results of the RFI time bin tests across a 10 m multi mode fiber channel. No accidental background coincidences are subtracted in obtaining these results. In the experimental details p indicates the presence of the piezoelectric actuator, while np is no piezoelectric actuator.

Experiment details	C	$\langle ZZ \rangle$	QBER_C	QBER_{ZZ}	Asym key rate [per coincidence]	Coin per second	Link time [s]	Key rate bits
40mA, np	0.864 ± 0.014	0.959 ± 0.011	0.068 ± 0.007	0.020 ± 0.005	0.078	7199	60	7198
40mA, np, BPF	0.908 ± 0.035	0.977 ± 0.016	0.046 ± 0.017	0.012 ± 0.008	0.103	2321	58	-
40mA, np, BPF	0.922 ± 0.034	0.970 ± 0.017	0.039 ± 0.017	0.015 ± 0.009	0.105	2426	30	-
40mA, p	0.876 ± 0.024	0.958 ± 0.009	0.062 ± 0.012	0.021 ± 0.004	0.081	7524	20	-
40mA, p	0.887 ± 0.024	0.957 ± 0.012	0.057 ± 0.012	0.021 ± 0.006	0.084	7581	20	-
40mA, p, BPF	0.898 ± 0.042	0.979 ± 0.017	0.051 ± 0.021	0.011 ± 0.008	0.101	2310	30	-
40mA, p, BPF	0.908 ± 0.030	0.977 ± 0.013	0.046 ± 0.015	0.011 ± 0.006	0.104	2387	30	-
43mA, np	0.845 ± 0.021	0.937 ± 0.011	0.078 ± 0.011	0.031 ± 0.006	0.060	10712	60	9983
43mA, np, BPF	0.926 ± 0.027	0.943 ± 0.013	0.037 ± 0.014	0.028 ± 0.007	0.091	6714	60	8180
43mA, np, BPF	0.906 ± 0.022	0.940 ± 0.013	0.047 ± 0.011	0.030 ± 0.006	0.082	6875	20	-

Continued on next page

Experiment details	C	$\langle ZZ \rangle$	$QBER_C$	$QBER_{ZZ}$	Asym key rate [per coincidence]	Coin per second	Link time [s]	Key rate bits
43mA, p	0.877 ± 0.012	0.939 ± 0.012	0.062 ± 0.006	0.030 ± 0.006	0.071	11109	20	-
43mA, p, BPF	0.879 ± 0.024	0.939 ± 0.014	0.061 ± 0.012	0.031 ± 0.007	0.071	6581	30	-
43mA, p, BPF	0.879 ± 0.024	0.942 ± 0.012	0.061 ± 0.012	0.029 ± 0.006	0.073	7066	30	-
44mA, p, BPF	0.882 ± 0.030	0.918 ± 0.015	0.059 ± 0.015	0.041 ± 0.007	0.063	6284	60	-

Table B.5: Results of the RFI time bin tests across a 15 m multi mode fiber channel. No accidental background coincidences are subtracted in obtaining these results. In the experimental details p indicates the presence of the piezoelectric actuator, while np is no piezoelectric actuator. Entries with * are for an experiment that is double in length.

Experiment details	C	$\langle ZZ \rangle$	QBER_C	QBER_{ZZ}	Asym key rate [per coincidence]	Coin per second	Link time [s]	Key rate bits
40mA,np	0.867 ± 0.018	0.957 ± 0.012	0.066 ± 0.009	0.022 ± 0.006	0.078	6936	60	6476
40mA, np, BPF	0.886 ± 0.018	0.954 ± 0.009	0.057 ± 0.009	0.023 ± 0.005	0.082	7015	20	-
40mA, np, BPF	0.910 ± 0.032	0.967 ± 0.017	0.045 ± 0.016	0.016 ± 0.009	0.098	2220	30	-
40mA, p,	0.876 ± 0.022	0.957 ± 0.010	0.062 ± 0.011	0.021 ± 0.005	0.080	6981	60	-
40mA, p	0.878 ± 0.016	0.958 ± 0.013	0.061 ± 0.008	0.021 ± 0.007	0.081	6951	20	-
40mA, p	0.868 ± 0.017	0.956 ± 0.013	0.066 ± 0.009	0.022 ± 0.006	0.077	6928	20	-
40mA, p, BPF	0.898 ± 0.033	0.977 ± 0.015	0.051 ± 0.017	0.011 ± 0.008	0.100	2327	30	-
43mA, np	0.866 ± 0.021	0.936 ± 0.012	0.067 ± 0.011	0.032 ± 0.006	0.066	10292	20	4323*
43mA, np, BPF	0.893 ± 0.018	0.946 ± 0.013	0.053 ± 0.009	0.027 ± 0.007	0.080	6372	60	2592
43mA, np, BPF	0.901 ± 0.017	0.941 ± 0.015	0.049 ± 0.008	0.029 ± 0.008	0.081	6701	30	4464*

Continued on next page

Experiment details	C	$\langle ZZ \rangle$	QBER_C	QBER_{ZZ}	Asym key rate [per coincidence]	Coin per second	Link time [s]	Key rate bits
43mA, p	0.843 ± 0.016	0.936 ± 0.008	0.078 ± 0.008	0.032 ± 0.004	0.059	10147	20	-
43mA, p, BPF	0.892 ± 0.032	0.941 ± 0.012	0.054 ± 0.016	0.030 ± 0.006	0.077	6453	30	-
43mA, p, BPF	0.897 ± 0.014	0.945 ± 0.012	0.051 ± 0.007	0.028 ± 0.006	0.081	6636	30	-
44mA, p, BPF	0.873 ± 0.023	0.932 ± 0.013	0.063 ± 0.011	0.034 ± 0.007	0.066	7248	60	-

Appendix C

Additional PORI Design Information

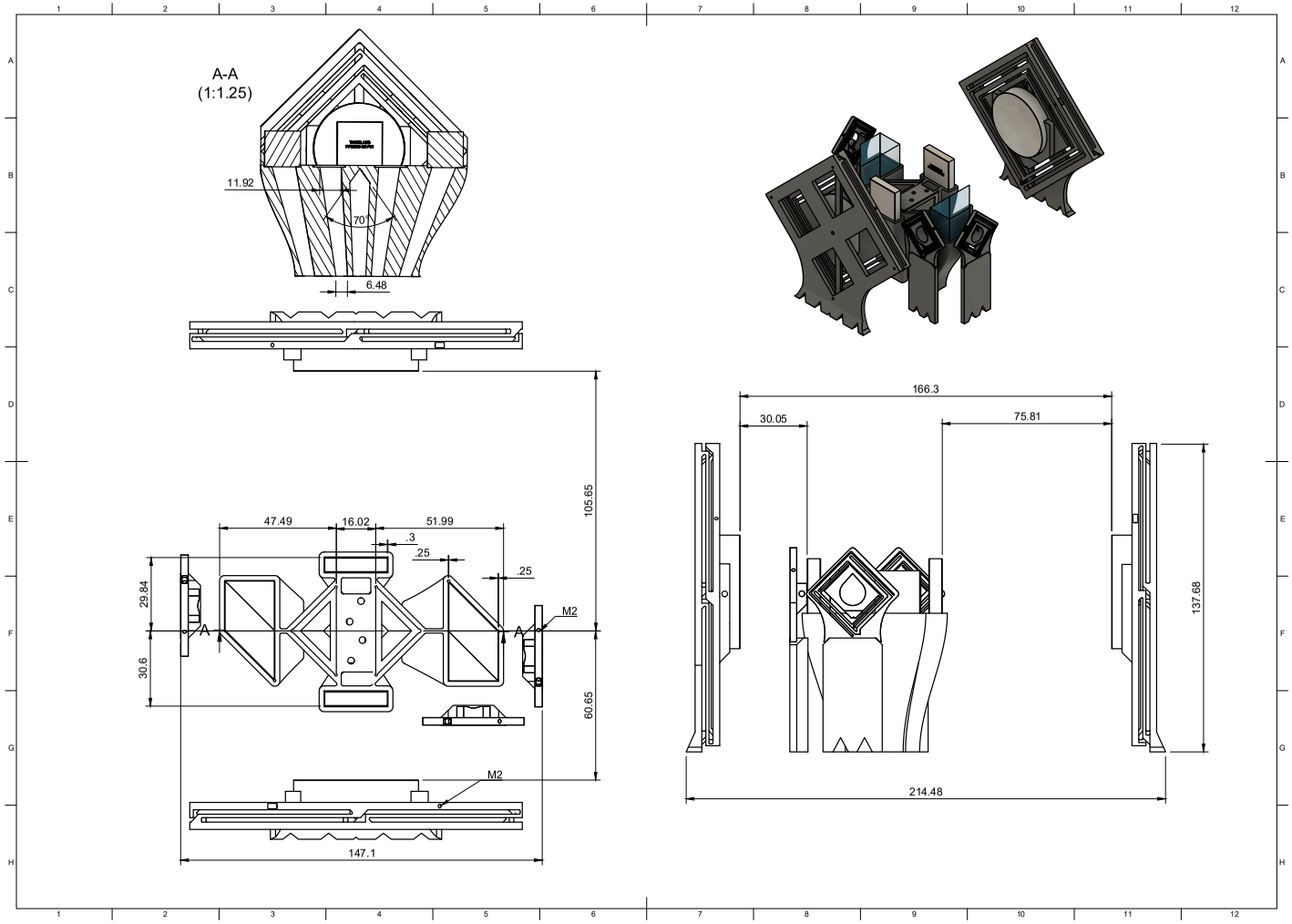

Figure C.1: CAD drawing of the PORI with some dimensions of interest shown

Appendix D

Thermal Analysis Tables

Additional tables from the algebraic thermal analysis of Sec. 5.2.2. Table D.1 and Table D.2 are for Titanium64-100 and Invar36 combination. While Table D.3 and Table D.4 are for other metals allows. The expansion joint is placed in the path that is for the curved mirror with radius R1.

Table D.1: Simulation results for the algebraic thermal analysis of several ORI configurations for Titanium64-100 as metal 1 and Invar36 as metal 2. These results are for scenario 1 over a 10 °C temperature range ($\Delta T = 10$). The standard deviation is average of the distribution of solutions for d_{mat_2}. Here only configurations with time delays of greater than 0.5 ns are considered.

R1 [m]	R2 [m]	Bounce 1	Bounce 2	Time Delay [ns]	d_{mat_2} [mm]	std (10^{-14}) [mm]
0.1500	0.1000	2	8	0.6810	3.8392	0.0000
0.1500	0.1000	2	6	0.6088	13.1581	0.3469
0.1500	0.1000	2	4	0.5010	28.7825	0.3469
0.1500	0.1500	2	8	0.5191	20.9416	0.0000
0.2000	0.1000	4	8	0.6808	5.8331	0.0867
0.2000	0.1000	4	6	0.6086	15.1520	0.3469
0.2000	0.1000	4	4	0.5008	30.7763	0.6939
0.2000	0.1000	2	6	0.9419	7.0690	0.0867
0.2000	0.1000	2	4	0.8341	22.6933	0.3469
0.2000	0.1500	4	8	0.5189	22.9354	0.3469
0.2000	0.1500	2	8	0.8521	14.8524	0.0000

Continued on next page

R1 [m]	R2 [m]	Bounce 1	Bounce 2	Time Delay [ns]	d_{mat_2} [mm]	std (10^{-14}) [mm]
0.2000	0.1500	2	6	0.7276	28.7807	0.3469
0.2000	0.2000	2	8	0.6909	31.7058	0.0000
0.3000	0.1000	8	8	0.6454	8.0740	0.1735
0.3000	0.1000	8	6	0.5732	17.3930	0.3469
0.3000	0.1000	6	8	0.8608	4.1886	0.0867
0.3000	0.1000	6	6	0.7886	13.5075	0.1735
0.3000	0.1000	6	4	0.6808	29.1318	0.6939
0.3000	0.1000	4	6	1.1100	6.9939	0.0867
0.3000	0.1000	4	4	1.0021	22.6182	0.0000
0.3000	0.1000	2	4	1.5019	10.4714	0.1735
0.3000	0.1000	2	2	1.3352	39.2944	0.0000
0.3000	0.1500	6	8	0.6988	21.2909	0.3469
0.3000	0.1500	6	6	0.5743	35.2192	0.0000
0.3000	0.1500	4	8	1.0202	14.7773	0.3469
0.3000	0.1500	4	6	0.8957	28.7056	0.0000
0.3000	0.1500	2	8	1.5200	2.6305	0.0000
0.3000	0.1500	2	6	1.3954	16.5588	0.3469
0.3000	0.1500	2	4	1.2677	39.9324	0.0000
0.3000	0.2000	6	8	0.5376	38.1443	0.6939
0.3000	0.2000	4	8	0.8590	31.6307	0.6939
0.3000	0.2000	2	8	1.3588	19.4839	0.3469
0.3000	0.2000	2	6	1.2152	38.0316	0.6939

Table D.2: Simulation results for the algebraic thermal analysis of several ORI configurations for Titanium64-100 as metal 1 and Invar36 as metal 2. These results are for scenario 2 over a 10 °C temperature range ($\Delta T = 10$). The standard deviation is average of the distribution of solutions for d_{mat_2}. Here only configurations with time delays of greater than 0.5 ns are considered.

R1 [m]	R2 [m]	Bounce 1	Bounce 2	Time Delay [ns]	d_{mat_2} [mm]	std (10^{-14}) [mm]
0.1500	0.1000	2	8	0.6810	46.8279	0.6939
0.1500	0.1000	2	6	0.6088	42.3686	0.0000
0.1500	0.1000	2	4	0.5010	34.8919	0.6939
0.1500	0.1500	2	8	0.5191	38.6440	0.6939
0.2000	0.1000	4	8	0.6808	24.6842	0.3469
0.2000	0.1000	4	6	0.6086	21.9316	0.6939
0.2000	0.1000	4	4	0.5008	17.3166	0.3469
0.2000	0.1000	2	8	1.0141	68.9938	0.0000
0.2000	0.1000	2	6	0.9419	64.4499	0.0000
0.2000	0.1000	2	4	0.8341	56.8315	0.0000
0.2000	0.1000	2	2	0.6674	42.7776	0.6939
0.2000	0.1500	4	8	0.5189	19.6326	0.0000
0.2000	0.1500	2	8	0.8521	60.6548	2.0817
0.2000	0.1500	2	6	0.7276	53.8634	1.3878
0.2000	0.1500	2	4	0.5999	42.4665	0.6939
0.2000	0.2000	2	8	0.6909	52.4371	0.6939
0.2000	0.2000	2	6	0.5474	43.3933	0.6939
0.3000	0.1000	8	8	0.6454	9.5696	0.1735
0.3000	0.1000	8	6	0.5732	8.2486	0.0000
0.3000	0.1000	6	8	0.8608	20.1801	0.0000
0.3000	0.1000	6	6	0.7886	18.2079	0.3469
0.3000	0.1000	6	4	0.6808	14.9013	0.3469
0.3000	0.1000	6	2	0.5141	8.8014	0.3469
0.3000	0.1000	4	8	1.1822	44.7139	0.6939
0.3000	0.1000	4	6	1.1100	41.7803	0.6939
0.3000	0.1000	4	4	1.0021	36.8616	0.6939
0.3000	0.1000	4	2	0.8355	27.7879	0.3469
0.3000	0.1000	2	8	1.6819	113.2602	0.0000
0.3000	0.1000	2	6	1.6097	108.6529	1.3878

Continued on next page

R1 [m]	R2 [m]	Bounce 1	Bounce 2	Time Delay [ns]	d_{mat_2} [mm]	std (10^{-14}) [mm]
0.3000	0.1000	2	4	1.5019	100.9283	1.3878
0.3000	0.1000	2	2	1.3352	86.6783	1.3878
0.3000	0.1500	6	8	0.6988	16.5607	0.0000
0.3000	0.1500	6	6	0.5743	13.6130	0.1735
0.3000	0.1500	4	8	1.0202	39.3300	0.6939
0.3000	0.1500	4	6	0.8957	34.9452	0.6939
0.3000	0.1500	4	4	0.7679	27.5870	0.0000
0.3000	0.1500	4	2	0.5012	13.9073	0.1735
0.3000	0.1500	2	8	1.5200	104.8048	0.0000
0.3000	0.1500	2	6	1.3954	97.9187	1.3878
0.3000	0.1500	2	4	1.2677	86.3629	0.0000
0.3000	0.1500	2	2	1.0009	64.8793	0.0000
0.3000	0.2000	6	8	0.5376	12.9940	0.0000
0.3000	0.2000	4	8	0.8590	34.0244	0.6939
0.3000	0.2000	4	6	0.7155	28.1854	0.3469
0.3000	0.2000	4	4	0.5013	18.4057	0.0000
0.3000	0.2000	2	8	1.3588	96.4726	0.0000
0.3000	0.2000	2	6	1.2152	87.3027	1.3878
0.3000	0.2000	2	4	1.0011	71.9438	1.3878
0.3000	0.2000	2	2	0.6678	43.3042	0.0000
0.3000	0.3000	4	8	0.5367	23.4616	0.3469
0.3000	0.3000	2	8	1.0365	79.8840	1.3878
0.3000	0.3000	2	6	0.8211	66.1171	0.0000

Table D.3: Simulation results for the algebraic thermal analysis of several ORI configurations for various metal alloys. These results are for scenario 1 over a 10 °C temperature range ($\Delta T = 10$). The standard deviation is average of the distribution of solutions for d_{mat_2}. Here only configurations with time delays of greater than 0.5 ns, and R1 and R2 > 0.15m. Furthermore, Bounce 1 and Bounce 2 are shortened to B1 and B2 to provide space.

metal1	metal2	R1 [m]	R2 [m]	B1	B2	pdiff [ns]	d_{mat_2} [mm]	std [mm]
301	AL 2014	0.3000	0.2000	2	8	0.5367	25.9459	1.6121
301	AL 2219	0.3000	0.2000	2	8	1.0011	27.4504	0.2122
301	FE 17-7PH	0.3000	0.2000	2	8	1.0009	20.0950	0.6329
301	A286	0.3000	0.3000	4	8	0.9419	27.3144	0.9035
301	A286	0.3000	0.3000	2	6	0.6674	5.3636	1.3700
301	410	0.3000	0.2000	2	6	0.6810	35.6945	0.2212
410	AL 2219	0.2000	0.2000	6	8	0.6674	5.7465	1.8894
410	FE 17-7PH	0.3000	0.2000	4	2	0.8608	31.6055	5.8576
410	RonHI	0.2000	0.2000	2	8	0.6810	26.2823	2.9766
410	RonHI	0.3000	0.2000	6	8	0.6086	39.6943	2.2975
410	RonHI	0.3000	0.2000	4	8	1.0141	11.9397	3.7028
A286	AL 2014	0.2000	0.2000	2	8	1.2152	16.1543	1.9944
A286	AL 2219	0.2000	0.2000	2	8	1.0021	18.3923	0.7223
A286	AL 2219	0.3000	0.3000	2	8	0.6678	32.8402	1.0850
A286	AL 5456	0.2000	0.2000	2	8	1.0141	6.3654	2.2312
A286	AL 5456	0.3000	0.2000	6	8	0.5474	24.3215	1.7221
A286	AL 5456	0.3000	0.2000	2	4	0.5732	26.3185	3.2110
A286	AL 5456	0.3000	0.3000	2	8	0.6808	14.7730	3.3517
A286	347	0.2000	0.2000	2	8	1.0202	3.4184	1.0554
A286	347	0.3000	0.2000	6	8	0.6678	22.0468	0.8146
A286	410	0.2000	0.2000	4	8	0.6674	31.2760	0.1598
A286	410	0.3000	0.2000	6	8	0.6909	5.5913	0.2361
AL 2219	RonHI	0.2000	0.2000	4	8	0.6988	38.7324	3.2110
AL 2219	RonHI	0.3000	0.2000	4	6	0.5013	14.9247	6.3666
AL 5456	RonHI	0.2000	0.2000	2	8	0.5732	10.7204	1.8789
AL 5456	RonHI	0.3000	0.2000	4	6	0.8957	29.7865	1.9461
AL 5456	RonHI	0.3000	0.2000	2	4	1.5200	32.5860	2.7040
AL 7079	AL X2020	0.2000	0.2000	2	6	0.6086	18.8690	6.4889

Continued on next page

metal1	metal2	R1 [m]	R2 [m]	B1	B2	pdiff [ns]	d_{mat_2} [mm]	std [mm]
AL 7079	AL 7075	0.2000	0.2000	4	8	0.5013	36.8371	2.4906
AL 7079	AL 7075	0.2000	0.2000	2	6	1.3588	33.6921	3.7750

Table D.4: Simulation results for the algebraic thermal analysis of several ORI configurations for various metal alloys. These results are for scenario 2 over a 10 °C temperature range ($\Delta T = 10$). The standard deviation is average of the distribution of solutions for d_{mat_2}. Here only configurations with time delays of greater than 0.5 ns, R1 and R2 $>$ 0.15m, and an std<0.25mm are considered. Furthermore, Bounce 1 and Bounce 2 are shortened to B1 and B2 to provide space.

metal1	metal2	R1 [m]	R2 [m]	B1	B2	pdiff [ns]	d_{mat_2} [mm]	std [mm]
301	AL 2014	0.3000	0.2000	6	8	0.5376	21.9697	0.1342
301	AL 2014	0.3000	0.2000	4	4	0.5013	30.5520	0.1867
301	AL 2014	0.3000	0.3000	4	8	0.5367	33.2224	0.2030
301	AL X2020	0.3000	0.2000	6	8	0.5376	13.8717	0.1399
301	AL X2020	0.3000	0.2000	4	4	0.5013	19.2905	0.1946
301	AL X2020	0.3000	0.3000	4	8	0.5367	20.9767	0.2116
301	AL 2219	0.2000	0.2000	2	8	0.6909	65.2063	0.0528
301	AL 2219	0.2000	0.2000	2	6	0.5474	51.6306	0.0418
301	AL 2219	0.3000	0.2000	6	8	0.5376	21.8445	0.0177
301	AL 2219	0.3000	0.2000	4	8	0.8590	52.3707	0.0424
301	AL 2219	0.3000	0.2000	4	6	0.7155	43.6058	0.0353
301	AL 2219	0.3000	0.2000	4	4	0.5013	30.3777	0.0246
301	AL 2219	0.3000	0.2000	2	8	1.3588	129.6911	0.1049
301	AL 2219	0.3000	0.2000	2	6	1.2152	115.9261	0.0938
301	AL 2219	0.3000	0.2000	2	4	1.0011	95.1518	0.0770
301	AL 2219	0.3000	0.2000	2	2	0.6678	63.5754	0.0514
301	AL 2219	0.3000	0.3000	4	8	0.5367	33.0329	0.0267
301	AL 2219	0.3000	0.3000	2	8	1.0365	99.3217	0.0804
301	AL 2219	0.3000	0.3000	2	6	0.8211	78.6598	0.0636
301	AL 5456	0.3000	0.2000	6	8	0.5376	22.4958	0.1430
301	AL 5456	0.3000	0.2000	4	4	0.5013	31.2836	0.1989
301	AL 5456	0.3000	0.3000	4	8	0.5367	34.0179	0.2163
301	AL 7075	0.3000	0.2000	6	8	0.5376	14.1050	0.1114
301	AL 7075	0.3000	0.2000	4	6	0.7155	28.1563	0.2224
301	AL 7075	0.3000	0.2000	4	4	0.5013	19.6149	0.1549
301	AL 7075	0.3000	0.3000	4	8	0.5367	21.3294	0.1685
301	AL 7079	0.2000	0.2000	2	8	0.6909	35.2272	0.1988

Continued on next page

metal1	metal2	R1 [m]	R2 [m]	B1	B2	pdiff [ns]	d_{mat_2} [mm]	std [mm]
301	AL 7079	0.2000	0.2000	2	6	0.5474	27.8931	0.1574
301	AL 7079	0.3000	0.2000	6	8	0.5376	11.8013	0.0666
301	AL 7079	0.3000	0.2000	4	8	0.8590	28.2929	0.1597
301	AL 7079	0.3000	0.2000	4	6	0.7155	23.5577	0.1330
301	AL 7079	0.3000	0.2000	4	4	0.5013	16.4114	0.0926
301	AL 7079	0.3000	0.2000	2	2	0.6678	34.3462	0.1939
301	AL 7079	0.3000	0.3000	4	8	0.5367	17.8458	0.1007
301	AL 7079	0.3000	0.3000	2	6	0.8211	42.4954	0.2399
301	FE 17-7PH	0.2000	0.2000	2	8	0.6909	67.0347	0.1573
301	FE 17-7PH	0.2000	0.2000	2	6	0.5474	53.0783	0.1246
301	FE 17-7PH	0.3000	0.2000	6	8	0.5376	22.4570	0.0527
301	FE 17-7PH	0.3000	0.2000	4	8	0.8590	53.8392	0.1264
301	FE 17-7PH	0.3000	0.2000	4	6	0.7155	44.8285	0.1052
301	FE 17-7PH	0.3000	0.2000	4	4	0.5013	31.2295	0.0733
301	FE 17-7PH	0.3000	0.2000	2	4	1.0011	97.8198	0.2296
301	FE 17-7PH	0.3000	0.2000	2	2	0.6678	65.3581	0.1534
301	FE 17-7PH	0.3000	0.3000	4	8	0.5367	33.9592	0.0797
301	FE 17-7PH	0.3000	0.3000	2	8	1.0365	102.1066	0.2396
301	FE 17-7PH	0.3000	0.3000	2	6	0.8211	80.8654	0.1898
301	A286	0.3000	0.2000	6	8	0.5376	39.0488	0.1881
301	20-CB	0.3000	0.2000	6	8	0.5376	16.9756	0.1600
301	20-CB	0.3000	0.2000	4	4	0.5013	23.6069	0.2225
301	20-CB	0.3000	0.3000	4	8	0.5367	25.6703	0.2420
301	347	0.2000	0.2000	2	8	0.6909	67.6055	0.2440
301	347	0.2000	0.2000	2	6	0.5474	53.5303	0.1932
301	347	0.3000	0.2000	6	8	0.5376	22.6482	0.0817
301	347	0.3000	0.2000	4	8	0.8590	54.2976	0.1959
301	347	0.3000	0.2000	4	6	0.7155	45.2102	0.1632
301	347	0.3000	0.2000	4	4	0.5013	31.4955	0.1137
301	347	0.3000	0.2000	2	2	0.6678	65.9146	0.2379
301	347	0.3000	0.3000	4	8	0.5367	34.2483	0.1236
301	410	0.2000	0.2000	2	8	0.6909	70.6563	0.0615
301	410	0.2000	0.2000	2	6	0.5474	55.9459	0.0487
301	410	0.3000	0.2000	6	8	0.5376	23.6702	0.0206

Continued on next page

metal1	metal2	R1 [m]	R2 [m]	B1	B2	pdiff [ns]	d_{mat_2} [mm]	std [mm]
301	410	0.3000	0.2000	4	8	0.8590	56.7479	0.0494
301	410	0.3000	0.2000	4	6	0.7155	47.2504	0.0411
301	410	0.3000	0.2000	4	4	0.5013	32.9167	0.0287
301	410	0.3000	0.2000	2	8	1.3588	140.5308	0.1223
301	410	0.3000	0.2000	2	6	1.2152	125.6153	0.1093
301	410	0.3000	0.2000	2	4	1.0011	103.1047	0.0898
301	410	0.3000	0.2000	2	2	0.6678	68.8891	0.0600
301	410	0.3000	0.3000	4	8	0.5367	35.7939	0.0312
301	410	0.3000	0.3000	2	8	1.0365	107.6231	0.0937
301	410	0.3000	0.3000	2	6	0.8211	85.2343	0.0742
301	InconelX	0.2000	0.2000	2	8	0.6909	30.9114	0.0641
301	InconelX	0.2000	0.2000	2	6	0.5474	24.4758	0.0508
301	InconelX	0.3000	0.2000	6	8	0.5376	10.3555	0.0215
301	InconelX	0.3000	0.2000	4	8	0.8590	24.8266	0.0515
301	InconelX	0.3000	0.2000	4	6	0.7155	20.6716	0.0429
301	InconelX	0.3000	0.2000	4	4	0.5013	14.4007	0.0299
301	InconelX	0.3000	0.2000	2	8	1.3588	61.4808	0.1276
301	InconelX	0.3000	0.2000	2	6	1.2152	54.9554	0.1140
301	InconelX	0.3000	0.2000	2	4	1.0011	45.1072	0.0936
301	InconelX	0.3000	0.2000	2	2	0.6678	30.1383	0.0625
301	InconelX	0.3000	0.3000	4	8	0.5367	15.6594	0.0325
301	InconelX	0.3000	0.3000	2	8	1.0365	47.0840	0.0977
301	InconelX	0.3000	0.3000	2	6	0.8211	37.2891	0.0774
301	RonHI	0.2000	0.2000	2	8	0.6909	56.5879	0.2197
301	RonHI	0.2000	0.2000	2	6	0.5474	44.8065	0.1740
301	RonHI	0.3000	0.2000	6	8	0.5376	18.9573	0.0736
301	RonHI	0.3000	0.2000	4	8	0.8590	45.4488	0.1765
301	RonHI	0.3000	0.2000	4	6	0.7155	37.8424	0.1469
301	RonHI	0.3000	0.2000	4	4	0.5013	26.3627	0.1024
301	RonHI	0.3000	0.2000	2	2	0.6678	55.1726	0.2142
301	RonHI	0.3000	0.3000	4	8	0.5367	28.6669	0.1113
347	AL 7075	0.3000	0.2000	6	8	0.5376	9.2504	0.2402
347	AL 7079	0.3000	0.2000	6	8	0.5376	6.0950	0.1148
347	AL 7079	0.3000	0.2000	4	6	0.7155	12.1668	0.2293

Continued on next page

metal1	metal2	R1 [m]	R2 [m]	B1	B2	pdiff [ns]	d_{mat_2} [mm]	std [mm]
347	AL 7079	0.3000	0.2000	4	4	0.5013	8.4759	0.1597
347	AL 7079	0.3000	0.3000	4	8	0.5367	9.2168	0.1737
347	InconelX	0.2000	0.2000	2	8	0.6909	14.0858	0.1657
347	InconelX	0.2000	0.2000	2	6	0.5474	11.1532	0.1312
347	InconelX	0.3000	0.2000	6	8	0.5376	4.7188	0.0555
347	InconelX	0.3000	0.2000	4	8	0.8590	11.3131	0.1331
347	InconelX	0.3000	0.2000	4	6	0.7155	9.4197	0.1108
347	InconelX	0.3000	0.2000	4	4	0.5013	6.5622	0.0772
347	InconelX	0.3000	0.2000	2	4	1.0011	20.5546	0.2418
347	InconelX	0.3000	0.2000	2	2	0.6678	13.7335	0.1616
347	InconelX	0.3000	0.3000	4	8	0.5367	7.1357	0.0839
347	InconelX	0.3000	0.3000	2	6	0.8211	16.9920	0.1999
410	AL X2020	0.3000	0.2000	6	8	0.5376	9.3804	0.2381
410	AL 7075	0.3000	0.2000	6	8	0.5376	9.7696	0.2004
410	AL 7079	0.2000	0.2000	2	8	0.6909	19.6608	0.2484
410	AL 7079	0.2000	0.2000	2	6	0.5474	15.5675	0.1967
410	AL 7079	0.3000	0.2000	6	8	0.5376	6.5865	0.0832
410	AL 7079	0.3000	0.2000	4	8	0.8590	15.7907	0.1995
410	AL 7079	0.3000	0.2000	4	6	0.7155	13.1479	0.1661
410	AL 7079	0.3000	0.2000	4	4	0.5013	9.1594	0.1157
410	AL 7079	0.3000	0.2000	2	2	0.6678	19.1691	0.2422
410	AL 7079	0.3000	0.3000	4	8	0.5367	9.9600	0.1258
410	InconelX	0.2000	0.2000	2	8	0.6909	15.3778	0.0808
410	InconelX	0.2000	0.2000	2	6	0.5474	12.1762	0.0640
410	InconelX	0.3000	0.2000	6	8	0.5376	5.1516	0.0271
410	InconelX	0.3000	0.2000	4	8	0.8590	12.3507	0.0649
410	InconelX	0.3000	0.2000	4	6	0.7155	10.2837	0.0540
410	InconelX	0.3000	0.2000	4	4	0.5013	7.1641	0.0376
410	InconelX	0.3000	0.2000	2	8	1.3588	30.5855	0.1606
410	InconelX	0.3000	0.2000	2	6	1.2152	27.3392	0.1436
410	InconelX	0.3000	0.2000	2	4	1.0011	22.4399	0.1179
410	InconelX	0.3000	0.2000	2	2	0.6678	14.9932	0.0787
410	InconelX	0.3000	0.3000	4	8	0.5367	7.7903	0.0409
410	InconelX	0.3000	0.3000	2	8	1.0365	23.4233	0.1230

Continued on next page

metal1	metal2	R1 [m]	R2 [m]	B1	B2	pdiff [ns]	d_{mat_2} [mm]	std [mm]
410	InconelX	0.3000	0.3000	2	6	0.8211	18.5506	0.0974
A286	AL X2020	0.3000	0.2000	6	8	0.5376	12.1232	0.2027
A286	AL 2219	0.3000	0.2000	6	8	0.5376	27.9377	0.1180
A286	AL 2219	0.3000	0.2000	4	6	0.7155	55.7692	0.2355
A286	AL 2219	0.3000	0.2000	4	4	0.5013	38.8513	0.1641
A286	AL 2219	0.3000	0.3000	4	8	0.5367	42.2471	0.1784
A286	AL 7075	0.3000	0.2000	6	8	0.5376	12.4420	0.1664
A286	AL 7075	0.3000	0.2000	4	4	0.5013	17.3023	0.2314
A286	AL 7079	0.2000	0.2000	2	6	0.5474	22.5237	0.2193
A286	AL 7079	0.3000	0.2000	6	8	0.5376	9.5296	0.0928
A286	AL 7079	0.3000	0.2000	4	8	0.8590	22.8466	0.2224
A286	AL 7079	0.3000	0.2000	4	6	0.7155	19.0229	0.1852
A286	AL 7079	0.3000	0.2000	4	4	0.5013	13.2522	0.1290
A286	AL 7079	0.3000	0.3000	4	8	0.5367	14.4105	0.1403
A286	FE 17-7PH	0.2000	0.2000	2	8	0.6909	88.8942	0.2433
A286	FE 17-7PH	0.2000	0.2000	2	6	0.5474	70.3868	0.1926
A286	FE 17-7PH	0.3000	0.2000	6	8	0.5376	29.7800	0.0815
A286	FE 17-7PH	0.3000	0.2000	4	8	0.8590	71.3957	0.1954
A286	FE 17-7PH	0.3000	0.2000	4	6	0.7155	59.4468	0.1627
A286	FE 17-7PH	0.3000	0.2000	4	4	0.5013	41.4133	0.1133
A286	FE 17-7PH	0.3000	0.2000	2	2	0.6678	86.6709	0.2372
A286	FE 17-7PH	0.3000	0.3000	4	8	0.5367	45.0330	0.1232
A286	347	0.3000	0.2000	6	8	0.5376	30.3837	0.1724
A286	347	0.3000	0.2000	4	4	0.5013	42.2527	0.2397
A286	410	0.2000	0.2000	2	8	0.6909	101.0915	0.1491
A286	410	0.2000	0.2000	2	6	0.5474	80.0446	0.1181
A286	410	0.3000	0.2000	6	8	0.5376	33.8662	0.0500
A286	410	0.3000	0.2000	4	8	0.8590	81.1921	0.1198
A286	410	0.3000	0.2000	4	6	0.7155	67.6035	0.0997
A286	410	0.3000	0.2000	4	4	0.5013	47.0956	0.0695
A286	410	0.3000	0.2000	2	4	1.0011	147.5170	0.2176
A286	410	0.3000	0.2000	2	2	0.6678	98.5631	0.1454
A286	410	0.3000	0.3000	4	8	0.5367	51.2121	0.0756
A286	410	0.3000	0.3000	2	8	1.0365	153.9817	0.2272

Continued on next page

metal1	metal2	R1 [m]	R2 [m]	B1	B2	pdiff [ns]	d_{mat_2} [mm]	std [mm]
A286	410	0.3000	0.3000	2	6	0.8211	121.9489	0.1799
A286	InconelX	0.2000	0.2000	2	8	0.6909	23.7029	0.1142
A286	InconelX	0.2000	0.2000	2	6	0.5474	18.7681	0.0904
A286	InconelX	0.3000	0.2000	6	8	0.5376	7.9406	0.0383
A286	InconelX	0.3000	0.2000	4	8	0.8590	19.0371	0.0917
A286	InconelX	0.3000	0.2000	4	6	0.7155	15.8510	0.0764
A286	InconelX	0.3000	0.2000	4	4	0.5013	11.0425	0.0532
A286	InconelX	0.3000	0.2000	2	8	1.3588	47.1436	0.2271
A286	InconelX	0.3000	0.2000	2	6	1.2152	42.1399	0.2030
A286	InconelX	0.3000	0.2000	2	4	1.0011	34.5883	0.1666
A286	InconelX	0.3000	0.2000	2	2	0.6678	23.1101	0.1113
A286	InconelX	0.3000	0.3000	4	8	0.5367	12.0077	0.0578
A286	InconelX	0.3000	0.3000	2	8	1.0365	36.1041	0.1739
A286	InconelX	0.3000	0.3000	2	6	0.8211	28.5934	0.1377
A286	RonHI	0.3000	0.2000	6	8	0.5376	20.7601	0.1398
A286	RonHI	0.3000	0.2000	4	4	0.5013	28.8698	0.1944
A286	RonHI	0.3000	0.3000	4	8	0.5367	31.3931	0.2114
AL 2014	AL 7079	0.3000	0.2000	6	8	0.5376	5.7138	0.1500
AL 2014	AL 7079	0.3000	0.2000	4	4	0.5013	7.9458	0.2087
AL 2014	AL 7079	0.3000	0.3000	4	8	0.5367	8.6403	0.2269
AL 2014	InconelX	0.2000	0.2000	2	6	0.5474	10.3739	0.2037
AL 2014	InconelX	0.3000	0.2000	6	8	0.5376	4.3891	0.0862
AL 2014	InconelX	0.3000	0.2000	4	8	0.8590	10.5226	0.2066
AL 2014	InconelX	0.3000	0.2000	4	6	0.7155	8.7615	0.1720
AL 2014	InconelX	0.3000	0.2000	4	4	0.5013	6.1037	0.1198
AL 2014	InconelX	0.3000	0.3000	4	8	0.5367	6.6371	0.1303
AL 2219	AL X2020	0.3000	0.2000	6	8	0.5376	8.3520	0.2188
AL 2219	AL 7075	0.3000	0.2000	6	8	0.5376	8.7470	0.1830
AL 2219	AL 7079	0.2000	0.2000	2	8	0.6909	16.8305	0.1745
AL 2219	AL 7079	0.2000	0.2000	2	6	0.5474	13.3265	0.1382
AL 2219	AL 7079	0.3000	0.2000	6	8	0.5376	5.6383	0.0585
AL 2219	AL 7079	0.3000	0.2000	4	8	0.8590	13.5175	0.1402
AL 2219	AL 7079	0.3000	0.2000	4	6	0.7155	11.2552	0.1167
AL 2219	AL 7079	0.3000	0.2000	4	4	0.5013	7.8409	0.0813

Continued on next page

metal1	metal2	R1 [m]	R2 [m]	B1	B2	pdiff [ns]	d_{mat_2} [mm]	std [mm]
AL 2219	AL 7079	0.3000	0.2000	2	2	0.6678	16.4096	0.1702
AL 2219	AL 7079	0.3000	0.3000	4	8	0.5367	8.5262	0.0884
AL 2219	AL 7079	0.3000	0.3000	2	6	0.8211	20.3030	0.2106
AL 2219	InconelX	0.2000	0.2000	2	8	0.6909	12.9091	0.0236
AL 2219	InconelX	0.2000	0.2000	2	6	0.5474	10.2215	0.0186
AL 2219	InconelX	0.3000	0.2000	6	8	0.5376	4.3246	0.0079
AL 2219	InconelX	0.3000	0.2000	4	8	0.8590	10.3680	0.0189
AL 2219	InconelX	0.3000	0.2000	4	6	0.7155	8.6328	0.0157
AL 2219	InconelX	0.3000	0.2000	4	4	0.5013	6.0140	0.0110
AL 2219	InconelX	0.3000	0.2000	2	8	1.3588	25.6754	0.0468
AL 2219	InconelX	0.3000	0.2000	2	6	1.2152	22.9503	0.0419
AL 2219	InconelX	0.3000	0.2000	2	4	1.0011	18.8375	0.0344
AL 2219	InconelX	0.3000	0.2000	2	2	0.6678	12.5863	0.0230
AL 2219	InconelX	0.3000	0.3000	4	8	0.5367	6.5397	0.0119
AL 2219	InconelX	0.3000	0.3000	2	8	1.0365	19.6631	0.0359
AL 2219	InconelX	0.3000	0.3000	2	6	0.8211	15.5726	0.0284
AL 5456	AL 7079	0.3000	0.2000	6	8	0.5376	6.0132	0.1488
AL 5456	AL 7079	0.3000	0.2000	4	4	0.5013	8.3621	0.2069
AL 5456	AL 7079	0.3000	0.3000	4	8	0.5367	9.0930	0.2250
AL 5456	InconelX	0.2000	0.2000	2	6	0.5474	10.9849	0.2011
AL 5456	InconelX	0.3000	0.2000	6	8	0.5376	4.6476	0.0851
AL 5456	InconelX	0.3000	0.2000	4	8	0.8590	11.1424	0.2040
AL 5456	InconelX	0.3000	0.2000	4	6	0.7155	9.2775	0.1699
AL 5456	InconelX	0.3000	0.2000	4	4	0.5013	6.4631	0.1183
AL 5456	InconelX	0.3000	0.2000	2	2	0.6678	13.5263	0.2477
AL 5456	InconelX	0.3000	0.3000	4	8	0.5367	7.0281	0.1287
AL 7075	AL 2219	0.3000	0.2000	6	8	0.5376	8.2995	0.1830
AL 7075	FE 17-7PH	0.3000	0.2000	6	8	0.5376	7.9069	0.2255
AL 7075	A286	0.3000	0.2000	6	8	0.5376	4.6045	0.1664
AL 7075	A286	0.3000	0.2000	4	4	0.5013	6.4032	0.2314
AL 7075	301	0.3000	0.2000	6	8	0.5376	2.9415	0.1114
AL 7075	301	0.3000	0.2000	4	6	0.7155	5.8718	0.2224
AL 7075	301	0.3000	0.2000	4	4	0.5013	4.0906	0.1549
AL 7075	301	0.3000	0.3000	4	8	0.5367	4.4481	0.1685

Continued on next page

metal1	metal2	R1 [m]	R2 [m]	B1	B2	pdiff [ns]	d_{mat_2} [mm]	std [mm]
AL 7075	347	0.3000	0.2000	6	8	0.5376	7.7960	0.2402
AL 7075	410	0.3000	0.2000	6	8	0.5376	7.2769	0.2004
AL 7075	Aluminum	0.2000	0.2000	2	8	0.6909	0.5492	0.0151
AL 7075	Aluminum	0.2000	0.2000	2	6	0.5474	0.4349	0.0119
AL 7075	Aluminum	0.3000	0.2000	6	8	0.5376	0.1840	0.0051
AL 7075	Aluminum	0.3000	0.2000	4	8	0.8590	0.4411	0.0121
AL 7075	Aluminum	0.3000	0.2000	4	6	0.7155	0.3673	0.0101
AL 7075	Aluminum	0.3000	0.2000	4	4	0.5013	0.2559	0.0070
AL 7075	Aluminum	0.3000	0.2000	2	8	1.3588	1.0923	0.0300
AL 7075	Aluminum	0.3000	0.2000	2	6	1.2152	0.9764	0.0268
AL 7075	Aluminum	0.3000	0.2000	2	4	1.0011	0.8014	0.0220
AL 7075	Aluminum	0.3000	0.2000	2	2	0.6678	0.5355	0.0147
AL 7075	Aluminum	0.3000	0.3000	4	8	0.5367	0.2782	0.0076
AL 7075	Aluminum	0.3000	0.3000	2	8	1.0365	0.8365	0.0230
AL 7075	Aluminum	0.3000	0.3000	2	6	0.8211	0.6625	0.0182
AL 7079	AL 2014	0.3000	0.2000	6	8	0.5376	11.3327	0.1500
AL 7079	AL 2014	0.3000	0.2000	4	4	0.5013	15.7597	0.2087
AL 7079	AL 2014	0.3000	0.3000	4	8	0.5367	17.1372	0.2269
AL 7079	AL 2219	0.2000	0.2000	2	8	0.6909	34.0536	0.1745
AL 7079	AL 2219	0.2000	0.2000	2	6	0.5474	26.9638	0.1382
AL 7079	AL 2219	0.3000	0.2000	6	8	0.5376	11.4082	0.0585
AL 7079	AL 2219	0.3000	0.2000	4	8	0.8590	27.3503	0.1402
AL 7079	AL 2219	0.3000	0.2000	4	6	0.7155	22.7729	0.1167
AL 7079	AL 2219	0.3000	0.2000	4	4	0.5013	15.8646	0.0813
AL 7079	AL 2219	0.3000	0.2000	2	2	0.6678	33.2019	0.1702
AL 7079	AL 2219	0.3000	0.3000	4	8	0.5367	17.2513	0.0884
AL 7079	AL 2219	0.3000	0.3000	2	6	0.8211	41.0797	0.2106
AL 7079	AL 5456	0.3000	0.2000	6	8	0.5376	11.0333	0.1488
AL 7079	AL 5456	0.3000	0.2000	4	4	0.5013	15.3433	0.2069
AL 7079	AL 5456	0.3000	0.3000	4	8	0.5367	16.6844	0.2250
AL 7079	FE 17-7PH	0.2000	0.2000	2	6	0.5474	26.1262	0.2364
AL 7079	FE 17-7PH	0.3000	0.2000	6	8	0.5376	11.0538	0.1000
AL 7079	FE 17-7PH	0.3000	0.2000	4	8	0.8590	26.5007	0.2398
AL 7079	FE 17-7PH	0.3000	0.2000	4	6	0.7155	22.0655	0.1997

Continued on next page

metal1	metal2	R1 [m]	R2 [m]	B1	B2	pdiff [ns]	d_{mat_2} [mm]	std [mm]
AL 7079	FE 17-7PH	0.3000	0.2000	4	4	0.5013	15.3718	0.1391
AL 7079	FE 17-7PH	0.3000	0.3000	4	8	0.5367	16.7154	0.1513
AL 7079	A286	0.2000	0.2000	2	6	0.5474	17.7665	0.2193
AL 7079	A286	0.3000	0.2000	6	8	0.5376	7.5169	0.0928
AL 7079	A286	0.3000	0.2000	4	8	0.8590	18.0212	0.2224
AL 7079	A286	0.3000	0.2000	4	6	0.7155	15.0051	0.1852
AL 7079	A286	0.3000	0.2000	4	4	0.5013	10.4532	0.1290
AL 7079	A286	0.3000	0.3000	4	8	0.5367	11.3669	0.1403
AL 7079	301	0.2000	0.2000	2	8	0.6909	15.6569	0.1988
AL 7079	301	0.2000	0.2000	2	6	0.5474	12.3972	0.1574
AL 7079	301	0.3000	0.2000	6	8	0.5376	5.2452	0.0666
AL 7079	301	0.3000	0.2000	4	8	0.8590	12.5749	0.1597
AL 7079	301	0.3000	0.2000	4	6	0.7155	10.4703	0.1330
AL 7079	301	0.3000	0.2000	4	4	0.5013	7.2941	0.0926
AL 7079	301	0.3000	0.2000	2	2	0.6678	15.2653	0.1939
AL 7079	301	0.3000	0.3000	4	8	0.5367	7.9317	0.1007
AL 7079	301	0.3000	0.3000	2	6	0.8211	18.8873	0.2399
AL 7079	347	0.3000	0.2000	6	8	0.5376	10.9515	0.1148
AL 7079	347	0.3000	0.2000	4	6	0.7155	21.8613	0.2293
AL 7079	347	0.3000	0.2000	4	4	0.5013	15.2296	0.1597
AL 7079	347	0.3000	0.3000	4	8	0.5367	16.5607	0.1737
AL 7079	410	0.2000	0.2000	2	8	0.6909	31.2233	0.2484
AL 7079	410	0.2000	0.2000	2	6	0.5474	24.7228	0.1967
AL 7079	410	0.3000	0.2000	6	8	0.5376	10.4600	0.0832
AL 7079	410	0.3000	0.2000	4	8	0.8590	25.0771	0.1995
AL 7079	410	0.3000	0.2000	4	6	0.7155	20.8802	0.1661
AL 7079	410	0.3000	0.2000	4	4	0.5013	14.5461	0.1157
AL 7079	410	0.3000	0.2000	2	2	0.6678	30.4424	0.2422
AL 7079	410	0.3000	0.3000	4	8	0.5367	15.8175	0.1258
AL 7079	RonHI	0.3000	0.2000	6	8	0.5376	13.8947	0.1361
AL 7079	RonHI	0.3000	0.2000	4	4	0.5013	19.3225	0.1893
AL 7079	RonHI	0.3000	0.3000	4	8	0.5367	21.0114	0.2058
AL 7079	Aluminum	0.2000	0.2000	2	8	0.6909	1.1566	0.0005
AL 7079	Aluminum	0.2000	0.2000	2	6	0.5474	0.9158	0.0004

Continued on next page

metal1	metal2	R1 [m]	R2 [m]	B1	B2	pdiff [ns]	d_{mat_2} [mm]	std [mm]
AL 7079	Aluminum	0.3000	0.2000	6	8	0.5376	0.3875	0.0002
AL 7079	Aluminum	0.3000	0.2000	4	8	0.8590	0.9289	0.0004
AL 7079	Aluminum	0.3000	0.2000	4	6	0.7155	0.7735	0.0003
AL 7079	Aluminum	0.3000	0.2000	4	4	0.5013	0.5388	0.0002
AL 7079	Aluminum	0.3000	0.2000	2	8	1.3588	2.3004	0.0010
AL 7079	Aluminum	0.3000	0.2000	2	6	1.2152	2.0563	0.0009
AL 7079	Aluminum	0.3000	0.2000	2	4	1.0011	1.6878	0.0007
AL 7079	Aluminum	0.3000	0.2000	2	2	0.6678	1.1277	0.0005
AL 7079	Aluminum	0.3000	0.3000	4	8	0.5367	0.5859	0.0003
AL 7079	Aluminum	0.3000	0.3000	2	8	1.0365	1.7618	0.0008
AL 7079	Aluminum	0.3000	0.3000	2	6	0.8211	1.3953	0.0006
AL X2020	AL 2219	0.3000	0.2000	6	8	0.5376	8.6944	0.2188
AL X2020	A286	0.3000	0.2000	6	8	0.5376	4.9233	0.2027
AL X2020	301	0.3000	0.2000	6	8	0.5376	3.1747	0.1399
AL X2020	301	0.3000	0.2000	4	4	0.5013	4.4149	0.1946
AL X2020	301	0.3000	0.3000	4	8	0.5367	4.8008	0.2116
AL X2020	410	0.3000	0.2000	6	8	0.5376	7.6660	0.2381
AL X2020	Aluminum	0.2000	0.2000	2	8	0.6909	0.6021	0.0215
AL X2020	Aluminum	0.2000	0.2000	2	6	0.5474	0.4767	0.0170
AL X2020	Aluminum	0.3000	0.2000	6	8	0.5376	0.2017	0.0072
AL X2020	Aluminum	0.3000	0.2000	4	8	0.8590	0.4836	0.0173
AL X2020	Aluminum	0.3000	0.2000	4	6	0.7155	0.4026	0.0144
AL X2020	Aluminum	0.3000	0.2000	4	4	0.5013	0.2805	0.0100
AL X2020	Aluminum	0.3000	0.2000	2	8	1.3588	1.1975	0.0428
AL X2020	Aluminum	0.3000	0.2000	2	6	1.2152	1.0704	0.0382
AL X2020	Aluminum	0.3000	0.2000	2	4	1.0011	0.8786	0.0314
AL X2020	Aluminum	0.3000	0.2000	2	2	0.6678	0.5870	0.0210
AL X2020	Aluminum	0.3000	0.3000	4	8	0.5367	0.3050	0.0109
AL X2020	Aluminum	0.3000	0.3000	2	8	1.0365	0.9171	0.0328
AL X2020	Aluminum	0.3000	0.3000	2	6	0.8211	0.7263	0.0260
Aluminum	AL 2014	0.2000	0.2000	2	8	0.6909	51.4883	0.0239
Aluminum	AL 2014	0.2000	0.2000	2	6	0.5474	40.7686	0.0190
Aluminum	AL 2014	0.3000	0.2000	6	8	0.5376	17.2488	0.0080
Aluminum	AL 2014	0.3000	0.2000	4	8	0.8590	41.3530	0.0192

Continued on next page

metal1	metal2	R1 [m]	R2 [m]	B1	B2	pdiff [ns]	d_{mat_2} [mm]	std [mm]
Aluminum	AL 2014	0.3000	0.2000	4	6	0.7155	34.4321	0.0160
Aluminum	AL 2014	0.3000	0.2000	4	4	0.5013	23.9869	0.0112
Aluminum	AL 2014	0.3000	0.2000	2	8	1.3588	102.4068	0.0476
Aluminum	AL 2014	0.3000	0.2000	2	6	1.2152	91.5377	0.0426
Aluminum	AL 2014	0.3000	0.2000	2	4	1.0011	75.1339	0.0349
Aluminum	AL 2014	0.3000	0.2000	2	2	0.6678	50.2005	0.0234
Aluminum	AL 2014	0.3000	0.3000	4	8	0.5367	26.0835	0.0121
Aluminum	AL 2014	0.3000	0.3000	2	8	1.0365	78.4265	0.0365
Aluminum	AL 2014	0.3000	0.3000	2	6	0.8211	62.1114	0.0289
Aluminum	AL X2020	0.2000	0.2000	2	8	0.6909	50.2821	0.0215
Aluminum	AL X2020	0.2000	0.2000	2	6	0.5474	39.8135	0.0170
Aluminum	AL X2020	0.3000	0.2000	6	8	0.5376	16.8448	0.0072
Aluminum	AL X2020	0.3000	0.2000	4	8	0.8590	40.3842	0.0173
Aluminum	AL X2020	0.3000	0.2000	4	6	0.7155	33.6254	0.0144
Aluminum	AL X2020	0.3000	0.2000	4	4	0.5013	23.4250	0.0100
Aluminum	AL X2020	0.3000	0.2000	2	8	1.3588	100.0078	0.0428
Aluminum	AL X2020	0.3000	0.2000	2	6	1.2152	89.3932	0.0382
Aluminum	AL X2020	0.3000	0.2000	2	4	1.0011	73.3737	0.0314
Aluminum	AL X2020	0.3000	0.2000	2	2	0.6678	49.0245	0.0210
Aluminum	AL X2020	0.3000	0.3000	4	8	0.5367	25.4724	0.0109
Aluminum	AL X2020	0.3000	0.3000	2	8	1.0365	76.5892	0.0328
Aluminum	AL X2020	0.3000	0.3000	2	6	0.8211	60.6564	0.0260
Aluminum	AL 2219	0.2000	0.2000	2	8	0.6909	51.4759	0.0091
Aluminum	AL 2219	0.2000	0.2000	2	6	0.5474	40.7588	0.0072
Aluminum	AL 2219	0.3000	0.2000	6	8	0.5376	17.2447	0.0030
Aluminum	AL 2219	0.3000	0.2000	4	8	0.8590	41.3431	0.0073
Aluminum	AL 2219	0.3000	0.2000	4	6	0.7155	34.4238	0.0061
Aluminum	AL 2219	0.3000	0.2000	4	4	0.5013	23.9812	0.0042
Aluminum	AL 2219	0.3000	0.2000	2	8	1.3588	102.3823	0.0181
Aluminum	AL 2219	0.3000	0.2000	2	6	1.2152	91.5158	0.0161
Aluminum	AL 2219	0.3000	0.2000	2	4	1.0011	75.1159	0.0132
Aluminum	AL 2219	0.3000	0.2000	2	2	0.6678	50.1885	0.0089
Aluminum	AL 2219	0.3000	0.3000	4	8	0.5367	26.0773	0.0046
Aluminum	AL 2219	0.3000	0.3000	2	8	1.0365	78.4077	0.0138

Continued on next page

metal1	metal2	R1 [m]	R2 [m]	B1	B2	pdiff [ns]	d_{mat_2} [mm]	std [mm]
Aluminum	AL 2219	0.3000	0.3000	2	6	0.8211	62.0966	0.0110
Aluminum	AL 5456	0.2000	0.2000	2	8	0.6909	51.5378	0.0251
Aluminum	AL 5456	0.2000	0.2000	2	6	0.5474	40.8078	0.0199
Aluminum	AL 5456	0.3000	0.2000	6	8	0.5376	17.2654	0.0084
Aluminum	AL 5456	0.3000	0.2000	4	8	0.8590	41.3928	0.0202
Aluminum	AL 5456	0.3000	0.2000	4	6	0.7155	34.4652	0.0168
Aluminum	AL 5456	0.3000	0.2000	4	4	0.5013	24.0100	0.0117
Aluminum	AL 5456	0.3000	0.2000	2	8	1.3588	102.5053	0.0499
Aluminum	AL 5456	0.3000	0.2000	2	6	1.2152	91.6257	0.0446
Aluminum	AL 5456	0.3000	0.2000	2	4	1.0011	75.2061	0.0366
Aluminum	AL 5456	0.3000	0.2000	2	2	0.6678	50.2488	0.0245
Aluminum	AL 5456	0.3000	0.3000	4	8	0.5367	26.1086	0.0127
Aluminum	AL 5456	0.3000	0.3000	2	8	1.0365	78.5019	0.0382
Aluminum	AL 5456	0.3000	0.3000	2	6	0.8211	62.1712	0.0303
Aluminum	AL 7075	0.2000	0.2000	2	8	0.6909	50.3350	0.0151
Aluminum	AL 7075	0.2000	0.2000	2	6	0.5474	39.8554	0.0119
Aluminum	AL 7075	0.3000	0.2000	6	8	0.5376	16.8625	0.0051
Aluminum	AL 7075	0.3000	0.2000	4	8	0.8590	40.4267	0.0121
Aluminum	AL 7075	0.3000	0.2000	4	6	0.7155	33.6608	0.0101
Aluminum	AL 7075	0.3000	0.2000	4	4	0.5013	23.4496	0.0070
Aluminum	AL 7075	0.3000	0.2000	2	8	1.3588	100.1130	0.0300
Aluminum	AL 7075	0.3000	0.2000	2	6	1.2152	89.4873	0.0268
Aluminum	AL 7075	0.3000	0.2000	2	4	1.0011	73.4509	0.0220
Aluminum	AL 7075	0.3000	0.2000	2	2	0.6678	49.0760	0.0147
Aluminum	AL 7075	0.3000	0.3000	4	8	0.5367	25.4992	0.0076
Aluminum	AL 7075	0.3000	0.3000	2	8	1.0365	76.6698	0.0230
Aluminum	AL 7075	0.3000	0.3000	2	6	0.8211	60.7202	0.0182
Aluminum	AL 7079	0.2000	0.2000	2	8	0.6909	49.7275	0.0005
Aluminum	AL 7079	0.2000	0.2000	2	6	0.5474	39.3745	0.0004
Aluminum	AL 7079	0.3000	0.2000	6	8	0.5376	16.6590	0.0002
Aluminum	AL 7079	0.3000	0.2000	4	8	0.8590	39.9389	0.0004
Aluminum	AL 7079	0.3000	0.2000	4	6	0.7155	33.2546	0.0003
Aluminum	AL 7079	0.3000	0.2000	4	4	0.5013	23.1666	0.0002
Aluminum	AL 7079	0.3000	0.2000	2	8	1.3588	98.9048	0.0010

Continued on next page

metal1	metal2	R1 [m]	R2 [m]	B1	B2	pdiff [ns]	d_{mat_2} [mm]	std [mm]
Aluminum	AL 7079	0.3000	0.2000	2	6	1.2152	88.4074	0.0009
Aluminum	AL 7079	0.3000	0.2000	2	4	1.0011	72.5645	0.0007
Aluminum	AL 7079	0.3000	0.2000	2	2	0.6678	48.4838	0.0005
Aluminum	AL 7079	0.3000	0.3000	4	8	0.5367	25.1915	0.0003
Aluminum	AL 7079	0.3000	0.3000	2	8	1.0365	75.7446	0.0008
Aluminum	AL 7079	0.3000	0.3000	2	6	0.8211	59.9874	0.0006
Aluminum	FE 17-7PH	0.2000	0.2000	2	8	0.6909	51.5341	0.0167
Aluminum	FE 17-7PH	0.2000	0.2000	2	6	0.5474	40.8049	0.0132
Aluminum	FE 17-7PH	0.3000	0.2000	6	8	0.5376	17.2642	0.0056
Aluminum	FE 17-7PH	0.3000	0.2000	4	8	0.8590	41.3899	0.0134
Aluminum	FE 17-7PH	0.3000	0.2000	4	6	0.7155	34.4627	0.0112
Aluminum	FE 17-7PH	0.3000	0.2000	4	4	0.5013	24.0083	0.0078
Aluminum	FE 17-7PH	0.3000	0.2000	2	8	1.3588	102.4981	0.0333
Aluminum	FE 17-7PH	0.3000	0.2000	2	6	1.2152	91.6192	0.0297
Aluminum	FE 17-7PH	0.3000	0.2000	2	4	1.0011	75.2008	0.0244
Aluminum	FE 17-7PH	0.3000	0.2000	2	2	0.6678	50.2452	0.0163
Aluminum	FE 17-7PH	0.3000	0.3000	4	8	0.5367	26.1067	0.0085
Aluminum	FE 17-7PH	0.3000	0.3000	2	8	1.0365	78.4964	0.0255
Aluminum	FE 17-7PH	0.3000	0.3000	2	6	0.8211	62.1668	0.0202
Aluminum	A286	0.2000	0.2000	2	8	0.6909	52.4306	0.0347
Aluminum	A286	0.2000	0.2000	2	6	0.5474	41.5148	0.0274
Aluminum	A286	0.3000	0.2000	6	8	0.5376	17.5645	0.0116
Aluminum	A286	0.3000	0.2000	4	8	0.8590	42.1099	0.0278
Aluminum	A286	0.3000	0.2000	4	6	0.7155	35.0622	0.0232
Aluminum	A286	0.3000	0.2000	4	4	0.5013	24.4259	0.0161
Aluminum	A286	0.3000	0.2000	2	8	1.3588	104.2811	0.0689
Aluminum	A286	0.3000	0.2000	2	6	1.2152	93.2130	0.0616
Aluminum	A286	0.3000	0.2000	2	4	1.0011	76.5090	0.0506
Aluminum	A286	0.3000	0.2000	2	2	0.6678	51.1193	0.0338
Aluminum	A286	0.3000	0.3000	4	8	0.5367	26.5609	0.0176
Aluminum	A286	0.3000	0.3000	2	8	1.0365	79.8619	0.0528
Aluminum	A286	0.3000	0.3000	2	6	0.8211	63.2482	0.0418
Aluminum	20-CB	0.2000	0.2000	2	8	0.6909	50.8733	0.0250
Aluminum	20-CB	0.2000	0.2000	2	6	0.5474	40.2816	0.0198

Continued on next page

metal1	metal2	R1 [m]	R2 [m]	B1	B2	pdiff [ns]	d_{mat_2} [mm]	std [mm]
Aluminum	20-CB	0.3000	0.2000	6	8	0.5376	17.0428	0.0084
Aluminum	20-CB	0.3000	0.2000	4	8	0.8590	40.8591	0.0201
Aluminum	20-CB	0.3000	0.2000	4	6	0.7155	34.0208	0.0167
Aluminum	20-CB	0.3000	0.2000	4	4	0.5013	23.7004	0.0116
Aluminum	20-CB	0.3000	0.2000	2	8	1.3588	101.1836	0.0497
Aluminum	20-CB	0.3000	0.2000	2	6	1.2152	90.4443	0.0445
Aluminum	20-CB	0.3000	0.2000	2	4	1.0011	74.2364	0.0365
Aluminum	20-CB	0.3000	0.2000	2	2	0.6678	49.6009	0.0244
Aluminum	20-CB	0.3000	0.3000	4	8	0.5367	25.7719	0.0127
Aluminum	20-CB	0.3000	0.3000	2	8	1.0365	77.4897	0.0381
Aluminum	20-CB	0.3000	0.3000	2	6	0.8211	61.3696	0.0302
Aluminum	301	0.2000	0.2000	2	8	0.6909	53.6948	0.0535
Aluminum	301	0.2000	0.2000	2	6	0.5474	42.5157	0.0423
Aluminum	301	0.3000	0.2000	6	8	0.5376	17.9880	0.0179
Aluminum	301	0.3000	0.2000	4	8	0.8590	43.1252	0.0429
Aluminum	301	0.3000	0.2000	4	6	0.7155	35.9076	0.0357
Aluminum	301	0.3000	0.2000	4	4	0.5013	25.0149	0.0249
Aluminum	301	0.3000	0.2000	2	8	1.3588	106.7955	0.1063
Aluminum	301	0.3000	0.2000	2	6	1.2152	95.4605	0.0950
Aluminum	301	0.3000	0.2000	2	4	1.0011	78.3537	0.0780
Aluminum	301	0.3000	0.2000	2	2	0.6678	52.3518	0.0521
Aluminum	301	0.3000	0.3000	4	8	0.5367	27.2013	0.0271
Aluminum	301	0.3000	0.3000	2	8	1.0365	81.7875	0.0814
Aluminum	301	0.3000	0.3000	2	6	0.8211	64.7732	0.0645
Aluminum	347	0.2000	0.2000	2	8	0.6909	51.5517	0.0196
Aluminum	347	0.2000	0.2000	2	6	0.5474	40.8188	0.0155
Aluminum	347	0.3000	0.2000	6	8	0.5376	17.2701	0.0066
Aluminum	347	0.3000	0.2000	4	8	0.8590	41.4039	0.0158
Aluminum	347	0.3000	0.2000	4	6	0.7155	34.4745	0.0131
Aluminum	347	0.3000	0.2000	4	4	0.5013	24.0164	0.0091
Aluminum	347	0.3000	0.2000	2	8	1.3588	102.5330	0.0390
Aluminum	347	0.3000	0.2000	2	6	1.2152	91.6504	0.0349
Aluminum	347	0.3000	0.2000	2	4	1.0011	75.2264	0.0286
Aluminum	347	0.3000	0.2000	2	2	0.6678	50.2623	0.0191

Continued on next page

metal1	metal2	R1 [m]	R2 [m]	B1	B2	pdiff [ns]	d_{mat_2} [mm]	std [mm]
Aluminum	347	0.3000	0.3000	4	8	0.5367	26.1156	0.0099
Aluminum	347	0.3000	0.3000	2	8	1.0365	78.5231	0.0299
Aluminum	347	0.3000	0.3000	2	6	0.8211	62.1879	0.0237
Aluminum	410	0.2000	0.2000	2	8	0.6909	51.6406	0.0156
Aluminum	410	0.2000	0.2000	2	6	0.5474	40.8892	0.0123
Aluminum	410	0.3000	0.2000	6	8	0.5376	17.2999	0.0052
Aluminum	410	0.3000	0.2000	4	8	0.8590	41.4754	0.0125
Aluminum	410	0.3000	0.2000	4	6	0.7155	34.5339	0.0104
Aluminum	410	0.3000	0.2000	4	4	0.5013	24.0579	0.0072
Aluminum	410	0.3000	0.2000	2	8	1.3588	102.7098	0.0309
Aluminum	410	0.3000	0.2000	2	6	1.2152	91.8085	0.0277
Aluminum	410	0.3000	0.2000	2	4	1.0011	75.3561	0.0227
Aluminum	410	0.3000	0.2000	2	2	0.6678	50.3490	0.0152
Aluminum	410	0.3000	0.3000	4	8	0.5367	26.1607	0.0079
Aluminum	410	0.3000	0.3000	2	8	1.0365	78.6585	0.0237
Aluminum	410	0.3000	0.3000	2	6	0.8211	62.2952	0.0188
Aluminum	InconelX	0.2000	0.2000	2	8	0.6909	49.2197	0.0205
Aluminum	InconelX	0.2000	0.2000	2	6	0.5474	38.9723	0.0162
Aluminum	InconelX	0.3000	0.2000	6	8	0.5376	16.4889	0.0069
Aluminum	InconelX	0.3000	0.2000	4	8	0.8590	39.5310	0.0165
Aluminum	InconelX	0.3000	0.2000	4	6	0.7155	32.9150	0.0137
Aluminum	InconelX	0.3000	0.2000	4	4	0.5013	22.9300	0.0096
Aluminum	InconelX	0.3000	0.2000	2	8	1.3588	97.8947	0.0408
Aluminum	InconelX	0.3000	0.2000	2	6	1.2152	87.5045	0.0365
Aluminum	InconelX	0.3000	0.2000	2	4	1.0011	71.8234	0.0299
Aluminum	InconelX	0.3000	0.2000	2	2	0.6678	47.9886	0.0200
Aluminum	InconelX	0.3000	0.3000	4	8	0.5367	24.9342	0.0104
Aluminum	InconelX	0.3000	0.3000	2	8	1.0365	74.9710	0.0312
Aluminum	InconelX	0.3000	0.3000	2	6	0.8211	59.3748	0.0247
Aluminum	RonHI	0.2000	0.2000	2	8	0.6909	51.1542	0.0143
Aluminum	RonHI	0.2000	0.2000	2	6	0.5474	40.5041	0.0113
Aluminum	RonHI	0.3000	0.2000	6	8	0.5376	17.1369	0.0048
Aluminum	RonHI	0.3000	0.2000	4	8	0.8590	41.0847	0.0115
Aluminum	RonHI	0.3000	0.2000	4	6	0.7155	34.2086	0.0096

Continued on next page

metal1	metal2	R1 [m]	R2 [m]	B1	B2	pdiff [ns]	d_{mat_2} [mm]	std [mm]
Aluminum	RonHI	0.3000	0.2000	4	4	0.5013	23.8313	0.0067
Aluminum	RonHI	0.3000	0.2000	2	8	1.3588	101.7423	0.0284
Aluminum	RonHI	0.3000	0.2000	2	6	1.2152	90.9437	0.0254
Aluminum	RonHI	0.3000	0.2000	2	4	1.0011	74.6463	0.0209
Aluminum	RonHI	0.3000	0.2000	2	2	0.6678	49.8748	0.0139
Aluminum	RonHI	0.3000	0.3000	4	8	0.5367	25.9143	0.0072
Aluminum	RonHI	0.3000	0.3000	2	8	1.0365	77.9176	0.0218
Aluminum	RonHI	0.3000	0.3000	2	6	0.8211	61.7084	0.0172
FE 17-7PH	AL 7075	0.3000	0.2000	6	8	0.5376	9.1396	0.2255
FE 17-7PH	AL 7079	0.2000	0.2000	2	6	0.5474	14.1640	0.2364
FE 17-7PH	AL 7079	0.3000	0.2000	6	8	0.5376	5.9927	0.1000
FE 17-7PH	AL 7079	0.3000	0.2000	4	8	0.8590	14.3671	0.2398
FE 17-7PH	AL 7079	0.3000	0.2000	4	6	0.7155	11.9626	0.1997
FE 17-7PH	AL 7079	0.3000	0.2000	4	4	0.5013	8.3337	0.1391
FE 17-7PH	AL 7079	0.3000	0.3000	4	8	0.5367	9.0621	0.1513
FE 17-7PH	InconelX	0.2000	0.2000	2	8	0.6909	13.8203	0.1277
FE 17-7PH	InconelX	0.2000	0.2000	2	6	0.5474	10.9429	0.1011
FE 17-7PH	InconelX	0.3000	0.2000	6	8	0.5376	4.6299	0.0428
FE 17-7PH	InconelX	0.3000	0.2000	4	8	0.8590	11.0998	0.1025
FE 17-7PH	InconelX	0.3000	0.2000	4	6	0.7155	9.2421	0.0854
FE 17-7PH	InconelX	0.3000	0.2000	4	4	0.5013	6.4385	0.0595
FE 17-7PH	InconelX	0.3000	0.2000	2	6	1.2152	24.5702	0.2269
FE 17-7PH	InconelX	0.3000	0.2000	2	4	1.0011	20.1671	0.1863
FE 17-7PH	InconelX	0.3000	0.2000	2	2	0.6678	13.4746	0.1245
FE 17-7PH	InconelX	0.3000	0.3000	4	8	0.5367	7.0012	0.0647
FE 17-7PH	InconelX	0.3000	0.3000	2	8	1.0365	21.0509	0.1944
FE 17-7PH	InconelX	0.3000	0.3000	2	6	0.8211	16.6717	0.1540
InconelX	AL 2014	0.2000	0.2000	2	6	0.5474	29.9164	0.2037
InconelX	AL 2014	0.3000	0.2000	6	8	0.5376	12.6574	0.0862
InconelX	AL 2014	0.3000	0.2000	4	8	0.8590	30.3452	0.2066
InconelX	AL 2014	0.3000	0.2000	4	6	0.7155	25.2666	0.1720
InconelX	AL 2014	0.3000	0.2000	4	4	0.5013	17.6018	0.1198
InconelX	AL 2014	0.3000	0.3000	4	8	0.5367	19.1403	0.1303
InconelX	AL 2219	0.2000	0.2000	2	8	0.6909	37.9750	0.0236

Continued on next page

metal1	metal2	R1 [m]	R2 [m]	B1	B2	pdiff [ns]	d_{mat_2} [mm]	std [mm]
InconelX	AL 2219	0.2000	0.2000	2	6	0.5474	30.0688	0.0186
InconelX	AL 2219	0.3000	0.2000	6	8	0.5376	12.7218	0.0079
InconelX	AL 2219	0.3000	0.2000	4	8	0.8590	30.4998	0.0189
InconelX	AL 2219	0.3000	0.2000	4	6	0.7155	25.3953	0.0157
InconelX	AL 2219	0.3000	0.2000	4	4	0.5013	17.6915	0.0110
InconelX	AL 2219	0.3000	0.2000	2	8	1.3588	75.5299	0.0468
InconelX	AL 2219	0.3000	0.2000	2	6	1.2152	67.5133	0.0419
InconelX	AL 2219	0.3000	0.2000	2	4	1.0011	55.4148	0.0344
InconelX	AL 2219	0.3000	0.2000	2	2	0.6678	37.0252	0.0230
InconelX	AL 2219	0.3000	0.3000	4	8	0.5367	19.2378	0.0119
InconelX	AL 2219	0.3000	0.3000	2	8	1.0365	57.8432	0.0359
InconelX	AL 2219	0.3000	0.3000	2	6	0.8211	45.8101	0.0284
InconelX	AL 5456	0.2000	0.2000	2	6	0.5474	29.3054	0.2011
InconelX	AL 5456	0.3000	0.2000	6	8	0.5376	12.3989	0.0851
InconelX	AL 5456	0.3000	0.2000	4	8	0.8590	29.7255	0.2040
InconelX	AL 5456	0.3000	0.2000	4	6	0.7155	24.7505	0.1699
InconelX	AL 5456	0.3000	0.2000	4	4	0.5013	17.2423	0.1183
InconelX	AL 5456	0.3000	0.2000	2	2	0.6678	36.0852	0.2477
InconelX	AL 5456	0.3000	0.3000	4	8	0.5367	18.7494	0.1287
InconelX	FE 17-7PH	0.2000	0.2000	2	8	0.6909	37.0639	0.1277
InconelX	FE 17-7PH	0.2000	0.2000	2	6	0.5474	29.3473	0.1011
InconelX	FE 17-7PH	0.3000	0.2000	6	8	0.5376	12.4166	0.0428
InconelX	FE 17-7PH	0.3000	0.2000	4	8	0.8590	29.7680	0.1025
InconelX	FE 17-7PH	0.3000	0.2000	4	6	0.7155	24.7860	0.0854
InconelX	FE 17-7PH	0.3000	0.2000	4	4	0.5013	17.2670	0.0595
InconelX	FE 17-7PH	0.3000	0.2000	2	6	1.2152	65.8935	0.2269
InconelX	FE 17-7PH	0.3000	0.2000	2	4	1.0011	54.0852	0.1863
InconelX	FE 17-7PH	0.3000	0.2000	2	2	0.6678	36.1369	0.1245
InconelX	FE 17-7PH	0.3000	0.3000	4	8	0.5367	18.7762	0.0647
InconelX	FE 17-7PH	0.3000	0.3000	2	8	1.0365	56.4554	0.1944
InconelX	FE 17-7PH	0.3000	0.3000	2	6	0.8211	44.7110	0.1540
InconelX	A286	0.2000	0.2000	2	8	0.6909	27.1812	0.1142
InconelX	A286	0.2000	0.2000	2	6	0.5474	21.5222	0.0904
InconelX	A286	0.3000	0.2000	6	8	0.5376	9.1059	0.0383

Continued on next page

metal1	metal2	R1 [m]	R2 [m]	B1	B2	pdiff [ns]	d_{mat_2} [mm]	std [mm]
InconelX	A286	0.3000	0.2000	4	8	0.8590	21.8307	0.0917
InconelX	A286	0.3000	0.2000	4	6	0.7155	18.1771	0.0764
InconelX	A286	0.3000	0.2000	4	4	0.5013	12.6629	0.0532
InconelX	A286	0.3000	0.2000	2	8	1.3588	54.0617	0.2271
InconelX	A286	0.3000	0.2000	2	6	1.2152	48.3237	0.2030
InconelX	A286	0.3000	0.2000	2	4	1.0011	39.6640	0.1666
InconelX	A286	0.3000	0.2000	2	2	0.6678	26.5014	0.1113
InconelX	A286	0.3000	0.3000	4	8	0.5367	13.7698	0.0578
InconelX	A286	0.3000	0.3000	2	8	1.0365	41.4022	0.1739
InconelX	A286	0.3000	0.3000	2	6	0.8211	32.7893	0.1377
InconelX	301	0.2000	0.2000	2	8	0.6909	19.9727	0.0641
InconelX	301	0.2000	0.2000	2	6	0.5474	15.8145	0.0508
InconelX	301	0.3000	0.2000	6	8	0.5376	6.6910	0.0215
InconelX	301	0.3000	0.2000	4	8	0.8590	16.0412	0.0515
InconelX	301	0.3000	0.2000	4	6	0.7155	13.3565	0.0429
InconelX	301	0.3000	0.2000	4	4	0.5013	9.3047	0.0299
InconelX	301	0.3000	0.2000	2	8	1.3588	39.7245	0.1276
InconelX	301	0.3000	0.2000	2	6	1.2152	35.5082	0.1140
InconelX	301	0.3000	0.2000	2	4	1.0011	29.1451	0.0936
InconelX	301	0.3000	0.2000	2	2	0.6678	19.4732	0.0625
InconelX	301	0.3000	0.3000	4	8	0.5367	10.1180	0.0325
InconelX	301	0.3000	0.3000	2	8	1.0365	30.4223	0.0977
InconelX	301	0.3000	0.3000	2	6	0.8211	24.0936	0.0774
InconelX	347	0.2000	0.2000	2	8	0.6909	36.7983	0.1657
InconelX	347	0.2000	0.2000	2	6	0.5474	29.1371	0.1312
InconelX	347	0.3000	0.2000	6	8	0.5376	12.3276	0.0555
InconelX	347	0.3000	0.2000	4	8	0.8590	29.5547	0.1331
InconelX	347	0.3000	0.2000	4	6	0.7155	24.6084	0.1108
InconelX	347	0.3000	0.2000	4	4	0.5013	17.1433	0.0772
InconelX	347	0.3000	0.2000	2	4	1.0011	53.6977	0.2418
InconelX	347	0.3000	0.2000	2	2	0.6678	35.8780	0.1616
InconelX	347	0.3000	0.3000	4	8	0.5367	18.6417	0.0839
InconelX	347	0.3000	0.3000	2	6	0.8211	44.3907	0.1999
InconelX	410	0.2000	0.2000	2	8	0.6909	35.5063	0.0808

Continued on next page

metal1	metal2	R1 [m]	R2 [m]	B1	B2	pdiff [ns]	d_{mat_2} [mm]	std [mm]
InconelX	410	0.2000	0.2000	2	6	0.5474	28.1141	0.0640
InconelX	410	0.3000	0.2000	6	8	0.5376	11.8948	0.0271
InconelX	410	0.3000	0.2000	4	8	0.8590	28.5171	0.0649
InconelX	410	0.3000	0.2000	4	6	0.7155	23.7444	0.0540
InconelX	410	0.3000	0.2000	4	4	0.5013	16.5414	0.0376
InconelX	410	0.3000	0.2000	2	8	1.3588	70.6198	0.1606
InconelX	410	0.3000	0.2000	2	6	1.2152	63.1244	0.1436
InconelX	410	0.3000	0.2000	2	4	1.0011	51.8124	0.1179
InconelX	410	0.3000	0.2000	2	2	0.6678	34.6183	0.0787
InconelX	410	0.3000	0.3000	4	8	0.5367	17.9872	0.0409
InconelX	410	0.3000	0.3000	2	8	1.0365	54.0830	0.1230
InconelX	410	0.3000	0.3000	2	6	0.8211	42.8321	0.0974
InconelX	RonHI	0.2000	0.2000	2	8	0.6909	44.0184	0.2371
InconelX	RonHI	0.2000	0.2000	2	6	0.5474	34.8539	0.1878
InconelX	RonHI	0.3000	0.2000	6	8	0.5376	14.7464	0.0794
InconelX	RonHI	0.3000	0.2000	4	8	0.8590	35.3536	0.1905
InconelX	RonHI	0.3000	0.2000	4	6	0.7155	29.4367	0.1586
InconelX	RonHI	0.3000	0.2000	4	4	0.5013	20.5069	0.1105
InconelX	RonHI	0.3000	0.2000	2	2	0.6678	42.9175	0.2312
InconelX	RonHI	0.3000	0.3000	4	8	0.5367	22.2993	0.1201
InconelX	Aluminum	0.2000	0.2000	2	8	0.6909	1.6645	0.0205
InconelX	Aluminum	0.2000	0.2000	2	6	0.5474	1.3180	0.0162
InconelX	Aluminum	0.3000	0.2000	6	8	0.5376	0.5576	0.0069
InconelX	Aluminum	0.3000	0.2000	4	8	0.8590	1.3368	0.0165
InconelX	Aluminum	0.3000	0.2000	4	6	0.7155	1.1131	0.0137
InconelX	Aluminum	0.3000	0.2000	4	4	0.5013	0.7754	0.0096
InconelX	Aluminum	0.3000	0.2000	2	8	1.3588	3.3106	0.0408
InconelX	Aluminum	0.3000	0.2000	2	6	1.2152	2.9592	0.0365
InconelX	Aluminum	0.3000	0.2000	2	4	1.0011	2.4289	0.0299
InconelX	Aluminum	0.3000	0.2000	2	2	0.6678	1.6229	0.0200
InconelX	Aluminum	0.3000	0.3000	4	8	0.5367	0.8432	0.0104
InconelX	Aluminum	0.3000	0.3000	2	8	1.0365	2.5354	0.0312
InconelX	Aluminum	0.3000	0.3000	2	6	0.8211	2.0079	0.0247
RonHI	AL 7079	0.3000	0.2000	6	8	0.5376	3.1518	0.1361

Continued on next page

metal1	metal2	R1 [m]	R2 [m]	B1	B2	pdiff [ns]	d_{mat_2} [mm]	std [mm]
RonHI	AL 7079	0.3000	0.2000	4	4	0.5013	4.3830	0.1893
RonHI	AL 7079	0.3000	0.3000	4	8	0.5367	4.7661	0.2058
RonHI	InconelX	0.2000	0.2000	2	8	0.6909	6.8658	0.2371
RonHI	InconelX	0.2000	0.2000	2	6	0.5474	5.4363	0.1878
RonHI	InconelX	0.3000	0.2000	6	8	0.5376	2.3001	0.0794
RonHI	InconelX	0.3000	0.2000	4	8	0.8590	5.5143	0.1905
RonHI	InconelX	0.3000	0.2000	4	6	0.7155	4.5914	0.1586
RonHI	InconelX	0.3000	0.2000	4	4	0.5013	3.1986	0.1105
RonHI	InconelX	0.3000	0.2000	2	2	0.6678	6.6940	0.2312
RonHI	InconelX	0.3000	0.3000	4	8	0.5367	3.4781	0.1201